Asymmetric current fluctuations and Andreev states probed with a Josephson junction

Q. Le Masne

THÈSE DE DOCTORAT DE
L'UNIVERSITÉ PARIS 6 - PIERRE ET MARIE CURIE

Spécialité :
Physique du solide

Présentée par

Quentin LE MASNE

Pour obtenir le grade de

DOCTEUR de l'UNIVERSITÉ PIERRE ET MARIE CURIE

Sujet de la thèse :

FLUCTUATIONS ASYMÉTRIQUES DE COURANT ET ÉTATS D'ANDREEV SONDÉS AVEC UNE JONCTION JOSEPHSON

soutenance le 29 octobre 2009

devant le jury composé de :

Nicolás AGRAÏT (Examinateur)
Joachim ANKERHOLD (Examinateur)
Olivier BUISSON (Rapporteur)
Roland COMBESCOT (Président du jury)
Jukka PEKOLA (Rapporteur)
Hugues POTHIER (Directeur de thèse)

Thèse préparée au sein du Service de Physique de l'Etat Condensé,
CEA-Saclay 91191 Gif-sur-Yvette

Avant-propos / Remerciements

Comme le financement de thèses dans le laboratoire d'électronique moléculaire, où je suis allé en stage de Master, ne s'adressait cette année là qu'aux étrangers, j'ai été frapper à la porte d'à côté, chez le groupe Quantronique (un peu par hasard, il faut l'avouer). Avant la première rencontre, j'ai voulu me renseigner sur ce qu'on y faisait, en lisant les thèses précédentes. Un peu dépassé par la partie scientifique, je me suis surtout concentré sur les remerciements. Ils étaient tellement dithyrambiques qu'ils m'ont presque convaincu à eux seuls de venir en thèse. Maintenant que vient mon tour d'écrire ces lignes, j'aimerais vanter moi aussi aux prochains curieux ce qu'ils gagneraient à passer quelque temps dans le groupe, et profiter de la chance que j'ai eue.

Il faut bien le reconnaître, tout a déjà été dit ou presque sur les qualités de cette équipe, alors j'ai presque honte de rajouter encore du miel, mais ils le méritent. Oui, les membres du groupe partagent tous un enthousiasme et une bonne humeur débordante, que ce soit pour la recherche comme pour plein d'autres sujets stimulants (sport, cinéma, littérature, macarons,...). Ce que d'aucuns pourraient considérer comme une certaine virulence dans leurs débats scientifiques provient surtout de leur rage de comprendre tout ce que vous serez capable de leur expliquer. Et oui, cela a été un vrai plaisir de faire partie pendant trois ans d'une équipe où l'on est encadré, formé et écouté, par des chercheurs que l'on estime. C'est indispensable pour mener à bien un projet de recherche qui promet inévitablement des moments difficiles, des échecs répétés, et des doutes sérieux avant d'aboutir. Ils m'ont appris l'importance d'un travail d'équipe, et j'en retiens que la recherche, c'est surtout aider et se faire aider. Enfin, trêve de science, j'ai surtout rencontré des amis amusants, intéressants et attachants.

Maintenant, quoi de mieux que cette section Remerciements pour tous vous remercier ? Alors merci Daniel, en premier lieu. Je considère que m'appeler six heures durant à mon camping depuis tes vacances, pour aller jusqu'à parsemer ma thèse de quelques "The" supplémentaires, est représentatif de ton engagement permanent pour le bon déroulement de la thèse. C'est aussi le signe de ton attachement aux thésards, tout simplement. Merci à vous, Hugues et Cristián, vous êtes deux formidables exemples de rigueur et d'enthousiasme. Merci de m'avoir accepté en thèse alors que je n'étais pas en stage chez vous, et d'avoir établi un superbe atelier de correction de thèse grande capacité pendant ma dernière ligne droite. Que serait une thèse en électronique sans la blague de Hugues sur "Cinquante Ohms, priez pour nous" et une rédaction de thèse concise et efficace sans la blague de Cristián sur le poisson frais ?

Merci à Pief et Pascal, pour m'avoir toujours accueilli et écouté quand je m'affalais sur une chaise dans leurs bureaux pour raconter mes malheurs (mais surtout pas pour leurs conseils sur les réparations automobiles, ils s'énerveraient

si je ne les remerciais que pour cela). A Denis, Patrice, Philippe aussi, pour toutes les discussions partagées, scientifiques ou non, ainsi que pour tous vos conseils et encouragements.

L'ambiance et le plaisir au travail étaient aussi largement alimentés par les autres doctorants et post-doctorants que j'ai cotoyés: merci à Hélène pour ses amusantes bougonnades, à François N. pour ses jolies chemises et son humour décalé (volontairement ?), ainsi qu'à François M., Charis, Florian, Agustin et Jean-Damien pour le temps qu'on a passé autour d'un thé le samedi après-midi, alors qu'on aurait dû être ailleurs. Thanks Maciej for the time shared facing this tough experiment and the long talks at night. Bonne chance à tous, ainsi qu'aux petits nouveaux : Yui, Max, Landry, Andreas. Bien sûr, il faut inclure aussi là-dedans tous les jeunes, du SPEC et d'ailleurs, avec qui j'ai partagé ces moments agréables et difficiles. Merci en particulier à Eva, pour son agréable compagnie pendant cette période de rédaction commune. Saluons aussi les anciens membres du groupe gravitant dans le même domaine, que l'on croisait souvent dans nos couloirs: Sophie, Frédéric, Anne, Benjamin, Maria Luisa, et bien sûr Marcelo.

Bien sûr, cette thèse n'aurait pas pu se faire sans le travail efficace des membres du SPEC : en premier lieu son responsable Eric Vincent et les secrétaires Sandrine Thunin, Nathalie Royer, Murielle Zyla, et Dijana Samson. Mais aussi Jean-Michel Richomme et sa sonnerie Panthère Rose, Pierre Janvier et son petit chauffage des pieds, et tous les membres, même à mi-temps, de l'atelier: Michel Juignet, Dominique Duet, Jean-Claude Tack, Jacques Proudowski, Philippe Forget et Vincent Padilla.

L'activité de recherche est aussi formidablement soutenue par des collègues et amis du groupe en visite, qui passent pour quelques heures ou quelques jours. J'aimerais remercier notamment Norman Birge, dont le recul sur les mesures de bruit (et la vie en général) a été essentiel, mais aussi Hermann Grabert, Joachim Ankerhold et Alfredo Levy Yeyati, trois théoriciens dont l'intérêt pour les résultats expérimentaux et la possibilité de les décrire étaient rafraîchissants. Ajoutons aussi Daniel Urban, pour son très gros travail sur l'expérience de mesure de bruit, et Konstantin Glaum, qui m'a décrit en détail tout ce qu'il savait sur l'aspect théorique du même sujet (j'ai fait de mon mieux pour en retenir quelque chose). De même, merci à toutes les personnes qui ont écouté mon histoire avec intérêt, qui m'ont parfois accueilli dans leurs laboratoires, ou avec qui j'ai tout simplement eu des discussions scientifiques aussi diverses qu'enrichissantes: Hélène Bouchiat, Sebastian Bergeret, Juan Carlos Cuevas, Michel Devoret, Julien Gabelli, Ronald Hanson, Leo Kouwenhoven, John Martinis, Fabien Portier, Bertrand Reulet, Christian Schönenberger, Vitaly Shumeiko, Lieven Vandersypen et Dominik Zumbühl.

Finally, I would like to thank very much the members of my thesis committee: Olivier Buisson, Jukka Pekola, Joachim Ankerhold, Nicolas Agraït and Roland Combescot.

Dans un autre registre, il m'est arrivé, lors de rares moments passés hors du labo, d'avoir une vie sociale. C'est dans ces moments là que j'ai pu profiter des longues discussions tardives avec mon colocataire Pierre et notre hôte régulière Naïs sur la difficulté de la thèse, autour d'un thé mal sucré, tout en réfléchissant au prochain article pour le mort-né International Journal of Nothing, le seul journal à facteur d'impact négatif. Merci à vous pour ces moments de détente, mais aussi à Laurent, qui a carrément participé à ma thèse, ainsi qu'à tous mes amis qui m'ont encouragé pour la soutenance (sauf ceux qui m'ont encouragé à ne pas y aller).

Bien sûr, merci à tous les membres de ma famille, qui ne se sont que modérément moqués de moi durant cette thèse et qui n'ont pas tous dormi durant la soutenance, pour ceux qui ont pu y être.

Enfin, j'aimerais dédier cette thèse d'abord à mes grands-parents maternels, disparus juste avant que j'aie pu leur donner une raison de m'appeler docteur, mais aussi à Zena, qui m'a littéralement porté jusqu'au bout, jusqu'a ce que j'aie fini de faire joujou avec la science et qu'on puisse enfin passer aux choses sérieuses.

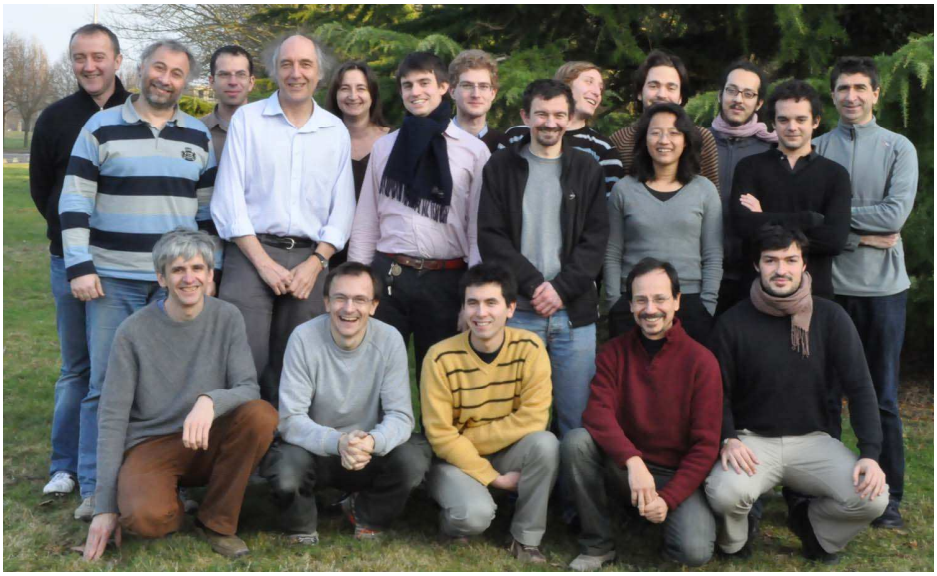

Le groupe Quantronique début 2009

Premier rang, de g. à d.: Hugues Pothier, Maciej Zgirski, François Nguyen, Cristián Urbina, Quentin Le Masne. *Debout, de g. à d.:* Pascal Senat, Denis Vion, Patrice Bertet, Daniel Estève, Dijana Samson, Agustin Palacios-Laloy, Matthias Kende, Philippe Joyez, Jean-Damien Pillet, Landry Bretheau (derrière), Charis Quay (devant), Florian Ong, François Mallet, Pief Orfila.

Contents

Chapter 1

Introduction

1.1 Josephson effect and mesoscopic physics

Experiments on the Josephson effect were initiated in 1963 by the observation by Anderson and Rowell [1] of "an anomalous dc tunneling current at or near zero voltage in very thin oxide barriers between superconducting Sn and Pb", thus confirming the striking predictions that Josephson had made in 1962 [2]. Various kinds of superconducting weak links were subsequently explored, but Josephson tunnel junctions, in which the coupling between electrodes proceeds through a large number of electronic channels with very small transmissions, have played a central role in the field since then. This is mainly due to the very simple form that the Josephson Hamiltonian adopts in this case, namely $\mathcal{H}_J = -E_J \cos\gamma$, where E_J is the Josephson energy proportional to the tunnel conductance, and γ the phase difference between the superconducting order parameters of both electrodes. The supercurrent-phase relation is given by the first Josephson relation $I = I_0 \sin\gamma$ where $I_0 = E_J/\varphi_0$ is the critical current with $\varphi_0 = \hbar/2e$, and the phase evolves according to the second Josephson relation $V = \varphi_0\dot{\gamma}$.

The Josephson junction is thus a simple system with a single degree of freedom, and Josephson junctions physics developed in many directions to investigate a wide range of physical problems [3]. An important example, thoroughly exploited in this thesis, is the switching out of the zero-voltage state of a current-biased Josephson junction. After switching, the voltage is finite, the phase evolves continuously, and the average supercurrent nearly vanishes. Depending on the parameters, this switching precisely implements either the celebrated Kramers problem of the thermally activated escape of a particle out of a metastable state trapped

in a potential well [4], or the problem of Macroscopic Quantum Tunneling (MQT) [5].

Josephson junctions also provided a novel electrical element, based on which many new devices have been implemented [3]. In the SIS mixer, the non-linearity of the current-voltage characteristic is exploited to mix the signal collected by an antenna with a local oscillator to produce a signal at a lower frequency where detection is performed. Another Josephson device widely used for applications is the famous dc-SQUID that consists of the parallel combination of two junctions forming a superconducting loop that can enclose a magnetic flux. The Hamiltonian and hence all the properties of the device are periodically modulated by the flux, with a period given by the flux quantum $\Phi_0 = h/2e$, which makes the dc-SQUID the most sensitive flux sensor [6]. Recently, the use of the dc-SQUID was further extended to microwave amplification by feeding the incoming signal through a microwave coil microfabricated above the SQUID loop [7, 8].

This thesis goes along this line of exploiting Josephson junctions for making a new device. In the first part, I describe a new generation of detectors that I have developed for analyzing the fluctuations of the current flowing through a mesoscopic conductor, a question that has generated recently a great interest in the mesoscopic physics community. Indeed, Levitov and Lesovik [9], followed by many others, have demonstrated that the asymmetry of the current distribution around its mean gives access to information present neither in the average value of the current, nor in its quadratic fluctuations. For example, in the simple case of a metallic diffusive wire, the diffusion time enters the frequency dependence of this asymmetry, which is related to the third moment of the fluctuations [10]. Our detector exploits the exponential dependence of the switching rate of a Josephson junction on the bias current for detecting current fluctuations added to it. Elaborating on a previous experiment developed in the Quantronics group, we have demonstrated in a model case that our detection scheme allows to access the asymmetry of current fluctuations, and that recent theories [11, 12] account quantitatively for the data.

The second part of this thesis also makes use of Josephson junctions as a tool to tackle a fundamental problem in mesoscopic superconductivity. Beyond the Josephson tunnel junction, there exists an even more elementary weak-link structure, namely the short single channel contact with arbitrary transmission. This very simple structure, which can be thought of as the building block of all short weak-links, can be fully analyzed

using the concept of Andreev reflection initially developed for describing normal-superconducting interfaces [13]. The coupling between the electrodes generates a set of two level systems, called the "Andreev bound states" pairs, which carry the supercurrent [14, 15, 16]. These doublets have been proposed recently as possible new Qubits [17].

The predictions of this theory can be tested using superconducting atomic contacts, which are simple systems with a small number of channels whose transmission can be varied and measured [18, 19]. In particular, the predictions for the supercurrent in the ground state have been successfully tested very recently by the Quantronics group, through the measurement of the switching current of a SQUID-like device consisting of an atomic contact in parallel with a regular Josephson junction [20]. However, the structure of the Andreev doublets has never been directly probed. During my thesis, I have designed and run new experiments aiming at characterizing the expected doublets of Andreev states, and obtained preliminary results.

The two parts of my thesis, together with the results, are now introduced in more details.

1.2 Detecting asymmetric noise with a Josephson junction

Noise is the signal...

The current flowing through a conductor always fluctuates around its mean value. While some of these fluctuations can simply originate on experimental artifacts or uncontrolled parameters, and can be in principle avoided by careful and proper design, there are fluctuations that arise from fundamental and unavoidable causes: the thermal fluctuations of the populations of the electronic states in the conductor or the randomness introduced by scattering processes of the charge carriers within the conductor. These fluctuations constitute an important source of information about the microscopic mechanisms behind charge transport.

Noise conveys useful information...

Working on vacuum diodes, Schottky determined in 1918 a link between the current fluctuations and the charge of the carriers. When charge transfer proceeds through independent and rare non-overlapping events, the spectral density at low frequency of the current noise reduces to:

$$S_2^D = 2qI_N$$

where q is the "effective charge" transferred at each event, and I_N the mean current flowing through the conductor. This noise, reminiscent of the one of the rain on a roof, results from the discreteness of charge carriers and has been coined shot noise. Shot noise has been widely exploited to characterize transport mechanisms [21]. Let us mention here the evidence for fractional charges $q = e/3$ at 1/3 Landau level filling of a two-dimensional electron gas [22, 23], the confirmation of shots with $q = 2e$ in Andreev reflection at a normal-superconducting contact [24], and the observation of large shots $q = ne$ due to Multiple Andreev reflections in superconducting atomic contacts [25]. In all these experiments, the noise was probed through its spectrum, which corresponds to the second-order correlation function of the fluctuations.

Meanwhile, a theoretical breakthrough arose when Levitov and Lesovik introduced in mesoscopic physics the concept of Full Counting Statistics [9, 26], giving access to higher order correlators of the noise. In this framework, one considers the fluctuation of the number N of electrons having passed across a conductor during a probing time τ_p. The random variable N is governed by a probability distribution $P(N, \tau_p)$, which provides a full description of current fluctuations. The second moment of N is equivalent to the second-order correlator of the current noise, i.e. to the noise spectrum. The third moment of N, equivalent to measuring $\langle \delta I_N^3 \rangle$, characterizes the asymmetry of the current fluctuations.

... but few experiments have measured noise asymmetry

Experimentally, accessing directly the probability distribution P of the current fluctuations remains an unsolved challenge. One can however access the moments of order p of the current fluctuations $\langle \delta I_N^p \rangle$, but measuring high order moments is very challenging because no measurable physical quantity has been found to directly determine a given moment.

The first experimental determination of a third moment was achieved for a tunnel junction by Reulet [27] who obtained $\langle \delta I_N^3 \rangle$ using microwave mixers operated at room temperature in a bandwidth large enough to obtain a measurable signal. These experiments represent a real tour de force, requiring very long averaging times and precise calibration of the microwave circuit. It soon became clear that an on-chip detector, close to the sample (as compared to the wavelength of the signals), would provide a better approach to measure the noise asymmetry. In 2004, Tobiska

and Nazarov precisely proposed to use a Josephson Junction as such an on-chip detector to access the full counting statistics of the noise [28]. The first experimental realization of such a detector was implemented by Pekola by adding the shot noise generated by a tunnel junction to the bias current of the junction [29].

This thesis pursues the experimental effort initiated in the Quantronics group for implementing such a scheme.

A new noise detector

Switching of a Josephson junction ...

The current-voltage characteristic of a Josephson junction measured at low temperature ($k_B T \ll E_J$) is shown in Fig. 1.1(a). Because of fluctuations of the bias current, switching out of the zero voltage state is observed at a current slightly smaller than the critical current I_0 at which the barrier height for switching out of the zero-voltage state vanishes. The escape process is characterized by the lifetime τ_{esc}, or conversely by the escape rate $\Gamma = \frac{1}{\tau_{\mathrm{esc}}}$, which, in the thermal regime, is essentially determined by the ratio of the barrier height to the temperature associated to the fluctuations and the dissipation. Switching is hysteretic, which makes the junction a real "sample-and-hold" detector and allows easy detection of switching by measuring the voltage across the junction. The exponential sensitivity of the escape rate Γ on the bias current makes a Josephson junction a sensitive current detector. It is also a fast detector since its response time is determined by the fast phase dynamics in the zero voltage state.

... can detect noise asymmetry

Although the main effect of an added noise on the escape rate is to increase the effective temperature of the escape process $T_{\mathrm{eff}} \propto -\ln \Gamma$, it was demonstrated theoretically that noise asymmetry also affects switching [11, 28, 30, 31, 32, 33, 34]. The second moment of the shot noise increases the switching rate, with a small correction due to the third moment. Experimentally, this smaller effect is accessed by inverting the sign of the current flowing through the noise source, thus inverting the contribution of the added noise to the bias current of the detector. The rate is measured in both cases (Γ_+ and Γ_-), and the rate asymmetry $R_\Gamma = \frac{\Gamma_+}{\Gamma_-}$, insensitive to even moments of the noise, is a measure of the third moment. The first experiment performed in the group during the thesis of Benjamin Huard [35, 36] confirmed the effect of the second

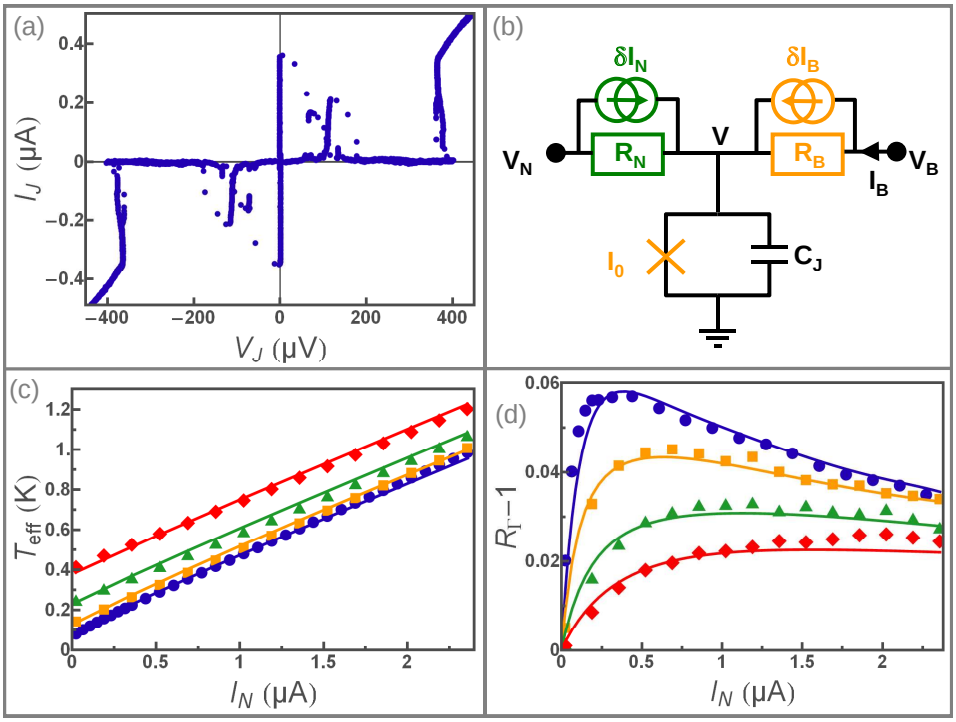

Fig. 1.1. Detector of asymmetric noise based on the switching of a current biased Josephson junction. The setup (b) consists of a Josephson junction ($I(V)$ characteristics in (a)) biased by a dc current to which a non-Gaussian asymmetric current noise is added. The variations of the escape temperature of the junction with the mean noise current is shown for different temperatures in (c). The asymmetry of the rate when the noise adds or subtracts to the dc current is shown in (d), where solid lines are predictions. This rate asymmetry measures the noise asymmetry.

moment and detected a rate asymmetry, but the data could not be quantitatively understood, probably due to spurious experimental artifacts. Another experiment [37] also demonstrated the sensitivity of switching to the third moment, and confirmed, by measuring the rate asymmetry for different noise sources, that a macroscopic resistor produces a symmetric noise. However, a proper comparison with theory could not be achieved neither.

A quantitative noise asymmetry detector

During this thesis, we have developed a new generation of experiments for measuring the rate asymmetry and achieving a quantitative comparison with theory in the simple case of the noise produced by a tunnel junction. This benchmark experiment confirms the possibility to use a Josephson junction as a quantitative detector for the asymmetric part of the noise.

The setup used in this experiment is represented in Fig. 1.1(b). The plasma frequency of the detector is designed to ensure that no quantum correction or quantum tunneling effects enter in the description of the escape rate. The noise produced by the tunnel junction is added through an on-chip RC filter to the dc bias of the Josephson junction detector. The noisy tunnel junction is voltage-biased, and its current I_N can be inverted.

The dominant effect of the second-moment of the noise on the escape temperature determined from the switching rate is shown in Fig. 1.1(c). The observed increase agrees with predictions without adjustable parameters. The third moment of the noise, accessed through the rate asymmetry, was measured at a fixed value of the rate and a given bias current for each effective temperature, as shown in Fig. 1.1(d). Although the existing published theory does not apply in principle to our setup, in which the noise transmission from source to detector and the dissipation experienced by the detector vary with frequency, we found that, apart from a scaling factor, the measured rate asymmetry is adequately described by the predictions [38]. Recently, Urban and Grabert [12] have been able to extend this theory by treating frequency dependent circuits, and have obtained a quantitative agreement with our data. This important theoretical progress demonstrates that the third moment of current noise can be quantitatively extracted from rate asymmetry measurements of a Josephson junction.

Conclusions & perspectives

The experiment described in the first part of this thesis demonstrates that a Josephson junction can be used to measure the third moment of current fluctuations. This on-chip detector strategy is versatile and efficient, as it does not require tedious microwave calibrations of the whole circuit including components and cables at room temperature, and can be applied to samples presenting arbitrary impedances. However, our experiment also shows that frequency effects are important. Achieving a better control of the transfer function from the noise source to the detector, so as to be able to describe the rate asymmetry by the frequency-independent theory, is a necessary step to consider this detector as a generic "Third-moment-meter". With this in hand, the next step would be to investigate interesting physical systems like quantum point contacts, for which the third moment is predicted to vary as $\sum \tau_n(1-\tau_n)(1-2\tau_n)$ [39] where $\{\tau_n\}$ are the transmissions of the channels, or the regime of multiple Andreev reflections in superconducting atomic point contacts in which

charge transfer involves a large number of electrons, and where the noise asymmetry can change sign as a function of the channel transmissions [40].

It is however important to note that Josephson junction detectors, initially proposed to extract the Full Counting Statistics of the current noise from the variations of the switching rate at different bias currents, face experimental difficulties that prevent from accessing moments beyond the third one, at least for a simple Josephson junction [11]. Note however that particular ranges of detection parameters facilitating such measurements have been proposed, but the requirements seem hardly achievable [41].

1.3 Towards Andreev states spectroscopy

Andreev bound states...

The second part of this thesis deals with the general picture of the Josephson effect that arose during the last years of the 20^{th} century within the framework of mesoscopic superconductivity, and which allows to treat on the same footing all the different possible weak links (tunnel junctions, point contacts, bridges of normal metal or of exotic materials like carbon nanotubes,...). Within this framework, the elementary Josephson weak link is a single conduction channel with arbitrary transmission τ connecting two superconducting electrodes. The central ideas are that any weak link can be decomposed into a set of such channels, and that within each channel the supercurrent is carried through a set of localized quasiparticle states which come in pairs, the "Andreev bound states".

...in a short single channel superconducting contact

An important simplification occurs when the channel is shorter than the superconducting coherence length because in this case the solution of the Bogolubov-De Gennes equation [42] consists of just a single pair of Andreev bound states. These states are described as resonant electron-hole quasiparticle states spreading slightly in both electrodes around the weak-link, with energies:

$$E_{\pm}(\delta,\tau) = \pm\Delta\sqrt{1-\tau\sin^2\left(\frac{\delta}{2}\right)}$$

where Δ is the superconducting gap, and δ is the superconducting phase difference between the order parameters of both reservoirs. The variations

of these energies with δ at different channel transmissions are shown in Fig. 1.2(a).

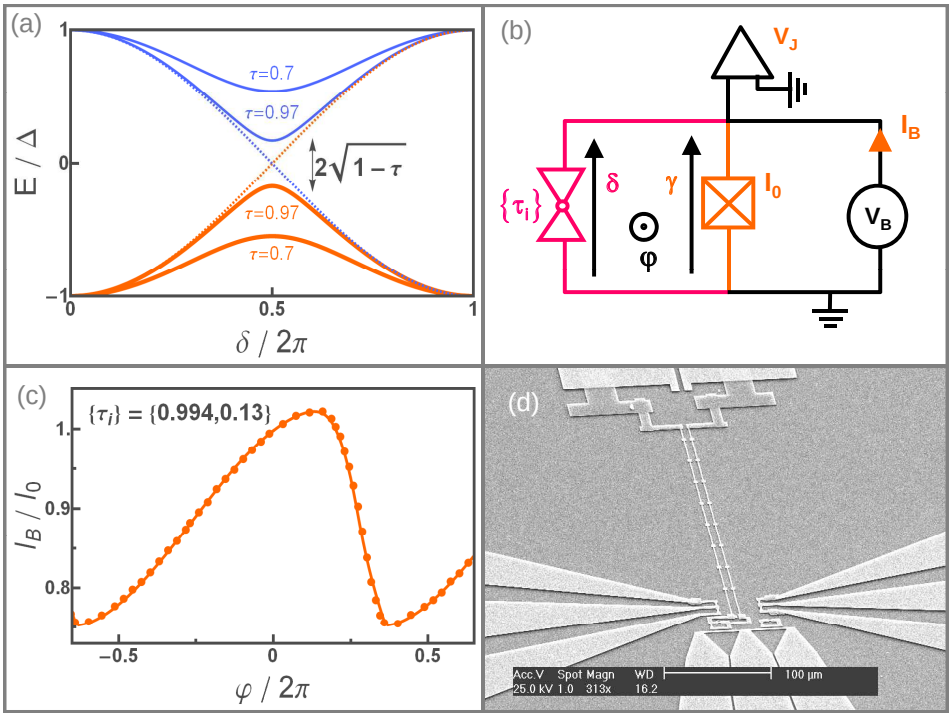

Fig. 1.2. (a) Energies of Andreev states versus the phase difference for a superconducting short single channel for transmissions 0.7 and 0.97. (b) Schematics of the Atomic SQUID circuit used for measuring the supercurrent through a superconducting atomic contact. (c) The variations of the switching current of the Atomic SQUID with the flux through its loop perfectly reflect the current-phase relation calculated from the independently measured transmissions of the contact. (d) Scanning electron micrograph of an Atomic SQUID circuit designed to perform the spectroscopy of the Andreev levels. A coplanar transmission line (at the bottom)) allows microwave flux excitation of the Atomic SQUID; the long thin wires (top region) are inductors that isolate the Atomic SQUID from the external circuit at high frequencies.

A potential qubit ?

The Andreev states in a short single channel Josephson structure constitute a two-level system that has been proposed as the basis for a new qubit by including it in a superconducting loop [17]. What is particularly interesting and novel is that, in contrast with all other superconducting qubits based on Josephson junction circuits [43], an "Andreev qubit" is a microscopic two level system like spin qubits in semiconducting quantum dots. There are several essential steps that have to be accomplished

before being able to attempt any quantum manipulation of an Andreev doublet. First, it is necessary to characterize the states and to be able to measure the current they carry. Second, it is necessary to perform the spectroscopy of the doublet. And finally, the relaxation time of the excited state, and the dephasing time of a quantum superposition of the two states, have to be measured, understood and controlled if possible.

Supercurrent in atomic contacts

The measurement of the current-phase relation of superconducting atomic contacts was recently performed in the Quantronics group [20] using a new circuit with a SQUID-like geometry, as shown in Fig. 1.2(b). This circuit consists of an atomic contact in parallel with a Josephson junction and has been nicknamed the "Atomic SQUID". First, the $I(V)$ characteristics of the contact is obtained by subtracting from the $I(V)$ of the Atomic SQUID that of the junction (obtained after completely breaking the atomic contact). The channel transmissions, accurately determined from this $I(V)$, are then used to calculate the expected current-phase relation of the contact. Secondly, the switching current of the Atomic SQUID is measured as a function of the flux through the loop [20, 36, 44, 45]. If the critical current of the junction is large, and the phase across the Josephson junction is subject to small fluctuations, this Atomic SQUID geometry allows an almost perfect phase bias of the contact. As shown in Fig. 1.2(c), the measured variations of the switching current are perfectly described by theory, if one considers simply the current-phase relation of the lower Andreev state of each channel.

New experiments to probe the Andreev doublet

During my thesis we carried out several experiments on Atomic SQUIDs with the aim of performing the microwave spectroscopy of the Andreev levels of the atomic contact. Although for the moment we have not reached this goal, several important technical locks have been overcome, and preliminary results have been obtained.

A spectroscopy experiment requires:

1. A well characterized atomic contact;
2. A phase-biasing circuit under control;
3. The controlled injection of an external excitation matching the Andreev frequency $\nu_A(\delta)$, which must lie in an experimentally accessible range;
4. A long enough relaxation time of the upper state in order to detect its population within the time scale of the measurement.

As mentioned above, we have already shown that the Atomic SQUID setup can fulfill the first two criteria. However, the last two require further developments.

Because we access the state of the Atomic SQUID through switching experiments, the phase across the atomic contact is in fact a dynamical variable with both thermal and quantum fluctuations. Depending on the actual design and parameters of the global circuit, there can be significant departures from an ideal phase-bias situation, and important modifications of the Andreev frequency as calculated for an isolated contact.

Bias current microwave excitation of an Atomic SQUID in the classical regime

We first attempted to excite the atomic contact during the measurement of its supercurrent-phase relation by adding a small microwave current to the dc bias-current of the Atomic SQUID, for a sample in the classical regime. Indeed, if a transition occurs from the lower to the upper Andreev state, which carries an opposite supercurrent, the switching current of the Atomic SQUID would be significantly modified. Although we have found that applying microwaves does affect switching of the Atomic SQUID, we could not relate the observed changes to the expected Andreev transition frequency. Furthermore, we found that the SQUID shunt capacitance, which was intentionally fabricated in order to be in the classical escape regime, prevented us from injecting large enough microwave currents in the atomic contact. Finally, the dissipation might have been too large to induce a sufficient population of the upper Andreev state.

Flux microwave excitation of an Atomic SQUID in the quantum regime

In order to both solve this coupling problem and control the lifetime of the excited state, we have designed and operated a new circuit (see Fig. 1.2(d)). For the former goal, the microwave excitation is performed via an on-chip coplanar antenna which couples to the flux threading the SQUID loop. For the latter, the low capacitance Atomic SQUID is isolated by nanofabricated inductors from the low impedance connecting lines. In order to test this on-chip electromagnetic environment, we have performed a preliminary experiment with a two-junctions symmetric SQUID. The plasma resonance of the SQUID could be observed using the flux excitation line, and the ensemble of the results validates the parameters of the new design.

An important consequence of these changes is that in this new circuit the phase across the junction is a quantum variable with sizable quan-

tum fluctuations, and switching is dominated at low temperatures by MQT. Moreover, the coupled quantum dynamics of the contact and the junction could lead, depending on the actual parameters, to very significant departures of the Andreev frequency from the value expected for the isolated contact.

Conclusions & perspectives

In the experiments described in the second part of this thesis we used a Josephson junction to probe the supercurrent of well-characterized atomic contacts. If the contribution of the Andreev ground state of each channel to the supercurrent is by now perfectly identified, the role of the excited states remains elusive. We have identified both practical and fundamental issues that have prevented us from performing the spectroscopy of Andreev doublets, and new experiments are under way.

If the spectroscopy is achieved, one could then envision to create, using well controlled microwaves pulses, coherent superpositions of the two Andreev states in one or several channels of an atomic contact. It is however important to note that, even if the coherence time is found to be long enough, controlling the possible coupling between the different channels would present a formidable challenge.

Part I

Detecting noise asymmetry using a Josephson junction

Chapter 2

Escape of a Josephson junction out of the metastable state

In this chapter, we review some results on the escape rate of a Josephson out of its zero-voltage state. Having defined in a first section the dynamics of the junction in the tilted washboard potential, we present the expressions for the rate in both the thermal activation regime and the Macroscopic Quantum Tunneling regime. The case of thermal activation is extended in the final section, where a non-Gaussian noise is added to the bias current of the junction. We compare recent theoretical predictions for the escape rate in this regime.

2.1 The Josephson junction in an electromagnetic environment

2.1.1 The Josephson junction

A Josephson junction [2] consists of two superconducting electrodes separated by a thin insulating layer (see [3] for a review of Josephson junction physics). It can be modeled as shown in Fig. 2.1 by a pure Josephson element in parallel with a capacitance C_J. The Josephson element allows the tunneling of Cooper pairs with the characteristic Josephson energy $E_J = \varphi_0 I_0$, where I_0 is the critical current of the junction and $\varphi_0 = \hbar/2e$ the reduced flux quantum. The critical current corresponds to the maximal possible supercurrent. The presence of the capacitor introduces another energy scale, the charging energy $E_C = \frac{e^2}{2C_J}$ of the capacitor, where e is the elementary charge. In this thesis, one only considers Josephson junctions in the regime $E_J \gg E_C$ in which charging effects are negligible.

The phase difference γ between the phase of the order parameters in the two superconducting electrodes is the relevant variable in this limit, and the Hamiltonian for the Josephson junction reduces to:

$$\mathcal{H}_J = -E_J \cos\gamma. \tag{2.1}$$

The phase difference γ is linked to the voltage drop V across the junction by the Josephson relation:

$$\varphi_0 \dot{\gamma} = V. \tag{2.2}$$

Since the number of charges having tunneled through the junction is the conjugated variable of the phase difference [46], the current operator is obtained as:

$$\hat{I} = \frac{1}{\varphi_0} \frac{\partial \mathcal{H}_J}{\partial \gamma}. \tag{2.3}$$

Hence, in a classical description of an electromagnetic circuit, the current through a phase-biased Josephson junction is:

$$I = I_0 \sin\gamma. \tag{2.4}$$

Let us now consider the case where the phase difference γ is not fixed, but is oscillating with a small amplitude around $\langle\gamma\rangle$. Using the Josephson relations (Eq. (2.2) and (2.4)), the voltage across the junction is related to the derivative of the current flowing through it by:

$$V \simeq \frac{\varphi_0}{I_0 \cos\langle\gamma\rangle} \frac{\mathrm{d}I}{\mathrm{d}t}, \tag{2.5}$$

which corresponds to the response of an inductor having an effective inductance

$$L_J = \frac{L_{J0}}{\cos\langle\gamma\rangle}. \tag{2.6}$$

We defined here the Josephson inductance at zero bias

$$L_{J0} = \frac{\varphi_0}{I_0}. \tag{2.7}$$

A pure Josephson junction in this regime can thus be thought in electrical engineering terms as a non-linear inductor.

2.1.2 The RCSJ Model

Practically, the junction is always embedded in an electrical circuit, therefore connected to an electromagnetic environment described by its admittance $Y(\omega)$ that controls the dynamical properties of the junction.

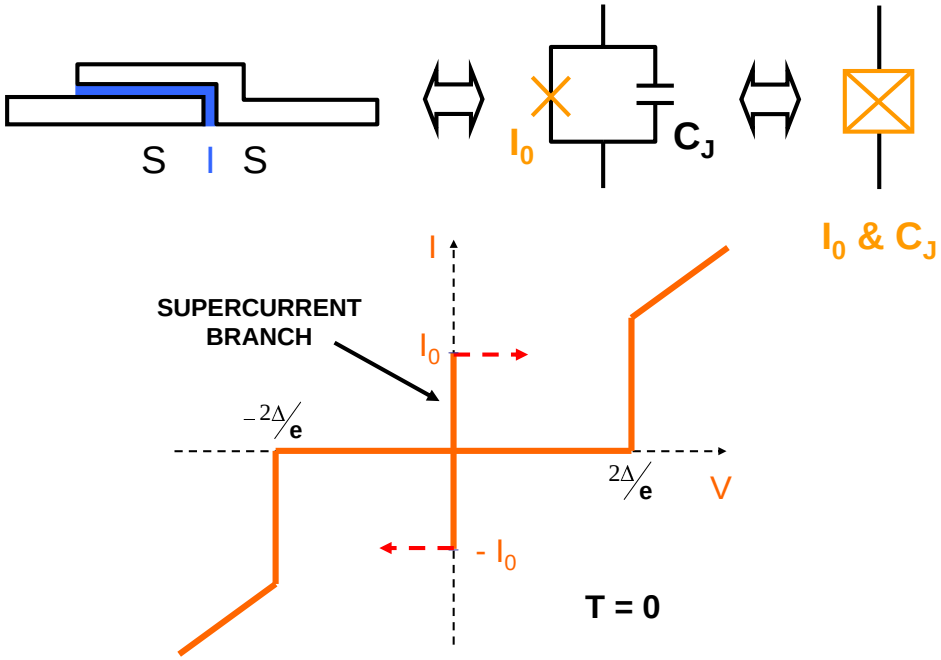

Fig. 2.1. Top: The Josephson junction is obtained at the overlap of two superconducting electrodes separated by a thin insulating layer. It is described by the parallel combination of a pure Josephson element and a capacitor. This association is usually represented by a crossed box symbol. **Bottom:** Schematic representation of the $I(V)$ characteristics of a current-biased Josephson junction within the RCSJ model, at zero temperature. The supercurrent branch is observed at zero voltage, up to the critical current I_0. For $0 \leq V \leq \frac{2\Delta}{e}$, the dc current is zero. Above $\frac{2\Delta}{e}$, the Josephson junction behaves like a normal metal tunnel junction of resistance R_J, related to the critical current by the Ambegaokar-Baratoff relation [47] (see Appendix B.6).

The simplest model for the electromagnetic environment has been proposed by Stewart and McCumber [48, 49] (see Fig. 2.2). In this model, the pure Josephson element of critical current I_0 is shunted by a capacitance C_J and a resistance R. It has thus been coined the Resistively and Capacitively Shunted Junction model (RCSJ). Using this RCSJ model is the key to describe the $I(V)$ characteristics of a Josephson junction, and specifically the supercurrent branch at zero voltage represented in Fig. 2.1. The switching out of the supercurrent branch to a dissipative state at finite voltage is the subject of this chapter.

Equations of the circuit

The equations describing the behavior of the circuit shown in Fig. 2.2 are obtained from Kirchoff's laws and Josephson relations:

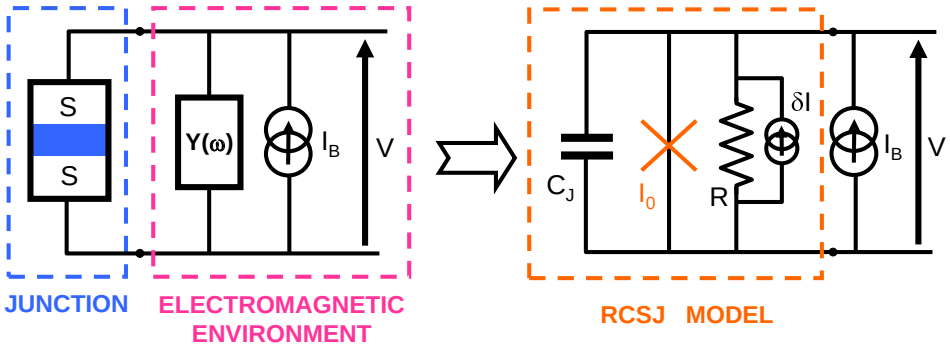

Fig. 2.2. Left: Electrical model for a current-biased Josephson junction embedded in an electromagnetic environment $Y(\omega)$, biased by a current I_B. **Right:** The RCSJ model considers a pure Josephson element shunted by a capacitance C_J and a resistance R. To the resistance R at temperature T are associated current fluctuations δI, represented here as a noise source in parallel.

$$\begin{cases} \frac{1}{\varphi_0} V = \dot{\gamma} \\ C_J \varphi_0^2 \ddot{\gamma} + \frac{\varphi_0^2}{R} \dot{\gamma} + E_J \left[\sin \gamma - s \right] = \varphi_0 \delta I \end{cases} \tag{2.8}$$

where $s = \frac{I_B}{I_0}$ is the reduced bias current. The Johnson-Nyquist current fluctuations δI originate from thermal fluctuations of the energy states populations in the resistor, and are introduced as a noise source in parallel with the resistance. The correlation function of the current fluctuations is obtained from the fluctuation-dissipation theorem as:

$$\langle \delta I(t) \delta I(t') \rangle = \frac{2 k_B T}{R} \delta(t' - t), \tag{2.9}$$

where T is the temperature of the resistor. The equilibrium position of the phase difference γ is found for $\langle \gamma \rangle = \arcsin s$ when $s < 1$. Using Eq. (2.6), the effective inductance of the biased junction is thus:

$$L_J(s) = \frac{L_{J0}}{\sqrt{1 - s^2}}. \tag{2.10}$$

Mechanical analogy: a particle in a tilted washboard potential

Electrical equations (2.8) are completely similar to the mechanical equations of motion of a fictitious massive particle evolving in a titled washboard potential $U(x, s) = -E_J \left[\cos x + s x \right]$ (see Fig. 2.3). The phase difference γ is equivalent to the position x of the particle, the voltage $\frac{1}{\varphi_0} V$ is equivalent to its velocity v, the mass of the particle corresponds to $m = C_J \varphi_0^2$, and the damping term is written as $\chi = \frac{1}{R C_J}$. The fluctuating force acting on the particle $\xi(t) = \varphi_0 \delta I(t)$ is characterized by:

$$\langle \xi(t)\xi(t')\rangle = \frac{2m\chi}{\beta}\delta(t'-t). \tag{2.11}$$

This term $\xi(t)$ can also be seen as a fluctuation of the tilt of the potential. This analogy is summarized in Table 2.1.

Element	Mechanical	Electrical
position	x	γ
velocity	v	V/φ_0
mass	m	$C_J\varphi_0^2$
damping	χ	$(RC_J)^{-1}$
potential	$U(x,s) = -E_J\left[\cos x + sx\right]$	$-E_J\left[\cos\gamma + s\gamma\right]$
noise	ξ	$\varphi_0\delta I$
correlation	$\langle \xi(t)\xi(t')\rangle = \frac{2m\chi}{\beta}\delta(t'-t)$	$\langle \delta I(t)\delta I(t')\rangle = \frac{2k_BT}{R}\delta(t'-t)$

Table 2.1. Correspondence between the RCSJ model for a Josephson junction and the dynamics of a fictitious particle in a tilted washboard potential.

Using the notations $\dot{x} = \partial_t x$ and $U'(x) = \partial_x U$, the equivalent equations are:

$$\begin{cases} v = \dot{x} \\ m\ddot{x} + m\chi\dot{x} + U'(x) = \xi(t). \end{cases} \tag{2.12}$$

In the following, the dynamics of the phase difference is often described with the equivalent mechanical model.

2.1.3 Dynamics of the fictitious particle

Switching out of the zero-voltage state

In order to get some insight of the dynamics of the particle, let us first consider a case without any fluctuations (i.e. at zero temperature in this classical model). Two states are possible for the particle (see Fig. 2.3):

- For $s < 1$, the potential U presents local minima, and the particle is trapped in one of them. Its position is fixed and the velocity is zero on average. This corresponds to the dc Josephson effect or the supercurrent branch, where the phase is constant. The current is given by Eq. (2.4).
- For $s \geq 1$ the local minima disappear and the particle runs down the potential. This corresponds to a running state with a finite voltage.

Switching between those two states is thus observed exactly at $s = 1$.

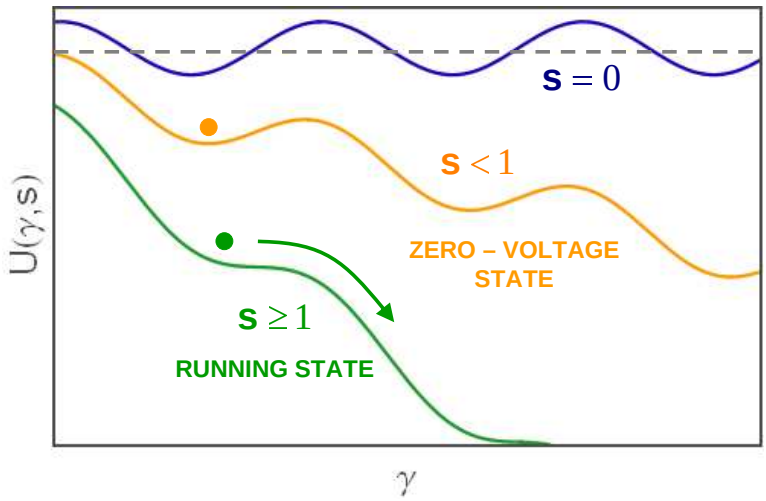

Fig. 2.3. Tilted washboard potential associated to the dynamics of the phase in absence of fluctuations (zero temperature in this classical model). For $s \leq 1$, the potential presents wells in which the particle is trapped. For $s \geq 1$, the wells disappear and the particle gets into to a running state.

However, in a practical experiment, the fluctuations are always present. Due to the current fluctuation δI, the state of the particle trapped in one of the wells is metastable. The particle oscillates in the well, and it has a finite probability to *escape* out of this well. The particle then undergoes a trajectory that extends over several wells and depends on the damping (see Fig. 2.4):

- If it has a sufficient kinetic energy, the particle is able to overcome the successive barriers, and it reaches a running state. There is then a finite voltage across the junction. The *switching* is thus again observed, but for a reduced bias current $s_{\mathrm{sw}} < 1$.
- If the particle does no gain a sufficient energy from one well to the next one due to large losses, it can be retrapped in one of the following wells, then escape again, and slowly evolve down the potential with this succession of escape and retrapping. This situation corresponds to the *phase diffusion regime*. The voltage across the junction thus evolves gradually from zero to an extremely small value, with no sudden change. Since experimentally the dynamics of the junction is monitored through the voltage across it, the measurement of the escape of the junction out of the zero-voltage state gets very delicate when approaching this regime.

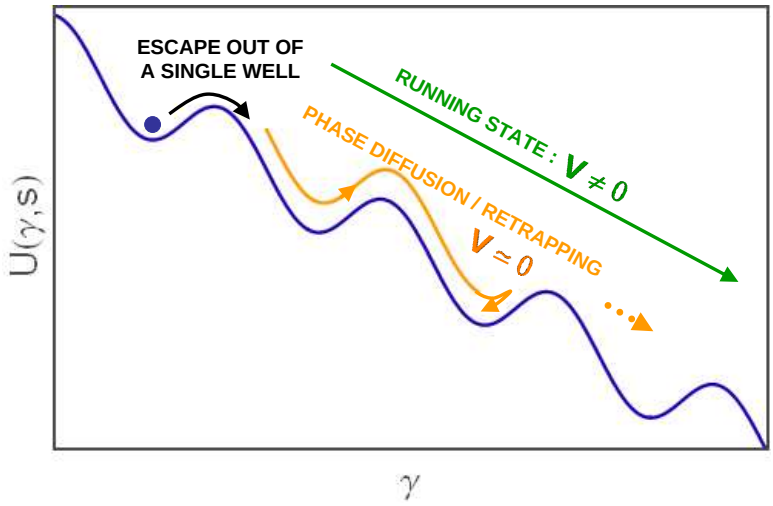

Fig. 2.4. Dynamics of the particle in presence of fluctuations (finite temperature in this classical model). The particle can overcome the barrier and escape out of the single well. The dynamics of the particle depends on the damping. If the damping is small, the particle gains enough energy to reach a running state, leading to a finite voltage. Otherwise, the particle enters a diffusion regime, escaping from one well to be retrapped in a following one, with a very small average velocity.

In the following, we describe all the different parts of the dynamics of the junction separately. We first present the response of the junction when subjected to a small periodic drive, and show the importance of the environment, which determines the dynamics. We then describe the escape out of a single well in presence of thermal fluctuations. The escape is a Poisson process described by a lifetime $\tau_{\rm esc}$ of the metastable state or an escape rate $\Gamma = \frac{1}{\tau_{\rm esc}}$. We show here how the escape of a particle out of single well can be used to characterize the properties of the fluctuations that triggered the escape. In particular, predictions for the behavior of the escape rate when the noise to which the junction is submitted is asymmetric are discussed.

Parameters of the dynamics

In order to describe the escape dynamics, we introduce here the relevant concepts of barrier height, plasma frequency and quality factor.

Barrier height In most of the aspects of theory, only the barrier height $\Delta U(s)$ enters, and not the complete potential $U(\gamma, s)$. It is given by:

$$\Delta U(s) = E_J \left[2\sqrt{1-s^2} - s(\pi - 2\arcsin(s))\right], \tag{2.13}$$

which is well approximated for s close to 1 (see Fig. 2.5(a)) by:

$$\Delta U_{\text{approx}}(s) = \frac{4\sqrt{2}}{3} E_J (1-s)^{3/2}. \tag{2.14}$$

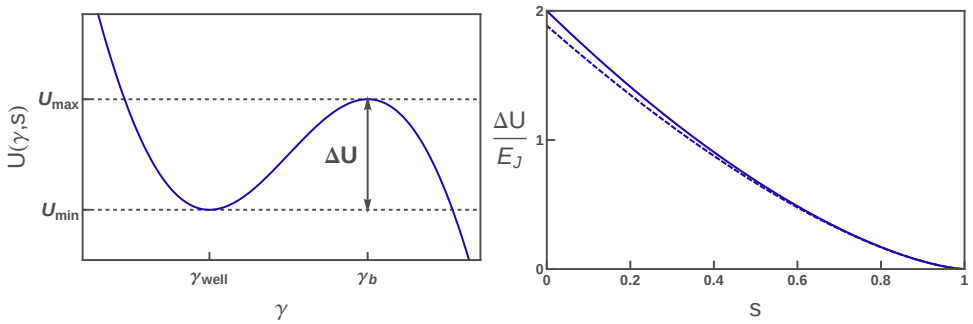

Fig. 2.5. Left: Tilted washboard potential in which the fictitious particle evolves (shown here for $s = 0.7$). In the region of the well, the potential can be approximated by a cubic potential (see Appendix B.1). **Right:** Barrier height from Eq. (2.13) as a function of the reduced bias current (solid line) and approximated expression of Eq. (2.14) (dashed line)

Frequency-response at small amplitudes - Plasma frequency When submitted to the noise arising from the environment, the phase undergoes oscillations around the local potential minimum. The characteristic frequency of the oscillations is the plasma angular frequency $\omega_p(s)$, determined by the curvature of the potential at the minimum:

$$\omega_p(s) = \sqrt{\frac{1}{C_J \varphi_0}} \sqrt{\frac{\partial^2 U(\gamma, s)}{\partial \gamma^2}}\Bigg)_{\gamma_{\text{well}}} = \omega_{p0} \left(1 - s^2\right)^{1/4}, \tag{2.15}$$

where

$$\omega_{p0} = \sqrt{\frac{I_0}{\varphi_0 C_J}} = \frac{1}{\sqrt{L_{J0} C_J}} \tag{2.16}$$

is the bare plasma angular frequency.

The small oscillations of the phase difference around the minimum value can be approximated by a monochromatic behavior. Under a small current excitation $\delta s_\omega = \delta I_\omega / I_0$ at angular frequency ω, Eq. (2.8) yields the phase response γ_ω:

$$\gamma_\omega = \frac{1}{j\omega L_J Y_{\text{tot}}(\omega)} s_\omega. \tag{2.17}$$

where Y_{tot} is the total admittance of the circuit seen from the bias line.

In the RCSJ model One has

$$Y_{\text{tot}}(\omega) = \frac{1}{R} + \frac{1}{j\omega L_J} + jC_J\omega. \tag{2.18}$$

which corresponds to a second order filter. The characteristic frequency of the circuit is simply $\omega_p(s)$ with a quality factor $Q(s) = RC_J\omega_p(s)$ for the resonance. One defines also the quality factor at zero bias

$$Q_0 = RC_J\omega_{p0}. \tag{2.19}$$

Using these two parameters, Eq. (2.8) reduces to:

$$\ddot{\gamma} + \frac{\omega_{p0}}{Q_0}\dot{\gamma} + \omega_{p0}^2\left[\sin\gamma - s\right] = \omega_{p0}^2\frac{\delta I}{I_0}. \tag{2.20}$$

For an arbitrary admittance For a junction shunted by an arbitrary admittance, the resonances of the circuit correspond to the complex poles of $\frac{1}{j\omega L_J Y_{\text{tot}}(\omega)}$, hence the complex zeros of $Y_{\text{tot}}(\omega)$, denoted $\{\omega_s\}$. The corresponding resonant frequencies are found as the real part of the complex solutions $\text{Re}(\omega_s)$, and the plasma frequency is the largest one. The quality factor of each resonant mode is found as:

$$Q_{\text{factor}} = \frac{\text{Re}\left(\omega_s\right)}{2\,\text{Im}\left(\omega_s\right)}. \tag{2.21}$$

This expression simplifies by defining an effective capacitor shunting the junction by:

$$C_J = \lim_{\omega\to\infty}\frac{Y_{\text{tot}}(\omega)}{j\omega} \tag{2.22}$$

and an effective admittance $Y(\omega)$ that excludes the Josephson element and the effective capacitor by:

$$Y(\omega) = Y_{tot}(\omega) - \frac{1}{j\omega L_J} - jC_J\omega. \tag{2.23}$$

In this case, the dissipation is described by $\text{Re}\left(Y(\omega_p)\right)$, and the quality factor of the mode at ω_p reduces to:

$$Q_{\text{factor}} = \frac{1}{\text{Re}\left(Y(\omega_p)\right)}C_J\omega_p. \tag{2.24}$$

2.2 Escape rate out of the zero-voltage state

The escape out of a single well is simply described in two limits (see Fig. 2.6):

- When the thermal fluctuations have a characteristic energy much higher than the energy related to the plasma frequency, $k_B T \gg \hbar\omega_p$, the junction can be treated as a non-linear, classical oscillator. In this regime, the escape is due to thermal fluctuations of the bias current that drive the particle over the barrier [50]. This regime is called the *thermal activation* regime.
- When the temperature is smaller than the crossover temperature T_{CO} [5] with

$$T_{CO} = \frac{\hbar\omega_p}{2\pi k_B}, \tag{2.25}$$

the energy levels of the anharmonic oscillator formed by the pure Josephson element and the capacitance in parallel are clearly separated. Due to quantum fluctuations arising from the environment, the escape of the particle is dominated by quantum tunneling from the ground state through the barrier (for a review, see [51]). Because the phase is a macroscopic variable, this limit was coined the regime of *Macroscopic Quantum Tunneling* (MQT).

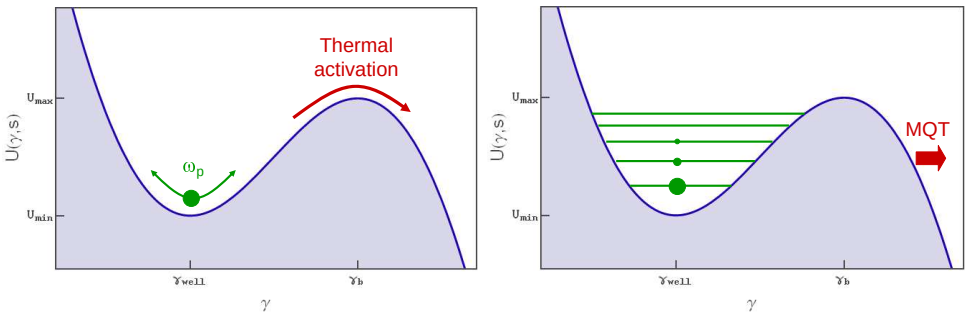

Fig. 2.6. Due to fluctuations in the environment, the particle can escape from the well. Depending on the amplitude of the thermal fluctuations, this escape can be thermally activated **(left)**, or occur through quantum tunneling of the phase **(right)** (see text for details). The plasma frequency $\omega_p/2\pi$ is the frequency of the small oscillations.

In the following, we shortly review these two escape regimes, while the crossover between the two regimes is not detailed here [5]. In the two cases, the escape rate Γ is written as an Arrhenius activation law:

$$\Gamma = A\, e^{-B}. \tag{2.26}$$

where the terms A and B both depend on the regime.

2.2.1 Thermal activation

Transition State Theory

In the case of thermal activation, a simple but already accurate expression of the escape rate is obtained with the Transition State Theory (TST) (see [50] for a review). This theory assumes that Boltzmann equilibrium is achieved for the particle everywhere in the well (no matter how). This approximation yields the simple results:

- A is the plasma frequency:

$$A = \frac{\omega_p(s)}{2\pi}. \tag{2.27}$$

- B is the ratio between the barrier height and the characteristic energy of the current fluctuations $k_B T$:

$$B = \frac{\Delta U(s)}{k_B T}. \tag{2.28}$$

The escape rate out of a single well is thus:

$$\Gamma_{\mathrm{TST}} = \frac{\omega_p(s)}{2\pi} e^{-\frac{\Delta U(s)}{k_B T}}. \tag{2.29}$$

Effect of the environment on the prefactor of the escape rate

The TST, which neglects in particular the possibility of recrossings of the barrier due to friction, only gives an upper bound for the rate. The exact value of the rate is of the form:

$$\boxed{\Gamma = \lambda\left(B, Q(s)\right) \tfrac{\omega_p(s)}{2\pi} e^{-B}.} \tag{2.30}$$

where $\lambda\left(B, Q(s)\right)$ is a prefactor taking into account dissipation through the quality factor. One should note here that the effect of the environment in the thermal activation regime is entirely taken into account by the prefactor. The prefactor λ was first calculated by Kramers in two limiting regimes [4, 50, 52, 53]:

- In the *underdamped* regime ($Q_0 \gg B$), the quality factor is extremely large and the particle looses only very little energy at each oscillation in the well. The energy of the particle becomes a slow variable, while the position and velocity are fast variables. This limit is thus coined energy diffusion. The escape of particles is a source of depletion of the high energy trajectories (close to the barrier top), while the coupling to the heat bath does not allow to repopulate them fast enough. This gives rise to a rate slightly lower than predicted by the TST. In this limit the prefactor is:

$$\lambda(B, Q(s)) = \kappa_1(B, Q(s)) = \frac{36}{5}\frac{B}{Q(s)}. \tag{2.31}$$

- In the *overdamped* regime ($Q_0 \ll B$), the particle slowly evolves by Brownian motion from the bottom of the well to the top, and has an energy following almost a Boltzmann equilibrium in the well. This limit is thus coined spatial diffusion. In this case, when the particle has crossed the top of the barrier, there is a finite probability that it comes back in the well instead of running down the potential, thus giving rise to a rate lower than predicted by the TST. In this limit, the prefactor is:

$$\lambda(Q(s)) = \kappa_2(Q(s)) = \frac{1}{2Q(s)}(\sqrt{1+4Q^2(s)} - 1). \tag{2.32}$$

However, those two limits do not correspond to the relevant experimental regime, which is typically $Q_0 \simeq B$. A complete expression of the escape rate in the thermal activation regime was derived by E. Pollak, P. Hanggi, H. Grabert and V. Mel'nikov [54, 55, 56], then confirmed in the range of intermediate quality factor by numerical simulations [57]. The exact prefactor in this case is:

$$\lambda = \kappa_2 \exp\left\{\frac{1}{2\pi}\int_{-\infty}^{+\infty}\frac{dy}{1+y^2}\ln\left(1 - e^{-\frac{\Delta E\left(1+y^2\right)}{4k_BT}}\right)\right\} \tag{2.33}$$

where

$$\Delta E = \kappa_1\kappa_2\left(1+\frac{1}{4Q^2}\right)^2\left(1+\frac{60}{Q}\sqrt{1+\frac{1}{4Q^2}}\kappa_2^{-8}\left[\psi_1(\kappa_2^{-2}) - \kappa_2^2 - \frac{\kappa_2^4}{2} - \frac{\kappa_2^6}{6}\right]\right) \tag{2.34}$$

is a quantity that, in the limit $Q_0 \to \infty$, approaches the energy loss during one oscillation of a particle having an initial energy equal to the barrier height. ψ_1 is the trigamma function (double derivative of the logarithm of the gamma function), and κ_1 and κ_2 are given by Eqs. (2.31) and (2.32). In practice, a simple interpolation formula between the two limits:

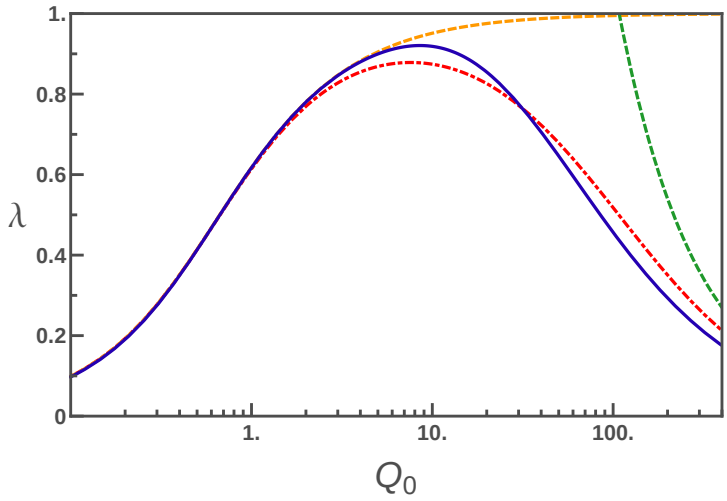

Fig. 2.7. Prefactor λ of the thermally activated escape rate calculated for a reduced barrier height $B = 15$. **Solid line:** Exact result of Eq. (2.33). **Dashed line:** Kramers' low (green) and high (orange) damping limits (Eqs. (2.31) and (2.32)). **Dashed-dotted line:** Simple interpolation between Kramers' limits given by Eq. (2.35).

$$\lambda_{\text{int}} = \left(\frac{1}{\kappa_2} + \frac{1}{\kappa_1} \right)^{-1} \tag{2.35}$$

approaches very well the complete expression,as can be seen in Fig. 2.7.

The calculation performed in the thermal activation regime relies heavily on the separation between the mean escape time and the relaxation time of the particle in the well. The theory is valid only when the mean escape time is much longer that all other time scale in the system, hence when the barrier is large enough compared to the amplitude of the fluctuations, so that $B \gg 1$. In order for the rate to represent less than 1% of the plasma frequency, corresponding in average to an escape event once every 100 oscillations, this yields a validity range $B > 5$.

Phase diffusion / Retrapping regime

After having escaped out of a well, the particle gains kinetic energy while running down the potential. This energy gain is higher when the tilt of the potential is larger. On the other hand, some energy is lost due to the work W_Q of the friction force, which increases with the velocity of the particle. The balance between the two energies determines the separation between running state and phase diffusion regimes [58, 56]. From the determination of the losses, a transition appears at a *threshold* in reduced bias current s_c given by:

$$s_c = \frac{4}{\pi Q_0}. \tag{2.36}$$

At $s > s_c$, the particle gains on average a sufficient energy to overcome all the successive barriers. At $s < s_c$, the particle is always retrapped after having escaped out of a single well.

However, this crude average vision is slightly improved by applying the fluctuation-dissipation theorem along the trajectory of a particle from one well to the next one. It appears that during this jump, the energy of the particle spreads over a width $\delta E = \sqrt{2k_B T W_Q}$ [56]. Due to this spreading, retrapping affects the escape rate even for values of s slightly larger than the threshold s_c.

The escape rate out of a single well predicted theoretically can thus only be probed experimentally by the switching out of the zero-voltage state when the reduced bias current is larger than the threshold s_c. The quality factor of a junction in which switching can be measured is thus bounded by:

$$Q_0 > \frac{4}{\pi}. \tag{2.37}$$

Resonant activation

When an external microwave current $I_{RF} \cos \omega_{\text{exc}} t$ is added to the bias of the Josephson junction, the escape of the particle is enhanced. The resonant activation phenomenon [59], which occurs at frequencies smaller than the plasma frequency, peaks at $\omega_{\text{exc}} \simeq \omega_p$. Experimentally, this enhancement is accessed through the ratio between the escape rate Γ_{exc} measured with an excitation and the escape rate Γ_0 obtained in the same conditions without microwaves. This increase in rate has been calculated in [60], but the result involves a large number of parameters and has to be evaluated numerically. An approximate expression for this enhancement within the RCSJ model, valid when the excitation is close to the plasma frequency, is given in [61] by:

$$\ln\left(\frac{\Gamma_{\text{exc}}}{\Gamma_0}\right) = c_{\text{fit}} Q_0 I_{RF}^2 \frac{\Delta U}{C_J \omega_p^2 (k_B T)^2} f(Q_0, \frac{\omega_{\text{exc}}}{\omega_{p0}} - 1) \tag{2.38}$$

where $c_{\text{fit}} \simeq 5$ depends on Q_0 (see [61]) and the resonant activation response function $f(Q_0, x)$ is given by:

$$\frac{f(Q_0,x)}{Q_0} = \begin{cases} \frac{e^{9x}}{q_+}\left(1 - 2x + \frac{2}{q_+}\right) + \frac{e^{2Q_0 x} - e^{9x}}{q_-}\left(1 + \frac{2}{q_-}\right) + \frac{2xe^{9x}}{q_-} & \text{if } x \leq 0 \\ e^{-2Q_0 x}\left(\frac{1}{q_+} + \frac{2}{q_+^2}\right) & \text{if } x \geq 0 \end{cases} \tag{2.39}$$

with $q_+ = 9+2Q_0$ and $q_- = 9-2Q_0$. In Fig. 2.8, the function $f(Q_0, x)$ is drawn for three values of Q_0. This function presents a maximum located in the range $\frac{\omega_{exc}}{\omega_{p0}} \in [0.95 - 1]$, slightly below the plasma frequency. For excitation frequencies above the plasma frequency, the function drops sharply to zero. Note that the width of this curve is not simply given by $1/Q_0$.

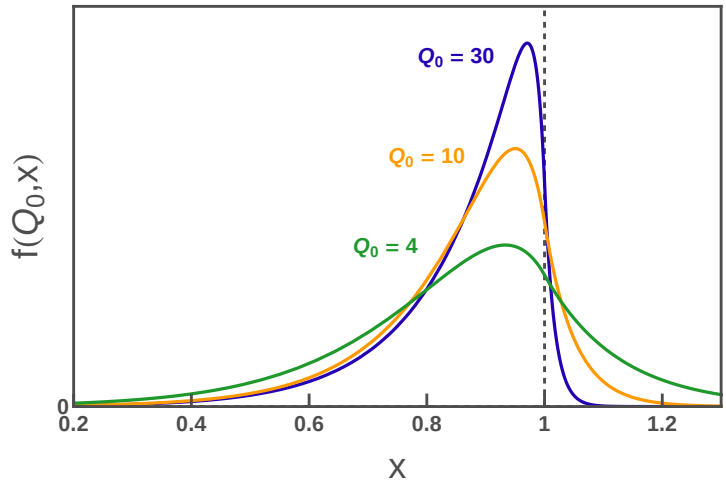

Fig. 2.8. Resonant activation response function $f(Q_0, x)$ in presence of an harmonic excitation on the bias current of the particle for three values of the quality factor Q_0.

2.2.2 Macroscopic Quantum Tunneling

We now turn to the MQT regime, where escape arises from tunneling across the barrier from the different energy levels.

Escape rate at zero temperature in the large quality factor limit

In this quantum tunneling regime, the escape rate at zero temperature and in the large Q_0 limit is obtained using the Wentzel-Kramers-Brillouin (WKB) approximation (see for example [62]):

$$\Gamma_q = A_q e^{-B_q} \tag{2.40}$$

where

$$B_q = \frac{36}{5}\frac{\Delta U(s)}{\hbar\omega_p(s)} \tag{2.41}$$

and

$$A_q = \frac{\omega_p}{2\pi}\sqrt{120\pi B_q}. \tag{2.42}$$

One can define an effective temperature by analogy with the thermal regime, by writing $B_q = \frac{\Delta U(s)}{k_B T_q}$, which yields $T_q = \frac{5}{36}\frac{\hbar\omega_p}{k_B}$. However, this effective temperature now slightly depends on the reduced bias currents through the the plasma frequency (see [51] for a review on the experimental side).

Around the crossover temperature, the rate crosses from this MQT regime to a thermal activated regime. At $T \gtrsim 2\,T_{CO}$, the quantum corrections to the escape rate are very small, and the thermal activation regime is recovered (for the complete description of the crossover, see [5]).

Effect of the environment

When the junction and the capacitance C_J is connected to an arbitrary admittance $Y(\omega)$ as defined from Eq. (2.23), the response of the junction to quantum fluctuations is modified, resulting in a change of the escape rate at zero temperature. Moreover, when this environment is at a finite temperature, even if this temperature is much smaller than the crossover temperature, the thermal current fluctuations arising from $Y(\omega)$ affect the escape rate. The two effects were derived in [51, 63, 64]. In the following, we develop these derivations for two reasons:

1. The method presented in [64] was extended in [65] to treat the effect of an asymmetric noise on the escape rate of a junction in an hybrid thermal activation-MQT regime.
2. In Chapter 6, we present an experiment where the escape rate of a Josephson junction in a MQT regime was measured in presence of an environment at temperature T. This environment presented a single low-frequency mode, and we will restrain the discussion on the effect of this mode on the escape rate, following the Appendix B of [64].

Escape rate at zero temperature

From tunneling theory In presence of $Y(\omega)$ at zero temperature, the escape rate was obtained in [51, 63] through a perturbation theory approach using the tunneling theory from [66]. Neglecting the effect of the environment on the prefactor, the escape rate in presence of this admittance could be casted into the form:

$$\Gamma_q^e = A_q e^{-B_q^e} \tag{2.43}$$

where $B_q^e = B_q + \Delta B_q$. The correction ΔB_q is obtained from the convolution of two functions:

$$\frac{\Delta B_q}{B_q^e} = \int_0^\infty F(t)G(\frac{\omega_p t}{2\pi})dt. \tag{2.44}$$

The function G is given by

$$G(x) = \frac{45}{\pi^4 C_J}\sum_{n=1}^{\infty}\frac{n}{(n+x)^4} = \frac{45}{\pi^4 C_J}\left[\zeta(3,x) - x\zeta(4,x)\right] \tag{2.45}$$

(where $\zeta(n,x)$ are the generalized Riemann functions). $G(\frac{\omega_p t}{2\pi})$ is a monotonic decaying function with a characteristic time $\tau_t = \frac{2\pi}{\omega_p}$. The function $F(t)$ is the step response function of the environment:

$$F(t) = \int_{-\infty}^{+\infty}\frac{Y(\omega)}{j\omega}e^{j\omega t}d\omega. \tag{2.46}$$

The correction ΔB_q will thus be significant only if the environment has a response within the time τ_t. In the case of an Ohmic environment R, where the response is instantaneous, this yields a first order correction $\frac{\Delta B_q}{B_q} \simeq \frac{0.87}{Q_0}$, which was observed in [67]. For an environment presenting a low-frequency mode with a slow temporal response, the integral is dominated by the response at $t = 0$. In this limit, the correction is given as a function of the characteristic inductance of the environment L_e defined from the expression

$$L_e^{-1} = \lim_{\omega\to\infty} j\omega Y(\omega). \tag{2.47}$$

In the perturbation approach where $\Delta B_q \ll B_q$, the correction is obtained from the ratio of the Josephson inductance L_J over L_e:

$$B_q^e \simeq B_q\left(1 + \frac{5}{2}\frac{L_J}{L_e}\right). \tag{2.48}$$

This expression is valid only if the inductance of the environment is large compared to the Josephson inductance $L_e \gg L_J$.

Simple derivation for a low-frequency mode When the environment consists of a low-frequency resonant circuit with a characteristic pulsation $\omega_e \ll \omega_p$ and a quality factor $Q_e \gg 1$, a simple derivation of the last expression was given by J. Martinis and H. Grabert in the Appendix B of [64]. Considering that the quantum fluctuations inducing tunneling are around the plasma frequency, thus much higher than ω_e, the response of the external resonant circuit is taken into account only by the inductance L_e defined above. The effect of the environment is understood as a modification of the equations of the circuit changing the potential $U(\gamma, s)$ into:

$$U^e(\gamma, s) = U(\gamma, s) + \frac{(\gamma - \gamma_0)^2}{2L_e} \tag{2.49}$$

which yields

$$\Delta U^e = \Delta U \left(1 + \frac{3L_J}{L_e}\right) \tag{2.50}$$

and

$$\omega_p^e = \omega_p \left(1 + \frac{L_J}{2L_e}\right). \tag{2.51}$$

In the limit $\frac{L_J}{L_e} \ll 1$, the ratio of the two terms coincides with Eq. (2.48).

Influence of finite temperature and cross-over temperature

In [64], Martinis and Grabert proposed also a simple derivation of the escape rate in the MQT regime when $Y(\omega)$ is at a temperature T much lower than the crossover temperatures T_{CO}. In this limit, the spectrum of the thermal fluctuations associated with $Y(\omega)$ extends up to $\sim k_B T/\hbar \ll \omega_p$, hence the fluctuations are slow at the scale of the junction dynamics, and the particle follows adiabatically the changes of the potential; it is meaningful to define an escape rate for each realization of the noise. The mean escape rate at finite temperature is obtained by the temporal averaging of the instantaneous rates.

The derivation starts by considering the escape rate at zero temperature

$$\Gamma_q^e = A_q e^{-B_q^e}. \tag{2.52}$$

The argument of the exponential has no reason *a priori* to be exactly equal to B_q, as was demonstrated in the previous paragraph, and we consider here the most general case. In the following, we neglect the dependence of the prefactor A_q^e on the bias current. The thermal current fluctuations δI due to $Y(\omega)$ add to the bias current I_B of the junction. Each realization of δI corresponds to a different barrier height, therefore a different B_q^e:

$$B_q^e(I_B + \delta I) = B_q^e + \frac{\partial B_q^e}{\partial I}\delta I. \tag{2.53}$$

The instantaneous rate corresponding to this fluctuation is then:

$$\Gamma_q^e(I_B + \delta I) = \Gamma_q^e(I) e^{-\frac{\partial B_q^e}{\partial I}\delta I}. \tag{2.54}$$

The mean rate at a finite temperature T obtained by temporal averaging is:

$$\Gamma_q^e(T) = \Gamma_q^e(T=0) e^{\frac{1}{2}\left(\frac{\partial B_q^e}{\partial I}\right)^2 \langle \delta I^2 \rangle}. \tag{2.55}$$

where $\langle \ldots \rangle$ denotes the time averaging, which corresponds also to an averaging over the realizations of the noise. In this last expression, we used the fact that δI presents Gaussian fluctuations with zero mean value.

The noise term $\langle \delta I^2 \rangle$ depends on the environment. It is related by the fluctuation-dissipation theorem to the real part of the admittance $Y(\omega)$ (see [64]). In the case where the environment is a low frequency resonant circuit with an inductance $L_e \gg L_J$, one obtains [64]

$$\Gamma_q^e(T) = \Gamma_q \exp\left\{-B_q \frac{L_J}{L_e}\left[\frac{5}{2} - 15\frac{k_B T}{\hbar\omega_p}\right]\right\} \tag{2.56}$$

where it is recalled that Γ_q represents the escape rate for infinite quality factor and zero temperature. In this exponent of the above expression, the first term is the zero temperature correction due to the modification of the dissipation by the environment, while the second one arises from thermal fluctuations in the environment.

2.3 Escape driven by an asymmetric noise

The goal of this section is to explain how the escape out of the zero-voltage state of a Josephson junction can be used to probe noise, and in particular the asymmetry of its probability distribution. So far, we only considered thermal fluctuations arising from macroscopic resistors, therefore Gaussian noise. In the following, we introduce predictions for the escape rate when the noise does not arise only from thermal fluctuations, but also from a specific noise source, producing for example shot noise which is not Gaussian [21]. Predictions have been derived for a noise presenting a finite second and third moment [11, 31, 32, 33, 65, 68], and neglecting higher order moments.[1]

The electrical setup considered in this part is shown in Fig. 2.9. A Josephson junction is biased by a current I_B flowing through a resistor R_B. To this resistor is associated a current source in parallel, producing Gaussian current fluctuations δI_B. In addition, a non-Gaussian noise source with impedance R_N is present. To this noise source is associated a current fluctuation δI_N. The equation describing this circuit is similar to Eq. (2.8):

$$C_J \varphi_0 \ddot{\gamma} + \frac{\varphi_0}{R}\dot{\gamma} + E_J\left[\sin\gamma - s\right] = \delta I_B + \delta I_N. \tag{2.57}$$

In all cases, the effect of the asymmetry of noise has been assumed to be weak. In Ref. [31, 32], the effect of noise on the prefactor was found

[1] Predictions concerning higher moments of noise like in [34, 69], or other effects of noise on Josephson junctions like in [70] and [71] are not discussed here.

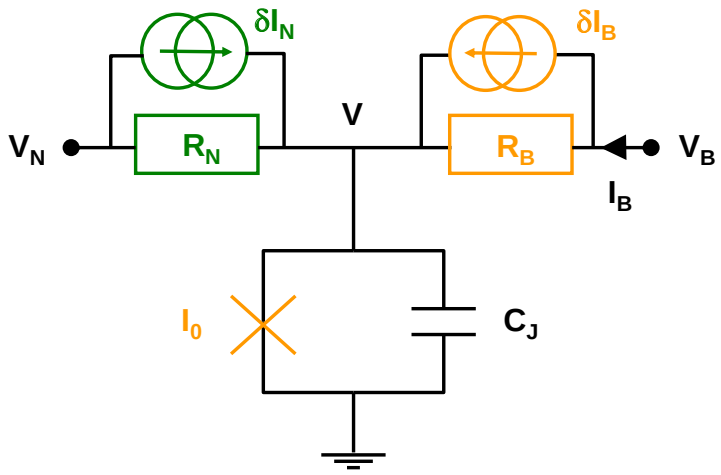

Fig. 2.9. Electrical setup considered in the theories addressing the effect of an asymmetric noise on the escape rate of a JJ out of the zero-voltage state. The junction is biased by a current I_B through a resistor R_B, which is a source of thermal noise δI_B. A noise source of impedance R_N produces additional, non-Gaussian fluctuations δI_N.

to be negligible, and most theoretical works only address the change in the exponent of the escape rate. Hence, the prediction for the thermal escape rate driven by an asymmetric noise is of the form:

$$\Gamma = A\, e^{-[B_2(T_{\rm eff})+B_3]} \tag{2.58}$$

where

$$B_2(T_{\rm eff}) = \frac{\Delta U}{k_B T_{\rm eff}} \tag{2.59}$$

represents the combined effect of the second moment of the asymmetric noise and the background thermal noise. The effective temperature thus accounts for the total power of current fluctuations applied on the bias of the Josephson junction. The noise asymmetry is expected to lead to a small corrective term $|B_3| \ll B_2(T_{\rm eff})$ in the exponent. Predictions for $T_{\rm eff}$ and B_3 derived using different techniques are presented in the following. Before presenting the predictions, we briefly define the frequency scales of the problem, and the statistical properties of the noise δI_N.

2.3.1 Frequency scales

The frequency scales of the problem are defined here from the smallest to the largest (see also Fig. 2.10):

- *The escape rate:* typically, escape rates probed experimentally are in the sub-MHz range, corresponding to a measurement time of 1 μs or more.

- *The plasma frequency:* the plasma frequency considered in the following experiment is around 1 GHz.
- *The thermal noise cut-off frequency:* At the relevant temperature of the experiment, which is of the order or 100mK (from 20mK to 500mK, thermal noise extends to frequencies of the order of $\frac{k_B T}{h} \simeq 2\,\mathrm{GHz}$ [21]).
- *The superconducting gap:* In the experiments described in this thesis, all superconductors are aluminum for which the frequency corresponding to the superconducting gap is $\frac{\Delta}{h} \simeq 50$ GHz.
- *Non-Gaussian noise cut-off frequency:* In the experimental case of a tunnel junction biased at a voltage V_N, the maximal frequency of the shot noise is $\frac{eV_N}{h}$ [21]. For $V_N \simeq 400\,\mu$V, which is the lowest voltage probed in the experiment presented in the following, it corresponds to frequencies higher than 100 GHz. At the scale of the plasma frequency, non-Gaussian noise thus appears completely frequency-independent.

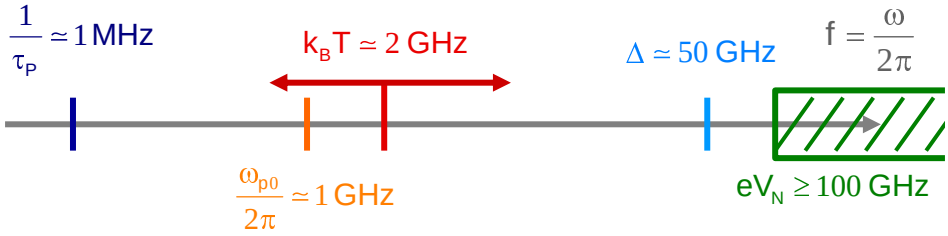

Fig. 2.10. Frequency scales corresponding to the values of the experiment described in the following chapter [38], where the effect of an asymmetric noise on the escape rate of a JJ out of the zero-voltage state is measured.

2.3.2 Noise statistical properties

In the framework of Full Counting Statistics (FCS), the properties of the current fluctuations are treated through the probability distribution function. Experimentally, this distribution is accessed its the moments or through its cumulants which are two ways to represent the same information (see [72] for details). However, moments and cumulants are equal up to the third order, as is recalled in Appendix B.3, and since this thesis only deals with moments up to the third one, it is not necessary here to make a distinction between moments and cumulants. In the following, we deal only with the moments.

Second-order correlation function

The second order correlation function or correlator is defined as:

$$\langle \delta I_N(t) \delta I_N(t') \rangle \,. \tag{2.60}$$

If the noise $\delta I_N(t)$ is assumed to be white, as is the case in the following predictions, this corresponds to:

$$\langle \delta I_N(t) \delta I_N(t') \rangle = S_2 \delta \left(t' - t \right), \tag{2.61}$$

where S_2 is the second moment, often called the variance. **This second moment corresponds to the mean power of the current fluctuations, the width of the probability distribution.**

Considering in the frequency space the fluctuation $\delta I_N(\omega)$ at angular frequency ω defined by:

$$\delta I_N(\omega) = \int_{-\infty}^{+\infty} \delta I_N(t) e^{-j\omega t} dt, \tag{2.62}$$

one defines the second-order spectral density of the fluctuations as

$$S_2^D(\omega) = \langle \delta I_N(\omega) \delta I_N(-\omega) \rangle \tag{2.63}$$

which is related to the correlation function by the Wiener-Khintchine theorem:

$$S_2^D(\omega) = \int_{-\infty}^{+\infty} \langle \delta I_N(0) \delta I_N(\tau) \rangle \, e^{-j\omega\tau} d\tau. \tag{2.64}$$

For a white noise (therefore a frequency independent spectral density), this simplifies to $S_2^D(\omega) = S_2$. The second-order correlation function and the second moment are equal for a white noise.

Third-order correlation function

Similarly, one defines the third order correlator:

$$\langle \delta I_N(t) \delta I_N(t') \delta I_N(t'') \rangle \,. \tag{2.65}$$

For a white noise, this simplifies to:

$$\langle \delta I_N(t) \delta I_N(t') \delta I_N(t'') \rangle = S_3 \delta \left(t' - t \right) \delta \left(t'' - t' \right). \tag{2.66}$$

where S_3 is the third moment. **This third moment is related to the asymmetry of the probability function around its mean value.**

The third-order spectral density is:

$$S_3^D(\omega_1, \omega_2) = \langle \delta I_N(\omega_1) \delta I_N(\omega_2 - \omega_1) \delta I_N(-\omega_2) \rangle \,. \tag{2.67}$$

which is related to the third-order correlation function by:

$$S_3^D(\omega_1, \omega_2) = \iint_{-\infty}^{+\infty} \langle \delta I_N(0) \delta I_N(\tau_1) \delta I_N(\tau_1 + \tau_2) \rangle \, e^{-j\omega_1\tau_1} e^{-j\omega_2\tau_2} d\tau_1 d\tau_2. \tag{2.68}$$

which simplifies to $S_3^D(\omega_1, \omega_2) = S_3$ for a white noise.

2.3.3 Escape rate in presence of an asymmetric noise

We now turn to the theoretical predictions for the effect of an asymmetric noise on the escape rate out of a single well.

The first prediction, obtained by J.T. Peltonen *et al.* [65] considers the adiabatic response of the junction to the noise. Therefore, it only deals with the effect of noise at frequencies much smaller than the plasma frequency. In our experiments, this corresponds to only a small fraction of the noise spectrum, as shown in Fig. 2.10. The damping in the junction dynamics, which appears in the following to be of central importance, does not enter in this approach.

The second prediction was obtained by E. Sukhorukov and A. Jordan [33] with a stochastic path integral formalism, in the two limits of low and high damping limits only, which were unfortunately out of the relevant experimental range.

The third prediction, obtained by J. Ankerhold [31, 32, 35] is based on a Fokker-Planck equation approach to calculate the escape rate. The resolution of the Fokker-Planck equation relies on the fact that escape is only a small perturbation to the Boltzmann equilibrium in the well. As was already discussed by Kramers, this assumption might not be appropriate for very large values of the quality factor.

The last prediction that we present, obtained by H. Grabert [11], relies on the calculation of the action along the escape trajectory using also a path integral formalism. Its validity range spans over the complete range of quality factor, and recovers the two limits of E. Sukhorukov and A. Jordan [33] calculated with a similar method.

All the predictions are compared at the end of the chapter.

Escape rate from an adiabatic model

In Ref. [65], the effect of δI_N on the escape rate is determined assuming an adiabatic response of the junction dynamics. This derivation is very similar to the one presented in Sec. 2.2.2 and in [64]. The Gaussian noise is due to a resistor at finite temperature T. For a fluctuation δI_N, the rate is expanded into:

$$\begin{aligned}\Gamma(I_B+\delta I_N) &\simeq \Gamma(I_B)+\frac{\partial\Gamma}{\partial I_B}\delta I_N+\frac{1}{2}\frac{\partial^2\Gamma}{\partial I_B^2}\delta I_N^2+\frac{1}{6}\frac{\partial^3\Gamma}{\partial I_B^3}\delta I_N^3\\ &\simeq \Gamma(I_B)\left(1-B'\delta I_N+\frac{1}{2}\left(B'^2-B''\right)\delta I_N^2\right.\\ &\qquad\left.+\frac{1}{6}\left(-B'''+3B'B''-B'^3\right)\delta I_N^3\right)\end{aligned}$$

where, in the thermal activation regime where $B \propto (1 - I_B/I_0)^{3/2}$,

$$\begin{cases} B' = \partial B/\partial I_B \simeq -3B/\left(2\left(1-s\right)I_0\right) \\ B'' = \partial^2 B/\partial I_B^2 \simeq 3B/\left(4\left(1-s\right)^2 I_0^2\right) \\ B''' = \partial^3 B/\partial I_B^3 \simeq -3B/\left(8\left(1-s\right)^3 I_0^3\right). \end{cases} \tag{2.69}$$

In practice, $B \gg 1$ and the modification of the escape rate (which is obtained by averaging over the realization of the noise) reduces to two leading terms:

$$\langle \Gamma \rangle = \Gamma(I_B) \exp\left\{\frac{1}{2}B'^2\left\langle \delta I_N^2 \right\rangle - \frac{1}{6}B'^3\left\langle \delta I_N^3 \right\rangle\right\} \equiv A\, \exp\left\{-\left[B_2 + B_3\right]\right\}, \tag{2.70}$$

where the brackets denote the average over the probability distribution (the correcting factor has been exponentiated). The two terms account for the effects of the second[2] and third moment: $B_2 = B - \frac{1}{2}B'^2\langle \delta I_N^2 \rangle$ and $B_3 = \frac{1}{6}B'^3\langle \delta I_N^3 \rangle$.

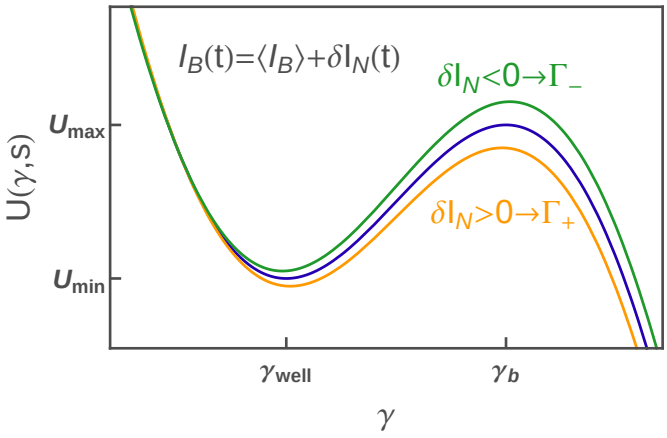

Fig. 2.11. In the adiabatic model, the effect of the noise at frequencies lower than $r\omega_p/2\pi$ with $r \ll 1$ is calculated by averaging the rates for each realization of the instantaneous current, therefore for each barrier height.

At that moment, it is important to stress the differences with the derivation of Ref. [64] performed in the MQT regime where $k_B T \ll \hbar\omega_p$, and considering only thermal fluctuations. In the MQT regime and in presence of only a thermal noise, the cut-off frequency of the thermal noise, $k_B T$, is much smaller than the plasma frequency, and the assumption of adiabatic response is valid. In contrast, in the thermal activation regime and in presence of an asymmetric noise δI_N, the noise spectrum

[2] This result was first obtained in [64].

extends to frequencies much larger than the plasma frequency. For this reason, the authors of Ref. [65] introduce a cut-off frequency $r\frac{\omega_p}{2\pi}$ with $r \ll 1$ on the noise (all the noise above this frequency is neglected, a possible experimental realization being with a filtering). The results here only describe the effect of the very low frequency part of the noise. The integrated average noise is then $\langle \delta I_N^2 \rangle = r S_2 \frac{\omega_p}{2\pi}$, and an effective temperature $T_{\rm eff}$ is obtained from $B_2 \equiv \Delta U / k_B T_{\rm eff}$:

$$T_{\rm eff} \simeq T + \frac{3}{2^{3/2}\pi\sqrt{1-s}} \frac{r\hbar\omega_p}{eI_0} \frac{S_2}{k_B}. \tag{2.71}$$

where we used the fact that, for typical parameters, the second term is very small compared to the first one. This result is reminiscent to a conclusion of Ref. [61], where the effect of a white noise irradiating a junction translates in an increased effective temperature. However, the result here does not depend on dissipation, and the effective temperature presented here can only be slightly different from the base temperature with reasonable parameters, which indicates that the model only grasps part of the effect. Experimentally, the effective temperature can be very large, and the authors of Ref. [65] introduce another model, based on resonant transitions in the MQT regime, to better describe the changes of $T_{\rm eff}$, and recover the result of Ref. [61]:

$$T_{\rm eff} = T + \frac{1}{2} R \frac{S_2}{k_B}. \tag{2.72}$$

However, it is only in the adiabatic model that the effect of S_3 was considered in [65], the low frequency cut-off yielding $\langle \delta I_N^3 \rangle = S_3 \left(r \frac{\omega_p(s)}{2\pi} \right)^2$, and from [37]:

$$B_3 = -\left(\frac{\varphi_0}{k_B T} \right)^3 S_3 \omega_{p0}^2 \, j_{\rm Ad}(s) \tag{2.73}$$

with

$$j_{\rm Ad}(s) = r^2 \frac{2^{3/2}}{3\pi^2} \sqrt{1+s}(1-s)^2 \simeq 0.13\, r^2 (1-s)^2 \tag{2.74}$$

(the exact s-dependence is slightly different from [37] because we took into account the dependence of the plasma frequency). As is shown in what follows, the theoretical results obtained by other authors can all be cast in a form similar to Eq. (2.74), but with different expressions for the function $j(s)$.

Overall this prediction has to be considered very carefully. One has to remember that it is valid only when the noise is filtered over $r\frac{\omega_p}{2\pi}$ with $r \ll 1$. In [37], it has been used with $r = 1$ to compare with experiments, which relies on the questionable assumption that the effect of the low

frequency part of the noise grasps a large part of the complete effect. We show in the end that when comparing with the other predictions, it is clear that this prediction allows only to grasp the qualitative behavior of B_3 but does not give a proper description of the effect.

Escape rate from a stochastic path integral formalism

A first derivation of the escape rate for an asymmetric noise taking into account the complete noise spectrum, and in particular the effect at the plasma frequency, was proposed in [33]. Using a stochastic path integral formalism, the authors derived the same expression for the effective temperature as in Eq. (2.72), and a corrective term B_3 due to the third moment in the limits of low and high damping written again

$$B_3 = -\left(\frac{\varphi_0}{k_B T}\right)^3 S_3 \omega_{p0}^2 \, j_{\mathrm{SPI}}(Q_0, s) \tag{2.75}$$

with

$$j_{\mathrm{SPI}}(Q_0, s) \simeq \begin{cases} 0.79\,(1-s)^2 & \text{when } \mathrm{Q}_0 \gg 1 \\ \frac{8\sqrt{2}}{45} Q_0^2 (1-s)^{5/2} & \text{when } \mathrm{Q}_0 \ll 1. \end{cases} \tag{2.76}$$

An extension of this theory was performed in [34] taking into account all the moments of noise. It appears however that in the relevant experimental regime and for a Poisson noise (as used so far experimentally), moments higher than the third one have no significant impact.

Two further predictions addressed the situation of intermediate quality factors, which is the experimentally relevant range.

Escape rate from a Fokker-Planck approach

The method described in [31, 32, 35] to determine the escape rate of a junction submitted to an asymmetric noise closely follows the initial determination performed by Kramers for the Gaussian case in the limit of large damping ($Q_0 \ll B$). The dynamics of the phase and of the velocity $v = \frac{1}{\varphi_0} V$ is described in terms of the probability density function $P(\gamma, v, t)$. Starting from the Langevin equation (2.57), one derives a Fokker-Planck equation (FPE) for $P(\gamma, v, t)$.[3]

[3] This derivation is done using a Kramers-Moyal expansion. The principle is to link the time derivative $\partial_t P(\gamma, v, t)$ with the spatial derivatives $\partial_\gamma^n \partial_v^m P(\gamma, v, t)$. Since the phase and the velocity are given at each time by the random force, they are also random variables as a function of time. One thus defines the moments of these variables, which are the coefficients appearing in the FPE.

For a Gaussian noise In absence of any asymmetric noise, the FPE reads:

$$\frac{\partial P(\gamma, v, t)}{\partial t} = L^0_{FP} P(\gamma, v, t) \tag{2.77}$$

with

$$L^0_{FP} = -v\frac{\partial}{\partial \gamma} + \omega_{p0}\frac{\partial}{\partial v}\left[\frac{v}{Q_0} + \omega_{p0}\frac{U'}{E_J}\right] + \frac{\omega^3_{p0}}{Q_0 E_J} k_B T \frac{\partial^2}{\partial v^2}. \tag{2.78}$$

and $v = \frac{1}{\varphi_0}V$. A trivial solution of this equation is the equilibrium Boltzmann distribution $P_{eq}(\gamma, v) = \frac{1}{Z}e^{-\beta\mathcal{H}(\gamma,v)}$, where $\mathcal{H}(\gamma, v) = \frac{1}{2}mv^2 + U(\gamma, s)$ is the Hamiltonian corresponding to the Langevin equation (2.57) and Z is the partition function. In this limit, the escape rate is obtained by finding the average flux of particle at the barrier top

$$\Gamma = \frac{\langle v\, \delta(\gamma - \gamma_b)\rangle_{\text{flux}}}{N_{\text{well}}} \tag{2.79}$$

where N_{well} corresponds to the statistical population of the well. The average flux is calculated from an out-of-equilibrium solution $P_{\text{flux}}(\gamma, v)$ of the equation (see [50] for a description of this calculation). To find such a solution, Kramers' ansatz is: $P_{\text{flux}}(\gamma, v) = P_{eq}(\gamma, v)\zeta(\gamma, v)$ where $\zeta(\gamma, v)$ represents the correction to the equilibrium, accounting both for the complete equilibrium deep in the well and the depopulation around the barrier top due to the escape.

With an asymmetric noise Since a translation of the Langevin equation (2.57) into a FPE would lead only to formal terms, the author of [31, 32] derives an effective Fokker-Planck equation describing the motion under an asymmetric noise. This is performed under the assumption that:

- The non-Gaussian character of the noise is weak
- Fluctuations are fast compared to the dynamics of the system, the noise appears almost white.

This allows to derive an effective FPE operator:

$$L_{\text{eff}} = L^0_{FP} + \frac{\omega^3_{p0}}{Q_0 E_J}\frac{1}{2}RS_2\frac{\partial^2}{\partial v^2} - \frac{\omega^6_{p0}S_3}{6}\frac{\partial^3}{\partial v^3}. \tag{2.80}$$

where the effect of the shot noise is accounted for by two terms. The first term, due to the second moment of the noise, contains a derivative at the second order. This term is valid whatever is the power of the asymmetric noise compared to the thermal noise. The presence of the noise third

moment is accounted for by the second term, which contains a derivative at the third order. This term is valid only in a perturbation approach.

The prefactor of $\frac{\partial^2}{\partial v^2}$ is $\frac{\omega_{p0}^3}{Q_0 E_J}\left[k_B T + \frac{1}{2} R S_2\right]$ in the effective FPE. By analogy with Eq. (2.78), the overall effect of the second moment is again captured with an effective temperature given by Eq. (2.72). This calculation shows, as Refs. [33, 61], that such an expression for the temperature is valid even if the power of the asymmetric noise is much larger than the power of the thermal noise. T_{eff} can thus be much larger than T.

Resolution The effective FPE is solved by considering the ansatz:

$$P_{\text{flux}} = P_{eq}\zeta e^{-G}, \tag{2.81}$$

where ζ still accounts for the out-of-equilibrium situation, and G accounts for the effect of the third moment. In this ansatz, the function G was expressed as the product of an arbitrary function of γ and a polynomial function of v up to the third order. A perturbation solution P_{flux} of the effective Fokker-Planck was then found by using the ratio $S_3/S_2^{3/2}$ as a small parameter, which allowed to express the escape rate for an arbitrary quality factor. In a first step [31, 32], the application of an effective FPE yielded a result at any Q_0 but only for a cubic approximation of the potential valid for $1 - s \ll 1$:

$$j_{\text{FP1}}(Q_0, s) = \frac{8\sqrt{2}}{9} \frac{Q_0^2 (1-s)^{\frac{5}{2}}}{5 + Q_0^2 \sqrt{1-s^2}} \tag{2.82}$$

which leads to the limits:

$$j_{\text{FP1}}(Q_0, s) \simeq \begin{cases} 0.89\,(1-s)^2 & \text{when } \mathrm{Q}_0 \gg 1 \\ \frac{8\sqrt{2}}{45} Q_0^2 (1-s)^{5/2} & \text{when } \mathrm{Q}_0 \ll 1. \end{cases} \tag{2.83}$$

This calculation was further improved by K. Glaum and J. Ankerhold using a polynomial function of v of order four and a better cubic approximation for the potential (denoted the bilocal approximation, see Appendix B.1) [73]. This modification, expected to provide only a small improvement, yielded a similar result for low quality factors, but changed significantly the result for large quality factors, probably pointing to some limitation of the theory in this range.[4] The result was expressed in the form:

$$j_{\text{FP2}}(Q_0, s) = \frac{1}{48} \alpha^{BI}(s) \left(\tilde{x}_b^{BI}(s)\right)^3 W_{\text{FP2}}\left[\frac{1}{Q_0 \sqrt{\alpha^{BI}(s)}}\right] \tag{2.84}$$

[4] This is not completely a surprise since the resolution is based on the assumption of quasi-equilibrium that is probably not completely valid for large quality factors.

where[5]

$$W_{\mathrm{FP2}}[y] = \frac{8}{15\,(1+2\varrho^2)}{}_3\mathrm{F}_2\left(\frac{6}{5}, 3, 1; \frac{6\varrho^2+8}{5}, 6; 1\right) \tag{2.85}$$

and ${}_3\mathrm{F}_2$ is the hypergeometric function.

Escape rate from a path integral approach

The calculation by H. Grabert in 2008 [11], based on a path integral formalism like done in [33], yields predictions for all values of the quality factor. In this formalism [74], the probability $p(\gamma_b|\gamma_{\mathrm{well}})$ for the particle to go from the minimum of the well $\gamma(t=0) = \gamma_{\mathrm{well}}$ to the barrier top at time t ($\gamma(t) = \gamma_b$) is given as a path integral, each path having an action A:

$$p(\gamma_b|\gamma_{\mathrm{well}}) \propto \int \exp\left\{-\frac{1}{2k_B}A\right\}. \tag{2.86}$$

All paths differ by the fluctuating force δI that lead to the barrier top. The probability is dominated by the path having the minimal action.

For a thermal noise, this path is the time reversal trajectory of the relaxation of a particle starting at the barrier top and relaxing down to the bottom of the well. From the time evolution of this trajectory noted $\gamma_{\mathrm{esc}}(t)$ and the associated fluctuating force, the action for this path is given as:

$$A = \frac{2}{T}\Delta U \tag{2.87}$$

which recovers the TST expression of the escape rate of Eq. (2.29) (the prefactor of the escape rate can not be accessed with such a path integral formalism).

The presence of an asymmetric noise slightly modifies the minimum action path. In a perturbation approach, when the effect of the third moment is much smaller than that of the second, the action is written as a sum of two terms:

$$A = A_2 + A_3 \tag{2.88}$$

where A_2 and A_3 respectively correspond to the contributions of the second and third moment of the total noise (the sum of the thermal noise and the asymmetric noise). The minimal action path in this situation is first obtained by neglecting the effect of the third moment. In this case, the term A_2 is found to be:

[5] $\alpha^{BI}(s)$ and $\tilde{x}_b^{BI}(s)$ are defined in Appendix B.1, as the terms defining the cubic approximation of the potential.

$$A_2 = \frac{2}{T_{\text{eff}}} \Delta U \tag{2.89}$$

where T_{eff} is again given by Eq. (2.72). The main results of [11] is that the correction A_3 corresponding to the third moment of the asymmetric noise can be calculated using the trajectory of minimal action obtained without the third moment, which yields:

$$A_3 = -2k_B \left(\frac{\varphi_0}{k_B T_{\text{eff}}} \right)^3 S_3 J \tag{2.90}$$

where J is an integral over the trajectory $\gamma_{\text{esc}}(t)$ corresponding to the minimal action path:

$$J = -\frac{1}{6} \int_{-\infty}^{+\infty} \dot{\gamma}_{\text{esc}}^3(t) dt \tag{2.91}$$

The integral depends on the complete dynamics of the particle in the well, and thus on the reduced bias current and the quality factor. The final result is of the form of Eq. (2.75) with[6]

$$j_{\text{FullQ}}(Q_0, s) = \frac{2}{3}(1-s)^2 W \left[\left(\frac{2}{1-s} \right)^{1/4} \frac{1}{Q_0} \right] \tag{2.92}$$

where $W[y]$ is a function tabulated in [11].[7] Recently, Urban and Grabert extended this formalism, used here for the RCSJ model, to the non-Markovian case. This allows to predict T_{eff} and B_3 for an arbitrary circuit and a colored noise. This development, which constitutes a milestone in escape rate calculation, is thoroughly exploited in the comparison with the experimental results of [38] presented in Chapter 4.

2.3.4 Summary

All predictions considering the complete noise spectrum agree on the behavior of the effective temperature, given by:

$$\boxed{T_{\text{eff}} = T + \tfrac{1}{2} R \tfrac{S_2}{k_B}} \tag{2.93}$$

and on the form of the corrective term B_3:

[6] Note that a minus sign is missing in Eqs.(78,92) of [11].

[7] This functions has the two limits $W[0] = 1.188...$ (that corresponds to the analytical prediction obtained for $Q_0 \gg 1$) and $W[y] \approx \frac{8}{15} \frac{1}{y^2}$ for $y \gg 1$ (that corresponds to the analytical prediction obtained for $Q_0 \ll 1$), which corresponds to the results of Ref. [33].

$$B_3 = -S_3\omega_{p0}^2 \left(\frac{\varphi_0}{k_B T_{\text{eff}}}\right)^3 j(Q_0, s). \tag{2.94}$$

In this last part, we compare the predictions of the various approaches through the terms $j(Q_0, s)$, which contains all the differences between them. The result of the adiabatic model has a separate status, since it gives a function $j_{\text{Ad}}(s)$ (Eq. 2.74) which does not depend on the quality factor, but on a cut-off parameter $r \ll 1$.

The prediction $j_{\text{FullQ}}(Q_0, s)$ presented by Grabert for the complete range of quality factor in [11] in the limit $1 - s \ll 1$ recovers the asymptotes $j_{\text{SPI}}(Q_0, s)$ calculated by Jordan and Sukhorukov, as can be seen in Fig. 2.12. Since the typical experimental quality factor of the Josephson junction is of the order of 10, it is clear from the figure that the predictions of [11] are necessary for the comparison with the experimental cases.

As expected, the results of the FPE approach, given by Eqs. (2.82) and (2.84), agree with the result of Grabert at low quality factor, but disagree at large quality factors where the resolution of the FPE is less reliable, as shown in Fig. 2.13.

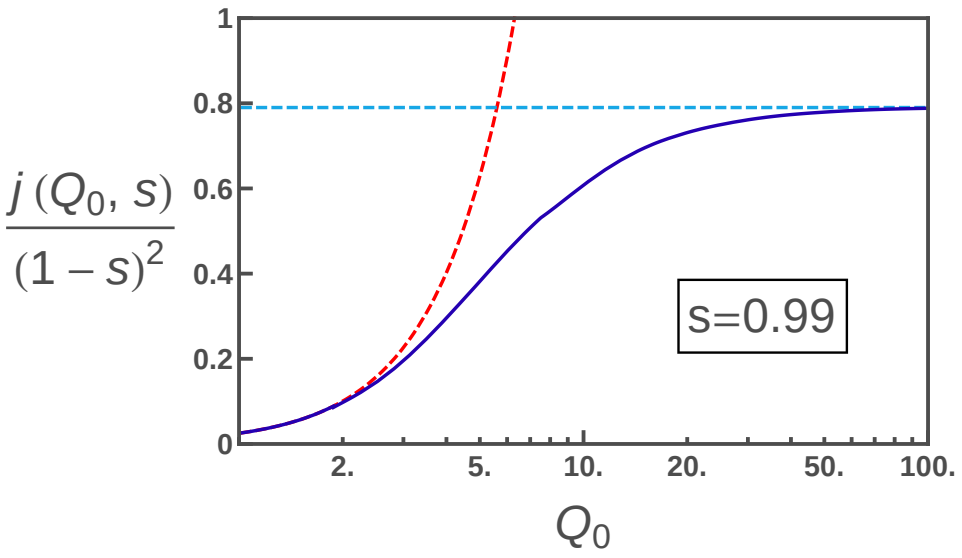

Fig. 2.12. Solid line: Function $j_{\text{FullQ}}(Q0, s)$ obtained by Grabert in [11] for $s = 0.99$ normalized by $(1 - s)^2$. **Dashed lines:** limits of low and high quality factor obtained by Sukhorukov & Jordan in [33]. Only the region in between those limits is easily accessed experimentally.

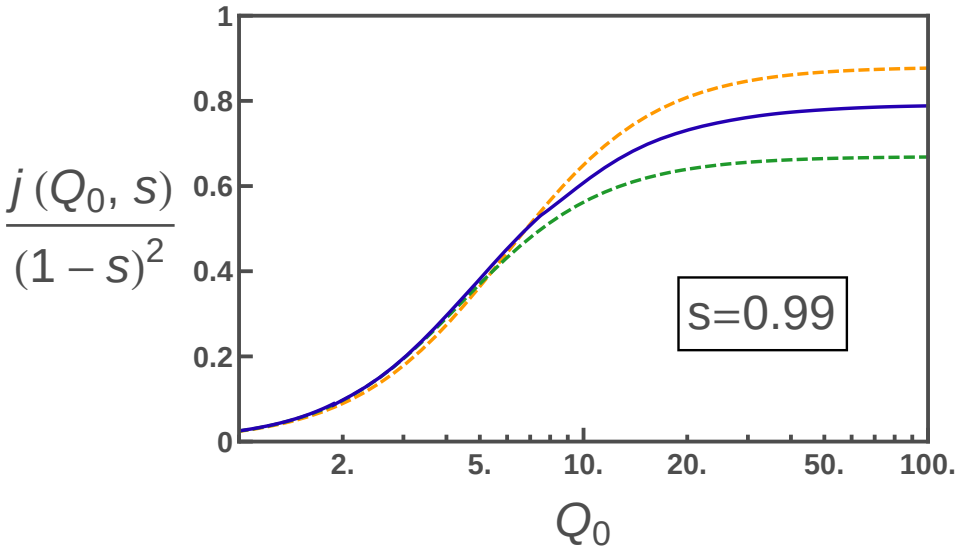

Fig. 2.13. Solid line: Grabert's result valid for all quality factor $j_{\mathrm{FullQ}}(Q_0, s)$. **Dashed lines:** Results of Ankerhold and Glaum $j_{\mathrm{FP1}}(Q_0, s)$ (top - orange) and $j_{\mathrm{FP2}}(Q_0, s)$ (bottom - green) obtained using a Fokker-Planck Equation.

Altogether, the theory by H. Grabert [11] covers the whole range of quality factors and coincides with the other predictions in the limits where they apply. As a consequence, it is taken as a reference in the following chapters.

To finish with, we present the different predictions for the parameters of the two experiments that probed the thermal escape driven by an asymmetric noise [38, 37]:

- In [37], the quality factor of the junction was $Q_0 = 2.5$, and the escape rate was measured in the range $s \in [0.5 - 0.9]$. The measured rate asymmetry was compared to prediction using $j_{\mathrm{Ad}}(s)$ with $r = 1$. In Fig. 2.14, we compare this expression to the predictions obtained by K. Glaum $j_{\mathrm{FP2}}(Q_0, s)$ and by H. Grabert $j_{\mathrm{FullQ}}(Q_0, s)$. It appears that the adiabatic model used in [37] yields a result significantly different from the other existing theories.
- In [38], the quality factor of the junction was estimated to be of the order of 5 and the escape rate was measured in the same range of s as the previous experiment. The calculation of H. Grabert was extended at $Q_0 = 5$ to arbitrary values of s [38, 75], yielding numerical results that are well approximated by:

$$j_{\mathrm{FullQ}_5}(s) = 0.81(1 - s)^{2.14}. \tag{2.95}$$

The various predictions are compared to this result in Fig. 2.15. The deviation between $j_{\mathrm{FullQ_5}}(s)$ and $j_{\mathrm{FullQ}}(5, s)$, which were calculated using the same method, confirms that a specific calculation far from the simple limit $1 - s \ll 1$ was needed in order to achieve a comparison with the experiment, which is performed in the range of $s \in [0.5 - 0.9]$.

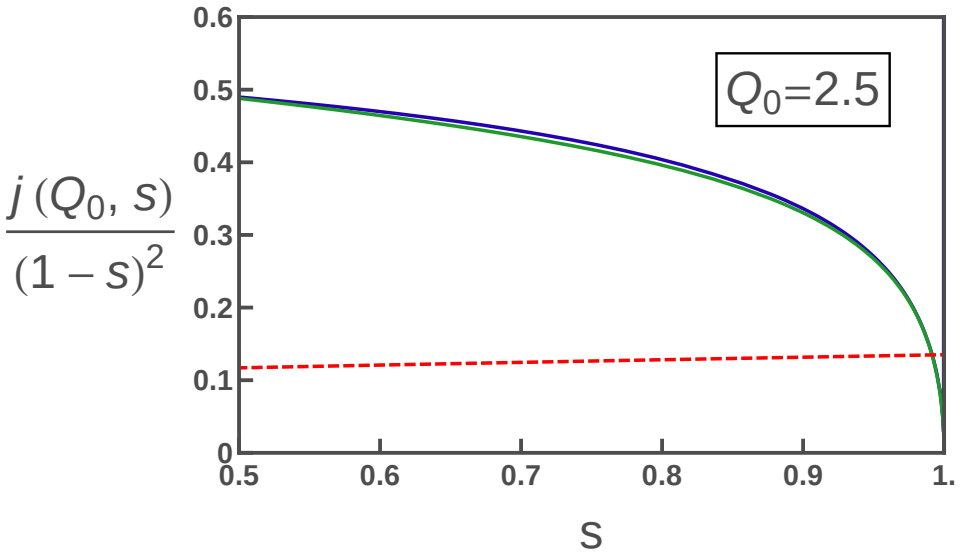

Fig. 2.14. Predictions for $j(Q_0, s)$ at $Q_0 = 2.5$, which corresponds to the experimental value in [37]). **Solid line:** Predictions of H. Grabert $j_{\mathrm{FullQ}}(2.5, s)$ (blue) and K. Glaum $j_{\mathrm{FP2}}(2.5, s)$ (green). **Dashed line:** Prediction $j_{\mathrm{Ad}}(s)$ from the adiabatic model presented in [65] used to perform a comparison with the experiment in [37], with r=1.

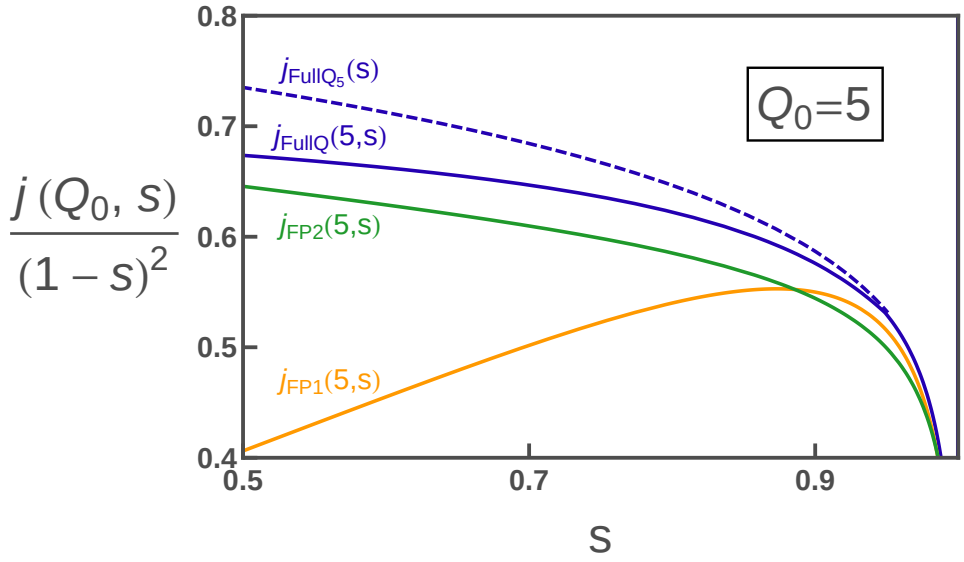

Fig. 2.15. Predictions for $j(Q_0, s)$ at $Q_0 = 5$, which corresponds to the approximate experimental value in [38]. **Dashed line:** Prediction of H. Grabert $j_{\mathrm{FullQ}_5}(s)$ from [75] valid in the range $s \in [0.5 - 0.9]$, and used in [38] to compare with the experiment. **Solid lines:** Predictions of H. Grabert $j_{\mathrm{FullQ}}(5, s)$ (blue), of K. Glaum $j_{\mathrm{FP2}}(5, s)$ (green), and of J. Ankerhold $j_{\mathrm{FP1}}(5, s)$ (orange). The behavior in s far from $1 - s \ll 1$ is, as expected, not properly taken into account by $j_{\mathrm{FP1}}(5, s)$ in [31, 32].

2.4 Conclusion

Having described the dynamics of a Josephson junction when it is submitted to current fluctuations on its bias current in the RCSJ model, we presented in this chapter the theoretical prediction for the thermal escape driven by a white asymmetric noise for this model. The effect of this noise on the escape rate of the junction out of its zero-voltage state is twofold:

- The effect of the second moment of the noise is captured by an effective temperature. This effective temperature is predicted to grow linearly with the second moment of the noise, which reflects the mean power of the fluctuations reaching the junction.
- The effect of the third moment has been calculated assuming that it is much weaker than that of the second moment. It is accounted for by a corrective term in the argument of the exponential in the escape rate. The different theories agree in their range of validity, only the one by Grabert [11] applying to the whole range of quality factors.

Chapter 3

Numerical simulation of the escape

In this chapter, we present numerical simulations, in order to probe the theoretical predictions for the effect of an asymmetric noise on the escape out of the zero voltage state of a Josephson junction. The escape rate has been calculated by a step-by-step integration of the stochastic equations of motion. Retrapping effects were not taken into account, therefore this simulation only concerns the escape rate out of a single well, allowing for direct comparison with theoretical predictions. The simulations presented in this part extend the previous results obtained by X. Waintal in [35].

3.1 Simulation algorithm

3.1.1 Equations of motion

Dimensionless equation

The setup described by the present simulation is shown in Fig. 3.1. It corresponds to the RCSJ model where the resistor R is a source of Johnson-Nyquist noise δI_B, assumed to be white noise with Gaussian behavior. An asymmetric noise with zero mean value δI_N is added to the current bias of the junction. The simulation is based on Eq. (2.57), rewritten in dimensionless time units $\tau = \omega_{p0} t$. The notation for the time derivative is kept, so that derivatives are replaced according to:

$$\dot{\gamma} = \frac{d\gamma}{dt} \Rightarrow \dot{\gamma} = \frac{d\gamma}{d\tau} \tag{3.1}$$

The equation of motion is:

$$\ddot{\gamma} + \frac{1}{Q_0}\dot{\gamma} + \sin\gamma = s + \delta s_B + \delta s_N \tag{3.2}$$

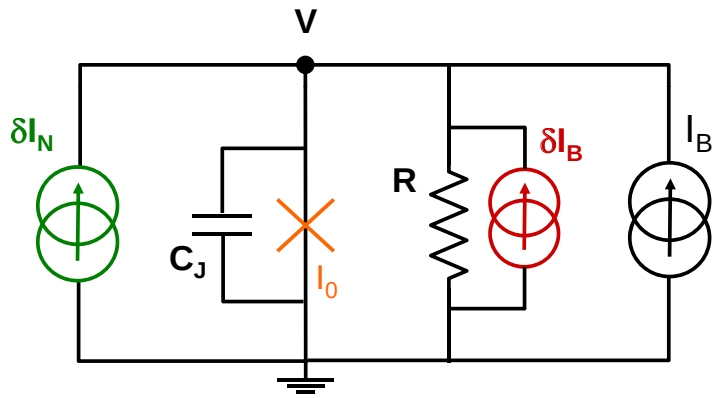

Fig. 3.1. Setup described by the numerical integration. To the resistor R is associated a Johnson-Nyquist noise δI_B with Gaussian character, shown as a parallel current source. An asymmetric noise δI_N with zero mean value is added to the bias current of the junction.

with δs_B the Gaussian noise, and δs_N the asymmetric noise.

Noise

Gaussian Noise The Gaussian term describes the thermal fluctuations in the resistor. The second order correlation function of this Johnson-Nyquist white noise is given by $\langle \delta I_B(t) \delta I_B(t') \rangle = \frac{2k_B T}{R} \delta(t'-t)$ where T is the temperature of this resistor. From the Gaussian assumption, odd order correlation functions are zero. Using $\delta(t) = \omega_{p0} \delta(\tau)$ and defining the reduced temperature

$$\theta = \frac{k_B T}{\varphi_0 I_0}, \tag{3.3}$$

the dimensionless correlation function is:

$$\langle \delta s_B(0) \delta s_B(\tau) \rangle = \frac{2\theta}{Q_0} \delta(\tau). \tag{3.4}$$

Poisson Noise The asymmetric current accounts here for tunneling events through a tunnel junction. The current in this case follows a Poisson process, and the corresponding noise is a Poisson noise. It can be described in terms of a sum of charge spikes centered at times t_i:

$$\sum_{t_i} e \delta(t - t_i) \tag{3.5}$$

corresponding to the successive tunneling events. This current has a mean value $\langle I_N \rangle$. Since noise terms are considered to have zero mean value in the theory, the mean current is subtracted to obtain the noise term:

$$\delta I_N = \sum_{t_i} e\delta(t - t_i) - \langle I_N \rangle \tag{3.6}$$

In dimensionless units, this noise is:

$$\delta s_N = \sum_{\tau_i} e_* \left[\delta(\tau - \tau_i) - \gamma_N\right] \tag{3.7}$$

where

$$e_* = \frac{e\omega_{p0}}{I_0} = \sqrt{\frac{2E_C}{E_J}} \tag{3.8}$$

is a reduced charge and

$$\gamma_N = \frac{\langle I_N \rangle}{e_* I_0} \tag{3.9}$$

is the reduced tunneling rate. In the experiment, the detector junction is in a regime $E_J \gg E_C$, so that e_* is small. In all the simulations, we take

$$e_* = 0.005 \tag{3.10}$$

which is a typical experimental value. The second and third order correlation functions of the Poisson noise (see Appendix B.3) in reduced units are:

$$\begin{cases} \langle \delta s_N(0)\delta s_N(\tau)\rangle = e_*^2 \gamma_N \delta(\tau) \\ \langle \delta s_N(0)\delta s_N(\tau)\delta s_N(\tau')\rangle = e_*^3 \gamma_N \delta(\tau' - \tau)\delta(\tau). \end{cases} \tag{3.11}$$

3.1.2 Discrete time equations of motion

Second-order algorithm

Rather than a simple Euler-type algorithm, we have used a second-order algorithm first implemented in 1992 by S. Linkwitz *et al.* [76, 57], that proved to be much more efficient. Due to the stochastic nature of the equations, standard higher order methods like Runge-Kutta, based on the continuity of the derivatives, are indeed not well suited. The derivation of the algorithm follows the work presented in [57], where the second order differential equation (3.2) is written as a pair of first order equations. This leads to:

$$\begin{cases} \dot{\gamma} = v \\ \dot{v} = -\frac{1}{Q_0}\dot{\gamma} + F(\gamma) + \delta s_B + \delta s_N. \end{cases} \tag{3.12}$$

with[1] $F(\gamma) = -\sin\gamma + s$. The numerical integration consists in computing the time evolution of the variables γ and v using Eq. (3.12). Time is

[1] The simulation has been performed using the exact potential while most of the theories used an approximated cubic potential. It can be shown both for the simulation and for the theory that this makes no difference for the simulated escape rate.

sampled in steps of size $d\tau$, and the problem is to calculate γ and v at time $\tau_{n+1} = (n+1)d\tau$ from their values at time $\tau_n = nd\tau$. In this aim, Eqs. (3.12) are integrated between τ_n and τ_{n+1}, and the resulting time integrals are expanded in Taylor series. While integrating the first equation (3.12.a), one encounters the integral $\int_{\tau_n}^{\tau_n+d\tau} v(\tau')d\tau'$ which is expanded at second order into:

$$\int_{\tau_n}^{\tau_n+d\tau} v(\tau')d\tau' = v_n d\tau + \frac{1}{2}\dot{v}_n d\tau^2. \tag{3.13}$$

Hence, the first discrete time equation is:

$$\gamma_{n+1} - \gamma_n = v_n d\tau + \frac{1}{2}\dot{v}_n d\tau^2 \tag{3.14}$$

where $\dot{v}_n$ is given from (3.12.b) by

$$\dot{v}_n = -\frac{1}{Q_0}v_n + F(\gamma_n) + \frac{1}{d\tau}\int_{d\tau}\delta s_B + \frac{1}{d\tau}\int_{d\tau}\delta s_N. \tag{3.15}$$

The instantaneous value of the noise were written as $\frac{1}{d\tau}\int_{d\tau}\delta s$. Note that the integral of the noise over a time step has no dependence on the step index but only on the step length, therefore $\int_{\tau_n}^{\tau_{n+1}}\delta s$ has been simplified to $\int_{d\tau}\delta s$. For the second equation (3.12.b), the integral over F is approximated using the values of γ at τ_n and τ_{n+1} by:

$$\int_{\tau_n}^{\tau_{n+1}} F(\gamma(\tau'))d\tau' \simeq \frac{F(\gamma_n)+F(\gamma_{n+1})}{2}d\tau. \tag{3.16}$$

The set of discrete time equations of motion forming the second order algorithm is thus:

$$\begin{cases} \gamma_{n+1} - \gamma_n = v_n d\tau + \frac{1}{2}\dot{v}_n d\tau^2 \\ v_{n+1} - v_n = -\frac{1}{Q_0}\left[\gamma_{n+1} - \gamma_n\right] + \frac{F(\gamma_n)+F(\gamma_{n+1})}{2}d\tau + \int_{d\tau}\delta s_B + \int_{d\tau}\delta s_N. \end{cases} \tag{3.17}$$

By dropping the term in $d\tau^2$ in (3.12.a), one recovers the Euler-type algorithm. It is however shown in the following that this second order term allows to perform this very demanding simulation much faster.

Probability laws for discrete noise terms

Numerically, the integrals $\int_{d\tau}\delta s_B$ and $\int_{d\tau}\delta s_N$ are replaced by random variables produced by random number generators, for which only the probability law is specified.

- For the Gaussian noise, the correlation function of Eq. (3.4) yields on average:

$$\left\langle \left(\int_{d\tau} \delta s_B \right)^2 \right\rangle = \int_{d\tau} \int_{d\tau} \langle \delta s_B(t') \delta s_B(t) \rangle \, dt dt' = \frac{2\theta}{Q_0} d\tau. \tag{3.18}$$

The Gaussian part of the noise is therefore accounted for in the algorithm by picking at each step a random variable X following a Gaussian law with zero mean value, variance 1, and by setting the noise integral to:

$$\int_{d\tau} \delta s_B = \sqrt{\frac{2\theta}{Q_0} d\tau} X. \tag{3.19}$$

Note the scaling as $\sqrt{d\tau}$.

- Integrating the asymmetric noise term expressed with Eq. (3.7) over a time step $d\tau$ yields:

$$\int_{d\tau} \delta s_N = e_* \left[dN - \gamma_N d\tau \right]. \tag{3.20}$$

We defined dN as a random variable corresponding to the number of charges having passed through the barrier during $d\tau$. In a Poisson process, this variable is governed by a Poisson law of parameter $\langle dN \rangle$ such that $P(dN = k) = e^{-\langle dN \rangle} \frac{(\langle dN \rangle)^k}{k!}$, where $\langle dN \rangle = \gamma_N d\tau$ is the mean value of dN.[2] The integral on the noise is therefore accounted for in the simulation by picking at each step a random variable Y following a Poisson law of parameter $\gamma_N d\tau$ and setting :

$$\int_{d\tau} \delta s_N = e_* \left[Y - \gamma_N d\tau \right]. \tag{3.21}$$

The quality of the noise generator used in the simulations is crucial, since the effect of the noise asymmetry is tiny. The random numbers used in the simulations presented no erroneous moments and no correlations over the time scale of the simulation, for both the Gaussian and Poisson distributions. Details on the practical implementation are presented in Appendix B.4.

3.2 Rate estimation

3.2.1 Evaluating escape rate from phase dynamics

Escape out of a single well

The escape rate of the superconducting phase difference out of a single well can be obtained from the evolution of the variables γ and v. The

[2] Another possibility to implement a Poisson process is to consider the time intervals $\tau_{i+1} - \tau_i$ between successive tunneling events, that are given by an exponential law. After a tunneling event at τ_i, the following event is found at $\tau_{i+1} = \tau_i + \Delta\tau$ with a probability $P(\tau_{i+1} - \tau_i = \Delta\tau) = \gamma_N \Delta\tau e^{-\gamma_N \Delta\tau}$. This method yields similar results [35].

phase is initialized at the bottom of the well, with zero initial velocity. The algorithm of Eq. (3.17) is iterated until a maximum simulation time τ_p is reached. Due to the action of the noise, the phase starts to oscillate in the well. During the simulation time, it can stay in the well or jump over the barrier. This jump defines an escape event happening at a time τ_{esc}. Theoretically, the escape is defined when the particle overcomes the barrier top, but in practice, this escape is detected when the phase gets larger than 4, a simple criterion ensuring the latter requirement with enough precision and allowing to take recrossings into account.

Over a large number of runs N, escape happens only in a fraction N_{esc} of the runs. $\hat{P} = N_{\text{esc}}/N$ is thus an estimator of the probability P that characterizes the escape process. This allows one to define the behavior of the escape rate out of a single well, which is the aim of this simulation. After the escape, the phase can be retrapped in a further well, leading to phase diffusion at a small velocity, or run away if the velocity is large enough [50]. The complete behavior depends on the amplitude of the noise, the barrier height and the quality factor, as described in Chapter 2. These effects, which concern the behavior of the phase once it escaped out of the well, are not addressed in this simulation.

Numerical estimation of the rate

Theoretically, the probability for the particle to escape between a time τ and $\tau + d\tau$ is given by: $p(\tau \leq \tau_{\text{esc}} < \tau + d\tau) = \Gamma d\tau e^{-\Gamma\tau}$, where Γ is the escape rate (see Appendix B.3). Hence, during a simulation time τ_p, the cumulative probability to have escaped is:

$$P = P(\tau_{\text{esc}} \leq \tau_p) = \int_0^{\tau_p} \Gamma e^{-\Gamma\tau} d\tau = 1 - e^{-\Gamma\tau_p}. \tag{3.22}$$

Numerically, the escape is characterized both by the escape times τ_{esc} and the estimator $\hat{P}$ evaluated from a large number of runs N. The great advantage of numerical simulations, compared to experiments, is that the escape times are easily recorded. There are thus two methods to estimate the escape rate:

- It can be deduced from the escape probability only, as done experimentally. The rate is then estimated using Eq. (3.22) by

$$\hat{\Gamma}_1 = -\frac{1}{\tau_p} \log(1 - \hat{P}). \tag{3.23}$$

  This estimation of the rate is however only meaningful when the estimator $\hat{P}$ is neither 0 nor 1, since no information is obtained when the particle either always or never escapes. It can be shown (see Appendix

B.3.6) that the relative error on the rate with this estimation method depends on P as:

$$\frac{\Delta\hat{\Gamma}_1}{\Gamma} \times \sqrt{N} = \frac{1}{\log(1-P)} \frac{P}{1-P}. \tag{3.24}$$

As expected, the error on the estimated rate drastically increases when P approaches 0 or 1, this method thus presents a strong limitation since the simulation parameters have to be tuned for P to avoid these limits.

- A second method is to use also the information on the escape times. To cope with the situation where the particle does not escape, we define the variable τ_i as:

$$\tau_i = \begin{cases} \tau_{\text{esc}} \text{ if the particle escapes} \\ \tau_p \text{ otherwise} \end{cases} \tag{3.25}$$

so that when the particle does not escape, one considers that the escape time is τ_p. The expected mean value of τ_i is obtained as:

$$\langle \tau_i \rangle = \int_0^{\tau_p} \tau_{\text{esc}} \Gamma e^{-\Gamma \tau_{\text{esc}}} d\tau_{\text{esc}} + \tau_p \int_{\tau_p}^{\infty} p(\tau) d\tau, \tag{3.26}$$

which yields:

$$\langle \tau_{\text{i}} \rangle = \frac{1}{\Gamma}(1 - e^{-\Gamma \tau_p}). \tag{3.27}$$

One defines $\hat{\tau} = \sum \tau_i$ as the estimator of $\langle \tau_{\text{i}} \rangle$. The rate should thus be calculated using $\hat{\tau}$ and solving Eq. (3.27) which can not be inverted analytically. However, one can use $\hat{P}$ as the estimated value of $1 - e^{-\Gamma \tau_p}$. Therefore, a simple estimator of the rate is:

$$\hat{\Gamma}_3 = \frac{\hat{P}}{\hat{\tau}}. \tag{3.28}$$

The calculation of the error performed with this estimator, kindly performed by L. Tournier [77], is reproduced in Appendix B.3.6. The error is:

$$\frac{\Delta\hat{\Gamma}_3}{\Gamma} \times \sqrt{N} = \frac{1}{\sqrt{P}}. \tag{3.29}$$

The error on the rate obtained for both methods is plotted in Fig. 3.2, and compared with the predictions of Eq.(3.24) and (3.29). Overall, the second method performs with a good precision on a wider range of P, since the error does not diverge as P approaches 1 but rather reaches the minimum $\frac{1}{\sqrt{N}}$. Noting that as long as $P \geq 0.5$ the error on the rate

obtained with the second method is close to this minimum value, one only ensures in the simulation that τ_p is large enough so that the particle escapes with $P \geq 0.5$, and the rate is obtained from Eq. (3.28). In the most precise simulations on rate asymmetry, τ_p is set to a large enough value to ensure that the particle always escapes, to have a minimum error.

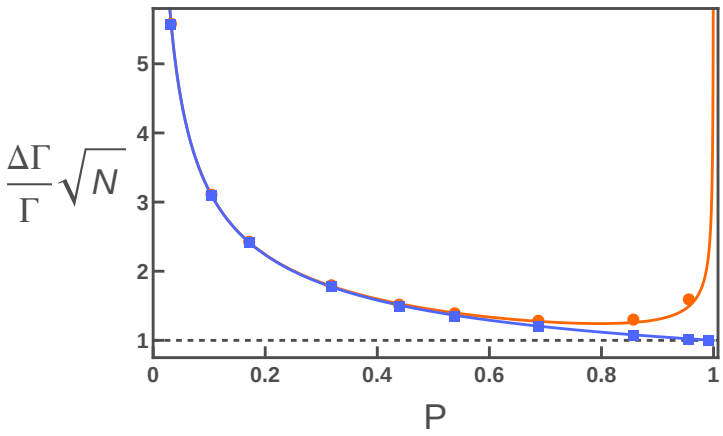

Fig. 3.2. Symbols: Relative error for the rate estimation over 10000 trajectories. The two methods to extract the rate are compared (circles for the first method and squares for the second method). **Solid lines:** predicted relative error for both methods. **Dashed line:** minimum relative error, reached only for $P = 1$ using the second method.

3.2.2 Simulation parameters

First, the behavior of the algorithm was probed by simple tests. The quality of the simulation was tested through the thermalization of the system, especially the energy equipartition. The impact of the time step on the thermalization and the sensitivity to the initials conditions were investigated to confirm the advantage of the second order algorithm over the simple Euler-type method. In those tests, only a Gaussian noise was used.

Thermalization

Having fixed a reduced temperature θ for the Gaussian noise, we monitor the evolution of the potential energy $E_U = -\cos(\gamma) - s\gamma$ and kinetic energy $E_K = \frac{1}{2}v^2$ when the particle oscillates at the bottom of the well (this was performed for an unbiased junction). The evolution of the kinetic en-

ergy[3] E_K, shown in Fig. 3.3(a), is computed using a time step $d\tau = 0.01$ until it converges to an asymptotic value E_K^∞. For the second-order algorithm, E_K converges to the expected equilibrium value $\frac{1}{2}\theta$, which is not the case for the Euler-type algorithm.

Figure 3.3(b) shows the dependence of the asymptotic kinetic energy E_K^∞ on the time step. For the second-order algorithm, $E_K^\infty = \frac{1}{2}\theta$ for time steps up to $d\tau \simeq 0.2$, which is not the case for the Euler-type algorithm when $d\tau > 0.002$. A systematic correction to the asymptotic energy is expected because the energy is calculated at discrete time steps, as discussed in [76, 78], but this correction is expected to be much smaller at such a small time step. The disagreement observed here rather shows the failure of the Euler-type algorithm, although it is difficult to explain why this failure starts at such low threshold.

The improper convergence of the Euler-type algorithm is also visible on the resulting value of the escape rate, shown in Fig. 3.4(a). The rate becomes time-step-dependent for $d\tau > 0.005$, while the rate calculated with the second-order algorithm stays constant up to $d\tau \simeq 0.2$.

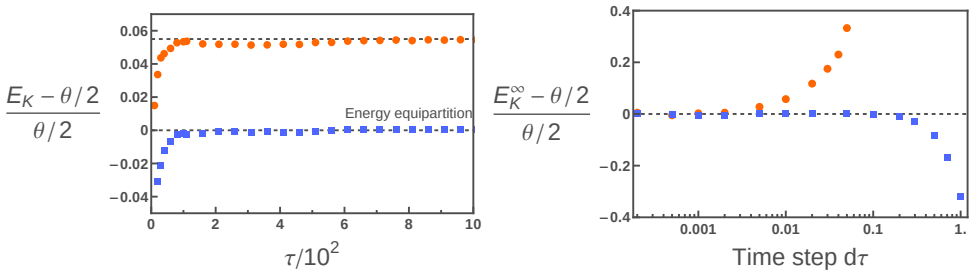

Fig. 3.3. Kinetic energy of the particle at $s = 0$, for $Q_0 = 5$ and a temperature $\theta = 0.04$. **Left:** Variation with time τ for the Euler-type (orange circles) and the second-order (blue squares) algorithm for a time step $d\tau = 0.01$. After a thermalization time, the energy converges to an equilibrium value E_K^∞. For the Euler-type algorithm, this equilibrium is not $\frac{1}{2}\theta$ as expected from energy equipartition, but is 5% above. **Right:** Average kinetic energy reached after a time $\tau = 5 \times 10^7$ as a function of the time step for the Euler-type (orange circles) and the second-order algorithm (blue squares).

Sensitivity to the initial conditions

During the thermalization time shown in Fig. 3.3(a), the escape rate is slightly dependent on the initial velocity. However, if the barrier is sufficiently large, this thermalization time is small compared to the escape time and does not affect the evaluation of the rate. This is the case in

[3] A similar plot for the potential energy brings similar information.

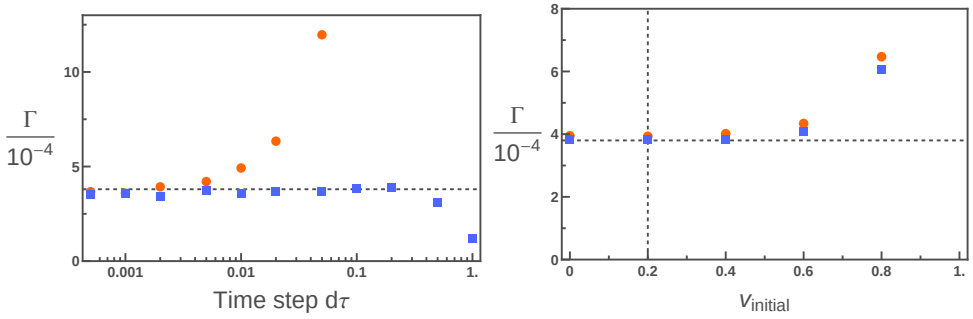

Fig. 3.4. Dependence on the simulation parameters for $Q_0 = 5$, $s = 0.76$ and $\theta = 0.04$. **Left:** Escape rate as a function of the time step for the Euler-type (orange circles) and the second-order (blue squares) algorithm. Dashed line corresponds to the predicted value (see further in text). **Right:** Escape rate as a function of the initial velocity ($d\tau = 0.002$ for the Euler-type algorithm (orange circles), $d\tau = 0.02$ for the second-order one (blue squares)). The value $v_{\text{initial}} = 0.2$ corresponds to the thermal velocity set by the condition of energy equipartition. The behavior presented here is similar for all values of Q_0.

all the simulations, as can be seen in Fig 3.4(b) where the rate has been calculated for various initial velocities v_{initial}. In the simulations, the particle was initialized for convenience at the bottom of the well with zero velocity.

Conclusion on the algorithms

These simple tests indicate that the use of the second order algorithm instead of the simplest one considerably reduces the simulation time, since it stands time steps more than one order of magnitude larger with a calculation time of each step only 25% longer. In the following, this algorithm was used with $d\tau = 0.02$**.**

3.3 Results on the escape rate

With this reliable algorithm in hands, the behavior of the rate was probed in two different situations. First, the rate was obtained in the well known case of a Gaussian noise, where the results could be compared quantitatively to the exact existing theory. This allowed to confirm the reliability of our simulations. Second, the escape rate was evaluated in the case where the junction was submitted only to a Poisson noise or to a mixture of both sorts of noise. The behavior of the rate in this regime was then compared with the recent theoretical predictions detailed in the previous chapter.

3.3.1 Escape rate for Gaussian noise

Prediction for the rate driven by Gaussian noise

The escape rate for a Josephson junction submitted to Gaussian noise is given in Eq. (2.30). In dimensionless units, this prediction is:

$$\Gamma = \lambda\left(B, Q(s)\right) \frac{(1-s^2)^{1/4}}{2\pi} e^{-\frac{\Delta U(s)}{\theta}} \tag{3.30}$$

where $\lambda\left(B, Q(s)\right)$ is the prefactor given in Eq. (2.33), $B = \frac{\Delta U(s)}{\theta}$ and

$$\Delta U(s) = 2\sqrt{1-s^2} - s(\pi - 2\arcsin(s)). \tag{3.31}$$

This prediction, and in particular the expression of the prefactor, was already tested numerically in [57, 76]. As a first step, we recovered these results.

Rate as a function of θ and Q_0

The rates were simulated for various temperatures and reduced bias currents s in the range corresponding to a moderate barrier height $B = \frac{\Delta U}{\theta} \in [5 - 9.5]$ ($B^{2/3} \in [3 - 4.5]$). The lower bound was chosen to keep a barrier sufficiently high compared to temperature. Only in this regime could the results be compared with theory, which is valid only for $B \geq 5$. The higher bound was set to limit the simulation time. Since the escape rate is predicted to behave as $\Gamma = \lambda \frac{\omega_p}{2\pi} e^{-B}$, a common method to probe if the simulated rate does follow such a behavior is to consider, instead of the rate, the function:

$$B^{2/3} = \left(\log\left[\lambda \frac{\omega_p}{2\pi}\right] - \log\left[\Gamma\right]\right)^{2/3}. \tag{3.32}$$

According to theory:

$$B = \frac{\Delta U}{\theta} \propto \frac{1}{\theta}\left(1-s\right)^{3/2}, \tag{3.33}$$

where we have considered the dimensionless form of the approximated expression of Eq. (2.14) for the barrier height. Hence, $B^{2/3}$ is expected to vary as $(1-s)$, with a slope proportional to $\theta^{-2/3}$. The very good agreement in Fig. 3.5(a) between the simulated $B^{2/3}$ and the prediction gives confidence in the correct thermalization of the particle. Using Eq. (3.32) to calculate $B^{2/3}$ however requires some self-consistency since the theoretical prefactor is also dependent on B.

A better and simpler way to check the agreement between simulation

and prediction is to plot the ratio $\frac{\Gamma_{\text{sim}}}{\Gamma_{\text{theo}}}$ of the simulated rate over the prediction as shown in Fig. 3.5(b). The agreement is excellent considering the statistical accuracy of 1%. This confirms the correct behavior of the simulations.

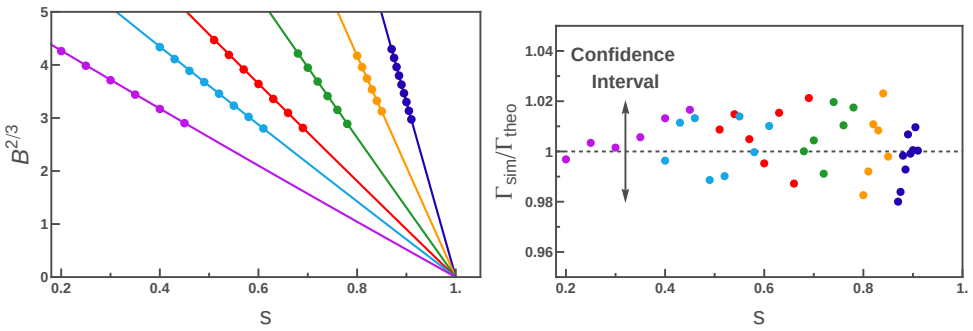

Fig. 3.5. Escape rate activated by Gaussian noise for $Q_0 = 5$ over $N = 10^4$ runs, yielding a statistical error of 1%. **Left:** $B^{2/3}$ plot for various θ (0.01, 0.02, 0.04, 0.07, 0.1, 0.16 from right to left). Points are from simulation and solid lines are predictions using the barrier height of Eq. (3.31). **Right:** Ratio between simulated rates and predicted rates for the same temperatures. With $N = 10^4$, 95% of the points are expected to be within 1 ± 0.02.

The rates were also simulated for various quality factors with $B = 10$. Dividing this rate by the value predicted from the Transition State Theory [50] (Eq. (2.29)) yields a determination of the prefactor. Figure 3.6 compares this estimation to the theoretical prediction. The very good agreement confirms the quality of the simulation, and extends the validation of the theory over a wider range of parameters.

3.3.2 Escape rate for Poisson noise

Having confirmed the reliability of the simulation with a Gaussian noise, we then introduced a Poisson noise source to probe its effect on the escape rate. Comparison is carried out with the predictions from Ref. [11].

Prediction for the effect of Poisson noise on the escape rate

The effect of Poisson noise can be separated in two contributions, due respectively to the second and third moment of the noise. The effect of the second moment of noise is a large increase of the escape rate. In analogy with the case of a Gaussian noise, the effect is characterized by an effective temperature that represents the power of the noise, give by Eq. (3.11). In reduced units, this temperature is:

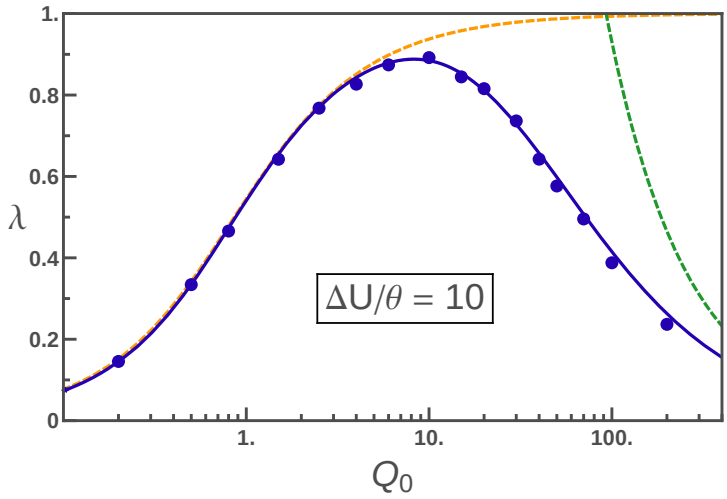

Fig. 3.6. Prefactor deduced from the simulations performed for various Q_0 at $s = 0.8$ and $\theta = 0.017$ (such that $B = 10$). **Solid line:** prediction for the prefactor of the escape rate $\lambda(B, Q(s))$ of Eq. (2.33) [55]. **Dashed lines:** Kramers limits κ_1 and κ_2 of low and high damping described in Eqs. (2.32) and (2.31) [4].

$$\theta_{\text{eff}} = \theta + \frac{1}{2} Q_0 e_*^2 \gamma_N \tag{3.34}$$

where θ is the temperature corresponding to the Gaussian noise. This expression is valid whatever is the second moment of Poisson noise compared to that of Gaussian noise; the effective temperature can in particular be much higher than θ.

The effect of the third moment is much smaller. Since the third moment is related to the asymmetry of the noise, the escape rate becomes also asymmetric. It is dependent on the relative sign of the reduced bias current and of the current giving rise to the noise δs_N. Keeping the latest constant, we considered the rates obtained for positive bias s (noted Γ_+), and for negative bias $-s$ (noted Γ_-). In theory (see Eq. (2.58)), these escape rates are expected to behave as:

$$\Gamma_+ \propto \exp\{-[B_2(\theta_{\text{eff}}) + B_3]\} \tag{3.35}$$

and

$$\Gamma_- \propto \exp\{-[B_2(\theta_{\text{eff}}) - B_3]\}. \tag{3.36}$$

The term $B_2 = \frac{\Delta U}{\theta_{\text{eff}}}$ corresponds to the effect of the second moment of Poisson noise, in analogy with $B = \frac{\Delta U}{\theta}$ for Gaussian noise at a temperature θ. The small corrective term B_3 accounts for the asymmetry of Poisson noise. It is assumed here that the prefactor is not affected by the noise asymmetry, which only enters through B_3. From Γ_+ and Γ_-, one builds two quantities:

- The geometric mean of the two rates, or mean rate, defined by

$$\overline{\Gamma} = \sqrt{\Gamma_+ \Gamma_-} \propto \exp[-B_2(\theta_{\text{eff}})]. \tag{3.37}$$

  This effective mean rate is only sensitive to the second moment of noise and is thus expected to behave exactly as the escape rate obtained in the Gaussian case for a temperature θ_{eff}, therefore follow Eq. (3.30).

- The rate asymmetry, defined as:

$$R_\Gamma = \frac{\Gamma_+}{\Gamma_-} = \exp[2|B_3|]. \tag{3.38}$$

  The departure from one of this quantity is a direct measurement of the effect of the third moment of the noise. In theory, the corrective term B_3 of Eq. (2.94) is given in reduced units by:

$$B_3 = -\gamma_N \left(\frac{e_*}{\theta_{\text{eff}}}\right)^3 j(Q_0, s) \tag{3.39}$$

  where $j(Q_0, s)$ corresponds in this chapter to the function $j_{\text{FullQ}}(Q_0, s)$ of Eq. (2.92), calculated by H. Grabert, that covers the full range of quality factors.

In order to probe the behavior of the mean rate and the rate asymmetry, Γ_+ and Γ_- were simulated with various sets of parameters (γ_N, Q_0 and s) and $N \geq 10^5$. The geometric mean rate was compared with the Gaussian prediction, while the rate asymmetry was compared with the prediction using the corrective term B_3.

Rates as functions of γ_N

The rates were first measured as a function of the noise amplitude. In the Gaussian case, this corresponds to changing the temperature. In the case of a Poisson noise, the amplitude was modulated with γ_N.

Following the procedure already used in the Gaussian case, the mean rates $\overline{\Gamma}$ calculated for $Q_0 = 5$, which corresponds to the experimental value of [38], were converted into $B^{2/3}$ functions shown in Fig. 3.7(a). These functions are compared to the theory for Gaussian noise using the predicted effective temperature of Eq. (3.34). In Fig. 3.7(b), the mean rates are divided by the predicted values: they appear to be about 1% larger. This is only a slight discrepancy at $Q_0 = 5$, but calculations at larger values of Q_0 give larger deviations, as discussed below.

The rate asymmetry is shown in Fig. 3.8, and compared with the prediction of Eq. (2.95) for $Q_0 = 5$. From this figure, it appears that the theoretical prediction is larger than the simulation results by 20%, but the s-dependence is correct.

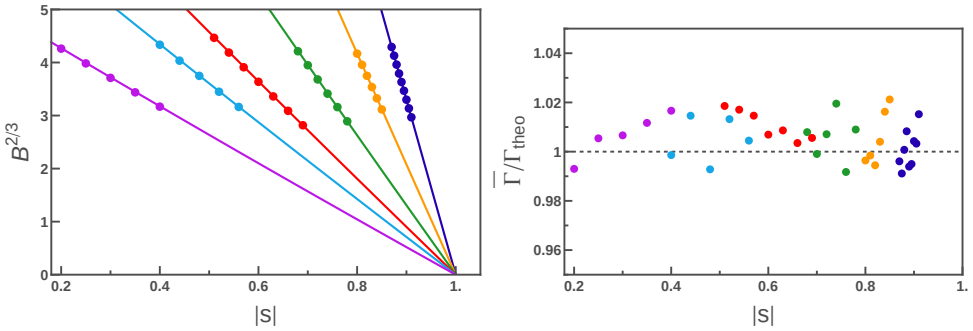

Fig. 3.7. Mean rate activated by a Poisson noise for $Q_0 = 5$ in absence of extra Gaussian noise ($\theta = 0$). **Left:** $B^{2/3}$ plot for various values of γ_N corresponding to θ_{eff} =0.01, 0.02, 0.04, 0.07, 0.1 and 0.16 from right to left. Points are the simulation and solid lines are the predictions for the Gaussian case using the expected effective temperature. **Right:** Ratio between the mean rates and the predicted values, for the same data.

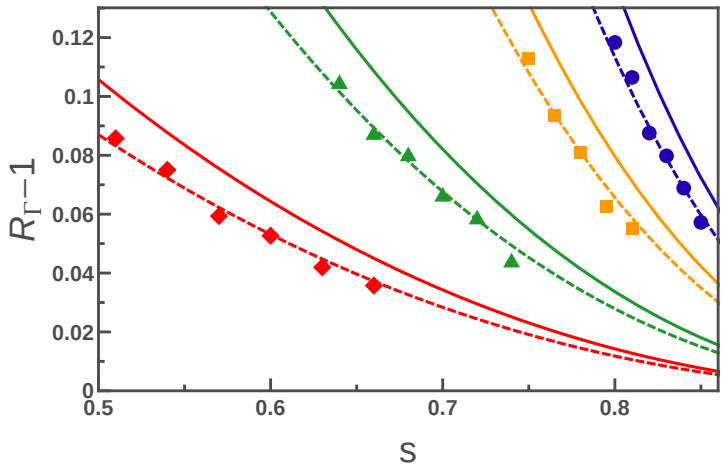

Fig. 3.8. Rate asymmetry for various effective temperatures, for $Q_0 = 5$, computed for the s range corresponding to $B \in [5-8]$ (with $\theta = 0.01$ and values of γ_N corresponding to $\theta_{\text{eff}} = 0.02, 0.03, 0.05, 0.08$). **Solid line:** predictions using the result from Eq. (2.95) that was calculated for $Q_0 = 5$ in the complete range of s. **Dashed line:** Same predictions scaled down by 20% to fit the simulation data.

Rates as functions of Q_0

Another set of simulations was performed to probe the dependence of the escape rate on Q_0. This is similar to the evaluation of the prefactor performed for the Gaussian case. For each value of Q_0, the rates were simulated after having chosen the parameters in two steps:

- γ_N was fixed to yield a given effective temperature;

- with this temperature, s is picked to yield a given value of B_2, while keeping $s \geq 0.99$ to be in the limit where Grabert's simplest results of Eq. (2.92) are valid [11].

Hence, the ratio $\frac{\gamma_N e_*^3}{\theta_{\text{eff}}^3}$ appearing in the theory is set with the first step, while $j(Q_0, s)$ is set with the second. Figure 3.9 represents the mean rate $\overline{\Gamma}$ divided by the prediction from the Transition State Theory as a function of the quality factor (see Eq. (2.29)). One thus expects to recover the prefactor prediction already checked in the Gaussian case, as was shown in Fig. 3.6. However, a slight disagreement is found in the range of intermediate quality factors. A tentative explanation is that this deviation is due to an effect of the asymmetry of the Poisson noise on the prefactor of the escape rate, an effect which is either not addressed by theory [11], or neglected [31, 32].
A similar deviation can be observed on the rate asymmetry, shown in Fig. 3.10. It should be noted however that, apart from this deviation, the qualitative behavior of the rate asymmetry, especially the position of the turnover, is perfectly described by theory.

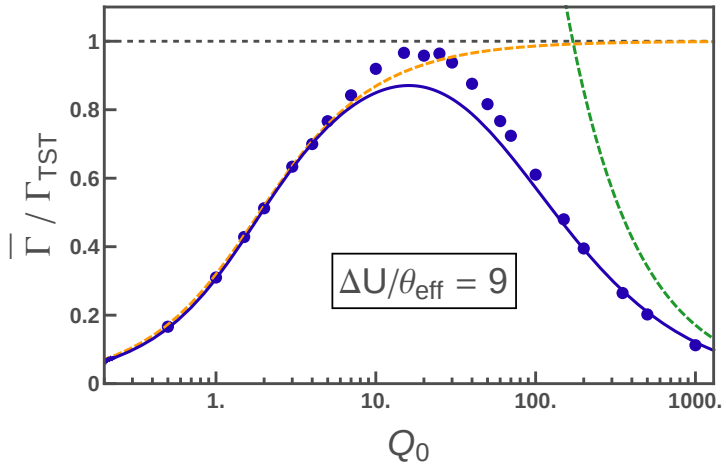

Fig. 3.9. Mean rate $\overline{\Gamma}$ divided by the prediction from TST (taken at the expected θ_{eff}) [50] for a Poisson noise source. γ_N is chosen to yield $\theta_{\text{eff}} = 0.00016$, with $\theta = 0.00012$, $s = 0.992$ so that $B_2 \simeq 9$. **Solid line:** Prediction for the prefactor in the Gaussian case. **Dashed line:** TST prediction and Kramers' low and high damping limits.

Rates as functions of s

The last set of simulations was performed to probe the variation of the escape rate with the reduced bias current s, for various values of Q_0.

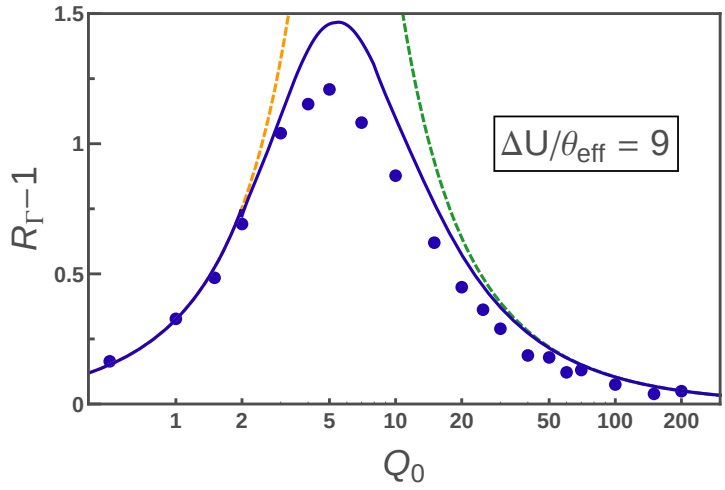

Fig. 3.10. Rate asymmetry. γ_N is chosen to yield $\theta_{\text{eff}} = 0.00016$, with $\theta = 0.00012$, $s = 0.992$ so that $B_2 \simeq 9$. **Solid line:** theoretical prediction. A discrepancy between simulations and theory is found for intermediate values of Q_0. **Dashed lines:** low-damping and high-damping limits of Eq. (2.76) calculated in [33].

Once Q_0, γ_N, and θ_{eff} were fixed, only s was varied, staying in the range $s \geq 0.99$. In Fig. 3.11, we plot the ratio between the mean rate $\overline{\Gamma}$ and the predicted rate for the Gaussian case. According to theory, this term should be equal to 1 at all values of Q_0 and s.
Only for low quality factors do the predicted effective temperature agrees with the simulations. Moreover, the deviation increases when s is reduced (i.e. when B is increased). Such a behavior is attributed again to a possible modification of the prefactor that appears at low damping, which is not considered by theory.
For $Q_0 = 2$ where the effective temperature is properly predicted, the rate asymmetry is compared with theory in Fig. 3.12. The good agreement between theory and simulation in this range of s (and B_2) gives confidence in the validity of the prediction on the s-dependence, at least for s close to 1.

Conclusion on the effect of Poisson noise

In a nutshell, the simulations show that the effect of Poisson noise on the escape rate is well accounted for by theory in the limit of high damping. However, for quality factors larger than 2, both the simulated effective temperature and the simulated rate asymmetry slightly deviate from the prediction, even if the qualitative behavior is very well predicted. A tentative explanation is that the third moment of noise not only affects the exponential part of the rate, but also the prefactor, an effect not taken

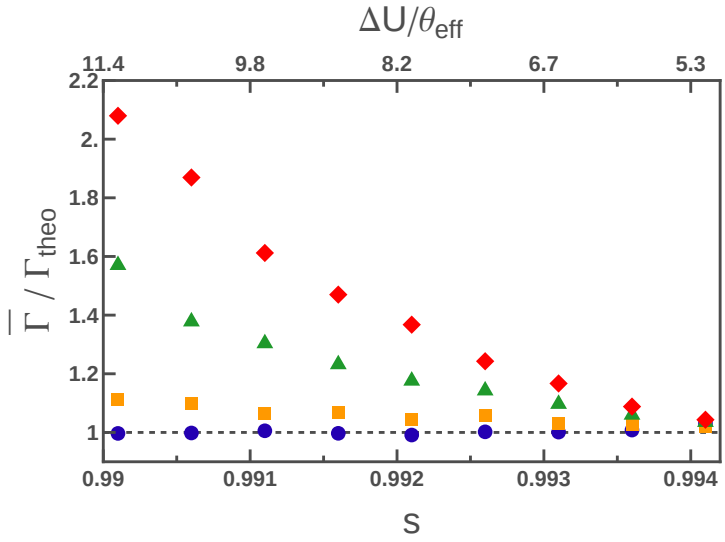

Fig. 3.11. Mean rate obtained for a Poisson noise source for Q_0=2, 10, 30 and 60 (dark blue circle, orange squares, green triangles, and red diamonds). The mean rate is divided by the prediction for the Gaussian case, so that all points should be on the dashed line, equals to 1. While the simulated rate equals as expected the predicted one for low Q_0, a sizeable deviation is found for larger values of Q_0. For each value of Q_0, γ_N and θ are fixed to have $\theta_{\text{eff}} = 0.000165$ (with γ_N=1.5, 0.25, 0.2, and 0.2 for increasing quality factors). The range in s corresponds to $B_2 \in [5 - 12]$.

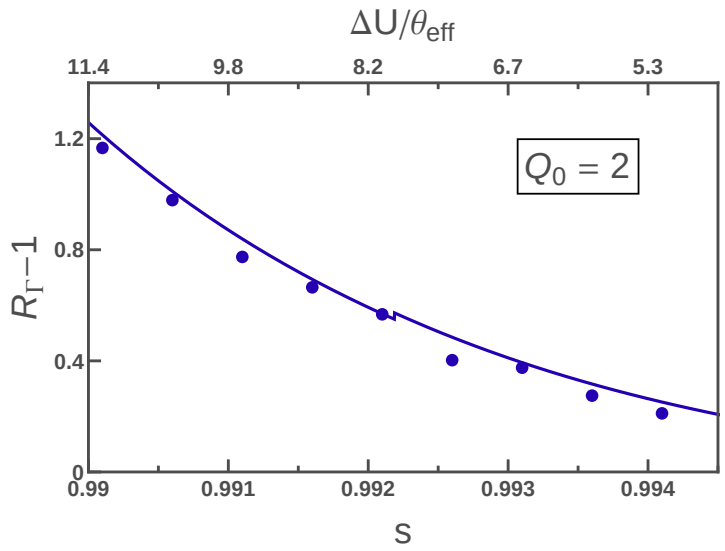

Fig. 3.12. Symbols: Rate asymmetry for $Q_0 = 2$. γ_N=1.5 and θ is fixed to have $\theta_{\text{eff}} = 0.000165$. **Solid lines:** theoretical prediction (the slight jump in the line is due to a discontinuity between the two limits of Eq. (2.92)).

into account by the theory. It does not come as a surprise that the discrepancy appears in this turnover region $Q_0 \simeq B$, where the dynamics crosses over between spatial-diffusion and energy-diffusion [55, 56]. For a set of parameters that corresponds to the experiments presented in the next chapter, where the quality factor is estimated around $Q_0 = 5$, theory appears to overestimate the rate asymmetry obtained with the simulations by 20%. An extension of the theory tackling the effect of asymmetric noise on the prefactor might resolve this discrepancy.

3.4 Effect of a low-frequency cutoff

In the experiment, the dc part of the noise is cut by an RC filter [35, 38] to ensure that the Poisson noise added to the bias current of the junction has zero mean value. To probe the effect of this cut-off on the rate asymmetry, we simulated the dynamics of the circuit shown in Fig. 3.13. In this circuit, both the Poisson noise δI_N and the Johnson-Nyquist noise δI_{B2} are filtered. Only the components of the noise at large enough frequencies reach the Josephson junction, while the low frequency part flows through the resistor R_2. Beware that two resistors are present, each of them producing a Johnson-Nyquist noise. For simplicity, we consider in this section that they have different resistances but are at the same temperature.

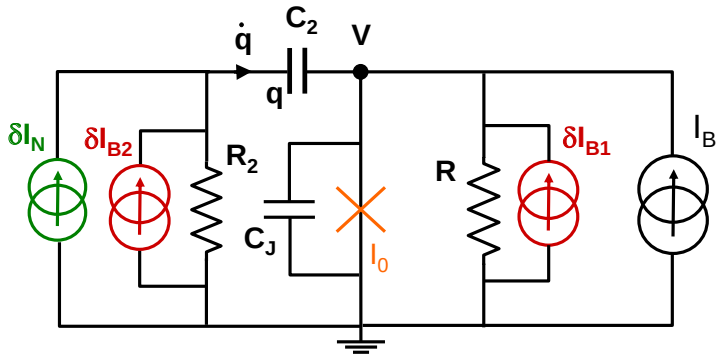

Fig. 3.13. Setup used to describe the low-frequency cutoff present in the experiment presented in the following chapter. The capacitor C_2 and the resistor R_2 play the role of a high-pass filter for the current fluctuations δI_{B2} and δI_N, while the noise δI_{B1} is unaffected.

3.4.1 Algorithm

Equations of motion for the RC-filtering circuit

The equations of motion for this circuit of Fig. 3.13 are:

$$\begin{cases} V = \varphi_0 \dot{\gamma} \\ V = -\frac{q}{C_2} + R_2(\delta I_{B2} + \delta I_N - \dot{q}) \\ C_J \dot{V} + \frac{V}{R} + I_0 \sin\gamma - \dot{q} = I_B + \delta I_{B1}. \end{cases} \tag{3.40}$$

They can be converted into three first-order differential equations for the three variables $\{V, \gamma, q\}$, where q is the charge on the coupling capacitor C_2. The dimensionless equations are:

$$\begin{cases} \dot{\gamma} = v \\ \dot{q^*} = -\frac{1}{Q_2}\dot{\gamma} - \frac{c}{Q_2} q^* + \delta s_{B2} + \delta s_N \\ \dot{v} = -\frac{1}{Q_0}\dot{\gamma} - \sin\gamma + s + \dot{q^*} + \delta s_{B1} \end{cases} \tag{3.41}$$

with $Q_2 = R_2 C_J \omega_0$, $c = \frac{C_J}{C_2}$ and $q^* = \frac{\omega_0}{I_0} q$.

RC-Algorithm

In the following, q^* is noted q for convenience. With the method presented in the first section, a Taylor expansion at second order of the time integrals appearing in the discrete time equations yields:

$$\begin{cases} \gamma_{n+1} - \gamma_n = v_n d\tau + \frac{1}{2}\dot{v}_n d\tau^2 \\ q_{n+1} - q_n = -\frac{c}{Q_2}\left[q_n d\tau + \frac{1}{2}\dot{q}_n d\tau^2\right] - \frac{1}{Q_2}\left[\gamma_{n+1} - \gamma_n\right] + \int_{d\tau} \delta s_{B2} + \int_{d\tau} \delta s_N \\ v_{n+1} - v_n = -\frac{1}{Q_0}\left[\gamma_{n+1} - \gamma_n\right] + \frac{F(\gamma_n) + F(\gamma_{n+1})}{2} d\tau + \left[q_{n+1} - q_n\right] + \int_{d\tau} \delta s_{B1} \end{cases} \tag{3.42}$$

with

$$\begin{cases} \dot{q}_n = -\frac{1}{Q_2} v_n - \frac{c}{Q_2} q_n + \frac{1}{d\tau}\int_{d\tau} \delta s_{B2} + \frac{1}{d\tau}\int_{d\tau} \delta s_N \\ \dot{v} = -\frac{1}{Q_0} v_n + F(\gamma_n) + \dot{q}_n + \delta s_{B1}. \end{cases} \tag{3.43}$$

Probability laws for the noise terms

Both Gaussian noises $\int_{d\tau} \delta s_{B1}$ and $\int_{d\tau} \delta s_{B2}$ are accounted for in this algorithm in a manner similar to the simplest case, with their respective standard deviation being $\sqrt{\frac{2\theta}{Q_0} d\tau}$ and $\sqrt{\frac{2\theta}{Q_2} d\tau}$. In the limit $c = 0$, one recovers the second-order algorithm presented in the first section for a RCSJ model, with the Gaussian noise being the sum of two terms. The mean value of Gaussian noise remains zero while the variance of the overall Gaussian noise is the sum of the variances of the two noises, hence $\frac{2\theta}{Q_0} + \frac{2\theta}{Q_2} = \frac{2\theta}{Q_{\text{eff}}}$ where we defined $Q_{\text{eff}} = \frac{1}{\frac{1}{Q_0} + \frac{1}{Q_2}}$.

3.4.2 Dynamics of the circuit

Cut-off frequency and Plasma frequency

The filter cuts the frequencies lower than $\frac{1}{R_2C_2} = \frac{c}{Q_2}$. This frequency has to be compared with the plasma frequency:

$$\nu_p = \frac{1}{2\pi}(1-s^2)^{1/4}. \tag{3.44}$$

When the cutoff frequency is much smaller than the plasma frequency, the filtering of the noise is expected to have a negligible effect on the escape rate. At the opposite, the escape rate due to Poisson noise should be strongly diminished when the cutoff is higher than the plasma frequency.

Quality factor

In the circuit of Fig. 3.13, the junction can not directly be considered within a simple RCSJ model. The complete environment has to be taken into account to calculate the quality factor of the phase dynamics for arbitrary values of c. It appears that in the relevant case of a low-frequency cutoff, i.e. $\frac{c}{Q_2} \ll 1$, the quality factor of the dynamics is well approximated by $Q_{\rm eff}$, and the junction is reasonably treated within an effective RCSJ model.[4] The effective temperature relevant for the escape rate with a Poisson noise is then:

$$\theta_{\rm eff} = \theta + \frac{1}{2}Q_{\rm eff}e_*^2\gamma_N. \tag{3.47}$$

3.4.3 Simulation results

We performed several tests to probe the effect of filtering, from energy equipartition to rate asymmetry.

[4] The admittance seen from the bias line is:

$$Y_{\rm tot}(\omega) = \frac{1}{R} + jC_J\omega + \frac{1}{jL_J\omega} + \frac{1}{R_2 + \frac{1}{jC_2\omega}} \tag{3.45}$$

where L_J is the Josephson inductance. When $c \ll 1$, the admittance simplifies to:

$$Y_{\rm tot}(\omega) = \frac{1}{R_{\rm eff}}\left[1 + jQ_{\rm eff}(\frac{\omega}{\omega_{p0}} - \frac{\omega}{\omega_{p0}})\right] \tag{3.46}$$

where $\frac{1}{R_{\rm eff}} = \frac{1}{R} + \frac{1}{R_2}$ and $Q_{\rm eff} = R_{\rm eff}C_J\omega_{p0}$. The environment thus behaves like a simple Ohmic environment with two resistors in parallel and a quality factor $Q_{\rm eff}$.

Energy equipartition

We first monitored the average kinetic energy $\langle E_K \rangle$ of the particle at long times, when the junction is submitted solely to a Poisson noise at $s = 0$ (the plasma frequency is thus equal to $\frac{1}{2\pi}$). For $c = 0$, the average kinetic energy reaches $\frac{1}{2}\theta_{\text{eff}}$, since there is no filtering. When c is increased, the particle decouples from the noise source. Its energy thus decreases, as shown in Fig. 3.14. In the limit $\frac{c}{Q_2} \gg \frac{1}{2\pi}$, where all frequencies below the plasma frequency are cut, the energy of the particle reaches zero.
In another simulation, the Poisson noise was set to zero and the temperature to a finite value θ. In this case, the energy of the particle reaches $\frac{1}{2}\theta$ at all values of c, even if the Johnson-Nyquist noise δs_{B2} is completely filtered for $\frac{c}{Q_2} \gg 1$. This is because at equilibrium, the variance of the noise obeys the fluctuation-dissipation theorem. If part of the fluctuations are filtered, part of the dissipation also, and both effects compensate each other.

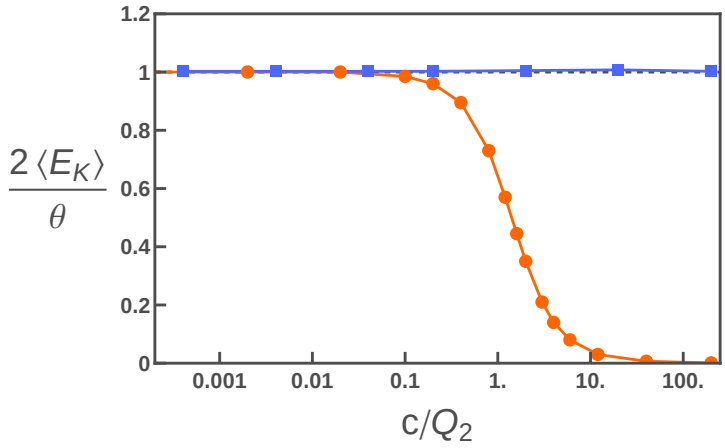

Fig. 3.14. Kinetic energy of the particle at $s = 0$ as a function of $\frac{c}{Q_2}$ for the two types of noise. **Dots:** Only Poisson noise is present ($\theta = 0$), with the parameters $Q_0 = 5$, Q_2=5, $\gamma_N = 640$ yielding $\theta_{\text{eff}} = 0.02$. **Squares:** the two sources of Gaussian noise are present ($\theta = 0.04$, $Q_0 = 5$, Q_2=5) and Poisson noise is set to zero. For large values of $\frac{c}{Q_2}$, the (non-equilibrium) Poisson noise is filtered so that the kinetic energy of the particle goes to 0, while for the (equilibrium) Gaussian noise, the energy is not affected by the cutoff.

Escape rates

We then probed the behavior of the escape rate when varying $\frac{c}{Q_2}$. The simulated rate is shown in Fig. 3.15 when the system is only submitted to a Poisson noise ($T = 0$). The reduced bias current is $s = 0.92$, yielding a plasma frequency of 0.1. The rates obtained for both signs of the

bias current are shown, the difference being due to the asymmetry of the noise. At very low values of $\frac{c}{Q_2}$, the rates are not affected by the cutoff. When $\frac{c}{Q_2}$ increases and approaches a significant fraction of the plasma frequency, the rates are reduced since part of the noise is filtered.[5]
The corresponding rate asymmetry is shown in Fig. 3.16, where it is normalized by its value at $c = 0$. Up to $\frac{c}{Q_2} \simeq 0.001$, the rate asymmetry $R_\Gamma - 1$ seems to remain unaffected by the low-frequency cutoff. However, the rate asymmetry starts to diminish when $\frac{c}{Q_2}$ is further increased. The general curve depends only slightly on the quality factor (in the small range of quality factor probed here, which is the relevant experimental range). This allows to determine a general condition for the maximum cutoff frequency yielding negligible effects on the observed rate asymmetry:

$$\frac{c}{Q_2} < \frac{\nu_p}{100}. \tag{3.48}$$

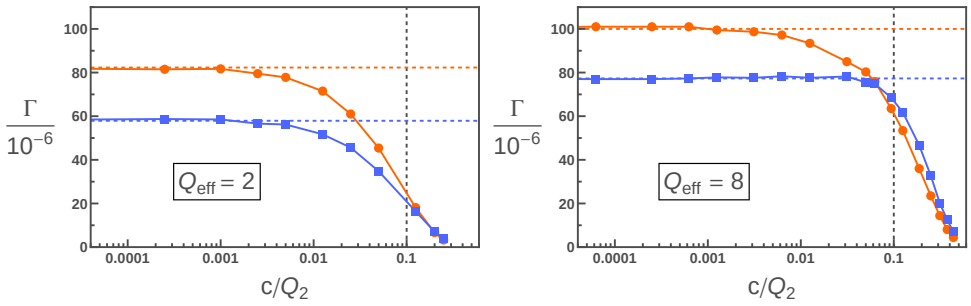

Fig. 3.15. Escape rates activated by Poisson noise for positive and negative bias (circles and square) as a function of $\frac{c}{Q_2}$. **Left:** Escape rates for $Q_2 = Q_0 = 4$. Rates are obtained for $s = 0.92$, $\theta = 0$ and γ_N is fixed to yield $\theta_{\text{eff}} = 0.00625$. Dashed vertical line corresponds to the plasma frequency. **Right:** Escape rate for $Q_2 = Q_0 = 16$.

[5] Surprisingly, the two rates behave slightly differently. The decrease is not similar for both bias signs and does not start for the same value of $\frac{c}{Q_2}$. This discrepancy in the behavior between the two rates is increased for higher values of Q_{eff}, and no clear explanation has been found presently.

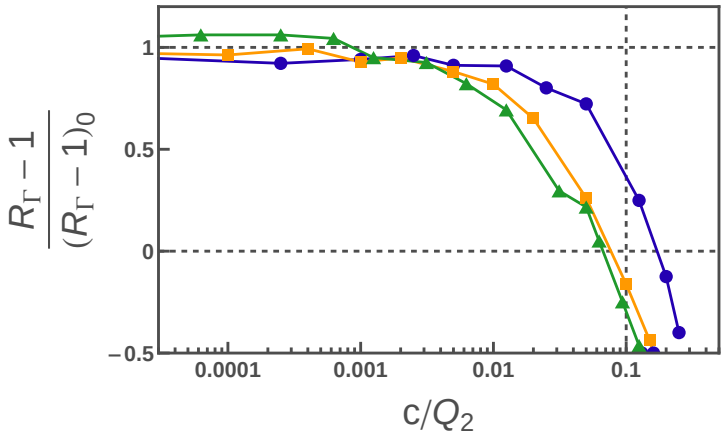

Fig. 3.16. Symbols: Rate asymmetry at $s = 0.92$ as a function of c/Q_2 for three values of effective quality factor (Q_{eff}=2, 5, and 8 (circles, squares, and triangles)). **Dashed vertical line:** plasma frequency at this bias current.

3.5 Conclusion

In this chapter, we have performed numerical simulations on the dynamics of a Josephson junction biased with a Poisson noise source.

- In a first part, we determined the effect of the asymmetry of the Poisson noise on the escape out of the zero-voltage state in the simple RCSJ model. We obtained the effective temperature and rate asymmetry, which account respectively for the effects of the second and the third moment, over a large set of parameters, and compared with theoretical predictions. While predictions and simulations agree in the range of low Q_0, both for the effective temperature and the rate asymmetry, a slight deviation appears for larger quality factor. We attributed this deviation to an effect of the noise asymmetry on the prefactor of the escape rate.
- In a second part, we evaluated the effect of an RC filtering of the Poisson noise on the rate asymmetry, since this corresponds to the actual experimental setup. The simulations indicate that the filtering does not affect the rate asymmetry if the cutoff frequency ν_{cutoff} is in the range:

$$\boxed{\nu_{\text{cutoff}} \lesssim \frac{\nu_{p0}}{100}.} \tag{3.49}$$

  where ν_{p0} is the plasma frequency. In our experiment where the plasma frequency was of the order of 1.5 GHz, the quality factor was 5 and the cutoff frequency was 5 MHz, this condition was fulfilled.

Chapter 4

Experimental detection of an asymmetric noise with a Josephson junction

In this chapter, we present an experiment accessing the second and third moment of the noise using a Josephson junction as a detector [38]. This experiment, which extends the experiments of [35, 36, 37, 65], is motivated by the need to develop an efficient on-chip detection system of the third moment of noise, as appeared from the first experiments that measured this quantity [27, 79, 80, 81]. When the noise under study is added to the bias current of a Josephson junction, the escape rate out of the zero-voltage state of this junction can be used to probe the second and third moments of this noise. A complete analysis of the experimental circuit and an extension of the present predictions [12] allows to achieve a quantitative agreement between measurement and theory, which constitutes a significant improvement towards the use of this detector on more exotic conductors.

4.1 Introduction

4.1.1 Direct measurement of the third moment of the fluctuations

A pioneering experiment

The first measurement of the third moment of shot noise was performed by Reulet *et al.* in 2003 [27, 79] on a tunnel junction. In the limit of large bias ($eV_N \gg k_BT$, where V_N is the voltage across the junction),

the number of tunneling events through a voltage-biased tunnel junction during a probing time τ_p follows a Poisson distribution and the second and third moment of the noise are simply:

$$\begin{cases} S_2 = e\,|I_N| \\ S_3 = e^2 I_N \end{cases} \tag{4.1}$$

where I_N is the mean current through the junction (see Fig. 4.1). The voltage fluctuations across the junctions were measured with an RF amplifier presenting an input impedance $R_0 = 50\,\Omega$ (see Fig. 4.2). To avoid a loss of signal due to impedance mismatches, the impedance R of the tunnel junction was also close to the $50\,\Omega$ impedance of the coaxial cables. In the lumped-element model presented in the top of Fig. 4.2, the current fluctuations i (due to the noise source) and i_0 (due to the probe resistor) both modulate the voltage across the sample, which results in a modulation of the noise itself. Since $R \simeq R_0$, this "feedback" effect gives a sizeable contribution to the third moment of the voltage fluctuations [82, 83].

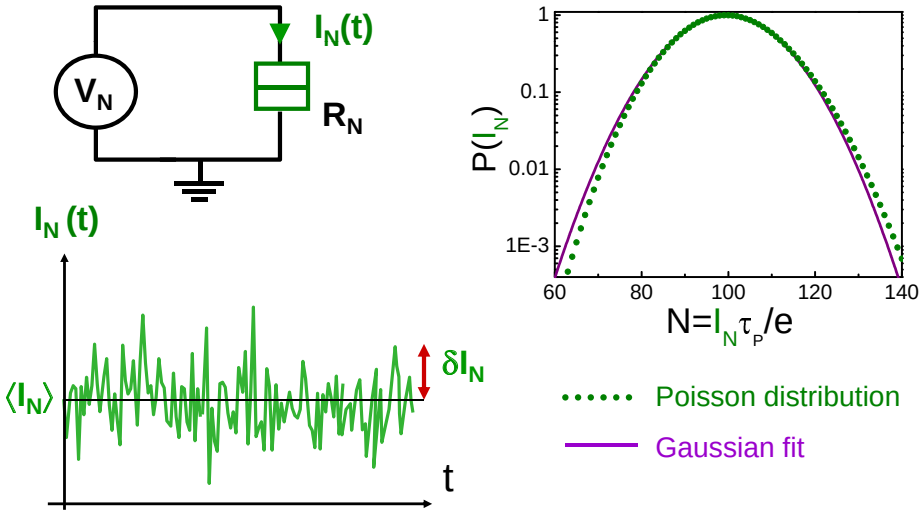

Fig. 4.1. Left: The current I_N through a voltage-biased tunnel junctions presents fluctuations δI_N, due to the statistical processes governing the tunneling. In the limit of large voltage ($eV_N \gg k_B T$), tunnel events through such a junction follow a Poisson process (see Appendix B.3 for details). **Right:** Poisson distribution describing the number N of electrons tunneling through the barrier during a given probing time τ_p (drawn for $\langle N \rangle = 100$). This distribution is fitted by a (symmetric) Gaussian distribution around the maximum to highlight the asymmetry of the Poisson distribution on the wings.

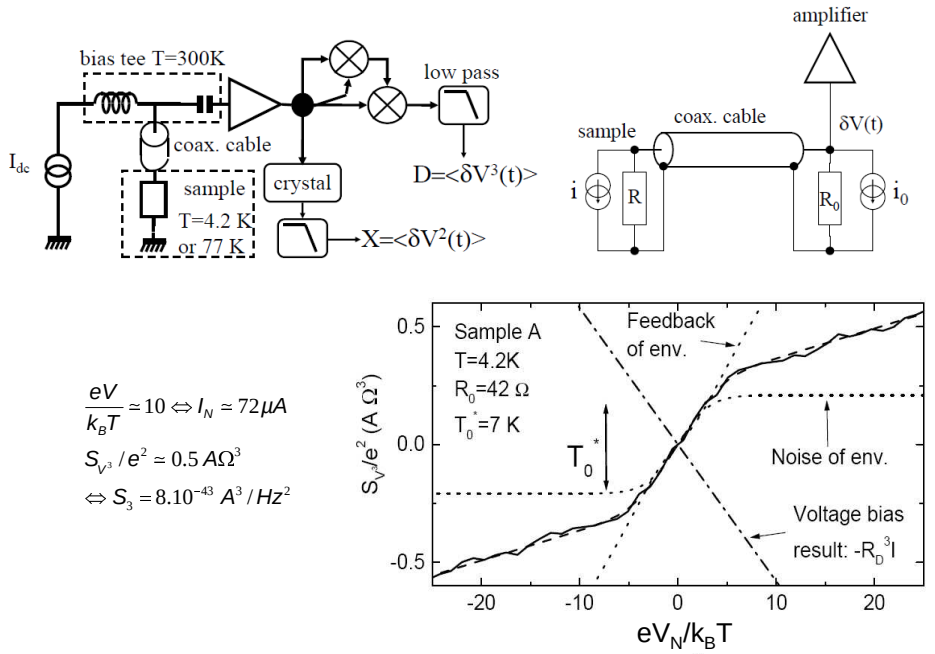

Fig. 4.2. Top Left: Setup used in [27, 79] to measure the third moment of the voltage noise across a tunnel junction. A bias tee is used to feed a constant dc current through the junction. **Top right:** Equivalent model at high frequency : the current fluctuations i emitted by the tunnel junction of impedance R, and i_0 emitted by the input impedance of the amplifier R_0 flow through the parallel combination of R and R_0. The output signal of the amplifier is mixed twice with itself to obtain a dc signal proportional to the third moment of the voltage fluctuations. **Bottom:** Measured third moment of the voltage fluctuations. The dash-dotted line corresponds to the expected result for a perfectly voltage biased sample. The dashed line fitting the data is the prediction obtained when taking into account "feedback" corrections.

Avoiding feedback effects

In 2005, Bomze *et al.* [80] performed another experiment on a tunnel junction, but in a regime where the "feedback" effect of the environment was negligible. A cryogenic amplifier was used to increase drastically the sensitivity, and the noise was sampled at room temperature by an analog-to-digital (A/D) converter. This reduced the constraints on the impedance of the sample, and allowed to reach the limit $R_N \gg R_0$. In this case, the tunnel junction was almost perfectly voltage biased and the third moment of the current noise was linear with the mean current, as shown in Fig. 4.3. This highly sensitive detection scheme was then used in 2008 to measure the third moment of noise on a Quantum Point Contact (QPC) for a conductance varying between almost 0 and $2e^2/h$ [81]. However, due to the large conductance of the sample in this case, "feedback" effects could not be avoided anymore. The third moment of

noise was extracted through the substraction of different contributions, a process very sensitive to the calibration of the measurements lines (see details in [81]).

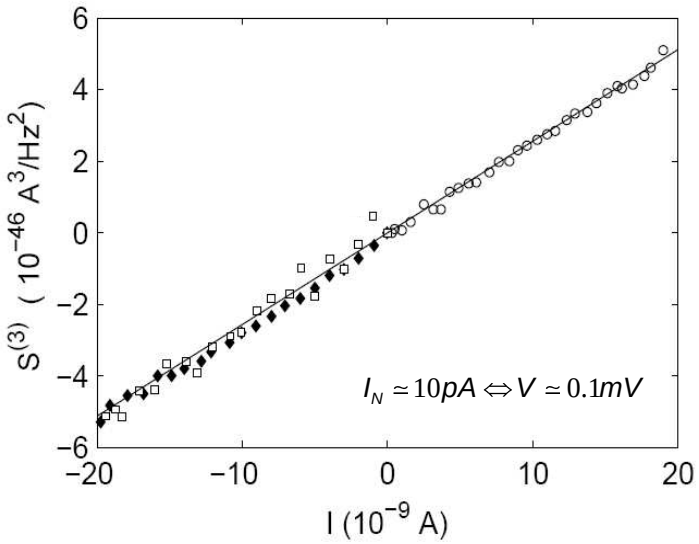

Fig. 4.3. Third moment of current fluctuations across a tunnel junction having an impedance R_N larger than 10 MΩ deduced from the voltage fluctuations over a probe resistor $R_0 = 9$ kΩ [80]. Different symbols corresponds to different measurement setups. The line is the theoretical expectation for a Poisson noise.

Sensitivity

In the measurements presented above, the signal-to-noise ratio for the third moment is determined by the Johnson-Nyquist current noise emitted by the probe resistor R_0. Since the amplitude of this noise scales as $\frac{1}{R_0}$, the signal-to-noise ratio was considerably increased in the second experiment (Bomze *et al.*) where R_0 was three orders of magnitude larger than in the case of Reulet *et al.*

In order to perform a simple comparison between detectors, we introduce the sensitivity σ_3 as the error obtained on the third moment when averaging during one second. Noting ΔS_3 the error on the third moment obtained for a measurement time t_{mst}, this yields:

$$\Delta S_3 = \sigma_3 \frac{1}{\sqrt{t_{\mathrm{mst}}}}. \tag{4.2}$$

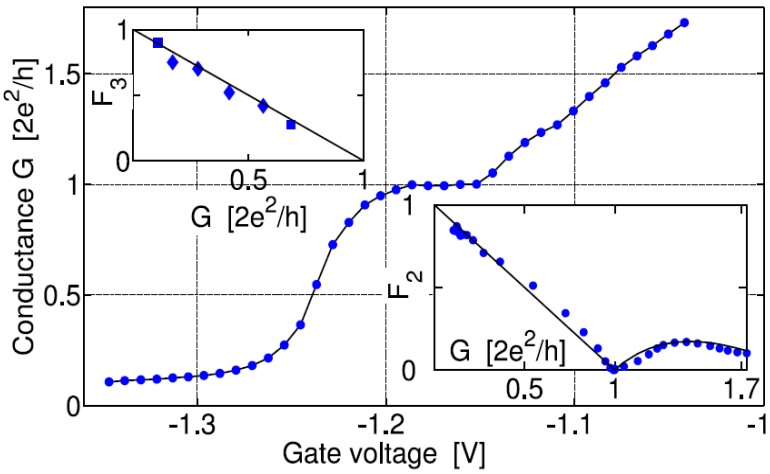

Fig. 4.4. Results obtained in [81]. **Main panel:** Conductance (in units of G_0) of the QPC. **Bottom:** Second moment of the noise divided by the Poisson expectation yields the Fano Factor F_2. Solid line is the predicted value. **Top left:** Fano Factor F_3 of the third moment (third moment divided by the Poisson expectation). Solid line is the predicted value.

In the experiment of Reulet *et al.*, a typical error for one point $\Delta S_3 = 2\, e^2 \mu$A was obtained for 10 h averaging[1], yielding a sensitivity $\sigma_3 = 370\, e^2\, \mu\text{A}/\sqrt{\text{Hz}}$ (the value of the error is obtained from Fig. 4.2). In the following experiment of Bomze *et al.*, the sensitivity was considerably increased, since the error was typically $\Delta S_3 = 2\, e^2$nA for an integration time of 250 s (corresponding to 10^{10} samples of 25 ns). This yields a sensitivity $\sigma_3 = 30\, e^2$ nA$/\sqrt{\text{Hz}}$, which allowed the measurement of the third moment in a QPC.

4.1.2 Towards on-chip detection

As appears from the two previous paragraphs, setups measuring the third moment of the noise by means of microwave signal processing proved to be efficient in the simplest cases. This technique however presents some drawbacks:

- The transmission from the noise source to the remote electronics needs to be carefully calibrated at all frequencies, in particular when "feedback" effects are present.
- Even with the best cryogenic amplifiers available nowadays, the sensitivity is barely sufficient.

Another strategy is to circumvent these difficulties by using an on-chip detector, which converts the properties of the high frequency fluctuations

[1] 12 days for the complete curve shown in Fig. 4.2.

into a simple easy-to-measure low frequency signal. In this spirit, a set of experiments was performed using a QPC as a detector, but this technique only applies to probe the slow sequential charging and decharging of a nearby Quantum Dot (QD) [84]. Looking for a on-chip detection scheme that could be applied to a large variety of noise sources, Tobiska and Nazarov [28] proposed to access the FCS of noise using a circuit containing a Josephson junction. They showed in particular that when the noise is added to the bias current of the Josephson junction, the difference in the escape rates out of the zero-voltage state for opposite bias currents reflects the asymmetry of noise.[2]

4.1.3 Probing shot noise with a Josephson junction

At the beginning of my work, a simplified version of this strategy, aiming at measuring only the third moment and not the FCS, had been explored experimentally by two groups: the group of J. Pekola at Helsinki University of Technology (HUT) [29, 37, 85] and the Quantronics group in Saclay [36, 35]. In both cases, the shot noise of a tunnel junction was added to the bias current of the Josephson junction (JJ), in order to extract the third moment of the noise.

To do so, one option is to have the full current in the noise source $I_N(t)$ flowing through the JJ. In this case however, the escape rate is modified not only by the noise, but also trivially by the dc current $\langle I_N \rangle$. To get rid of this contribution, the dc part $\langle I_N \rangle$ of the current was either compensated for or filtered out.

Experiments performed at the Helsinki University of Technology

The first detection of shot noise with a JJ was reported in [29]. The tunnel junction and the Josephson junction were placed in series but the dc part of I_N flowing through the JJ was compensated for with an opposite current on the bias line of the JJ. Large inductances were placed on all lines to increase their impedances at high frequency (see Fig. 4.5), in order to ensure that all the noise from the tunnel junction flows through the detector, which presents the lowest impedance. It was observed that, by increasing I_N, the noise yields a drastic increase of the escape rate. This effect could be interpreted as an increase of the effective temperature of the escape due to the second moment of the noise.

[2] Another use of a Josephson junction as a detector of higher order moments had already been proposed by Lesovik, based on the interplay of the noise with the ac Josephson supercurrent. [71]

In subsequent experiments [37, 85], the third moment of noise was accessed through the asymmetry in the escape rate for opposite bias situations. The current in the noise source was changed alternatively from $+I_N$ to $-I_N$. The second moment S_2 being only related to $|I_N|$, any difference in the rate between the two configurations is attributed to the asymmetry of the noise, i.e. essentially to S_3. Comparing the effect of the noise of a tunnel junction and the noise of a macroscopic resistor, which is symmetric, this experiment indeed demonstrated that a Josephson junction is sensitive to the third moment of the noise (see Fig. 4.5).

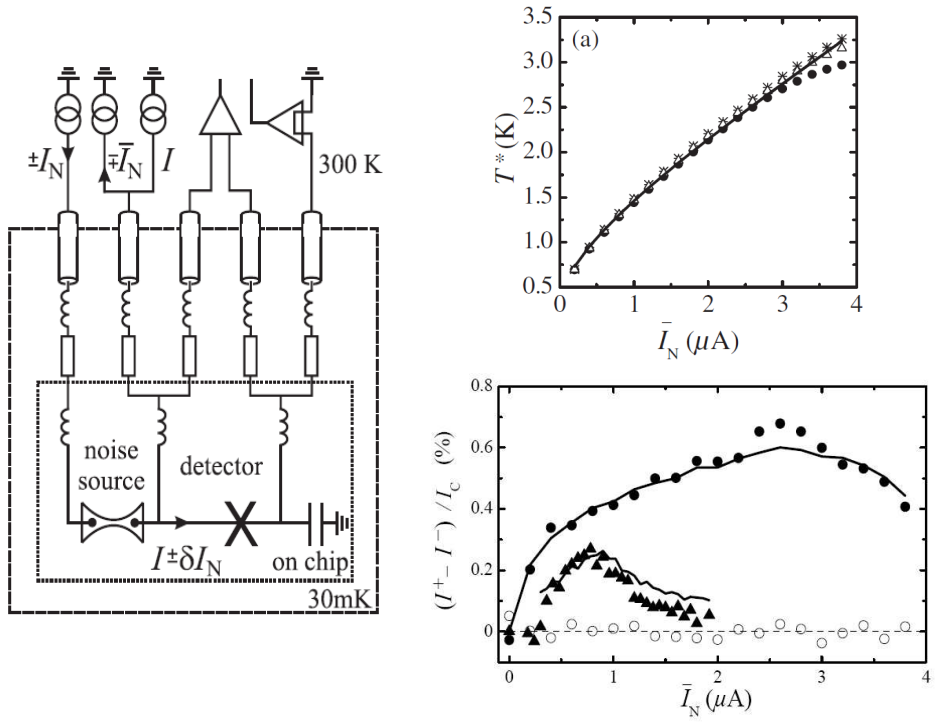

Fig. 4.5. Left: Setup used in the experiment performed at HUT [37, 85]. Noise source and detector are placed in series. The fluctuations of I_N add to the bias of the detector Josephson junction, but the dc component does not contribute (thanks to a compensation). Inductor on all the lines ensure that the noise flows in the Josephson junction, which presents the smallest impedance. **Top right:** Effective temperature of the escape of the JJ detector in [37] (various symbols correspond to various samples). Solid line is a fit with a model based on transitions between levels in the MQT regime. **Bottom right:** Asymmetry in the mean escape current. This asymmetry is defined as the difference between the mean escape current of the Josephson junction obtained for opposite signs of I_N. I_C is the critical current of the junction. Full symbols are measured for two tunnel junctions having different resistances, while open symbols corresponds to a case where the noise source is an ordinary resistor (with zero third moment of noise). Lines are adjusted comparisons with the adiabatic model described in [65] and summarized in Chapter 2.

A quantitative comparison of the results of this experiment with theory cannot be carried out easily, because theory deals with a JJ in the thermal escape regime and in an environment well described by an RCSJ model [11, 31, 33], whereas in this experiment, thermal escape was only obtained in an intermediate range of current, and the environment was essentially inductive. Moreover, the observation of escape was complicated by retrapping effects that arised because of the low quality factor of the JJ. In [37], the authors compared their data with the adiabatic model described in the previous chapter [65]. Using the frequency cutoff introduced in this theory as an adjustable parameter, it was possible to find a reasonable agreement with the data.

Experiments performed in the Quantronics Group

The measurement presented by Huard *et al.* was designed to achieve a quantitative comparison between theory and experiment, and thus to extract the third moment of noise from such measurement [35, 36]. This required to operate in the regime corresponding to the theoretical predictions, in which escape is due to thermal activation, and where the circuit can be described within the RCSJ model [31].

In this experiment, the dc part of $I_N(t)$ was removed from the current bias of the Josephson junction detector by on-chip filtering. The current through the noise source was separated into a fluctuating part that flew through the detector, and a dc part that returned through a resistor (see Fig. 4.6). Numerical simulations presented in Chapter 3 confirm that the effect of the low frequency cutoff on the statistics of the noise reaching the Josephson junction detector can be neglected.

Using independently measured parameters, the effect of the second moment of the noise was well explained. However, the measured asymmetry in escape rates appeared in strong disagreement with the predictions. A tentative explanation for this disagreement is a spurious leakage in the coupling capacitor between noise source and detector, which causes some dc current to flow through the JJ and hence contribute to the rate asymmetry.

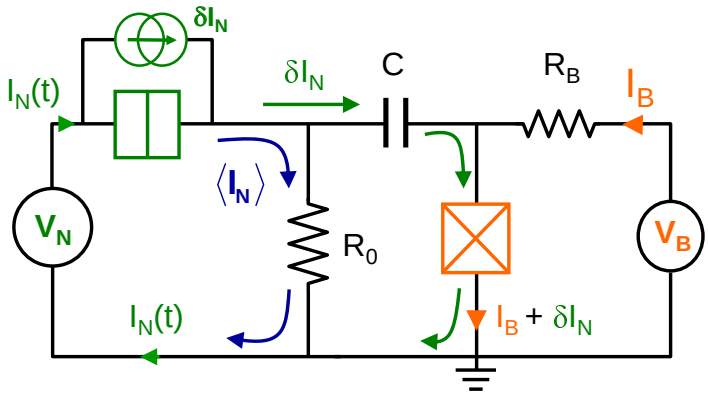

Fig. 4.6. Simplified setup used in the first experiment performed in the Quantronics group [35]. The noise from a tunnel junction (green double box) biased at dc with a current I_N couples through a capacitor C to a Josephson junction detector (orange crossed box), which is current-biased on its supercurrent branch. The filter formed by R_0 and C separates the signal flowing through the junction into two parts. The low frequency part, in particular the dc component, flows in the resistor, letting the detector unaffected. In contrast, the high frequency part of noise adds through the capacitor to the bias current of the JJ detector.

4.2 Experimental setup

We present here a second generation experiment [38] that aims at solving these difficulties and adress the discrepancies between theory and experiment that appeared in [35]. The goal is to achieve a reliable understanding with the present theories of the effect of the shot noise on the escape rate of the JJ out of its zero-voltage state, in order to use the JJ as a detector for the third moment of noise of an arbitrary conductor.

4.2.1 Schematic setup

The setup that we implemented is shown schematically in Fig. 4.7 and pictures of one of the sample are presented in Fig. 4.8. To strengthen the decoupling at dc between the noise source and the detector, we fabricated two coupling capacitors instead of one using a more robust technology than in [35]. The noise source was again a tunnel junction. The large capacitor C_N ensures a constant voltage across the noise source at high frequency. Due to a change in the relative position of the resistor R_3 and the tunnel junction compared to the previous experiment (compare Fig. 4.6 and Fig. 4.7), the fluctuating part of the noise here *subtracts* from the bias current of the junction, which inverts the sign of the rate asymmetry.

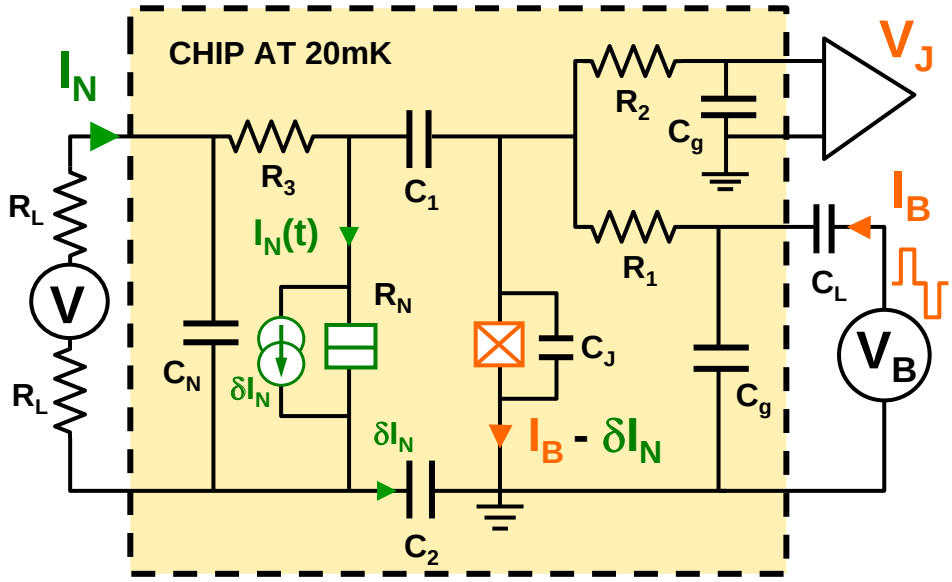

Fig. 4.7. Detailed setup of the experiment presented in this chapter and in [38]. Compared to the setup presented in Fig. 4.6, two coupling capacitors C_1 and C_2 are used. The voltage V_J across the junction monitors the switching to the dissipative state, through the resistor R_2. Capacitor C_J lowers the JJ plasma frequency $\frac{\omega_{p0}}{2\pi}$ close to 1.5 GHz at zero bias. Capacitors C_N and C_g shunt the impedance of the external connections lines at ω_{p0}, therefore the admittance shunting the JJ is determined only by on-chip elements. Two large resistors R_L allow to fix the average value of I_N. C_L is a capacitor placed on the bias line at room temperature whose role is to avoid spurious offsets arising from thermoelectric voltages (see text for more details).

4.2.2 Requirements

The design was developed with three goals in mind:

- Place the detecting junction in the thermal activation regime, without retrapping effects.
- Ensure a possible independent control on all the parameters characterizing the detection.
- Measure the escape rate with a simple technique and a good signal-to-noise ratio.

Constraints on the detection

- For the escape to be described by thermal activation, the temperature has to exceed the crossover temperature T_{CO} (see Eq. (2.25)). Considering that the lowest accessible temperature is approximately 20 mK, and assuming the measurement is easier at the lowest temperature, the plasma frequency is limited to:

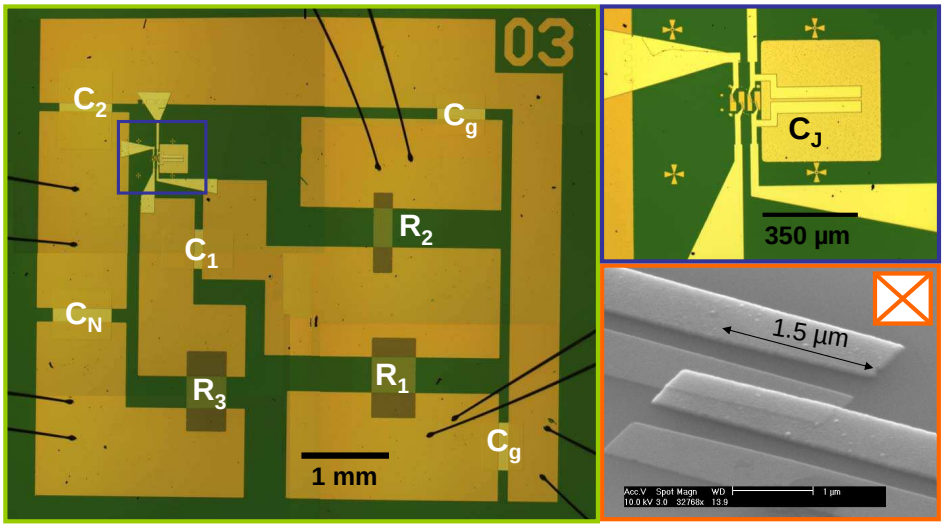

Fig. 4.8. Left: Large scale picture of Sample JJD2, presented in this chapter. Large pads are in aluminum, and capacitors were obtained from parallel aluminum films separated by Si_3N_4 (see Chapter 7 for more details). **Top right:** Connections to the two junctions. One observes the capacitor C_J in parallel of the detector. **Bottom right:** SEM micrograph of the detector Josephson junction under an angle of 50°. The junction is formed at the overlap of the two middle electrodes, while external electrodes result from the shadow mask evaporation technique.

$$\nu_{\mathrm{p0}} \leq 2.5\ \mathrm{GHz}. \tag{4.3}$$

- The critical current of the JJ, which sets a scale for measuring the noise, should be as small as possible. However, the switching signal of a Josephson junction with too small a critical current is difficult to detect [86]. In pratice, a critical current of 500 nA yields a good sensitivity and an easy switching detection (if the critical current is too large, the bias current flowing through the resistors heats them excessively, introducing artifacts in the experiments).
- Achieving a plasma frequency below 2.5 GHz with $I_0 = 500$ nA imposes a capacitance in parallel of the junction of the order of 10 pF, which is much larger than the intrinsic capacitance of the junction (of the order of 100 fF for a 1 μm^2 area [87]). An additional capacitor C_J was therefore fabricated in parallel with the junction, with a technic presented in details in Chapter 7.
- To use the simple RCSJ model, the impedance $Z(\omega)$ seen from the junction should be equivalent to a resistance for frequencies close to the plasma frequency, where the junction is most sensitive. To diminish the impact of the connections lines on this impedance, we used shunting capacitors C_N and C_g. At the plasma frequency, those ca-

pacitors are expected to present a very small impedance compared to that of the lines, typically 50 Ω, in order to shunt them. This requirement yields:

$$C_g, C_N \gg 5\,\mathrm{pF}. \tag{4.4}$$

Within this limit, the admittance across the JJ reduces, at the plasma frequency, to the on-chip elements presented in Fig. 4.9:

$$Y(\omega) \simeq Y_1(\omega) + Y_2(\omega) + Y_3(\omega) \simeq \frac{1}{R_1} + \frac{1}{R_2} + \frac{1}{R_3} = \frac{1}{R_{||}}. \tag{4.5}$$

The circuit fits in the RCSJ model, with a resistance

$$R_{||} = \left(\frac{1}{R_1} + \frac{1}{R_2} + \frac{1}{R_3}\right)^{-1} \tag{4.6}$$

shunting the junction at the plasma frequency.

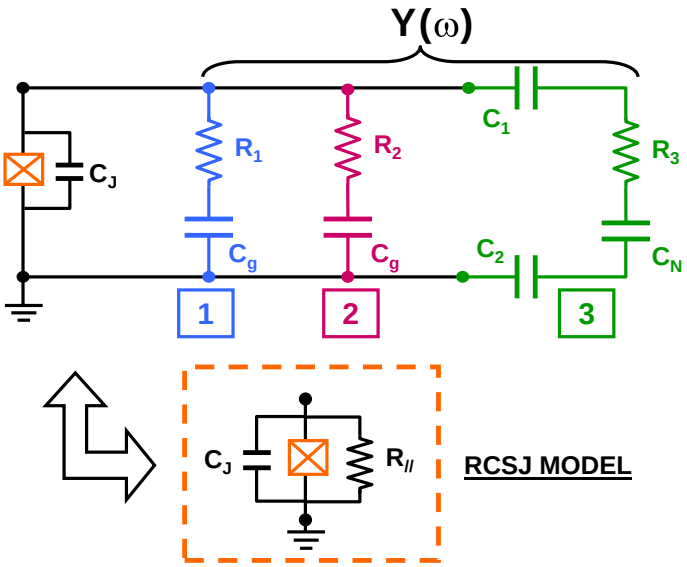

Fig. 4.9. Equivalent admittance seen in parallel of the junction (see text for conditions). Capacitors C_g and C_N behave as very small impedances around the plasma frequency, and shunt the external lines. The environment can thus be limited to three on-chip branches shown here. In this limit, the setup is properly described by the RCSJ model with an effective resistance $R_{||} = \left(\frac{1}{R_1} + \frac{1}{R_2} + \frac{1}{R_3}\right)^{-1}$.

- To avoid the retrapping effects presented in the Chapter 2 [56, 58], which strongly complicate the interpretation of the switching measurement, the quality factor Q_0 of the junction should be large enough in

the explored range of reduced bias current s: $Q_0 > \frac{4}{\pi s}$. Practically, due to the very large effect of noise on the rate, s is varied in the range $[0.5 - 1]$. The quality factor is thus bounded to:

$$Q_0 > 3. \tag{4.7}$$

Using $Q_0 = R_{||} C_J \omega_{p0}$, this requires $50\,\Omega \leq R_{||} \leq 200\,\Omega$. The definition of $R_{||}$ as the parallel combination of all the on-chip resistors implies that each resistor has a value larger than $50\,\Omega$. Nevertheless, the resistance values should be kept as small as possible to avoid heating effects.

- In the underdamped regime, the magnitude of the voltage that appears at switching $V_{\rm sw}$ is controlled by the mean switching current $I_{\rm sw}$ and the biasing resistor by

$$V_{\rm sw} \simeq (R_1 + 50) I_{\rm sw} \tag{4.8}$$

(here $R_1 + 50\,\Omega$ corresponds to the sum of the on-chip bias resistor and the impedance of the bias line). If R_1 is too large, $V_{\rm sw} \simeq \frac{2\Delta}{e}$ and a finite current flows after the junction has switched, resulting in the apparition of quasiparticles in the junction electrodes and heating of the biasing circuit. It takes then longer for the junction to reset, and one prefers to choose R_1 such that:

$$V_{\rm sw} < \frac{2\Delta}{e}. \tag{4.9}$$

- With the previous requirements fulfilled, other constraints are satisfied. Current pulses can be sent through the biasing line with a short rising time (controlled by $R_1 C_g$). The response time of the voltage measurement on-chip $R_2 C_g$ is anyway much shorter than the actual response time of the measurement line ($4\,\mu$s), therefore the value of R_2 does not limit the response time of the detector.

Constraints on the noise source and the coupling

- In order to simplify the fabrication process, the noise source and the detector junction are two tunnel junctions fabricated in the same evaporation step with aluminum electrodes, superconducting at low temperature. The noise source is thus also a Josephson junction. However, when biased at a voltage V_N larger than twice the superconducting gap, this junction is expected to behave as a normal metal tunnel junction in terms of the noise moments S_2 and S_3 [40]. For the experiment

to be performed in this regime, the current through the tunnel junction must exceed $I_N^{\min} = \frac{2\Delta}{eR_N}$.[3] With a large value of the resistance of the tunnel junction R_N, the minimum current is small and the effect of the noise can be set to a negligible amplitude. In practice, we chose R_N of the order of $\frac{h}{e^2} \simeq 26\,\mathrm{k}\Omega$, which corresponds to the characteristic resistance of samples of interest like QPCs.

- If the thermal fluctuations associated to the resistor R_3 modulate the voltage across the noise source, it induces the "feedback" effects described earlier. In practice, the impedance of the noise source is much larger than that of the JJ in series with the coupling capacitor in a broad frequency range, and the current fluctuations associated with both the resistor and the noise source flow essentially in the detection branch, leaving the voltage across the noise source unaffected. Feedback effects can thus be neglected.
- The capacitors C_1 and C_2 in series form an equivalent capacitor $C_C = \frac{C_1 C_2}{C_1 + C_2}$. The -3 dB point of the first order RC filter formed by R_3 and C_C is at $(R_3 C_C)^{-1}$. The numerical simulations presented in the previous chapter confirm that this cutoff has no effect on the statistics of the noise that reaches the detector if:

$$\frac{1}{R_3 C_C} \leq \frac{\nu_{p0}}{100} \sim 10\,\mathrm{MHz}. \tag{4.10}$$

4.2.3 Chip parameters

The experimental results on two samples will be discussed. Many tests were performed on Sample JJD1, but it turned out that the behavior of the detector junction was imperfect, as discussed later. Reliable results could be obtained on Sample JJD2, therefore we first present the results obtained with Sample JJD1 then those obtained with Sample JJD2. The parameters of both samples are given in Table 4.1, which summarizes the nominal values of the design and the values measured *in-situ*, as described in the following section.

[3] As will be presented further, the switching of the detector when the noise source is biased below the gap is not understood, therefore all the measurements are done for V_N above 2Δ

Parameter	Sample JJD1	Sample JJD2
R_J	926 Ω	745 Ω
I_0^{AB}	0.340 μA	0.420 μA
I_0	0.358 μA	0.437 μA
C_J	13 pF	12.5 ± 0.5 pF
ω_{p0}	1.5 GHz	1.65 GHz
Q_0	10	12
R_N	30.8 kΩ	22.9 kΩ
$I_N^{\min}$	11 nA	15 nA
C_1	250 pF	230 pF
C_2	350 pF	345 pF
C_g	200 pF	190 pF
C_N	150 pF	140 pF
C_L	220 μF	220 μF
R_1	200 Ω	215 Ω
R_2	500 Ω	515 Ω
R_3	200 Ω	215 Ω
R_L	1.5 MΩ	1.5 MΩ

Table 4.1. Parameters of the two samples presented in this chapter. R_J is the normal resistance of the detector junction, while R_N is the resistance of the tunnel junction, I_0^{AB} corresponds to the prediction of the critical current from the Ambegaokar-Baratoff prediction [47] (see text for details). The critical current is obtained from switching experiments described further. Plasma frequencies and quality factors were estimated from the others parameters, based on a RCSJ model. The values of the capacitor were measured independently only for Sample JJD2, while the values for Sample JJD1 are estimations from typical results. The values of the resistances R_1, R_2, and R_3 differ between the two samples due to a technological change.

4.3 Circuit characterization & measurement techniques

The sample was mounted on a small printed circuit board thermally anchored to the mixing chamber of a dilution fridge with a base temperature of 20 mK. Connections lines were heavily attenuated and filtered to reduce spurious noise. The description of the connections is given in Chapter 8.

4.3.1 Junctions

Detector JJ

The $I(V)$ characteristics of the detector junctions of Samples JJD 1 and JJD 2 are shown in Fig. 4.10(a) and 4.10(b). Using the superconducting gap voltage $\Delta/e \simeq 200\,\mu$V determined from the $I(V)$ characteristics

and the normal resistance of the junction R_J, one predicts the critical currents in Table 4.1 using the Ambegaokar-Baratoff relation from Eq. (B.94) [47] (in this section, we considered in a good approximation that the gap are the same in both electrodes, although they differ because of different thicknesses. See Appendix B.6 for more details). This prediction is in good agreement with the values precisely deduced by the switching measurements described further. On the $I(V)$ characteristics, two unexpected features are observed:

- Near 100 & 150 μV in Sample JJD1, and 100 μV in Sample JJD2, the current is not zero. The observed current peaks are attributed to inelastic Cooper pair tunneling mediated by resonances in the circuit at the corresponding frequencies $\frac{2eV}{h}$, although it is difficult to attribute these frequencies (25 & 35 GHz) to specific parts of the circuit configuration.
- At $V_J \simeq 400\,\mu$V, the $I(V)$ characteristics is not vertical, but shows a slight "back-bending". This effect is often attributed to a reduction of the gap with heating [36]. Indeed, at that voltage, a dissipative current starts to flow in the junction and creates a stationary population of quasiparticles in the electrodes of the JJ which reduces the superconducting gap. The higher the current, the smaller the gap, thus producing a back-bending of the curve. This feature is discussed in more details in Appendix A.

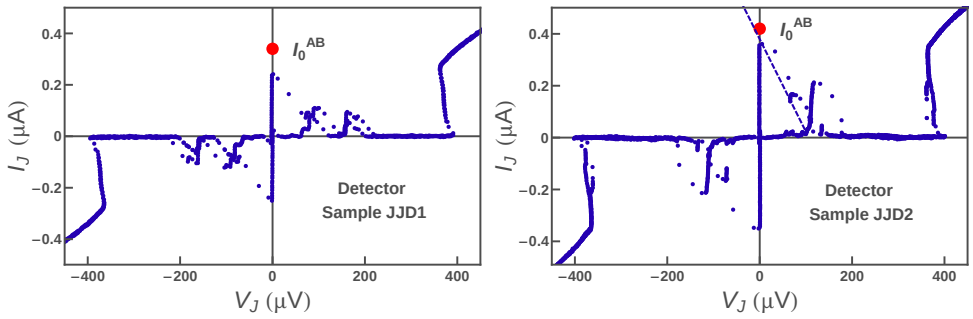

Fig. 4.10. Left: $I(V)$ characteristics of the detector of Sample JJD1. We attribute the resonances near $V_J = 100\,\mu$V and $150\,\mu$V to inelastic tunneling mediated by the modes of the electromagnetic environment. The large dot gives the prediction for the critical current I_0^{AB} using the Ambegaokarr-Baratoff relation. **Right:** $I(V)$ characteristics of the JJ detector of Sample JJD2, with similar remarks. The dashed line corresponds to the predicted load line of the measurement.

Current calibration The detector junction is neither perfectly current biased, nor voltage biased (see Fig. 4.11). It is connected to a voltage source through a heavily attenuated 50 Ω coaxial line and two resistors R_1 and R_m in series. R_m is a probe resistor across which the voltage is measured, giving access to the current I_B flowing through the detector junction. It allows to calibrate the ratio $\frac{dI_B}{dV_B}$ that relates the voltage of the source V_B and the current I_B. For example, this ratio was found to be 683 nA/V for Sample JJD2. To compare this measured value with the nominal attenuation of the line, we can model the complete line having a total attenuation a in dB with a symmetric combination of three resistors (see Fig. 4.11 and Appendix B). In the limit of large attenuation, the values of the resistances are given by:

$$R_{\text{eff}} \simeq 50\,\Omega \quad \text{and} \quad 2\frac{r_{\text{eff}}}{R_{\text{eff}}} \simeq 10^{-\frac{a}{20}}. \tag{4.11}$$

The ratio $\frac{dI_B}{dV_B}$ can thus be expressed as

$$\frac{dI_B}{dV_B} \simeq \frac{1}{R_{\text{eff}} + R_m + R_1}\frac{r_{\text{eff}}}{R_{\text{eff}}}. \tag{4.12}$$

For Sample JJD2, the measured value of $\frac{dI_B}{dV_B}$ corresponded to an effective attenuation of 80.5 dB, in good agreement with the 79 dB nominal attenuation of the coaxial line.

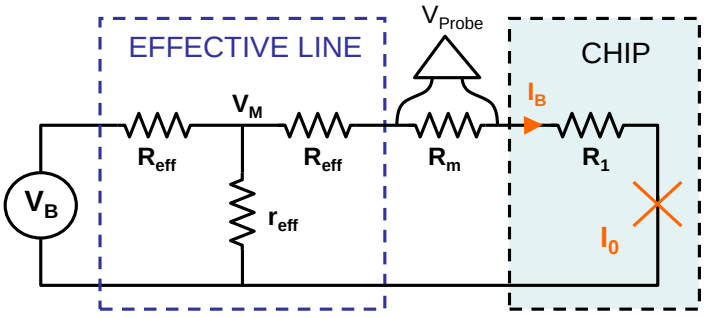

Fig. 4.11. Simplified scheme of the biasing line of the detector junction. The line is composed of a series of attenuators and filters, which can be modeled by a symmetric combination of the resistors R_{eff} and r_{eff}.

Switching voltage The total resistance on the biasing line of Sample JJD2 was $R_{\text{eff}} + R_m + R_1 = 275\,\Omega$ which gives a load line

$$I = I_{\mathrm{sw}} - \frac{V}{275\,\Omega} \tag{4.13}$$

shown in Fig. 4.10(b).

Noise source

The $I(V)$ characteristics of the tunnel junctions used as noise sources are shown in Figs.4.12 and 4.13. At large scale, the characteristics is linear, as expected from a tunnel junction. At the scale of twice the superconducting gap, the characteristics of a Josephson junction is observed, although measuring the supercurrent required some care due to the presence of spurious noise. The curves also present a back-bending behavior at twice the superconducting gap.

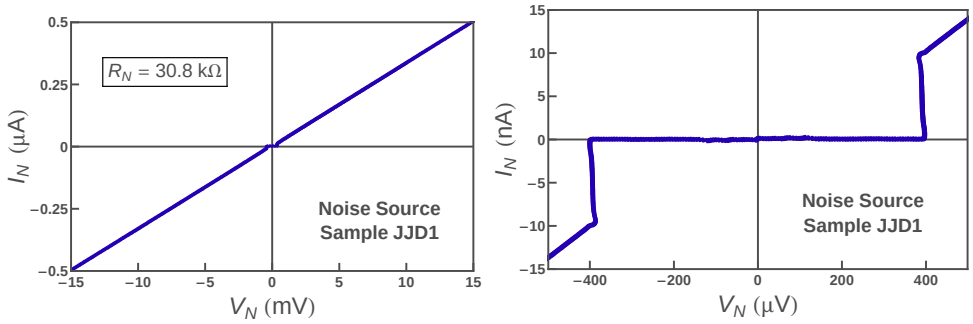

Fig. 4.12. Left: Large scale $I(V)$ characteristics of the tunnel junction of Sample JJD1. **Right:** At the scale of the superconducting gap.

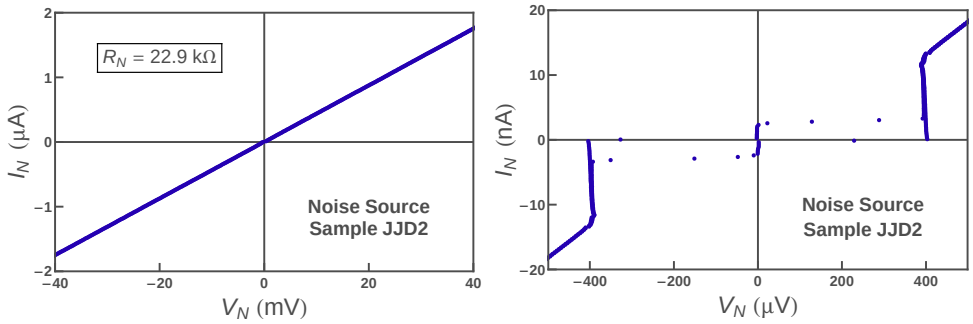

Fig. 4.13. Left: Large scale $I(V)$ characteristics of the tunnel junction of Sample JJD2. **Right:** At the scale of the superconducting gap.

Noise The complete expression for the second moment of shot noise at zero frequency produced by a tunnel junction at finite temperature is given [21] by:

$$S_2 = e\,|I_N|\coth\left[\frac{eV_N}{2k_BT}\right]. \tag{4.14}$$

In the experiment, V_N is always higher than $\frac{2\Delta}{e}$. For temperatures lower than 500 mK, this implies that the tunnel junction used here as a noise source is always in the large bias regime and finite temperatures effects are neglected:

$$\frac{eV_N}{2k_BT} \geq 5 \quad \text{therefore} \quad \coth\left[\frac{eV_N}{2k_BT}\right] \simeq 1. \tag{4.15}$$

Coulomb Blockade The tunnel junction is a small junction, thus with a small intrinsic capacitance. However, the total capacitance seen from this tunnel junction is the series combination of the coupling capacitor C_1 and C_2 and the capacitance C_J across the detector, thus a large capacitance of the order of 10 pF. Coulomb Blockade effects [88] are therefore absent.

4.3.2 Rate measurements

The measurement of the escape rate of the Josephson junction is performed by applying current pulses of amplitude I_B and duration τ_p with a typical shape shown in Fig. 4.14. During a pulse, the phase difference across the junction has a finite probability P to go over the barrier and escape:

$$P = 1 - e^{-\Gamma\tau_p}. \tag{4.16}$$

If the escape occurs, the phase runs down the potential and a finite voltage develops across the junction. In order to lengthen this voltage pulse and facilitate its measurement, the bias current is reduced to a value $I_{\text{sus}} < I_B$ during a time $\tau_{\text{sus}} \gg \tau_p$. The probability that switching occurs during this "sustain" time is negligible. The voltage pulse is amplified and detected at room temperature. The system is then "reset" by lowering the current to zero or even a slightly negative value; if the junction has switched, it gets retrapped back on the supercurrent branch.

In order to measure simultaneously the escape probability for positive and negative bias, signals with opposite signs and same amplitudes are sent alternatively, as it is shown in Fig. 4.14. This experiment is repeated a large number of times N, typically $N = 10^4$. Hence, the signal sent to the junction is a burst of current pulses, as shown in Fig. 4.15. The escape probability is the ratio of resulting voltage pulses across the JJ over N. The repetition period of the signal is called t_{signal}.

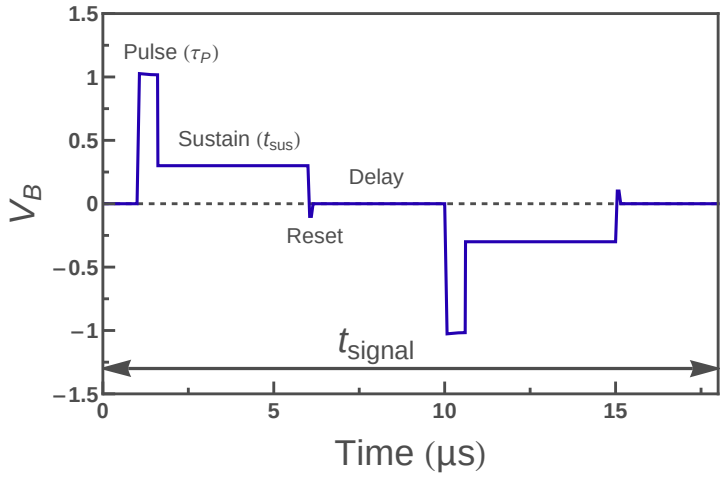

Fig. 4.14. Typical signal used to obtain the escape rate. The pulse time corresponds to the effective probing time. Sustain time allows to facilitate the detection, by holding the voltage across the junction. The symmetry of this signal allows to probe simultaneously escape rate for positive and negative bias.

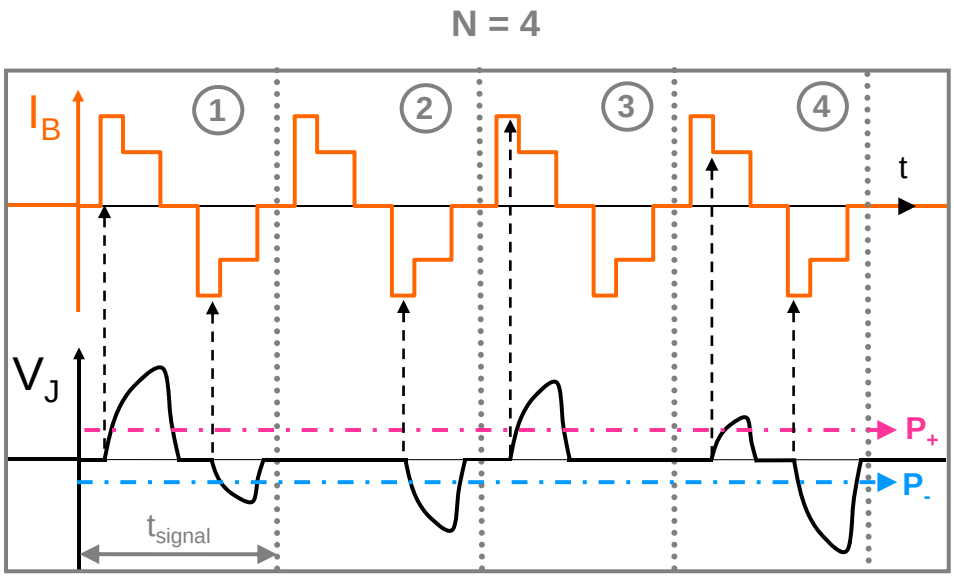

Fig. 4.15. Illustrative example of the escape probability measurement procedure. In this case, $N = 4$ current signals are sent to the detector. During the probing pulse, the junction can escape, producing a voltage pulse. A non-zero voltage is held during all the sustain time. When the voltage crosses a threshold, the event is detected, yielding the escape probability as the ratio of detected events over N. The escape probability is measured simultaneously for positive (P_+) and negative (P_-) pulses using two thresholds detectors.

Tuning the pulse shape This method assumes that the current in the junction is constant during the pulse. If the current presents an overshoot, the switching will be dominated by this imperfection because of the extreme sensitivity of the escape rate to the current amplitude. Since the signal synthesized at room temperature by the voltage source is distorted by the heavily attenuated and filtered line, the current flowing through the junction during the pulse has no reason to be perfectly constant. The distortion is compensated by tuning the pulse shape with the following procedure :

- An histogram of the escape instants during the pulses is performed, as shown in Fig.4.16. The probability to escape at time $t_{\rm esc}$ between time t and $t+dt$ is given by $p = \Gamma dt\, e^{-\Gamma t}$. In the case of low escape probability $P \ll 1$, one has $\Gamma t \ll 1$ for all t, and p is a constant $p \simeq \Gamma dt$. The histogram shown in Fig. 4.16 was measured in this regime, and used to tune the pulse. The outcome of such a tuning procedure is shown in Fig. 4.17 where only the effective pulse part is shown. It is clear from the shape that the main effect to be compensated is the ringing in the cable for a short rise time.
- The pulse synthesized by the voltage source is tuned manually until a flat histogram is obtained for a long pulse duration $\tau_p \simeq 20\,\mu$s. At long times, after an oscillatory behavior, the current in the junction is exactly given by the dc value measured with $\frac{dI_B}{dV_B}$. Only the beginning of this pulse shape is kept to obtain the desired shape and duration of shorter pulses.

Signal symmetry dc current offsets in the junction would lead to an artificial asymmetry in our measurement of the escape probability for positive and negative biasing signs. To avoid offsets, that might result from thermoelectric voltages, the signal is fed to the biasing line through a large unbiased capacitor $C_{\rm in} = 220\,\mu$F placed at room temperature.[4] This capacitor blocks the dc connection between the first stage of the dilution fridge and the line at room temperature, preventing dc current to flow in the attenuators. The use of this large capacitor was only possible when sending a symmetric bias signal to the detector junction.

[4] We added also two capacitors in parallel of values 1 μF and 100 nF to ensure a fast response.

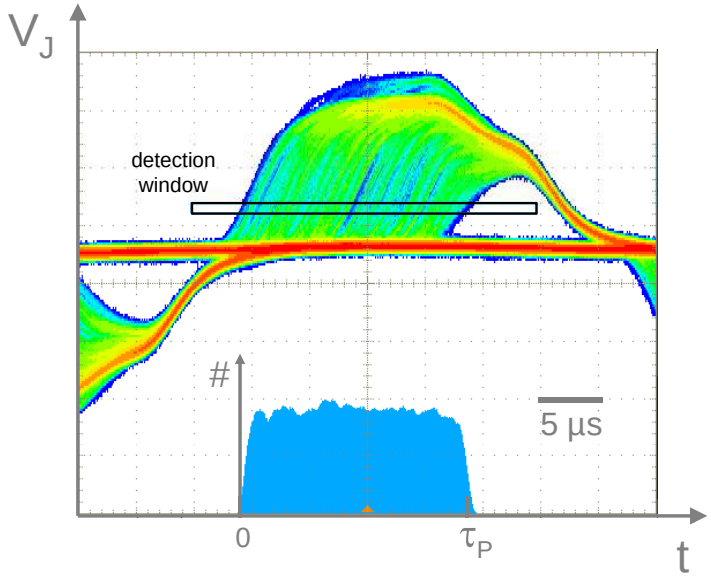

Fig. 4.16. Screen capture of an oscilloscope in histogram mode using a pulse with $\tau_p \simeq 21\ \mu$s. Many traces are shown, corresponding to the voltage across the junction during the measurement time. When switching occurs, a finite voltage develops across the junction. The histogram shown in the bottom part of the figure corresponds to the number of traces crossing the detection window shown in the middle, accumulated over a long time. The escape probability being here smaller than 0.1, the histogram is expected to be completely flat at this scale.

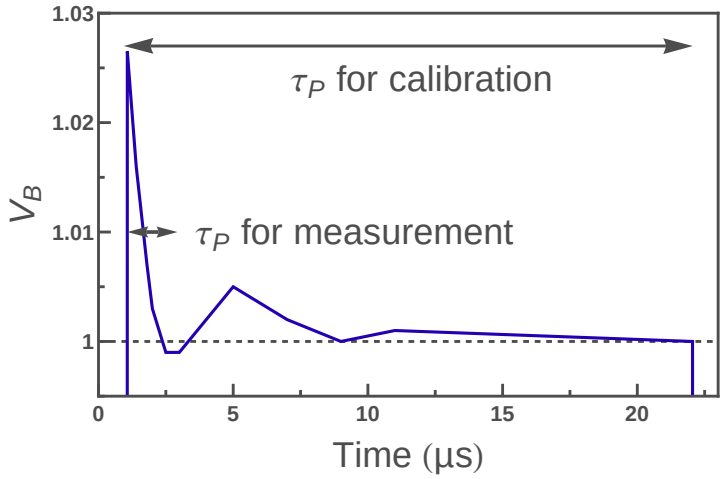

Fig. 4.17. Time trace of the signal synthesized by the voltage source, focused on the pulse, with $\tau_p \simeq 21\ \mu$s. Due to the improper transmission of the biasing line, the shape of the pulse sent from the voltage source has to be tailored to obtain a suitable square bias current pulse on the junction.

4.4 Results on Sample JJD1

4.4.1 Detection parameters

The escape probability is measured as a function of the pulse height I_B for positive and negative bias, in the range of current where P goes from 0 to 1, as shown in Fig. 4.18(a) (this curve is taken when the current through the noise source is the lowest). The escape probability used here is the mean value of the probabilities obtained for both bias signs, in order to eliminate the asymmetry due to the third moment of the noise, that is addressed further. The escape probability is converted into a rate using $\Gamma = -\frac{1}{\tau_p}\ln(1-P)$. Theoretically, this rate is expressed from Eq. (2.30) as [50]:

$$\Gamma = \lambda \frac{\omega_p(I_B/I_0)}{2\pi} e^{-\frac{\Delta U(I_B/I_0)}{k_B T_{\text{eff}}}}, \tag{4.17}$$

where compared to Eq. (2.30), we introduced the effective escape temperature T_{eff} that represents the noise power, and which can be higher than the fridge temperature T. Fitting the measured rate with this expression allows to extract the critical current and an effective temperature.[5] A visual way to confirm the correct dependence of the rate with the barrier height is to represent the function

$$B^{2/3}(I_B/I_0) = \left(\ln \lambda \frac{\omega_p(I_B/I_0)}{2\pi\Gamma(I_B/I_0)}\right)^{2/3}, \tag{4.18}$$

as shown in Fig. 4.18(b). In the thermal activation regime and considering the approximate expression of the barrier height from Eq. (2.14), this function is predicted to vary as:

$$B^{2/3} = \left(\frac{\Delta U(I_B/I_0)}{k_B T_{\text{eff}}}\right)^{2/3} \propto T_{\text{eff}}^{-2/3}\,(1 - I_B/I_0)\,. \tag{4.19}$$

Hence the function $B^{2/3}$ should vary linearly with $s = I_B/I_0$, as observed in Fig. 4.18(b). The critical current $I_0 = 0.358\,\mu\text{A}$ corresponds to the intersection between this line and the current axis. The effective temperature $T_{\text{eff}}^0 \simeq 70\,\text{mK}$ is obtained from the slope (in the following, T_{eff}^0 represents the effective temperature measured for the lowest current in the noise source). T_{eff}^0 is higher than the fridge temperature $T = 20\,\text{mK}$, a discrepancy partly due to Joule heating of the resistors and to insufficient

[5] This is performed using the exact expression for the barrier height ΔU from Eq. (2.13). The prefactor for our experimental range of quality factors and barrier height is approximated to $\lambda \simeq 0.8$.

filtering of black-body radiation of the fridge elements placed at higher temperatures. The heating of the bias resistor is discussed in details in Appendix A.2. In the following, one considers that the base temperature of the measurement is not given by the fridge temperature, but by $T_{\rm eff}^0$.

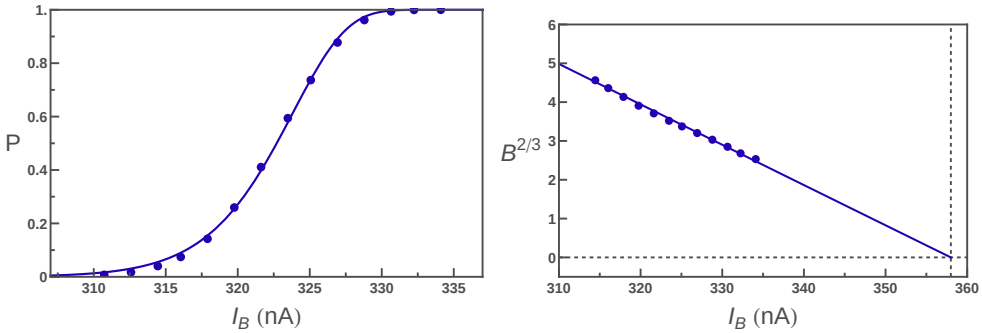

Fig. 4.18. Left: Variation of the escape probability with the bias current I_B. Data obtained using $N = 10^5$ pulses of duration $\tau_p = 0.94\,\mu$s ($\tau_{\rm sus} = 3\,\mu$s and $t_{\rm signal} = 18\,\mu$s). The solid line is the fit using Eq. (4.17), that yields $I_0 = 0.358\,\mu$A and $T_{\rm eff}^0 \simeq 70\,$mK. **Right:** Similar data shown as a $B^{2/3}$ function using Eq. (4.18). The solid line is a prediction with the same critical current and effective temperature. The dashed vertical line corresponds to I_0.

4.4.2 Effect of the shot noise

When the current in the noise source is switched on, shot noise increases the effective temperature. This effect is demonstrated in the $B^{2/3}$ plots of Fig. 4.19, where the slope diminishes with I_N (the slope is proportional to $T_{\rm eff}^{-2/3}$). The values of $s = I_B/I_0$ for which P goes from 0 to 1 shift down with I_N from $s \simeq 0.93$ to $s \simeq 0.6$.

In Figure 4.19, the lines corresponding to the fits of the experimental results do not extrapolate to the same point at $B^{2/3} = 0$. In other words, the apparent critical current changes when increasing the amplitude of the shot noise, while it is only expected to affect the effective temperature. The apparent critical current is plotted in Fig. 4.20 as a function of I_N.

In order to confirm that this unexpected behavior of the critical current was not an experimental artifact, we set the shot noise to a negligible amplitude, and then increased the fridge temperature. As can be seen in Fig. 4.21, the effective temperature follows the fridge temperature, except for the smallest values as discussed in Sec. 4.4.1. In this situation, the behavior of the critical current with temperature is properly described by the Ambegaokar-Baratoff prediction [47] (see Fig. 4.20 and Appendix B.6 for more details). This measurement indicates that the behavior of

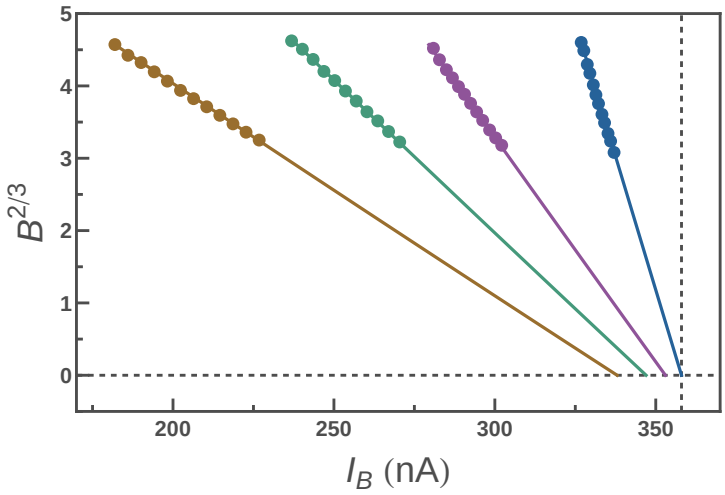

Fig. 4.19. Dots: $B^{2/3}$ functions obtained from escape rate measurements performed for $I_N = 0.011,\ 0.21,\ 0.52$, and $1.15\,\mu$A from right to left. **Solid lines:** Fits using Eq. (4.19) and the exact expression of the barrier height from Eq. (2.14). The effective temperature is obtained from the slope, and the critical current is read from the intersection between the fit and the current axis. When I_N is increased, the absolute value of the slope diminishes, denoting the increase in effective temperature. But, unexpectedly, the extrapolated critical current also decreases, since all the lines do not cross at a single point on the current axis.

the critical current under simple thermal fluctuations did not present any unexpected features. The evolution of the critical current of the detector was thus well understood for the case of an elevated fridge temperature, but very surprising in the case of shot noise.

A possible explanation can be proposed: the shot noise spectrum extends up to a frequency corresponding to the energy eV_N [21], which is here much larger than the superconducting gap (the smallest value being $eV_N \simeq 2\Delta$), as can be seen in Fig. 2.10. This high-frequency noise is energetic enough to break Cooper pairs in the electrodes forming the detector. The population of quasiparticles created through this process reduces the superconducting gap in the electrodes and thus the critical current.

From this measurement on Sample JJD1, we concluded that the shot noise induced of a change in the critical current of the detector, probably through the creation of quasiparticles. Since this change prevented us from measuring the effect of the shot noise reliably, we designed a second sample in order to protect the detector from those quasiparticle effects. For this purpose, we used normal metal pads as quasiparticles traps, as discussed further.

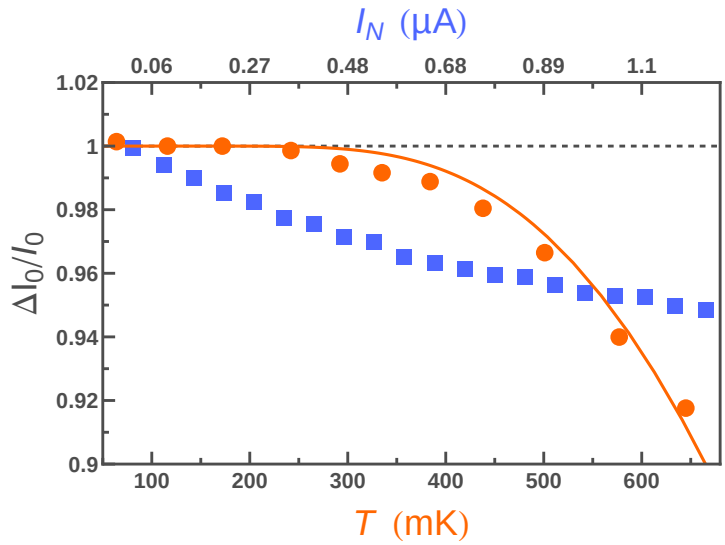

Fig. 4.20. Symbols: Relative change of the apparent critical current (with respect to $I_0 = 0.358\mu$A) as a function of the fridge temperature (dots) or the current in the noise source I_N (squares). Both affect the effective temperature, and scales in current and temperature are linked by Eq. (4.23). **Solid line:** Prediction of the BCS theory for the modification of the critical current with the temperature of the electrodes, for two electrodes having the same superconducting gap (see Appendix B.6 for details).

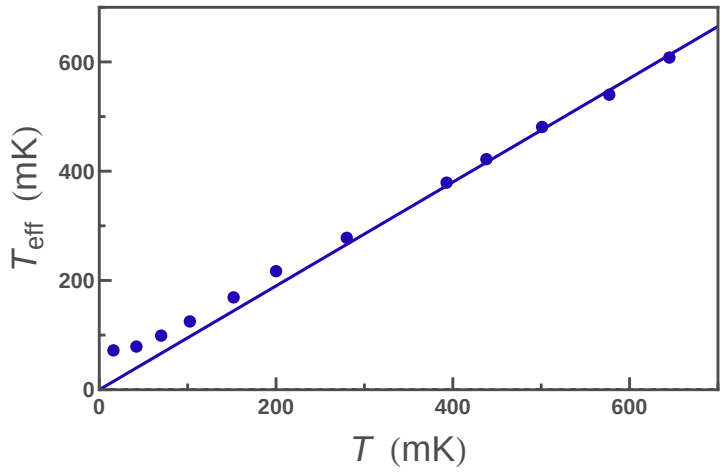

Fig. 4.21. Dots: Effective temperature extracted from switching measurement for various fridge temperatures T. **Solid line:** the line $T_{\rm eff} = 0.95T$, probably accounting for a slight miscalibration of the thermometer. At low fridge temperature, the effective temperature saturates down to 70 mK.

4.4.3 Retrapping effects

When the noise amplitude was increased at very large values, the range of reduced bias current where switching occurs was reduced down to $I_B \simeq 50\,\mathrm{nA}$. In this region, the escape appeared to be dominated by the retrapping effects predicted below $s \simeq \frac{4}{\pi Q_0}$, as seen in Fig. 4.22 where the transition from 0 to 1 of the escape probability gets narrower when increasing the effective temperature. This turnover, which had already been observed in [89, 90, 91, 92], was used in [37] to evaluate the quality factor from the reduced bias current. In our case, this was not possible since the evolution of the critical current due the shot noise prevented us from defining a value $s \simeq \frac{I_B}{I_0}$ independent of I_N, especially for the large values of I_N used in this case (up to $7.5\,\mu\mathrm{A}$, corresponding to a change in critical current of the order of $\frac{\Delta I_0}{I_0} \simeq 40\%$ if one extrapolates the curve shown in Fig. 4.20).

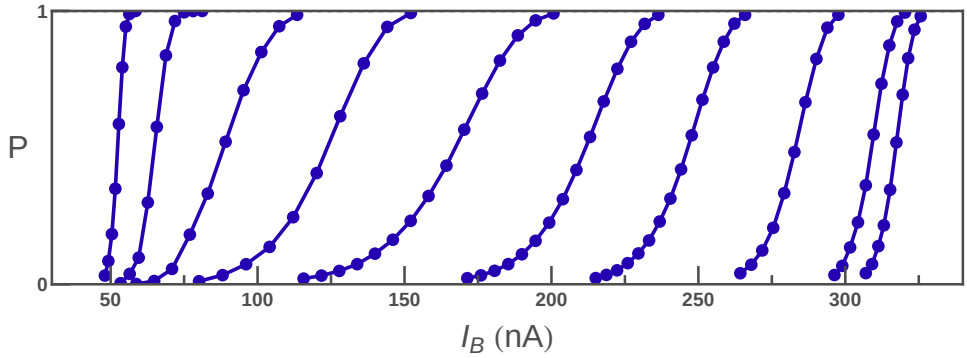

Fig. 4.22. Escape probabilities obtained when increasing the effective temperature. **From right to left:** First three curves: At $I_N = 0.012\,\mu\mathrm{A}$ when increasing the fridge temperature (20, 100, and 200 mK from right to left). Next curves: Escape probabilities obtained at $T = 400\,\mathrm{mK}$ for $I_N = 0.012$, 0.520, 1.25, 2.2, 3.3, 5.3, 7.4 μA. For very large effective temperature (last four curves), increasing I_N does not anymore broaden the escape probability curve. This is interpreted as an effect of retrapping.

4.5 Results on Sample JJD2

The experimental results on Sample JJD1 suggested that the response of the detector was affected by quasiparticles in the electrodes, leading to changes of the critical current with the noise power. We present now results on Sample JJD2 on which we attached "quasiparticles traps" (see Fig. 4.23), i.e. large normal electrodes in good contact with the electrodes of the junction, to remove rapidly the quasiparticles [93].

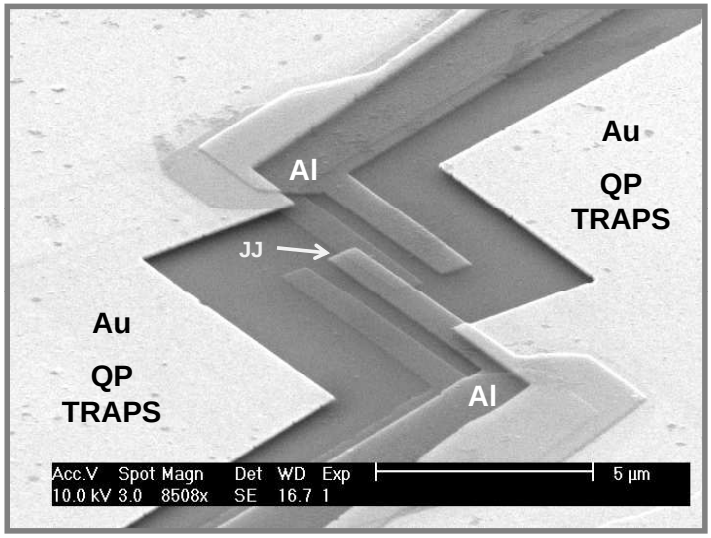

Fig. 4.23. SEM Micrograph of the detector junction of Sample JJD2, taken with an angle of 50°. Large normal metal pads (bright zone) were placed in good contact with the superconducting electrodes (light gray zone) of the detector to evacuate quasiparticles.

4.5.1 Effect of noise on the effective temperature

Experimental detection

Figure 4.24(a) was produced at $T = 20$ mK using exactly the procedure described in Sec. 4.4.1. The corresponding variations of the critical current are plotted in Fig. 4.25. The variation are now smaller than in Sample JJD1, and also non-monotonous. Recent calculations by D. Urban *et al.* [12] suggest that the variations of the apparent critical current could be due to the frequency dependence of the circuit. Actually, in such a case, the use of a $B^{2/3}$ plot to extract an effective temperature and the critical current looses its validity, as detailed further in text. Anyway, the remaining 2% relative variations of the critical current were considered small enough to be neglected at first order. In Fig. 4.24, we repeated the fitting procedure when fixing a common critical current $I_0 = 0.437\ \mu$A for all curves.

This procedure was repeated at various fridge temperatures. From the $B^{2/3}$ plots, we extracted the variation of the critical current and of the effective temperature with I_N, shown in Fig. 4.25 and 4.26.

The variation of the apparent critical current with the noise amplitude is very similar at all fridge temperatures. We again neglected these variations and considered a constant critical current $I_0 = 0.437\,\mu$A for all values of I_N and fridge temperatures up to 370 mK. The effective tem-

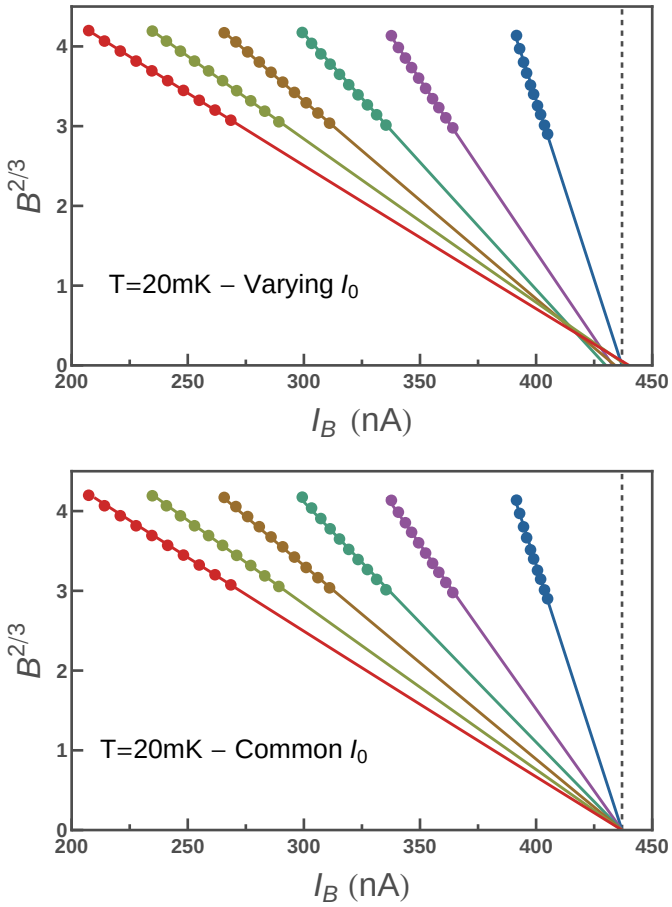

Fig. 4.24. Top: $B^{2/3}$ plots taken at $I_N = 0.02$, 0.44, 0.86, 1.27, 1.69 and 2.11 μA (from right to left). The critical current is left as a fit parameter for each curve. Data were obtained with $N = 10^5$ pulses of duration $\tau = 0.53$ μs ($\tau_{\rm sus} = 3$ μs and $t_{\rm signal} = 18$ μs). **Bottom:** Same data. The fits have only the slope as a parameter, the critical current being fixed at the common value $I_0 = 0.437$ μA.

peratures presented in Fig. 4.26 are extracted from fits using a common critical current.

At all temperatures of the fridge, the effective temperature increases with the current in the noise source with a similar slope, from the base temperature up to above 1.2 K. Note that the effective temperature can be higher than the critical temperature of the superconductor without any incidence. The two properties are absolutely not related one to each other: the effective temperature is only a measure of the noise power.

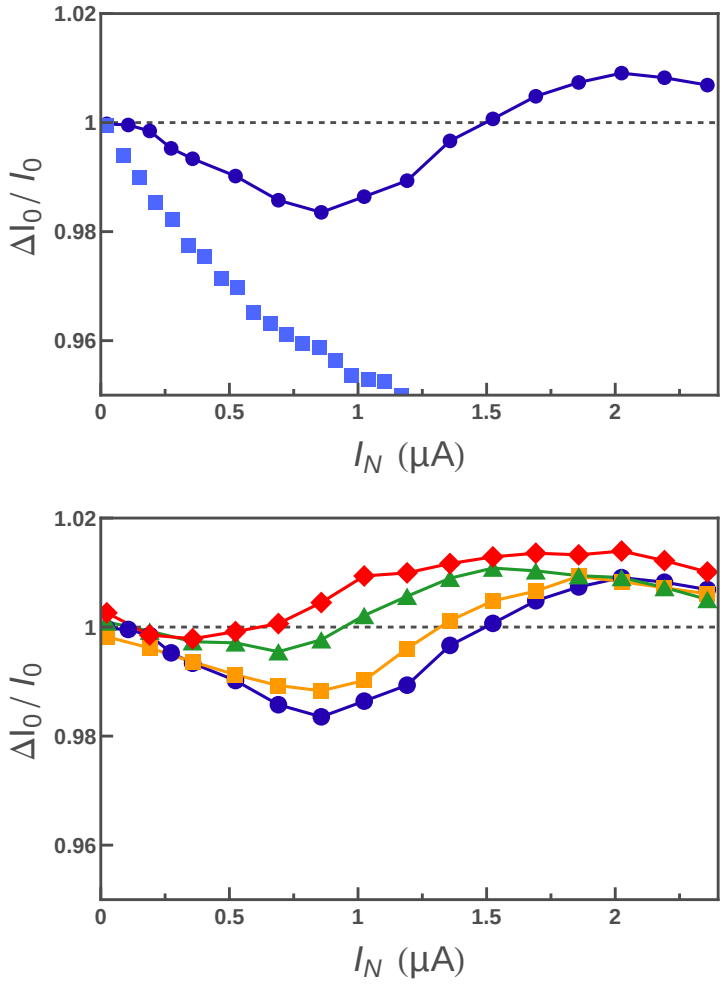

Fig. 4.25. Top: Relative changes at $T = 20$ mK of the apparent critical current of Sample JJD2 with I_N (with respect to $I_0 = 0.437\ \mu$A) deduced from the $B^{2/3}$ plots of Fig. 4.24 (linked circles). Compared to the same effect measured on Sample JJD1 (squares). **Bottom:** Relative variation (with respect to $I_0 = 0.437\ \mu$A) of the apparent critical current as a function of I_N for $T = 20$ mK (dots), 110 mK (squares), 218 mK (triangles), and 370 mK (diamonds)

Comparison with predictions

RCSJ Model The predicted effective temperature can be expressed from the amplitude of the total noise reaching the junction. In presence of different noise sources, one has to evaluate the contribution of each of them to the escape process:

- On the one hand, let us first consider the different contributions separately. The junction is placed in parallel with three branches described

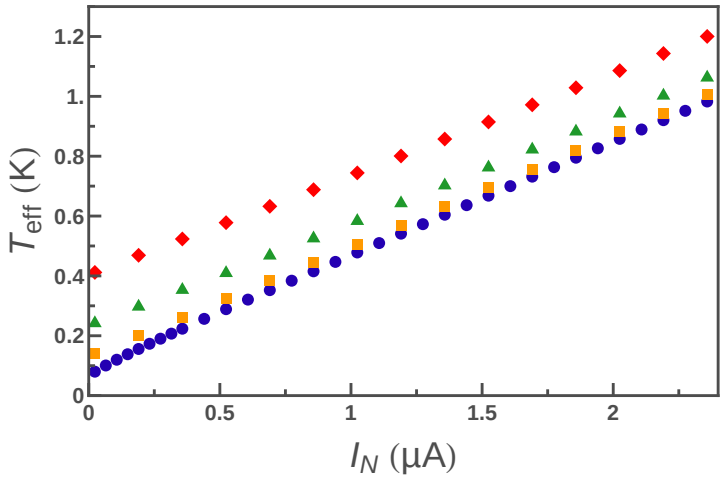

Fig. 4.26. Effective temperature as a function of I_N, for $T = 20$ mK (dots), 110 mK (squares), 218 mK (triangles), and 370 mK (diamonds) extracted using $I_0 = 0.437\,\mu$A.

in Fig. 4.9. The total spectral density of the noise reaching the junction, which can be described by a short-circuit when it is biased on the supercurrent branch, is the sum of the noise spectral densities emitted by each branch (see [94] for more details). The three resistors and the noise source are sources of white current fluctuations, therefore the total spectral density is:

$$S_{\text{eff}}^{D} = \frac{2k_B T_1}{R_1} + \frac{2k_B T_2}{R_2} + \frac{2k_B T_3}{R_3} + e\,|I_N|\,. \tag{4.20}$$

- On the other hand, to the admittance $Y(\omega) = \frac{1}{R_{||}}$ in parallel to the junction in the equivalent circuit of Fig. 4.9 is associated a noise source with spectral density:

$$S_{\text{eff}}^{D} = \frac{2k_B T_{\text{eff}}}{R_{||}}. \tag{4.21}$$

Matching the two expressions (4.20) and (4.21) leads to:

$$T_{\text{eff}} = \frac{R_{||}}{R_1} T_1 + \frac{R_{||}}{R_2} T_2 + \frac{R_{||}}{R_3} T_3 + \frac{1}{2} R_{||} \frac{e}{k_B}\,|I_N|\,. \tag{4.22}$$

When all the resistors are at the same temperature T, one obtains:

$$T_{\text{eff}} = T + \frac{1}{2} R_{||} \frac{e}{k_B}\,|I_N| \tag{4.23}$$

which is the expression for an RCSJ model presented in Eq. (2.72). This prediction is compared with the data in Fig. 4.27. At all temperatures,

the predicted slope is larger than the measured one, which is, moreover, not exactly the same for the different curves. This suggests that $R_{||}$ does not correctly describe the admittance across the junction at the relevant frequencies.

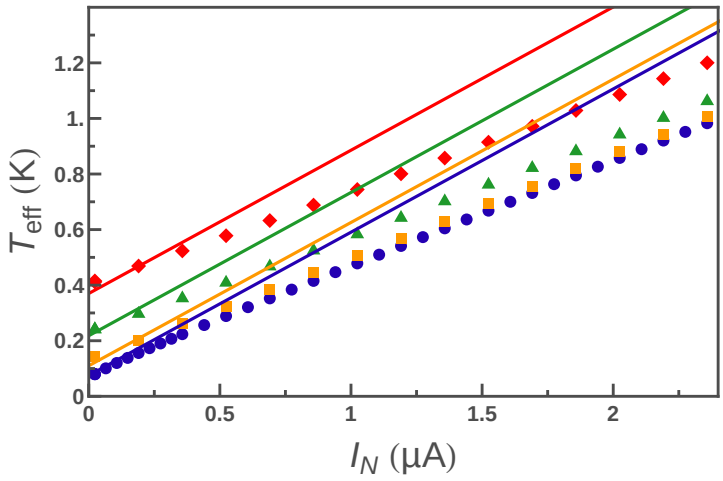

Fig. 4.27. Symbols: Measured effective temperature for $T = 20$ mK (dots), 110 mK (squares), 218 mK (triangles), and 370 mK (diamonds). **Solid lines:** Predicted effective temperature from the lumped-element model of the environment (Eq. 4.23). The disagreement suggests that this model is inaccurate.

Frequency dependence of the parameters In order to understand this discrepancy, we performed an analysis of the actual circuit at microwave frequencies, which revealed the origin of this mismatch. Due to the millimeter size of the on-chip connection pads, the circuit is expected to present resonances at a few tens of GHz. But with the supplementary on-chip resistors, theses resonances have a poor quality factor, and their effects span over a wide frequency range. This affects the system down to the plasma frequency. The environment of the junction, that is now written $Y^e(\omega)$, is frequency-dependent, and thus deviates from a simple Ohmic behavior. Moreover, the shot noise reaching the junction becomes a colored noise. A current fluctuation $\delta I_N(\omega)$ emitted by the noise source leads to a current $\alpha(\omega)\delta I_N(\omega)$ through the detector, where $\alpha(\omega)$ is a transfer function. The microwave simulation software Sonnet was used to model the effective environment of the junction and the transfer function.

For the simulation we considered the large scale circuit presented in the left panel of Fig. 4.8, but in absence of the junctions and of the

capacitance C_J. Capacitances and resistors were modeled with lumped elements, and only the sample elements were taken into account (therefore excluding the effects of the connection lines. This simulation is thus only valid for sufficiently large frequencies).

- We first placed only a pair of ports at the position where the detector junction is connected, and computed the admittance $Y^e(\omega)$ seen from this point.
- We then placed a second pair of ports at the position where the noise source is connected, and computed the admittance matrix between the two ports:

$$\begin{pmatrix} I_2 \\ I_2 \end{pmatrix} = \begin{pmatrix} Y_{11}\, Y_{12} \\ Y_{21}\, Y_{22} \end{pmatrix} \begin{pmatrix} V_1 \\ V_2 \end{pmatrix} \tag{4.24}$$

  where I_i and V_i are the current through and the voltage drop across the pair of ports (1 for noise source, 2 for detector). Assuming $V_2 = 0$ for a detector on its supercurrent branch, the current flowing through the port 1 (detector) as a function of the current flowing through the port 2 (noise source) yields the transfer function:

$$\alpha = \frac{I_2}{I_1} = \frac{Y_{21}}{Y_{11}}. \tag{4.25}$$

Plasma frequency and quality factor The real part of $Y^e(\omega)$ obtained from the simulation is plotted in Fig. 4.28. At the lowest frequency, it reduces to the value calculated from the lumped-element model $\frac{1}{R_{||}} = \frac{1}{89\,\Omega}$. But it strongly departs from this value at larger frequencies, and especially in the range of the plasma frequency of the junction (typically 1.5 GHz).

- The plasma frequency of the junction is obtained from:

$$C_J\omega_p - \frac{1}{L_J(s)\,\omega_p} + \mathrm{Im}\left[Y^e(\omega_p)\right] = 0 \tag{4.26}$$

  where $L_J(s)$ is the Josephson inductance (see Sec. 2.1.3). The plasma frequency at zero bias is found to be $\nu_{p0} \simeq 1.5$ GHz, slightly lower than the value $\sqrt{\frac{I_0}{\varphi_0 C_J}} \simeq 1.7\,\mathrm{GHz}$ found when considering a frequency-independent environment. The s-dependence of the plasma frequency is plotted in Fig. 4.29. It is compared with the approximate expression:

$$\nu_p(s) = \nu_{p0}\left(1 - s^2\right)^{1/4} \tag{4.27}$$

  that corresponds to the standard s-dependence. The very good agreement between the two curves allows one to consider that the plasma

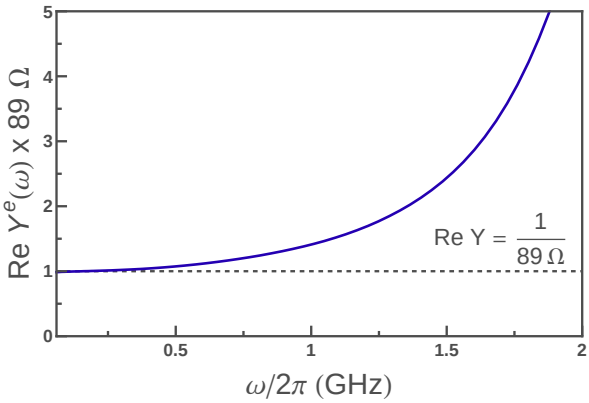

Fig. 4.28. Real part of $Y^e(\omega)$ calculated using a microwave simulation software in units of the expected lumped-element value $1/R_{||} = 1/89\,\Omega$ above the low frequency cutoff, shown as a dashed line.

frequency obtained with the complete environment is just slightly scaled down,[6] and is given by Eq. (4.27). Since experimentally $s \in [0.5 - 0.93]$, the plasma frequency is tuned in the range $[1 - 1.4\,\text{GHz}]$.

- The quality factor is also modified by the environment. At zero bias, it is given by :

$$Q_0 = \frac{1}{\text{Re}\left[Y^e\left(\omega_{p0}\right)\right]} C_J \omega_{p0} \simeq 4.5 \tag{4.28}$$

compared to a nominal value of 12 with the simple lumped-element model. As a function of s, the quality factor is

$$Q(s) = \frac{1}{\text{Re}\left[Y^e\left(\omega_p\left(s\right)\right)\right]} C_J \omega_p(s) \tag{4.29}$$

plotted in Fig. 4.29. It is compared to $Q_0\left(1 - s^2\right)^{1/4}$, which is the s-dependence in the RCSJ model. It is clear from this figure that the effect of the environment on the quality factor cannot be described by a simple numerical factor, since the s-dependence is strongly different. In the relevant experimental range $s \in [0.5 - 0.93]$, we considered that $Q_0 = 5$ was a simple and sufficient approximation.

Transfer function The magnitude of the simulated transfer function is shown in Fig. 4.30. At low-frequency, its behaviour is due to the on-chip filtering designed on purpose. Between 50 MHz and 300 MHz, it is equal to unity, in agreement with the lumped element model. But at

[6] Since the cross-over temperature is rescaled down, the condition on the thermal activation regime remains fulfilled.

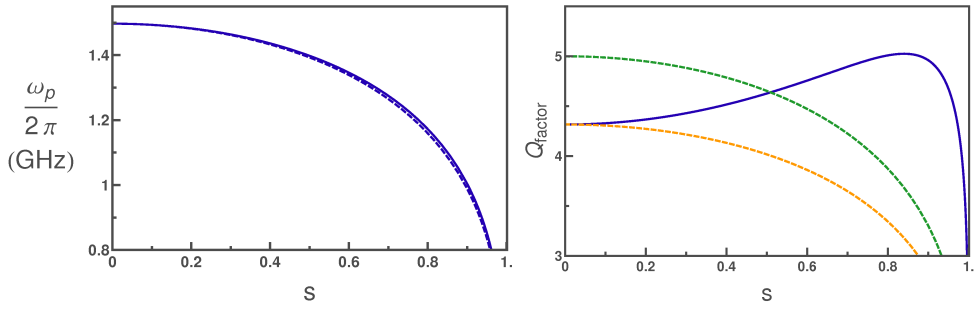

Fig. 4.29. Left: Plasma frequency of the junction obtained from the microwave simulation software at all reduced bias currents (solid line) compared to the approximation for the dependence in s of Eq. (4.27) (dashed line). **Right:** Quality factor of the junction obtained from the microwave simulation (solid line) compared to the approximate expressions $Q_0\left(1-s^2\right)^{1/4}$ (bottom dashed line) and $5\left(1-s^2\right)^{1/4}$(top in dashed line)

higher frequency, the magnitude of the transfer function exceeds unity. The fact that it can be larger than unity is due to the resonant behavior of the circuit that enhances fluctuations at those frequencies. And in the experimental range [1 − 1.5 GHz] in which the plasma frequency is tuned, the transfer function strongly deviates from one and its variations have to be taken into account.

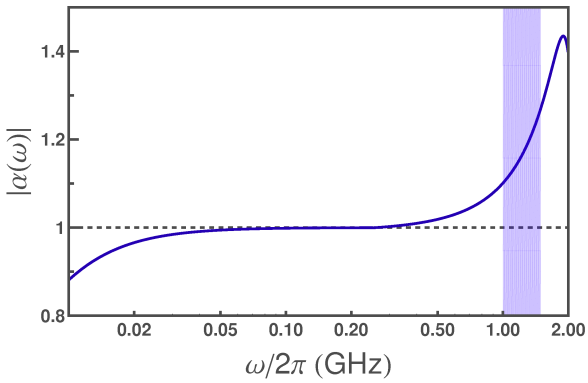

Fig. 4.30. Magnitude of the transfer function $\alpha(\omega)$. The cutoff at low frequency is due to the designed RC filter. Above 500 MHz, the magnitude deviates from unity, which is the value expected in the lumped element model. The relevant experimental range for the plasma frequency is shown with blue background.

Model A model circuit describing accurately the behavior of the environment and of the transfer function in the range [1 − 1.5 GHz] is shown in Fig. 4.31.

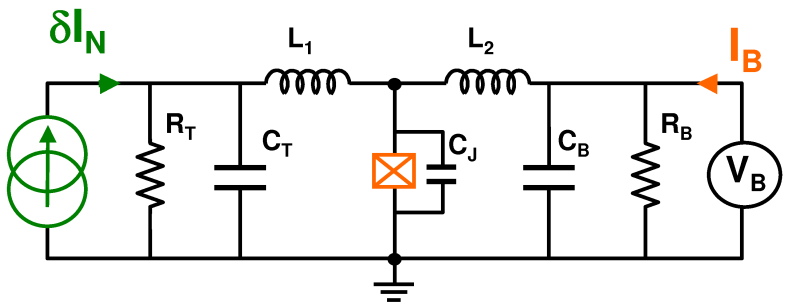

Fig. 4.31. Model circuit designed to capture the behavior of $Y^e(\omega)$ and $\alpha(\omega)$ obtained by microwave simulations in the range [1 − 1.5 GHz] with: $R_T = 163\Omega$, $R_B = 203\Omega$, $L_1 = 4.9$nH, $L_2 = 8.15$ nH, $C_T = 0.6$ pF, $C_B = 0.85$ pF.

Within this model, the admittance seen across the junction and the transfer function are:

$$Y_m(\omega) = \frac{1}{jL_1\omega + \frac{1}{(R_T)^{-1}+jC_T\omega}} + \frac{1}{jL_2\omega + \frac{1}{(R_B)^{-1}+jC_B\omega}} \tag{4.30}$$

and

$$\alpha_m(\omega) = \frac{1}{1 - L_1C_T\omega^2 + j\frac{L_1}{R_T}\omega}. \tag{4.31}$$

The transfer function is calculated assuming that the JJ behaves as a short circuit. The comparison between the Sonnet calculations and this model circuit are plotted in Fig. 4.32.

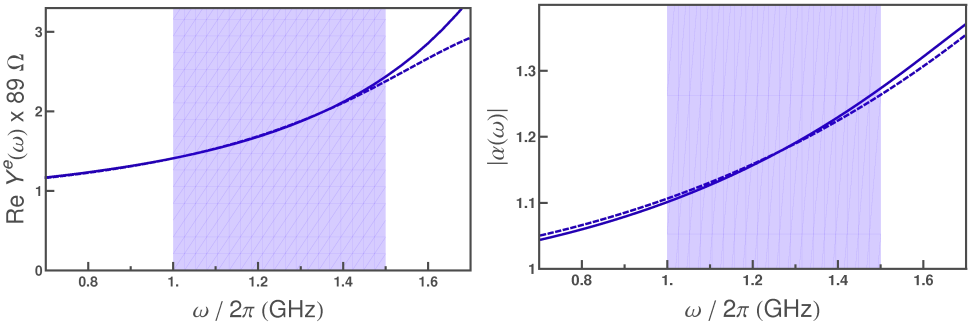

Fig. 4.32. Left: Re $[Y^e(\omega)]$ calculated with the microwave simulation software (solid line) compared to Re $[Y_m(\omega)]$ from the model circuit (dashed line). **Right:** transfer function $\alpha(\omega)$ calculated with the microwave simulation software (solid line) compared to the transfer function $\alpha_m(\omega)$ from the model circuit (dashed line).

Escape temperature from a harmonic assumption A simple, although possibly naive, prediction for the effective temperature is obtained for the frequency-dependent circuit when considering that the response of the junction is dominated by its dynamics at the plasma frequency. The effective temperature can then be expressed following the procedure that yielded Eq. (4.23), but with some changes:

- The spectral density of the noise $e\,|I_N|$ is replaced by $S_2^D(\omega) \simeq e\,|\alpha(\omega_p)|^2\,|I_N|$.
- The resistor $R_{||}$ is replaced by $(\mathrm{Re}\,[Y^e\,(\omega_p)])^{-1}$.

The effective temperature writes at first order:

$$T_{\mathrm{eff}} \simeq T_{\mathrm{eff}}^0 + K\,(\omega_p)\,|I_N|\,. \tag{4.32}$$

where

$$K\,(\omega_p) = \frac{1}{2}\frac{e}{k_B}\frac{|\alpha(\omega_p)|^2}{\mathrm{Re}\,[Y^e\,(\omega_p)]}. \tag{4.33}$$

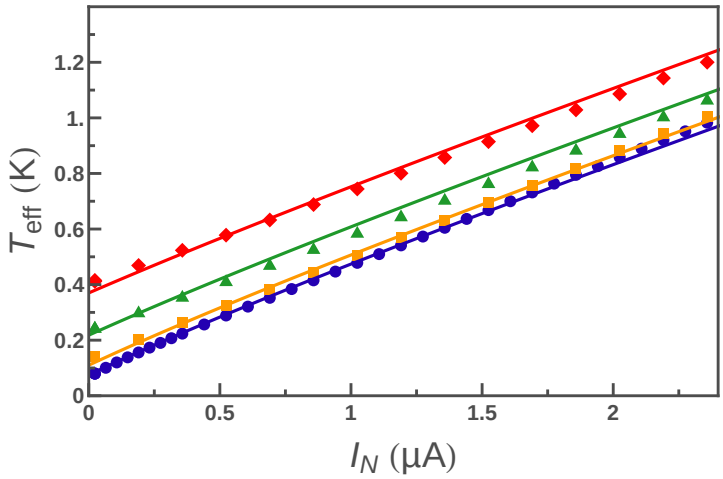

Fig. 4.33. Symbols: Experimental effective temperature from Fig. 4.26. **Solid lines:** Expected effective temperature obtained from Eq. 4.32, based directly on the results obtained using a microwave simulation software.

In principle, since the temperature with this complete model is dependent on the plasma frequency $\omega_p(s)$, it is also dependent on the reduced bias current. This dependence on the temperature with the reduced bias current should be seen on the $B^{2/3}$ functions shown in Fig. 4.24. However, although a large range of s is spanned by this complete measurement, each curve taken separately for a given value of I_N only corresponds to a small range of s. Since the s-dependence of the plasma frequency is

very smooth, the effective temperature is thus almost constant for each curve. At this level, one assumes a single effective temperature for each value of I_N. In Fig. 4.33, the temperature calculated at the reduced bias current corresponding to $P = 0.6$ from Eq. (4.32) is compared with the experimental result; the agreement is now correct, without any adjustable parameter, which gives confidence in our understanding of the effect of the second moment of the shot noise on the escape rate of a Josephson junction out of its zero-voltage state.

Escape temperature with a complete resolution In the time interval between the publication of this experimental results [38] and the writing of this manuscript, D. Urban and H. Grabert [12] developed a generalization of the theory presented in [11]. This generalized theory allows to compute the escape rate out of the zero-voltage state for a Josephson junction in an arbitrary environment current-biased by a colored asymmetric noise. Using the model circuit of Fig. 4.31, they computed the escape rate for various values of I_N in the range of s corresponding to the experiment, and reproduced the $B^{2/3}$ functions, as shown in Fig. 4.34.

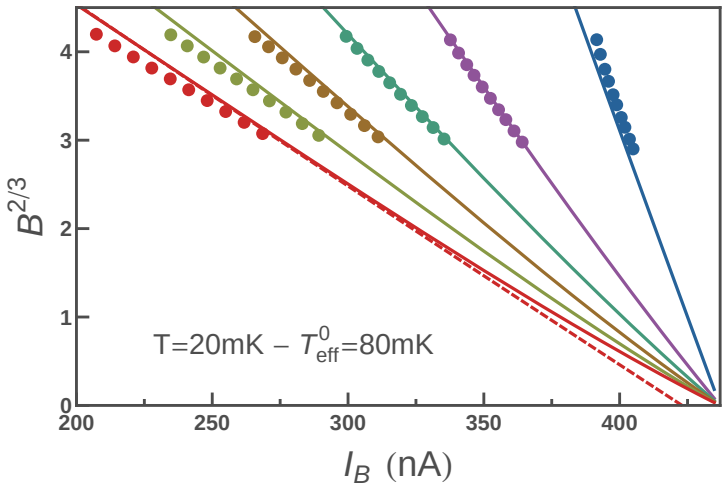

Fig. 4.34. Symbols: Experimental $B^{2/3}$ functions obtained at $T = 20$ mK, already presented in Fig. 4.24. **Solid Lines:** Prediction obtained with a generalization of the theory presented in [11] (see text) for $I_N = 0.02$, 0.44, 0.86, 1.27, 1.69 and 2.11 μA from right to left (similar to the experimental curves) and $T^0_{\rm eff} = 80$ mK. **Dashed line:** Fit of the prediction obtained for $I_N = 2.11\,\mu$A with the Eq. (4.19) and a critical current kept as a free parameter.

An important feature of this predicted $B^{2/3}$ functions is that they are not anymore linear as $(1 - s)$, the definition of an effective temperature thus looses it validity, since it becomes strongly s-dependent (as

was already the case in the simple harmonic assumption, althougth we neglected this effect). However, for the sake of comparison with the experiment, it is possible to extract an effective temperature by fitting the predicted $B^{2/3}$ functions with the expression from Eq. (4.19) in the range $B^{2/3} \in [3 - 4.3]$ and with a critical current $I_0 = 0.437\,\mu$A, as is done for the experimental curves.[7] The effective temperature corresponding to the predicted response is compared with the one extracted from the experimental data, as shown in Fig. 4.35, without any adjustable parameters.

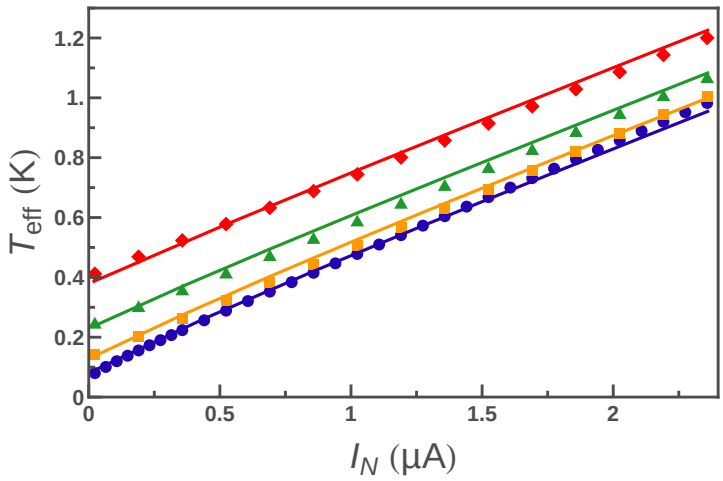

Fig. 4.35. Symbols: Experimental effective temperature from Fig. 4.26. **Solid lines:** Expected effective temperature by performing a complete calculation of the escape rate from the model circuit of Fig. 4.31 [12], using the base temperatures $T = 80$ mK, 128 mK, 230 mK and 380 mK.

The correct agreement with the data confirms that the response of the junction is properly captured by this generalized theory, and that the harmonic assumption performed in the previous section leads to a good understanding of this response.

4.5.2 Rate asymmetry

Having understood the effect of the second moment of the noise on the effective temperature of the junction, the effect of the asymmetry of the noise on the escape rate is now described.

[7] When the critical current is kept as a free parameter in this procedure, its apparent value depends on I_N. This effect possibly accounts for part of the modulation of the apparent critical current observed in Fig. 4.25.

Experimental detection

The effect of the noise asymmetry on the rate is seen by changing the relative sign of the currents through the noise source and through the detector.

- When the bias current of the detector junction and the third moment of noise seen by this detector have the same sign, the rate is higher than for a Gaussian noise at the same effective temperature, denoted $\Gamma(T_{\text{eff}})$. Since the noise δI_N as defined in Fig. 4.7 *subtracts* from the bias current, this situation is accessed when I_N and I_B are of opposite sign. Two configurations are thus possible:
  - $\{I_N \leq 0 \text{ and } I_B \geq 0\}$, with a rate $\Gamma_+(-I_N)$
  - $\{I_N \geq 0 \text{ and } I_B \leq 0\}$, with a rate $\Gamma_-(+I_N)$.
- When the junction bias current and the third moment of noise have opposite signs, the rate is lower than $\Gamma(T_{\text{eff}})$. Experimentally, this situation is obtained in the two configurations:
  - $\{I_N \geq 0 \text{ and } I_B \geq 0\}$, with a rate $\Gamma_+(+I_N)$
  - $\{I_N \leq 0 \text{ and } I_B \leq 0\}$, with a rate $\Gamma_-(-I_N)$.

This summarizes into the expected relations:

$$\begin{cases} \Gamma_+(-I_N) = \Gamma_-(+I_N) > \Gamma(T_{\text{eff}}) \\ \Gamma_+(+I_N) = \Gamma_-(-I_N) < \Gamma(T_{\text{eff}}) \end{cases} \tag{4.34}$$

In the conditions of this experiment, the relative effect on the rate due to the third moment is a tiny effect, typically a few percent, at most 6 %. The escape rate being very sensitive to the bias current and to the temperature, which are submitted to offsets and drifts, several experimental effects can produce such a rate asymmetry and one needs to be particularly careful with the measurement. A single measurement of the rate is therefore not sufficient to separate the very tiny contribution of the third moment from the large effect due to the second moment. To eliminate part of the effect of spurious drifts, we define the two quantities:

$$R_\Gamma^+ = \Gamma_+(-I_N)/\Gamma_+(+I_N) \text{ and } R_\Gamma^- = \Gamma_-(+I_N)/\Gamma_-(-I_N). \tag{4.35}$$

which we call rate asymmetries. If the bias current I_B drifts slightly with time, both $\Gamma_+(-I_N)$ and $\Gamma_+(+I_N)$, which are measured with the same bias pulse, should be modified the same way. As long as this drift stays small, their ratio R_Γ^+ should be almost constant. Moreover, the two rate asymmetries are expected to be equal in absence of artifacts.

Rate asymmetry as a function of current in the noise source The procedure to measure the asymmetry signal $R_\Gamma^\pm$ as a function of I_N is as follows:

1. A given value of I_N is chosen.
2. A curve similar to the one presented in Fig. 4.18(a) is measured where the evolution of the mean escape rate $\frac{1}{2}\left[\Gamma_+\left(+I_N\right)+\Gamma_-\left(+I_N\right)\right]$ is monitored as a function of the bias current with $N = 10^4$ pulses in order to extract the effective temperature $T_{\text{eff}}(+I_N)$.
3. The current in the noise source is first fixed to $+I_N$;
   a) The amplitude of the detector bias current is adjusted to obtain a switching probability $P = 0.6$ for the positive bias current, corresponding to a rate $\Gamma = 1.76$ MHz and a reduced barrier height $B \simeq 6.5$.
   b) The escape rates $\Gamma_+\left(+I_N\right)$ and $\Gamma_-\left(+I_N\right)$ are measured simultaneously using $N = 10^5$ pulses.
4. The current in the noise source is then inverted and fixed to $-I_N$.
   a) The amplitude of the detector bias current pulses is kept constant.
   b) The escape rates $\Gamma_+\left(-I_N\right)$ and $\Gamma_-\left(-I_N\right)$ are obtained similarly.
5. From the steps 3 and 4, one extracts a value for R_Γ^+ and R_Γ^-. These steps are repeated typically 100 times each, except at the lowest temperature where we repeated 250 times. This corresponds to $2\times100\times10^5 = 2\times10^7$ signals of 18 μs, therefore a measurement time of 6 min for each value of I_N, which yields two measurements of the rate asymmetry R_Γ^+ and R_Γ^-.[8]

A typical outcome of this procedure is found in Fig. 4.36. We reproduced in this figure the four different rates extracted for 100 repetitions of steps 3 and 4 at $T = 110$mK. As can be seen in some cases, a spurious difference in amplitude between the positive and negative bias pulses was large enough to induce a significant difference between the rates in absence of any effect of shot noise. The difference between the rates corresponds to a difference of 0.3 nA between the current amplitude of the two pulses, which a relative difference of 0.1%. We attributed this slight difference to the signal generators, that appeared to provide a slightly asymmetric signal in some ranges.[9] On the bottom left panel of this figure, one can also observe that the rate could drift a little during the measurement,

[8] In fact, to avoid relaxations effects, we introduced latency times between two measurements at different values of I_N, so that the measurement time of one point was typically 10 min.

[9] The spurious offsets were essentially predominant for the lowest effective temperature, where the dependence of the escape probability with the bias current is the steepest. At larger temperatures, these offsets could be neglected.

or even jump due to sudden change in the conditions, but the moving average of R_Γ that we performed was almost insensitive to such tiny effects.

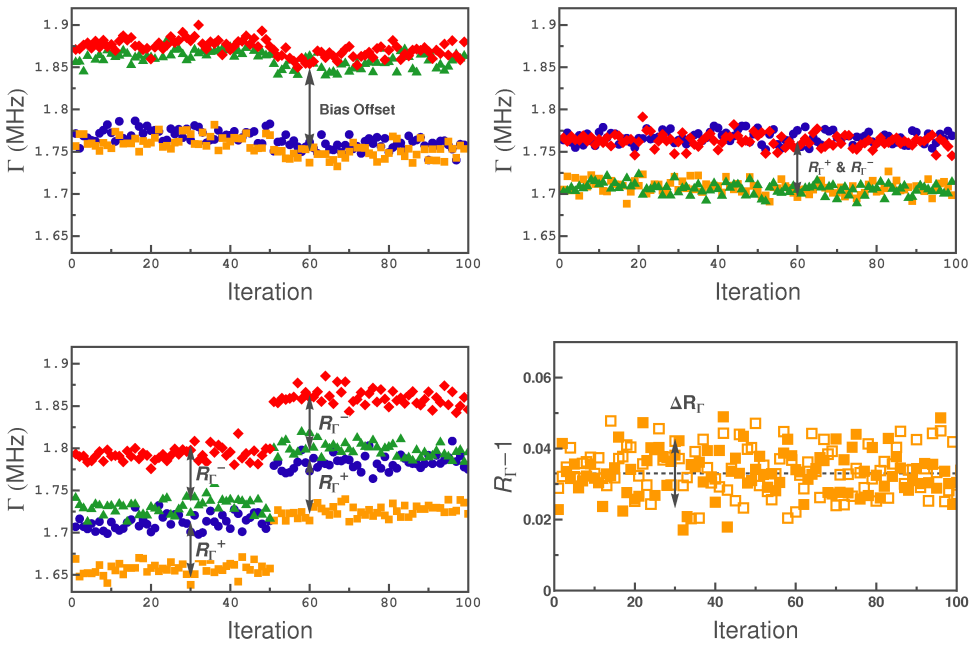

Fig. 4.36. Top Left: Rates obtained at $T = 110\,\mathrm{mK}$ from the procedure described in text for the lowest $I_N = 0.02\,\mu\mathrm{A}$, corresponding to the 100 measurements. Blue circles and orange squares corresponds to the rates obtained for the positive bias pulse ($\Gamma_+(-I_N)$ and $\Gamma_+(+I_N)$) while red diamonds and green triangles correspond to the rates obtained for the negative bias pulse ($\Gamma_-(+I_N)$ and $\Gamma_-(-I_N)$). The rate asymmetry R_Γ^+ (resp. R_Γ^-) corresponds to the difference between circles and squares (resp. diamonds and triangles). At this value of I_N, all points should be almost at the same value. However, due probably to some offset on the bias current, there is a residual difference. With our definition of the rate asymmetry, this perturbation has no effect. **Top Right:** Rates obtained for $I_N = 2\,\mu\mathrm{A}$, with similar symbols. One this figure, no spurious offset is observed and the Eq. (4.34) is fulfilled. **Bottom Left:** Rates obtained for $I_N = 0.2\,\mu\mathrm{A}$, with similar symbols. One this figure, a sudden jump is seen after 50 iterations. This jump appeared because the measurement was stopped for some time, then restarted, and some uncontrolled parameter (temperature,...) could have drifted in the meanwhile. However, the space between the curves, that corresponds to the rate asymmetries R_Γ^+ and R_Γ^- seen in **bottom right panel** evolve only slightly and does not suffer from this drift.

Overall, we extracted the mean values of the rate asymmetries $\left\langle R_\Gamma^+ \right\rangle$ and $\left\langle R_\Gamma^- \right\rangle$, that are shown in Fig. 4.37. The error on the measurement can be estimated from the statistical error on the rate of Eq. (3.24) and

$$\frac{\Delta R_\Gamma}{R_\Gamma} = \sqrt{2}\frac{\Delta\Gamma}{\Gamma}. \tag{4.36}$$

Considering $R_\Gamma \simeq 1$, the error is estimated with $N = 10^7$ (for one sign of the rate asymmetry only) and $P = 0.6$ as:

$$\Delta R_\Gamma \simeq \sqrt{2}\frac{1}{\sqrt{10^7}}\sqrt{\frac{0.6}{0.4}}\frac{1}{\ln(0.4)} = 0.06\,\%. \tag{4.37}$$

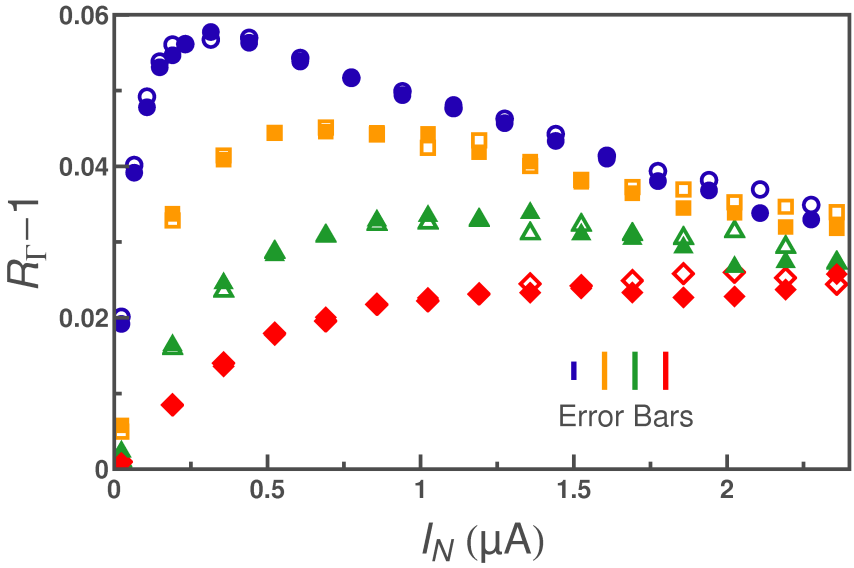

Fig. 4.37. Rate asymmetry as a function of I_N, taken at $P = 0.6$ ($\Gamma = 1.76$ MHz). Filled (open) symbols corresponds to measurement with positive (negative) currents through the detector JJ for $T = 20$mK (dots), 110mK (squares), 218mK (triangles), 370 mK (diamonds). The statistical error bar is shown for each separate curve (20 mK to 370 mK from left to right).

Accounting for these error bars, and except for small discrepancies at large values of I_N that are not understood presently, $\langle R_\Gamma^+ \rangle$ and $\langle R_\Gamma^- \rangle$ have very similar values. **The agreement between the two measurements gives confidence in the reliability of the procedure.**

The curves present a maximum which shifts to higher values of I_N when increasing T, while the third moment of the noise grows linearly with I_N. This can be surprising at first sight, but it is just a result of the combined effect of the second and third moment of noise on the rate asymmetry. To grasp this behaviour qualitatively, one represents the effect of the noise asymmetry as a current shift ΔI_B to obtain a given rate (see [37, 38]). This shift in current is related to the change in the rate by:

$$\Delta\Gamma \propto \frac{\partial\Gamma}{\partial I_B}\Delta I_B. \tag{4.38}$$

The current shift ΔI_B increases with I_N due to the third moment of the noise, but $\frac{\partial\Gamma}{\partial I_B}$, which can be considered as the sensitivity of the rate, diminishes due to the increased effective temperature. The shape of R_Γ is thus a convolution between the increasing effect of the third moment (linear increase observed at small values of I_N) and the loss of sensitivity due to the second moment (decrease in I_N^{-2} observed at larger values of I_N). It is therefore expected to present the observed maximum.

Sensitivity

In order to compare the performance of a Josephson junction with other conventional detectors, we estimated here its sensitivity for the second and third moment, as was done at the beginning of this chapter. The total time of the measurement is $t_{\text{mst}} = N \times t_{\text{signal}}$, the statistical error for the escape probability is thus:

$$\frac{\Delta P}{P} \simeq \frac{1}{\sqrt{N}} \simeq \sqrt{\frac{t_{\text{signal}}}{t_{\text{mst}}}}. \tag{4.39}$$

The error on the rate at $P \simeq 0.5$ (see Eq. (3.24)) is linked to the escape probability by:

$$\frac{\Delta\Gamma}{\Gamma} \simeq \frac{\Delta P}{P} \tag{4.40}$$

but can also be expressed as an error on the effective temperature:

$$\frac{\Delta\Gamma}{\Gamma} = \frac{\Delta U}{k_B T_{\text{eff}}^2}\Delta T_{\text{eff}}. \tag{4.41}$$

- The error performed on the measurement of the second moment is obtained as:

$$\Delta S_2 = \frac{2k_B}{R_{||}}\Delta T_{\text{eff}} \simeq \frac{2k_B T_{\text{eff}}}{BR_{||}}\sqrt{\frac{t_{\text{signal}}}{t_{\text{mst}}}} \simeq \sigma_2\sqrt{\frac{1}{t_{\text{mst}}}} \tag{4.42}$$

  where B is the typical reduced barrier height at which the measurement is performed and where we defined σ_2 as the sensitivity of the detector (the error on the measurement of the second moment when measuring during one second). The order of magnitude can be obtained by assuming that the effective temperature is the lowest one $T_{\text{eff}} = 70$ mK (where the escape is the most sensitive) and $B = 6.5$, $t_{\text{signal}} = 18\,\mu$s, $R_{||} = 90\,\Omega$. This yields:

$$\sigma_2 \simeq 80\, e\ \text{pA}/\sqrt{\text{Hz}}. \tag{4.43}$$

- The same calculation can be performed for the third moment of the noise. In our case $Q_0 = 5$ and the rate asymmetry is expanded into:

$$R_\Gamma - 1 \simeq S_3 \omega_{p0}^2 \left(\frac{\varphi_0}{k_B T_{\text{eff}}}\right)^3 0.81(1-s)^{2.14}. \tag{4.44}$$

Since the measurement is performed at almost constant B, the term $(1-s)$ is better expressed as:

$$1 - s = \left(\frac{3B}{4\sqrt{2}} \frac{k_B T_{\text{eff}}}{E_J}\right)^{2/3}. \tag{4.45}$$

Therefore, the rate asymmetry becomes:

$$R_\Gamma - 1 \simeq S_3 \omega_{p0}^2 \left(\frac{\varphi_0}{k_B T_{\text{eff}}}\right)^3 0.81 \left(\frac{3B}{4\sqrt{2}} \frac{k_B T_{\text{eff}}}{E_J}\right)^{1.4}. \tag{4.46}$$

Considering that the error on the effective temperature is completely negligible, the error on the third moment of noise is:

$$\Delta S_3 = \left(\frac{k_B}{\varphi_0}\right)^3 \frac{1.23}{\omega_{p0}^2} \left(\frac{3B}{4\sqrt{2}} \frac{k_B}{E_J}\right)^{-1.4} \left(T_{\text{eff}}^0 + \frac{1}{2} \frac{R_{||}}{k_B} S_2\right)^{1.6} \Delta R_\Gamma. \tag{4.47}$$

where we have used Eq. (4.23) for the effective temperature, but placed T_{eff}^0 as the base temperature. Using the statistical expression

$$\Delta R_\Gamma \simeq \frac{\Delta R_\Gamma}{R_\Gamma} = \sqrt{2} \frac{\Delta \Gamma}{\Gamma} = \sqrt{\frac{t_{\text{signal}}}{t_{\text{mst}}}} \tag{4.48}$$

with the same parameters as for the second moment, a critical current $I_0 = 0.4\,\mu$A and a plasma frequency $\nu_{p0} = 1.5$ GHz, the error can be evaluated at the top of the curve taken at $T = 20$ mK in Fig. 4.37, so for $I_N = 0.2\,\mu$A, with:

$$\Delta S_3 = \sigma_3 \sqrt{\frac{1}{t_{mst}}} \tag{4.49}$$

where the sensitivity on the third moment is:

$$\sigma_3 \simeq 60\, e^2\, \text{nA}/\sqrt{\text{Hz}} \tag{4.50}$$

- Experimentally, from the error bar of Eq. (4.37), one has at $I_N = 0.2\,\mu$A an error on the third moment $\Delta S_3 = 0.02 \times 0.2\, e^2\,\mu$A for a measurement time of 360 s. The empirical sensitivity is close to:

$$\sigma_3 \simeq 75\, e^2\, \text{nA}/\sqrt{\text{Hz}}. \tag{4.51}$$

in good agreement with the rough prediction.

This sensitivity on the third moment measured through the escape rate of a Josephson junction is thus of the same order of magnitude as the one found when directly monitoring voltage fluctuations with a cryogenic amplifier [80], calculated at the beginning of this chapter. In a sense, it seems quite disappointing that the Josephson junction, which plays the role of a large gain cryogenic amplifier, does not allow to considerably improve the sensitivity. In fact, the main difference between the two techniques comes from the sampling cycle time, here given by $t_{\text{signal}} = 18\mu s$, although only a small fraction of the signal is a measurement pulse, while in the case of [80], the sampling cycle time is 25 ns, three order of magnitude smaller. It should be possible to decrease t_{signal} by one order of magnitude through a careful tuning, but probably not further without more technical add-on. This plays a considerable role on the sensitivity, and limits the efficiency of the Josephson junction as a detector.

Rate asymmetry as a function of the reduced bias current Using different pulse durations, and/or measuring the asymmetry at different escape probabilities, we obtained the variation of the rate asymmetry with the reduced bias current s for $I_N = 0.334\ \mu$A at $T = 20$ mK (which corresponds to the maximum of the rate asymmetry in Fig. 4.37). This measurement is shown in Fig. 4.38. It appears that the rate asymmetry increases when the reduced bias current is lowered. A qualitative explanation is that at lower s, thus at larger barrier height, the escape is due to larger fluctuations, which present also the largest asymmetry.

Since the asymmetry increases when lowering s, it is tempting to have long bias pulses to increase the rate asymmetry and thus have a large signal. However, long bias pulses also correspond to long measurement times. Therefore the sensitivity, which corresponds to the measurement time needed to obtain a given signal-to-noise ratio, is not improved.

Comparison with predictions

In order to compare the measured asymmetry with the theoretical predictions, the frequency-dependence of the admittance $Y(\omega)$ and of the transfer function $\alpha(\omega)$ has to be taken into account. The theoretical model however assumes that the circuit is described by the RCSJ model and that the noise is white, therefore it does not apply directly here.

For the case of the second moment and the resulting effective temperature, we went further than the RCSJ model with the assumption that the plasma frequency was the only relevant frequency entering the spectral density. However, in the case of the third moment, the transfer function translates into a frequency dependence of the spectral density

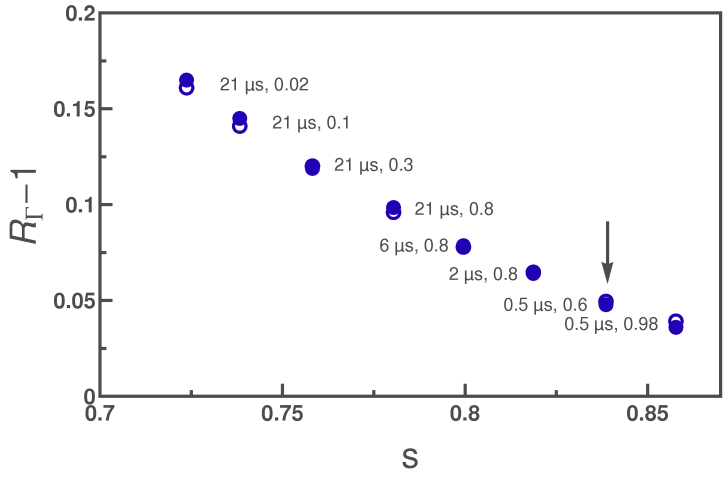

Fig. 4.38. Rate asymmetry as a function of the reduced bias current s for $I_N = 0.334\,\mu$A and $T = 20$ mK. The various points correspond to measurements performed for different escape probabilities and different pulse lengths (for each point, the pulse duration τ_p and the escape probability P are indicated). If P is smaller and the pulse longer, the reduced bias current s is smaller. The arrow corresponds to the measurements presented in Fig. 4.37.

as a function of two frequencies ω_1 and ω_2 (see Eq. (2.67)):

$$S_3^D(\omega_1, \omega_2) = \alpha(\omega_1)\alpha(\omega_1 - \omega_2)\alpha(-\omega_2)e^2 I_N \tag{4.52}$$

It is therefore difficult to think of a simple model using two relevant frequencies. Two ways to compare with theory are then possible:

- One takes the simple theory assuming white noise and an RCSJ model, and compare to the data, as was done in [38]. The prediction for the rate asymmetry is computed using the measured effective temperature of Fig. 4.26, the parameters for the environment extracted from the microwaves simulations ($Q_0 = 5$ and $\nu_{p0} = 1.5$ GHz), and the prediction for the rate asymmetry computed at all values of reduced bias current for $Q_0 = 5$ presented in Eq. (2.95). By scaling this prediction by a factor 1.5, an agreement with the experiment was found for all values of the temperature, which is quite remarkable since the theory should not be applicable (see Fig. 4.39). In [38], we explained this factor by the presence of the transfer function: since the transfer function evolves within $1 \leq |\alpha| \leq 1.2$ in the relevant range of plasma frequencies, one might expect that the third moment of the noise is scaled by a term of the order of $1 \leq |\alpha|^3 \leq 1.7$.
- The most rigorous approach is to use the generalization [12] of the theory presented in [11] and the model circuit presented in Fig. 4.31. D. Urban and H. Grabert computed recently the rate asymmetry along

theses lines. Their results are compared to the data in Figs. 4.40 and 4.41. It it clear from the figure that this complete approach achieves a quantitative agreement with the measured rate asymmetry, which confirms the correct understanding of this detection circuit.

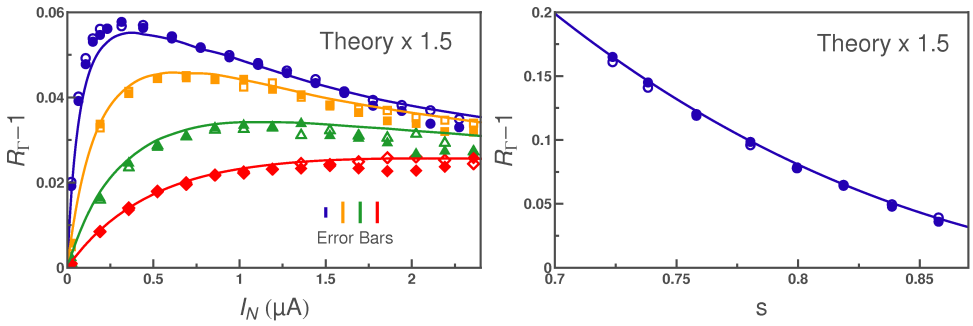

Fig. 4.39. Comparison between the experiment and the predicted rate asymmetry for a white noise, calculated assuming $Q_0 = 5$ with the measured values of the effective temperature. The theory has been scaled up by a factor 1.5. These figures were published in [38].

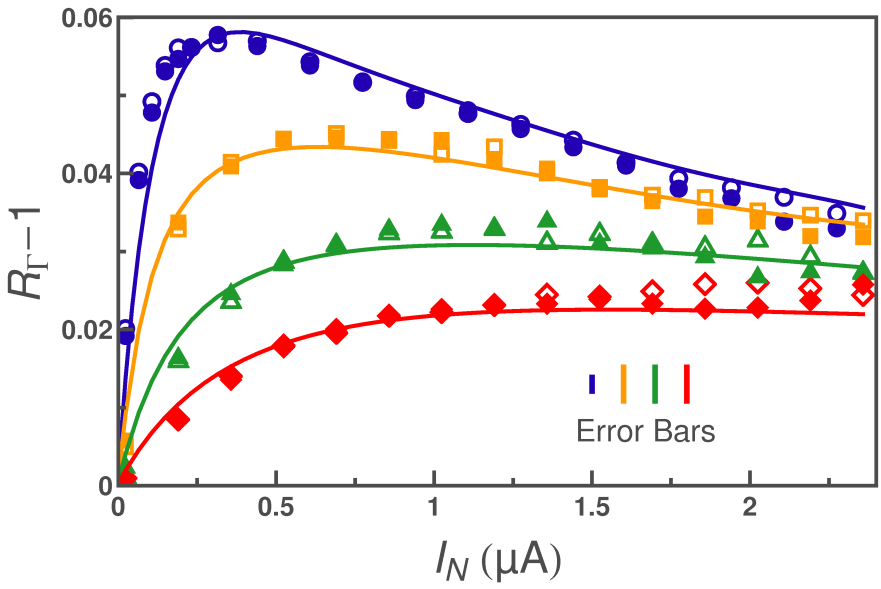

Fig. 4.40. Comparison between the experiment and the predicted rate asymmetry using a generalized non-Markovian [12] theory applied to the model circuit presented in Fig. 4.31.

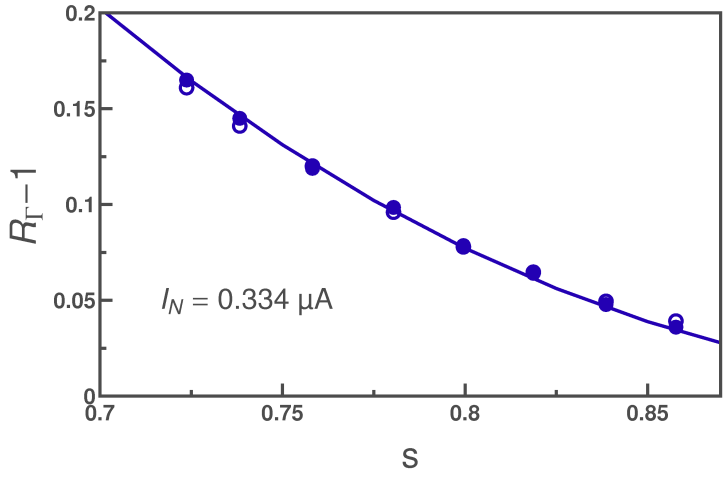

Fig. 4.41. Comparison between the experiment and the predicted rate asymmetry using a generalized non-Markovian [12] theory applied to the model circuit presented in Fig. 4.31.

4.5.3 Off-road measurements

Since the noise source was in practice a Josephson junction, two side measurements were performed with a voltage V_N lowered below the superconducting gap, in a regime where the Josephson junction is not equivalent to a simple tunnel junction.

Noise source biased near $V_N = 400\,\mu$V

On Sample JJD1, the noise source was biased at $V_N \simeq \frac{2\Delta}{e}$, where the $I(V)$ characteristics presents a back-bending behavior shown in Fig. 4.42. At five different currents, we monitored the evolution with s of the escape probability P for positive and negative values of I_N (see Fig. 4.42), and compared to a situation far from the superconducting gap, at a larger current. One observes that the asymmetry effect obtained on the back-bending part of the characteristics can be much larger than in the case of the simple quasiparticle tunneling obtained at larger voltage bias. At $I_N = 3.4\,$nA, one observes even that the curves cross each other, an effect which cannot be explained by a contribution from a finite third moment only. Although the effect on the rate asymmetry of a non-linear $I(V)$ curve was addressed in [95], this theory can barely be applied here, where the non-linearities of the experimental curve are presently not described by a model.

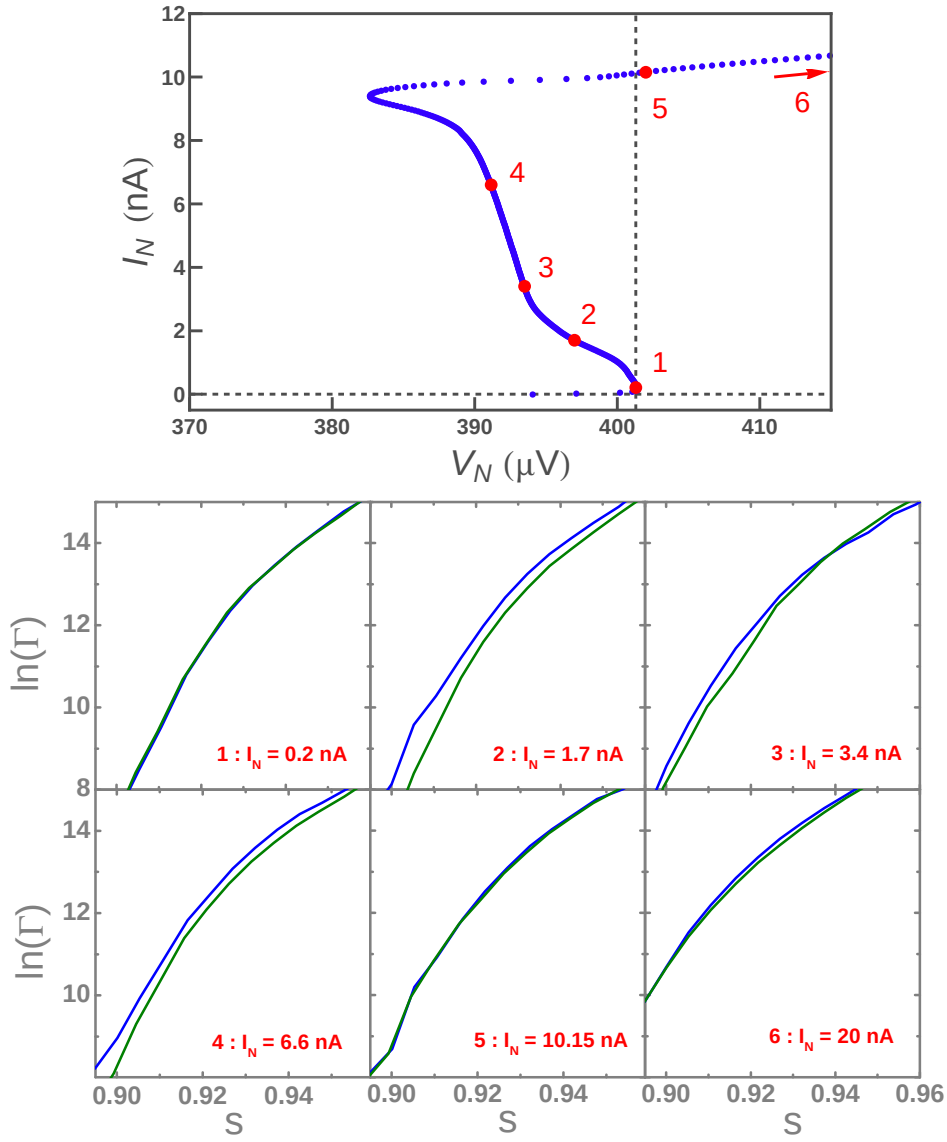

Fig. 4.42. Top: $I(V)$ curve of the noise source around $V_N = 400\ \mu$V, presenting strong non-linearities. The rate asymmetry was measured when biasing the noise source on this branch, for five different currents. **Bottom:** Evolution of the escape rate Γ as a function of the reduced bias current for the two signs of I_N, when the noise source is biased on the back-bending branch (the five first panels on top figure) and well above the superconducting gap, at a larger current, where the asymmetry is already sizeable, typically $R_\Gamma - 1 \simeq 0.03$ (panel 6, for comparison).

Noise source biased on the supercurrent branch

Again on Sample JJD1, we measured the rate asymmetry with the noise source biased on the supercurrent branch. The asymmetry was measured using the same procedure, and appeared to be sizeable, even if the supercurrent was extremely small. On this branch, the sign of the asymmetry was opposite, as can be seen in Fig. 4.43.

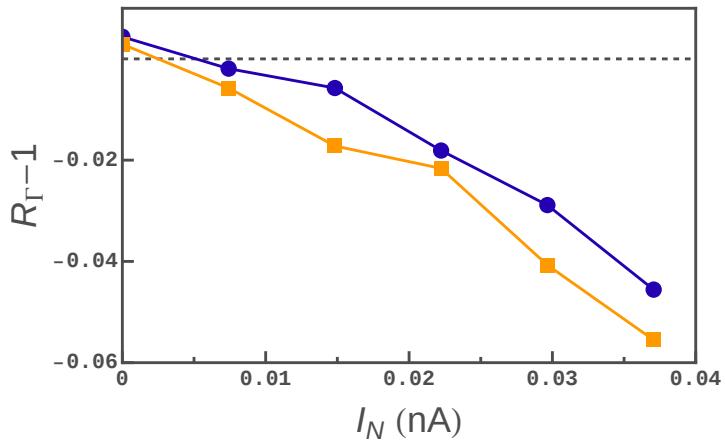

Fig. 4.43. Rate asymmetry $\langle R_\Gamma^+ \rangle$ (circles) and $\langle R_\Gamma^- \rangle$ (squares) measured when the noise source was biased on the supercurrent branch, thus for very low current. Note that the sign of the asymmetry is opposite to the one in Fig. 4.37.

It appeared moreover that when the noise source was biased on the supercurrent branch, the escape probability was not constant along the measurement time, as shown on the histogram in Fig 4.44. We checked at the opposite that, at the same escape probability but when the noise source was biased above the gap, the histogram appeared completely flat. Since an increased escape probability is observed at the beginning of the pulse when the tunnel junction is biased on the supercurrent branch, we checked that changing the rise time had no effect on the shape of the histogram. Overall, it appeared that the asymmetry on the supercurrent branch could not be meaningfully measured with our technique, and this phenomenon was not further investigated.

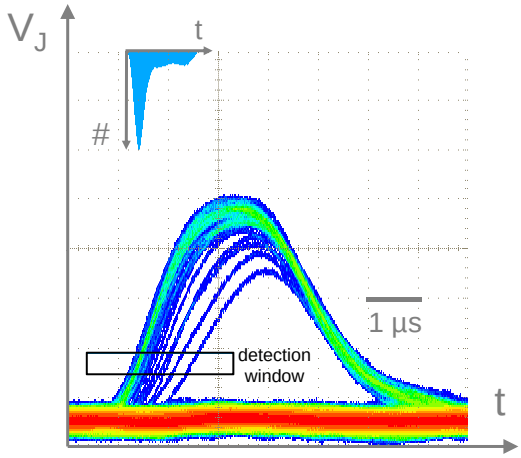

Fig. 4.44. Screen capture of the switching measurement when the noise source is biased on the supercurrent branch. On the top part, an histogram is shown as in Fig. 4.16 (beware that it is pointing downward). The pulse has been tuned to ensure that this histogram is flat when the noise source is not on the supercurrent branch (at low P). Surprisingly, this is not the case anymore here.

4.6 Perspectives

4.6.1 Controlling the frequency-dependence of the circuit

The experiments presented in this chapter confirmed the necessity to achieve a perfect control of the dynamics of the detector, especially the plasma frequency and the quality factor. A possibility to measure independently those parameters would be to use the resonant activation of the junction [61], a measurement that we could not achieve in this experiment due to a poor transmission of the biasing line at high frequency. However, even such a measurement would leave some uncertainty on the quality factor (see uncertainties in [51]), while this quality factor can enter in the expression of the rate asymmetry at the second power. Moreover, even having properly determined the dynamical parameters of the detection, the transfer function cannot be calibrated in situ, as was done in another use of a Josephson junction as an on-chip detector, but at much higher frequency [96]. One thus needs a better design of the circuit, in order to avoid spurious resonances that complicate the understanding.

Using the microwave simulation software Sonnet, we designed a new circuit for a next generation of experiments. In order to achieve a frequency independent transmission between the noise source and the detector, we reduced considerably the overall size of the circuit and especially the superconducting coupling loop between the noise source and the de-

tector, which tremendously affects the transfer function. The design presented in Fig. 4.45 has a transfer function whose magnitude stays in the range 1 ± 0.01 up to 10 GHz, and a real part of the admittance seen by the junction that decreases linearly with increasing frequency, up to 5% at 10 GHz. A sample using this new design, aiming at having a plasma frequency of the order of 5 GHz, is presently being fabricated by the group of N.O. Birge at Michigan State University, where the experiment will take place.

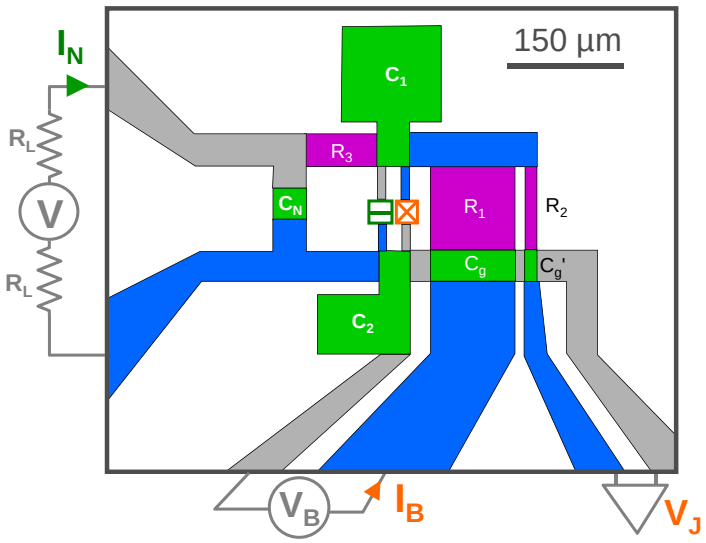

Fig. 4.45. The new design presented in this figure uses the notations of Fig.4.7. Two different layers of aluminium are used (here in gray and blue) and all the capacitors are formed at the overlap between them (shown in green). Resistors (shown in purple) are made with an additional layer. The design is performed assuming a surface capacitance of 0.015 pF/μm^2 and a sheet resistance for the resistors of 100 Ω per square.

4.6.2 Signal optimization

For further measurement, the amplitude of the signal can be enhanced by fine tuning the parameters. We derive here optimal parameters within the accessible range (set by the constraints presented in the beginning of this chapter). The main free parameters of the detection are the plasma frequency and the quality factor. In order to gain some insight on how the different parameters influence the rate asymmetry signal, we considered from Eq. (2.94):

$$R_\Gamma - 1 \propto S_3 \omega_{p0}^2 \frac{1}{T_{\text{eff}}^3} j(Q_0, s) \tag{4.53}$$

with $j(Q_0, s) \propto Q_0^2 (1-s)^{5/2}$ for low Q_0 and $j(Q_0, s) \propto (1-s)^2$ for high Q_0. Moreover one can modify Eq. (2.72) into:

$$T_{\text{eff}} \propto \frac{Q_0}{\omega_{p0}} S_2 \tag{4.54}$$

and we also considered, as was the case in the previous paragraph:

$$1 - s \propto \left(\frac{T_{\text{eff}}}{E_J} \right)^{2/3} = \left(\frac{Q_0}{\omega_{p0}^3} S_2 \right)^{2/3} \tag{4.55}$$

with $E_J \propto \omega_{p0}^2$. From this expression, one can evaluate the magnitude of the correction due to the third moment in two limits:

- In the low Q_0 limit:
$$R_\Gamma - 1 \propto \frac{S_3}{S_2^{4/3}} Q_0^{2/3} \tag{4.56}$$
therefore one has to *increase* the quality factor to improve the signal.
- In the high Q_0 limit:
$$R_\Gamma - 1 \propto \frac{S_3}{S_2^{5/3}} \omega_{p0} \frac{1}{Q_0^{5/3}}, \tag{4.57}$$
therefore one has to *decrease* the quality factor and increase the plasma frequency, down to the limit set both by the condition of thermal activation regime and the condition of $Q_0 \geq 3$ to avoid retrapping effects. An optimum is thus found in the intermediate range of quality factor, as was already noticed in [31], and as can be seen also in Fig. 3.10 where the rate asymmetry has been computed for various Q_0.

The underlying conclusion is that the quality factor should be low enough so that the increase of the effective temperature is small when the current in the noise source is increased, but one should remain in the underdamped limit. The plasma frequency, which can be seen as a bandwidth, should be increased as much as reasonably possible. Experimentally, three parameters are tuned for the detection : I_0, C_J and $R_{||}$. In order to grasp the role of each parameter, $R_\Gamma - 1$ as a function of I_N is shown by varying each one of them separately in Fig. 4.46.

- According to the requirements expressed in the beginning of this chapter, an optimum situation for the detection would be $I_0 \simeq 0.4\,\mu$A, and

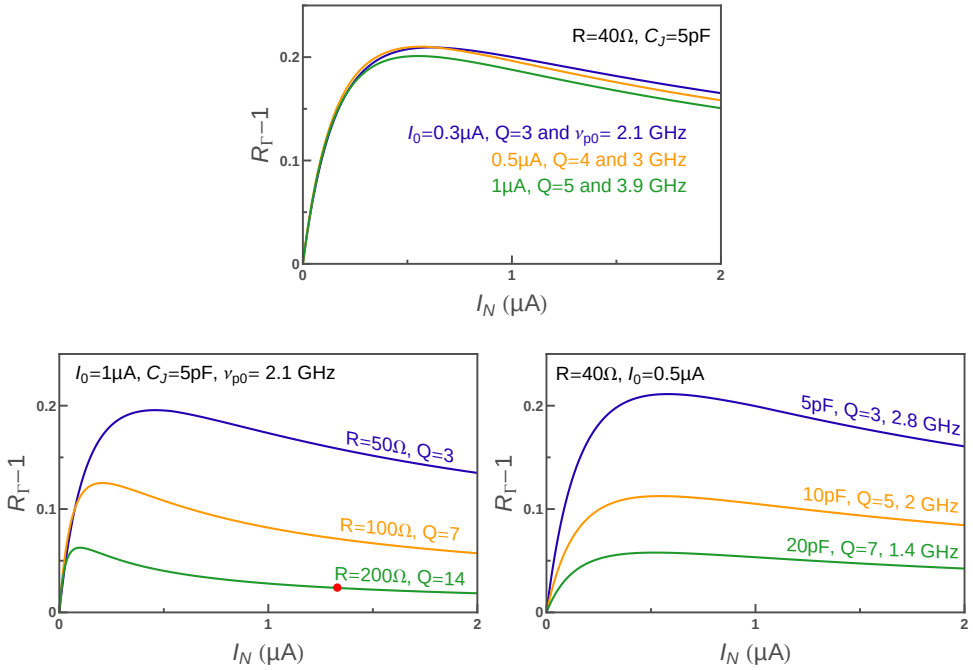

Fig. 4.46. Rate asymmetry obtained by varying one of the thee parameters : critical current, parallel resistance, or capacitor across the junction, and leaving the two other unchanged **Top:** Changing the critical current. **Left:** Changing the parallel resistance. The red dot represent the maximum I_N before reaching the retrapping regime. **Right:** Changing the capacitor across the junction.

$C_J \simeq 3$ pF and $R_{||} \simeq 50\,\Omega$ so that $\nu_{p0} \simeq 3.2$ GHz with a quality factor $Q_0 \simeq 3$. The rate asymmetry could thus reach a typical value of $R_\Gamma - 1 \simeq 0.2$, which is three times larger than in the present experiment for the same conditions.

- However, the best would be to increase the plasma frequency much more. But then, the detector junction would not be in a thermal activation regime at the lowest temperatures. Therefore, in order to stay in the thermal activation regime, the base temperature should be increased accordingly. Assuming that all measurements are performed with a fridge temperature being twice the cross-over temperature, the rate asymmetry could be as large as $R_\Gamma - 1 \simeq 1$ (15 times larger than in the present experiment) when increasing the plasma frequency to $\upsilon_{p0} \simeq 10$ GHz.

4.6.3 Towards the measurement of the Multiple Andreev Reflections

In the near future, this detector could be used to probe the noise of a superconducting point contact in the regime of Multiple Andreev Reflections (more details on the superconducting point contacts are found in the following chapters and in [19]). As probed experimentally in [25, 97] through the second moment of noise, the current when $V_N \leq 2e/\Delta$ in such systems results from the simultaneous tunneling of large packets of charges, "giant" shots with an increased number of charges when the bias voltage is decreased towards zero. For a single superconducting channel having a transmission τ, the predicted second and third moment of the noise [40] are shown in Fig. 4.47. Using a detector junction similar to the one used in this chapter would be sufficient to measure the third moment of noise for the large enough but not perfect transmission (typically higher than 0.4), as shown in Fig. 4.48. This would shed light on the interplay between the different contributions of the charge transmissions.

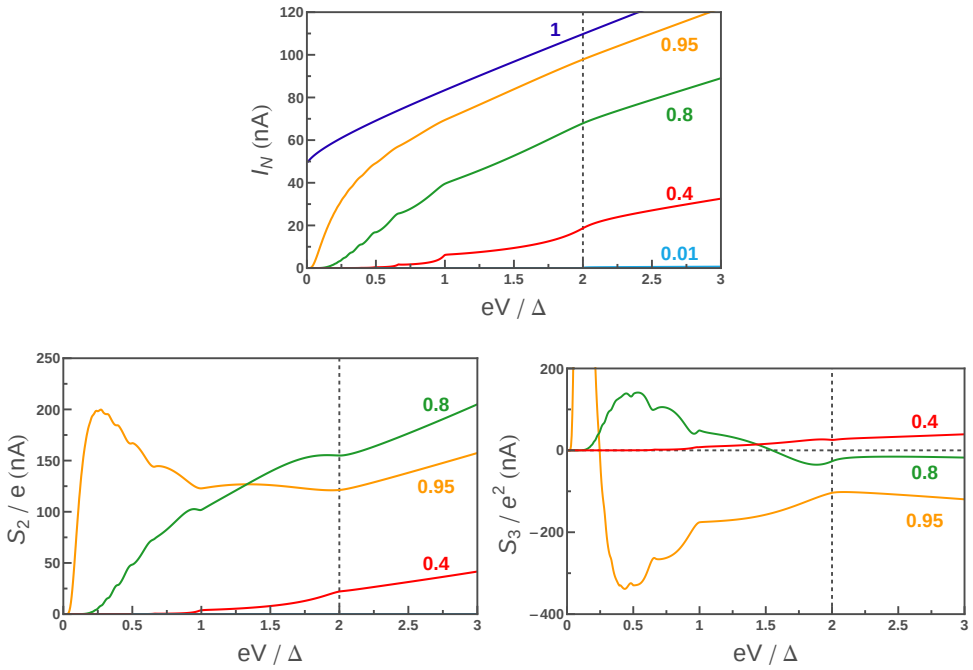

Fig. 4.47. Top: Current-voltage characteristics of a superconducting channel, for various transmissions. **Left:** Second moment of noise (the curves for the transmissions 0.01 and 1 are not shown, since the result is just very close to 0 everywhere). **Right:** Third moment of noise. (All curves were presented in [40]. Courtesy of J.C. Cuevas and W. Belzig)

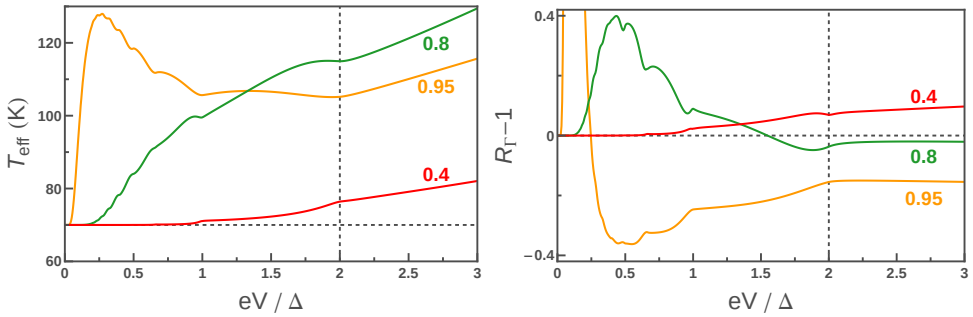

Fig. 4.48. Left: Predicted effective temperature for a detector junction $I_0 \simeq 0.4\,\mu$A, $C_J \simeq 3$pF and $R_{||} \simeq 50\Omega$ when the noise source is a single superconducting channel (three different values of the transmission are shown, see Fig. 4.47), with a base effective temperature of $T^0_{\rm eff} = 70\,$mK. **Right:** Expected rate asymmetry for the same parameters with the technique presented in this chapter.

Such an experiment might also allow to perform a measurement in the normal regime, with a point contact biased above the gap, playing the role of a normal QPC. One could think that this measurement could also be done directly with a QPC in a 2D electron gas, but these conductors present non-linearities of the conductance for voltage bias larger than $100\,\mu V$, and the corresponding current for a single channel (of the order of a few nA) would be too small for the present detection scheme. Note that this measurement was already performed by [81], but only in the regime $eV \leq k_B T$.

4.7 Conclusion

In this chapter, we presented the use of a JJ as a detector of the second and third moment of noise.

- We performed a measurement of the effect of shot noise arising from a tunnel junction on the escape rate of a JJ out of its zero-voltage state. The effect of the second moment of noise, that translates into an increase of the effective temperature of the escape, was quantitatively understood without any adjustable parameters by a microwave analysis of the circuit and simple harmonic approximation of the response of the detector. The effect of the third moment of the noise is linked to a rate asymmetry that was measured accurately over a large range of currents in the noise source. Due to the frequency dependence of the circuit, it is impossible to achieve a meaningful comparison between the measured rate asymmetry and the predictions that assumes only a white noise. It appears however that the measured behaviour is quali-

tatively well described by these simple predictions using an adjustable factor.

- D. Urban and H. Grabert generalized the theory presented in [11] to the frequency-dependent case, both for the spectral density of the noise and the environment of the detector, which allows a comparison with the measurement. Using this theory and a model circuit reproducing the frequency dependence of our sample, one obtains a quantitative understanding for both the effective temperature and the rate asymmetry. This confirms that the Josephson junction can be used as reliable detector for the second and third moment of noise.

- However, from the simulations performed in Chapter 3, it appears that a slight discrepancy can be found between the simulated rate and the predicted one, leaving some uncertainty on the predictions. Willing to further probe the theory without uncertainties, and being aware of the requirements on the circuit and its effect on the rate asymmetry, we designed a new setup to be frequency independent up to 10 GHz. This would allow both a comparison with the present analytical theories, facilitating the extraction of the third moment of the noise, and would also enable to increase the plasma frequency of the detector, therefore considerably improving the magnitude of the rate asymmetry signal.

- One should note also that the extreme sensitivity of the rate asymmetry to the plasma frequency and the quality factor (even through resonant activation), two parameters that can hardly be accessed with a large precision, explains the difficulty to extract in a reliable way the third moment of noise from the rate asymmetry.

- As for moments at order higher than three, it appears that, at least for the present setup, that it is not possible to access any of them. As a last word, one can signal that a solution might come from other setups that have been envisioned [41, 69] to access either directly the fourth cumulant or the FCS by measuring the tail of the distribution.

Asymmetric Noise Probed with a Josephson Junction

Q. Le Masne,[1] H. Pothier,[1,*] Norman O. Birge,[2] C. Urbina,[1] and D. Esteve[1]

[1]*Quantronics group, Service de Physique de l'Etat Condensé (CNRS URA 2464), CEA-Saclay, 91191 Gif-sur-Yvette, France*

[2]*Department of Physics and Astronomy, Michigan State University, East Lansing, Michigan 48824, USA*

(Received 10 November 2008; published 10 February 2009)

Fluctuations of the current through a tunnel junction are measured using a Josephson junction. The current noise adds to the bias current of the Josephson junction and affects its switching out of the supercurrent branch. The experiment is carried out in a regime where switching is determined by thermal activation. The variance of the noise results in an elevated effective temperature, whereas the third cumulant, related to its asymmetric character, leads to a difference in the switching rates observed for opposite signs of the current through the tunnel junction. Measurements are compared quantitatively with recent theoretical predictions.

DOI: 10.1103/PhysRevLett.102.067002 PACS numbers: 85.25.Cp, 72.70.+m, 73.23.−b, 74.50.+r

The current through voltage-biased electrical conductors exhibits fluctuations, which, in contrast to equilibrium Johnson-Nyquist noise, are not symmetric with respect to the average current. This translates into finite odd cumulants in the distribution of the number of electrons transferred through the conductor in a given time. Whereas the full counting statistics of this number can be calculated for arbitrary conductors [1,2], up to now high order cumulants have been measured in very few experiments. The third cumulant has been successfully accessed by signal processing the time-dependent current [3–5], but with setups that are restricted either to low impedance samples, which leads to large environmental effects [3], or to low frequencies [4,5]. As an alternative strategy, Tobiska and Nazarov [6] proposed to use a Josephson junction (JJ) as a large bandwidth on-chip noise detector [7–9]. It has a high intrinsic sensitivity, and can be coupled to noise sources over a large range of impedances. The detection principle relies on the exponential current sensitivity of the switching of a JJ from a metastable zero-voltage branch to a dissipative one. When biased at a current I_J slightly below its critical current I_0, the rate of switching is therefore very sensitive to noise in the current. The first detection of asymmetric noise with a JJ was reported in Refs. [7,8]. However, the JJ detector, which was placed in an inductive environment, had a very large plasma frequency, and the dynamics of the junction changed regime as the noise intensity increased, from macroscopic quantum tunneling (MQT) to retrapping [10] through thermal activation. The measured asymmetry in the escape rates could only be compared to an adiabatic model [11], using empirical parameters. For a detector to be of practical use it must have a well characterized and a simple enough response, so that information on the noise can be reliably extracted. As quantitative theories have been developed for a JJ in the thermal regime placed in a resistive environment [12–14], we designed an experiment in this framework, allowing for a detailed, quantitative comparison with theory.

The principle of our experiment is to add the current noise from a noise source to the dc bias current of a JJ (see Fig. 1). The dynamics of a JJ placed in a resistive environment are described by the resistively and capacitively

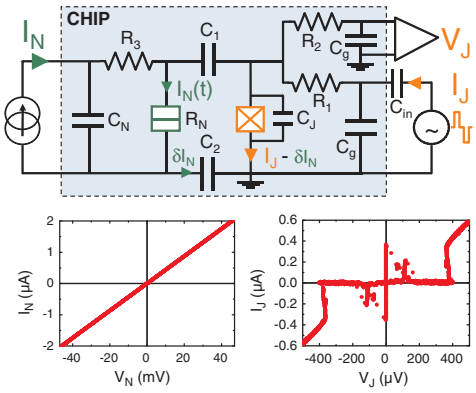

FIG. 1 (color online). Top: Experimental setup. Noise from a tunnel junction (green double box) biased at dc with a current I_N couples through capacitors $C_1 = 230$ pF and $C_2 = 345$ pF to a Josephson junction (JJ) detector (orange crossed box), which is current-biased on its supercurrent branch. The voltage V_J across the junction monitors the switching to the dissipative state. Capacitor $C_J = 12.5$ pF lowers the JJ plasma frequency to $\omega_{p0}/2\pi \simeq 1.5$ GHz. Capacitors $C_N = 190$ pF and $C_g = 140$ pF shunt the external impedance at ω_{p0}, so that the impedance across the JJ is determined only by on-chip elements. Resistors $R_1 = R_3 = 215\ \Omega$ and $R_2 = 515\ \Omega$ were fabricated with thin Cr films. Bottom left: IV characteristic of the tunnel junction, linear at this scale, with inverse slope $R_N = 22.9\ \mathrm{k}\Omega$. Bottom right: IV characteristic of the JJ detector, with critical current $I_0 = 437$ nA. We attribute a resonance near $V_J \sim 120\ \mu$V to a mode of the electromagnetic environment of the junction.

shunted junction (RCSJ) model [15], with the voltage related to the average velocity of a fictitious particle placed in a tilted washboard potential. The tilt of the potential is determined by the reduced parameter $s = I_J/I_0$. At $s < 1$ the potential presents local minima where the particle can be trapped. The voltage is then zero: this corresponds to the supercurrent branch. The frequency of small oscillations is called the plasma frequency ω_p. Johnson-Nyquist current noise related to the finite temperature T of the environment of the junction is modeled as a fluctuating force on the particle, which triggers escape from the local minimum ("switching"). When $k_B T > \hbar\omega_p/2\pi$, the switching rate Γ is given by Kramer's formula [16] $\Gamma = A \exp[-B_2(T)]$ with $A \simeq \omega_p/2\pi$ for moderate quality factors Q, $\omega_p = \omega_{p0}(1 - s^2)^{1/4}$ the plasma frequency in the tilted potential, $\omega_{p0} = \sqrt{I_0/\varphi_0 C_J}$ the bare plasma frequency determined by the capacitance C_J and critical current I_0 of the junction, with $\varphi_0 = \hbar/2e$, and

$$B_2(T) = (4\sqrt{2} I_0 \varphi_0/3k_B T)(1 - |s|)^{3/2}. \quad (1)$$

Recently, this result was extended to the situation in which an additional delta-correlated noise $\delta I_N(t)$, characterized by a finite third cumulant S_3 defined by $\langle \delta I_N(t)\delta I_N(t')\delta I_N(t'')\rangle = S_3\delta(t' - t)\delta(t'' - t')$ and a second cumulant $\langle \delta I_N(t)\delta I_N(t')\rangle = S_2\delta(t' - t)$ adds to the current through the JJ [12–14]. The effect of higher order cumulants is assumed to be weak. The corresponding fluctuating force leads to a modification of the rate: $\Gamma = A \exp\{-[B_2(T_{\rm eff}) + B_3]\}$. The second cumulant yields an increased effective temperature $T_{\rm eff}$ given by

$$2k_B T_{\rm eff}/R_{\|} = 2k_B T/R + S_2. \quad (2)$$

Here, R is the parallel combination of all the resistances which produce Johnson-Nyquist noise across the junction. The resistance $R_{\|}$ characterizes the friction acting on the fictitious particle and is, in a simple model, given by the total resistance across the junction, including both R and the resistance R_N of the noise source. This expression indicates that the second cumulant of noise from the noise source S_2 simply adds to the Johnson-Nyquist noise of the rest of the circuit. The third cumulant gives rise to the additional term

$$B_3 = -S_3(\varphi_0/k_B T_{\rm eff})^3 \omega_{p0}^2 j(s) \quad (3)$$

with $j(s)$ a function of the tilt that depends on the quality factor [14]. When reversing the sign of the average current I_N through the noise source, S_2 remains unchanged whereas S_3 changes sign. Therefore, the departure from 1 of the rate ratio

$$R_\Gamma = \Gamma(+I_N)/\Gamma(-I_N) = \exp(2|B_3|) \quad (4)$$

is a measure of nonsymmetric noise ($S_3 \neq 0$).

The experimental setup is shown schematically in Fig. 1. As it is well established that current noise through a tunnel junction is Poissonian ($S_2 = e|I_N|$ and $S_3 = e^2 I_N$, with e the electron charge), we use such a device (green double box) as a benchmark noise source. The JJ detector (orange crossed box) is coupled to it through capacitors C_1 and C_2. The finite frequency part δI_N of the current through the tunnel junction $I_N(t)$ flows through the JJ detector, owing to the high-pass filter formed by R_3, C_1 and C_2 (3 dB point at 5 MHz). The switching of the JJ current-biased at I_J is signaled by the appearance of a voltage V_J across it. The low plasma frequency of 1.5 GHz guarantees $k_B T > \hbar\omega_p/2\pi$ even at the lowest temperature of our experiment (20 mK) [17]. In the relevant range of frequencies slightly below $\omega_{p0}/2\pi$, numerical simulations of the actual circuit indicate that the quality factor of the Josephson oscillations Q is close to 5, insuring an underdamped dynamics, and no effect of retrapping [7,10] as long as $s \gg 4/\pi Q \simeq 0.25$.

The sample was fabricated on a thermally oxidized high resistivity (10^3 to 10^4 Ω cm) Si wafer. All on-chip resistors are 10 nm-thick Cr layers, with 215 $\Omega/\square$ sheet resistance at 4 K, placed between mm-size pads. Capacitors were obtained from parallel aluminum films separated by 29 nm-thick sputtered silicon nitride as an insulator [18]. The tunnel junction and the JJ detector were fabricated at the same time by shadow evaporation of 20 nm and 80 nm-thick aluminum films. Their current-voltage characteristics are shown in Fig. 1. The tunnel junction has an area of 0.09 μm^2 and a tunnel resistance $R_N = 22.9$ kΩ. It was biased at voltages larger than twice the superconducting gap $2\Delta/e = 0.4$ mV (which corresponds to $I_N = 0.02$ μA), so that it behaves as a normal metal junction, with Poissonian noise. The JJ detector, with area 1 μm^2, has a supercurrent $I_0 = 0.437$ μA. It was biased in series with a resistor $R_1 = 215$ Ω through a 50 Ω coaxial line equipped with attenuators. When switching occurs at a supercurrent $I_{\rm sw}$, the voltage across the junction jumps to $(R_1 + 50\ \Omega)I_{\rm sw} < 2\Delta/e$, so that the current through it drops to zero and no quasiparticles are generated. Moreover, gold electrodes in good contact with the Al films were fabricated a few μm away from the junctions in order to act as traps for spurious quasiparticles [19] that could be excited by the high frequency noise. Apart from the Cr resistors and the Au traps, all conductors on the chip are superconducting aluminum films.

The sample was thermally anchored to the mixing chamber of a dilution refrigerator. The tunnel junction was biased by a floating voltage supply through two 1.5 MΩ resistors. The on-chip capacitance $C_N = 190$ pF on the bias line is large enough to maintain the voltage across the tunnel junction at $V_N = R_N I_N$ for all relevant frequencies. Escape rates of the JJ were measured using 2×10^5 current pulses of duration $\tau = 0.53$ μs with alternatively positive ($+I_J$) and negative ($-I_J$) amplitude, separated by 9 μs. They were fed through a nonpolarized capacitor $C_{\rm in} = 200$ μF placed at room temperature, which prevents dc thermoelectric currents from unbalancing the pulses. The switching rates Γ_+ and Γ_- for the two signs of I_J were deduced from the switching probability $P = 1 - e^{-\Gamma\tau}$

measured as the fraction of the current pulses which led to a voltage pulse.

We first demonstrate that the switching of the detector junction is well described by the model of thermal activation whatever the current in the noise source. Figure 2(a) shows, for various currents $I_N > 0$, the s dependence of $B^{2/3} = [-\ln(\Gamma/A)]^{2/3}$. Data fall on straight lines that extrapolate to 0 for $I_J = I_0$, as expected from Eq. (1). This allows us to extract an effective temperature $T_{\rm eff}$, whose dependence on I_N is shown in Fig. 2(b), with data taken at four different base temperatures T. We do find a linear dependance with correct extrapolations at $I_N = 0$ (values slightly above T are attributed to imperfect filtering), as expected from Eq. (2) with $S_2 = eI$. Understanding the slope quantitatively requires an accurate model of the actual circuit at microwave frequencies: the RCSJ model assumes that the JJ is simply connected to a capacitor, a resistance $R_\parallel$ and a current source, in parallel. In the limit $Q \gg 1$, $R_\parallel$, which describes friction, has to be replaced

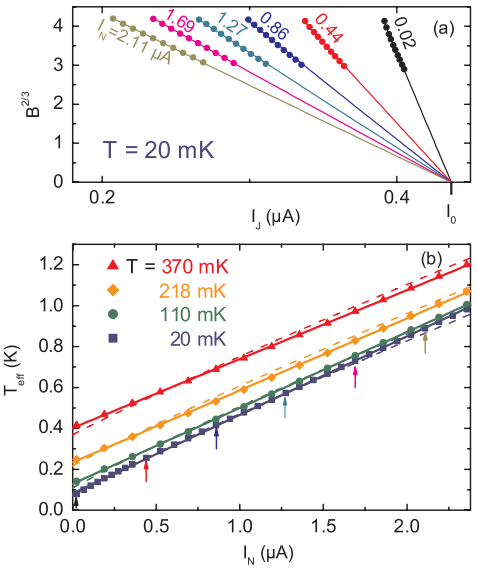

FIG. 2 (color online). (a) Dependence of $B^{2/3} = (-\log(\Gamma/A))^{2/3}$ on the current I_J through the JJ detector, for data taken at $T = 20$ mK and currents through the tunnel junction $I_N = 0.02$ to 2.11 μA, by steps of 0.42 μA. Linear dependence is a signature of the thermal activation regime. (b) Effective temperature extracted from the slope of data sets as in (a), as a function I_N, for various temperatures T. Arrows indicate the data points corresponding to the plots in (a). Solid lines are linear interpolations. Dashed line are the predictions from full theory, taking into account the frequency dependence of the admittance $Y(\omega)$ across the JJ and of the transfer function $\alpha(\omega)$ from noise source to JJ detector.

with $R_\parallel(\omega_p) \equiv 1/\mathrm{Re}(Y(\omega_p))$, with $Y(\omega)$ the total admittance of the circuit across the JJ. Microwave simulations indicate that $R_\parallel(\omega_p)$ varies almost linearly from 63 Ω at 1 GHz to 36 Ω at 1.5 GHz, and that a current $I_N(\omega)$ through the tunnel junction leads to a current $\alpha(\omega)I_N(\omega)$ through the JJ detector, with a transfer function $\alpha(\omega)$ varying from 1.1 at 1 GHz to 1.27 at 1.5 GHz. Since escape is determined essentially by the noise at ω_p, we replace S_2 by $\alpha^2(\omega_p)eI_N$. Altogether, the prediction $T_{\rm eff} \simeq T + \alpha^2(\omega_p)R_\parallel(\omega_p)eI_N/2k_B$ is in agreement with the data (see dashed lines in Fig. 2; to fit the 20 mK data, we used $T = 72$ mK), apart from the slight change in slope when varying T which could be attributed to variations in the kinetic inductance of the superconducting electrodes.

We now discuss the effect of noise asymmetry. The $B^{2/3}$ plots for opposite signs of the current through the noise source are undistinguishable within the symbol size, demonstrating that the effect of the second cumulant S_2 is dominant. In the limit $eV_N \gg k_BT$, theory predicts that the effect of S_3 is to shift the curves by $\Delta I_J \sim 0.6B(\omega_{p0}/Q)(S_3/S_2) = 0.6Be/R_\parallel C_J \sim 0.2\% I_0$, which is difficult to measure reliably [20]. In our experiment, we measured directly the asymmetry ratio R_Γ defined by Eq. (4), which varies by several percent (see Fig. 3). We first set the amplitude I_J of the current pulses at a value corresponding to a switching probability $P \sim 0.6$, for which the statistical precision on the rates is good [21]. We then measured 100 times Γ_+ and Γ_-, with alternatively $+I_N$ and $-I_N$ through the noise source. This allows for two independent measurements of R_Γ: $R_\Gamma^+ = \Gamma_+(-I_N)/\Gamma_+(+I_N)$ and $R_\Gamma^- = \Gamma_-(+I_N)/\Gamma_-(-I_N)$ [22]. In Fig. 3(a), we show with full and open symbols the corresponding measurements. The rate ratio R_Γ differs from 1, a signature of asymmetric noise, as soon as $I_N \neq 0$. The statistical uncertainty on R_Γ is smaller than the symbols. Small differences between R_Γ^+ and R_Γ^-, in particular around $I_N = 2$ μA, are not understood. As for the comparison with theory, a difficulty arises because of the frequency dependence of the transfer function $\alpha(\omega)$, which results in a colored third cumulant at the detector $S_3(\omega_1, \omega_2) = \alpha(\omega_1)\alpha(\omega_2 - \omega_1)\alpha(-\omega_2)e^2I_N$. In the following, and in the absence of indication as to which frequencies are important, we compare however with the only existing theory, which assumes white noise ($S_3 = e^2I_N$). The corresponding predictions, Eqs. (3) and (4) with $j(s) \simeq 0.81(1-s)^{2.14}$ [23], are shown as solid lines in Fig. 3(a), scaled by an arbitrary factor 1.5. R_Γ exhibits a maximum as a function of I_N due to the opposite variations of S_3 and $T_{\rm eff}$ with I_N. For $T_{\rm eff}$, we used interpolations between the measured values shown in Fig. 2. When scaled up by 1.5, which might be due to frequency dependent transmission $[\alpha(\omega)]$, theory accounts well for the experimental data. Feedback corrections due to the detector, described in [13], are neglected since $R_\parallel/R_N \ll 1$ [14]. Note that there is no feedback associated to the series resistance R_3 like in Ref. [3] because the current noise associated to R_3 does

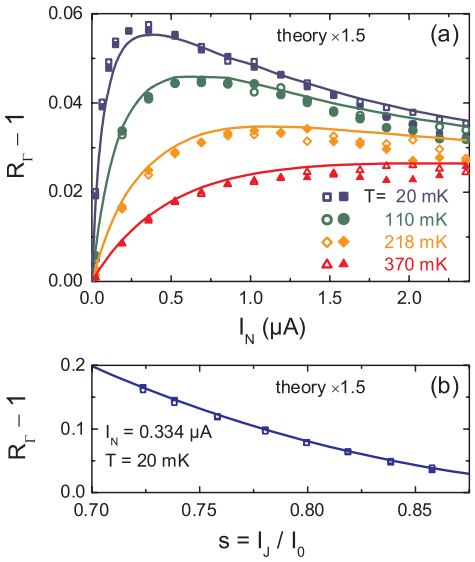

FIG. 3 (color online). (a) Rate asymmetry $R_\Gamma - 1$ as a function of current in noise source I_N for various temperatures T. Filled (open) symbols correspond to measurements with positive (negative) current through the JJ detector. Solid lines are theoretical predictions scaled by a factor 1.5. (b) Dependence of $R_\Gamma - 1$ on $s = I_J/I_0$, at $I_N = 0.334$ μA, obtained with measurement pulses of various lengths. Solid line is theoretical prediction scaled by 1.5.

not flow through the noise source, but through the JJ detector. In Fig. 3(b), we also compare with theory the s dependence of R_Γ. In order to perform this measurement, we used pulses of various durations (0.53 to 21 μs), which allows us to obtain the switching rates at different values of s. For the longest pulses, the rate asymmetry is as large as 16%. Here also, theory scaled by 1.5 accounts precisely for the data.

Qualitative agreement between experiment and theory gives confidence for the use of the JJ as a measuring device for S_3, even if the application to a wider range of systems requires some theory for colored noise. A limitation concerns situations with strong nonlinearities in the voltage dependence of the cumulants, where feedback effects could become sizeable [24,25]. For quantitative measurements of S_3 on other systems, it is not only important to tune the plasma frequency of the junction in the GHz range as done in this work, but also to improve the microwave design, in particular with more compact electrodes, so as to avoid frequency dependent factors in the analysis. Proposals to access the full counting statistics with a JJ embedded in more complex circuits [6] remain to be investigated.

We acknowledge technical support from Pascal Senat and Pief Orfila, and discussions with B. Huard, H. Grabert, B. Reulet, J. Ankerhold, and within the Quantronics group. Work supported by ANR contracts Electromeso and Chenanom, and Region Ile-de-France for the nanofabrication facility at SPEC. N. O. B. acknowledges support by NSF Grant No. DMR-0705213.

*Corresponding author: hugues.pothier@cea.fr

[1] L. S. Levitov and G. B. Lesovik, JETP Lett. **55**, 555 (1992).
[2] Y. Nazarov, Ann. Phys. (Leipzig) **16**, 720 (2007).
[3] B. Reulet, J. Senzier, and D. E. Prober, Phys. Rev. Lett. **91**, 196601 (2003).
[4] Yu. Bomze *et al.*, Phys. Rev. Lett. **95**, 176601 (2005).
[5] G. Gershon *et al.*, Phys. Rev. Lett. **101**, 016803 (2008).
[6] J. Tobiska and Yu. V. Nazarov, Phys. Rev. Lett. **93**, 106801 (2004).
[7] A. V. Timofeev *et al.*, Phys. Rev. Lett. **98**, 207001 (2007).
[8] J. T. Peltonen *et al.*, Physica E (Amsterdam) **40**, 111 (2007).
[9] B. Huard *et al.*, Ann. Phys. (Leipzig) **16**, 736 (2007).
[10] V. I. Mel'nikov, Phys. Rep. **209**, 1 (1991).
[11] In the regime of thermal activation, the predictions of this adiabatic model disagree by a factor 6 with those of the complete theories of Refs. [12–14].
[12] J. Ankerhold, Phys. Rev. Lett. **98**, 036601 (2007); **99**, 139901 (2007).
[13] E. V. Sukhorukov and A. N. Jordan, Phys. Rev. Lett. **98**, 136803 (2007).
[14] H. Grabert, Phys. Rev. B **77**, 205315 (2008). We corrected for a minus sign missing in Eqs. (78,92).
[15] A. Barone and G. Paterno, *Physics and Applications of the Josephson Effect* (Wiley, New York, 1982).
[16] For a review, see J. Ankerhold, *Quantum Tunneling in Complex Systems* (Springer, Berlin, 2007).
[17] The asymmetry signal increases with the detection bandwidth determined by ω_p. However, it becomes more difficult to achieve a frequency-independent coupling.
[18] The results of the experiment described in Ref. [9] were presumably dominated by a leakage in capacitors.
[19] P. Joyez *et al.*, Phys. Rev. Lett. **72**, 2458 (1994).
[20] In Ref. [7], the effect of S_3 was detected as the shift ΔI_J. According to theory and using the parameters given by the authors, the expected shift would have been much larger than observed, had the thermal activation regime been achieved.
[21] The expression for the uncertainty on R_Γ in Ref. [9] should be divided by $\sqrt{2}$.
[22] The signs in front of I_N account for the fact that in our setup, the noise current *subtracts* from the bias current.
[23] This analytical expression interpolates between the results of numerical calculations of $j(s)$ performed for $Q \sim 5$ and in the working interval $0.5 < s < 0.9$, along the lines of Ref. [14] [H. Grabert (private communication)].
[24] In measurements with the noise source biased near $V = 2\Delta/e$, where the IV characteristic is very nonlinear, we found strong asymmetries in the switching rates.
[25] D. F. Urban and H. Grabert, arXiv:0810.2938.

Part II

Probing Andreev States in superconducting atomic contacts

Chapter 5

Josephson effect and Andreev states

In this chapter, we review the description of the Josephson effect in terms of Andreev bound states. Having introduced the theoretical framework in which the Andreev states are relevant, we describe experiments probing the Josephson effect in atomic contacts between two superconducting electrodes. At the beginning of this thesis work, the dc supercurrent and in particular the current-phase relation had already been measured in the Quantronics group [20], and found to be in quantitative agreement with predictions. Most of the results could be satisfactorily accounted for by just considering the contribution of the ground Andreev state of the different conductions channels characterizing the contact. As a first step towards the spectroscopy of the two Andreev levels of a channel, we conducted a new series of similar measurements. We retrieved the previous results and completed the theoretical description to account for finite temperature effects corresponding to the thermal population of the Andreev states. We also observed, in slightly different samples developed for the spectroscopy measurements, new behaviors which, although not really understood, point to a possible role of the excited Andreev levels.

5.1 Andreev Bound States

In the Landauer formalism describing coherent transport in terms of independent conduction channels [98], the origin of the pair of Andreev states appearing in a short, clean, and coherent channel[1] between two

[1] This signifies that the channel characteristic length L is in the limit $L \ll \xi, l_e, L_\phi$ where $\xi = \hbar v_F/\Delta$ is the superconducting coherence length, l_e the elastic mean free path and L_ϕ the phase coherence length. In the case L exceeds ξ, more than one pair of states can exist.

superconducting electrodes is particularly simple to grasp in the case of a perfectly transmitted (or "reflectionless") channel ($\tau = 1$), as illustrated in Fig. 5.1 [16].

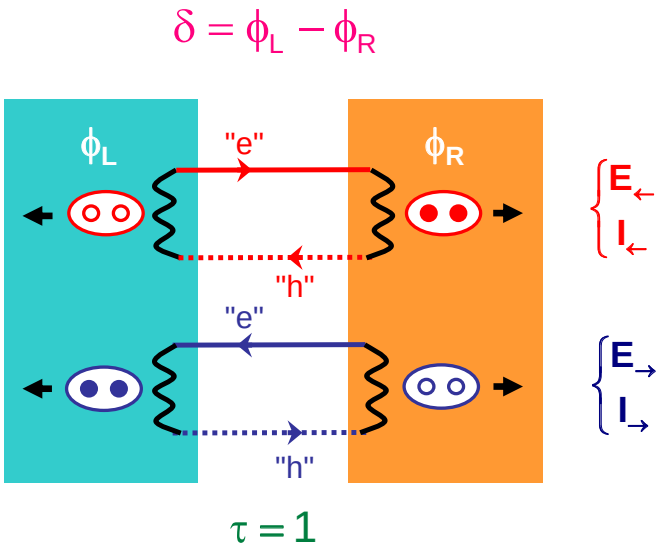

Fig. 5.1. Schematic representation of the two Andreev bound states in a short reflectionless channel connecting two superconducting electrodes with different phases ϕ_L and ϕ_R. The wiggly lines represent an Andreev reflection in which an electron (hole) is reflected as a hole (electron) acquiring the local superconducting phase. The upper (lower) loop corresponds to the transfer of Cooper pairs to the right (left).

A right-moving electron is Andreev reflected at the right interface, with some probability amplitude dependent on its energy, into a left-moving hole at the same energy and a Cooper pair is transferred to the electrode [13]. It also acquires a phase shift corresponding to the phase of the local superconducting order parameter. In turn, this left-moving hole is Andreev reflected as a right-moving electron at the left electrode, leading to the destruction of a Cooper pair. These successive reflections interfere constructively, like in a Fabry-Pérot interferometer, when the phase shift acquired along one round-trip is an integer multiple of 2π. A similar process occurs for left-moving electrons reflected as right-moving holes. From theses two processes, two resonant quasiparticle states appear in the channel region, with energies:

$$E_{\rightleftarrows}(\delta) = \mp\Delta \cos\frac{\delta}{2}\mathrm{sgn}\left[\sin\frac{\delta}{2}\right], \tag{5.1}$$

symmetric with respect to the Fermi level and lying within the superconducting energy gap, as shown in Fig. 5.2.[2]

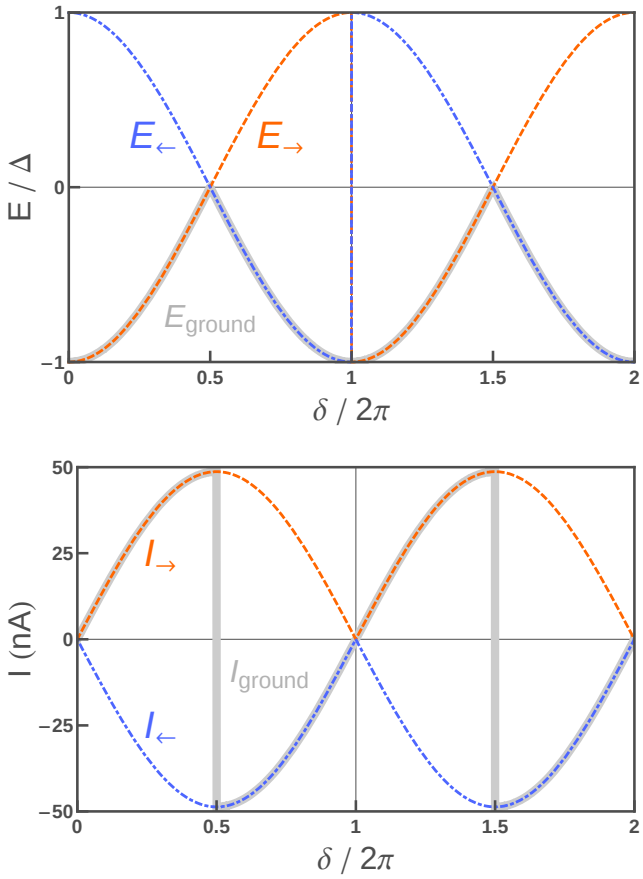

Fig. 5.2. Top: Energies $E_{\rightleftarrows}(\delta)$ of the two Andreev states in a reflectionless channel from Eq. (5.1) (dashed lines). Global ground state energy (solid thick line). **Bottom:** Supercurrent $I_{\rightleftarrows}(\delta)$ carried by the two Andreev states in a reflectionless channel from Eq. (5.4), calculated for $\Delta = 200\,\mu$eV (dashed lines). Ground state supercurrent (solid thick line).

In fact, these two states are detached from the continuum of states with its well-known gap edge singularities at $\pm\Delta$ and the local density of states is:

$$n(E)/n_F = \frac{1}{2}\,|E/\Delta|\sqrt{\left(\frac{E}{\Delta}\right)^2 - 1}\,\frac{1}{(E/\Delta)^2 - 1 + \sin^2\frac{\delta}{2}}, \tag{5.2}$$

[2] The "leaky" Andreev levels described in [99] outside the gap are neglected in the limit $L \ll \xi$.

where n_F is the density of states at the Fermi level in the normal state.[3] This DOS is depicted in Fig. 5.3.

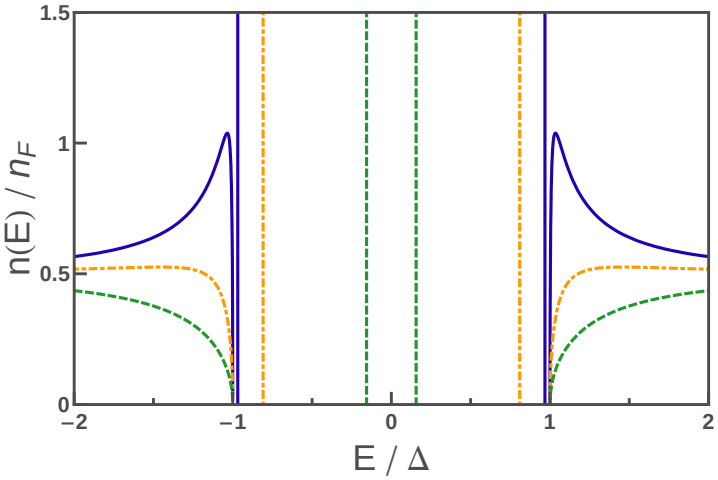

Fig. 5.3. Local density of states at the atomic contact for a single reflectionless channel at $\delta = 0.08, 0.2, 0.45$ (blue solid, orange dashed-dotted, and green dashed). The vertical lines represent the reflectionless levels within the superconducting gap (see [45] for details).

These two reflectionless Andreev states, noted $\{|\rightarrow\rangle, |\leftarrow\rangle\}$, carry opposite supercurrents[4] given by:

$$I_{\rightleftarrows} = \frac{1}{\varphi_0}\frac{\partial E_{\rightleftarrows}}{\partial \delta} = \pm\frac{e\Delta}{\hbar}\sin\frac{\delta}{2}. \tag{5.4}$$

At zero temperature, only the state of lower energy is occupied. Since the two reflectionless levels cross at $\delta = \pi$, the state $|\rightarrow\rangle$ is occupied for $0 \leq \delta \leq \pi$ and the state $|\leftarrow\rangle$ is occupied for $\pi \leq \delta \leq 2\pi$, resulting in a ground state energy:

$$E_{\text{ground}}(\delta) = -\Delta\left|\cos\frac{\delta}{2}\right|. \tag{5.5}$$

The current carried by the channel in this ground state is:

$$I_{\text{ground}}(\delta) = \frac{1}{\varphi_0}\frac{\partial E_{\text{ground}}}{\partial \delta} = \frac{e\Delta}{\hbar}\text{sgn}\left(\cos\frac{\delta}{2}\right)\sin\frac{\delta}{2}. \tag{5.6}$$

[3] This formula is extended to the case of channel of transmission τ smaller than 1 as:

$$n(E)/n_F = \frac{1}{2}|E/\Delta|\sqrt{\left(\frac{E}{\Delta}\right)^2 - 1}\frac{1+\sqrt{1-\tau}}{(E/\Delta)^2 - 1 + \tau\sin^2\frac{\delta}{2}}. \tag{5.3}$$

[4] positive currents are counted from left to right.

This ground state current is the dc Josephson current in a single reflectionless channel, shown in Fig. 5.2.

If the channel is not perfectly transmitted ($\tau < 1$), a right-moving electron in the state $|\leftarrow\rangle$ can also be simply reflected as a left-moving electron in the state $|\rightarrow\rangle$, as depicted in Fig. 5.4. The existence of this finite reflection probability thus couples the two reflectionless states, therefore lifting the degeneracy at $\delta = \pi$. The two resulting states, denoted $\{|-\rangle, |+\rangle\}$, are called the "adiabatic Andreev states". They will often be referred simply as the "Andreev states" in what follows, and have energies $E_\pm$ shown in Fig. 5.5:

$$E_\pm(\delta, \tau) = \pm\Delta\sqrt{1 - \tau \sin^2\left(\tfrac{\delta}{2}\right)}. \tag{5.7}$$

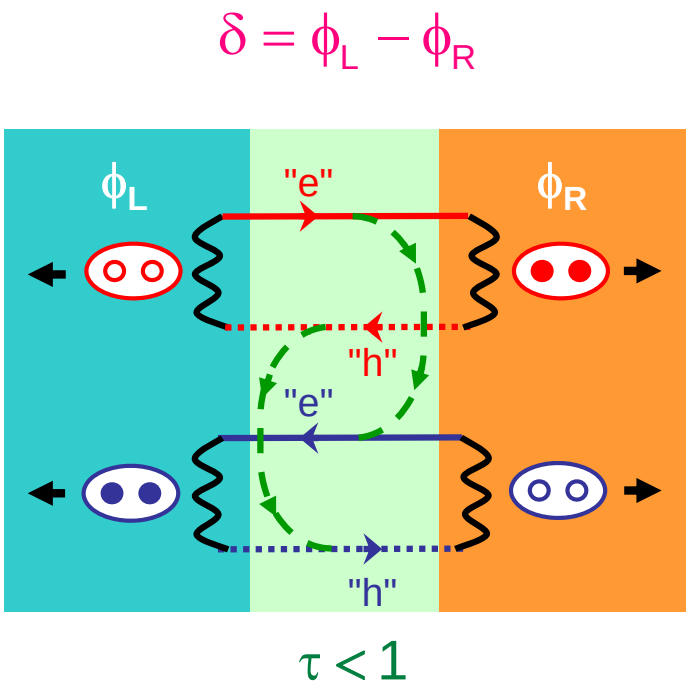

Fig. 5.4. Schematic representation of the scattering mechanisms in a short reflective channel. In addition to the Andreev reflection processes (black wiggly lines), a normal reflection process (green dashed lines) connects electron (hole) states traveling in different directions, thus mixing the two reflectionless states of Fig. 5.1. This gives rise to the "adiabatic Andreev states".

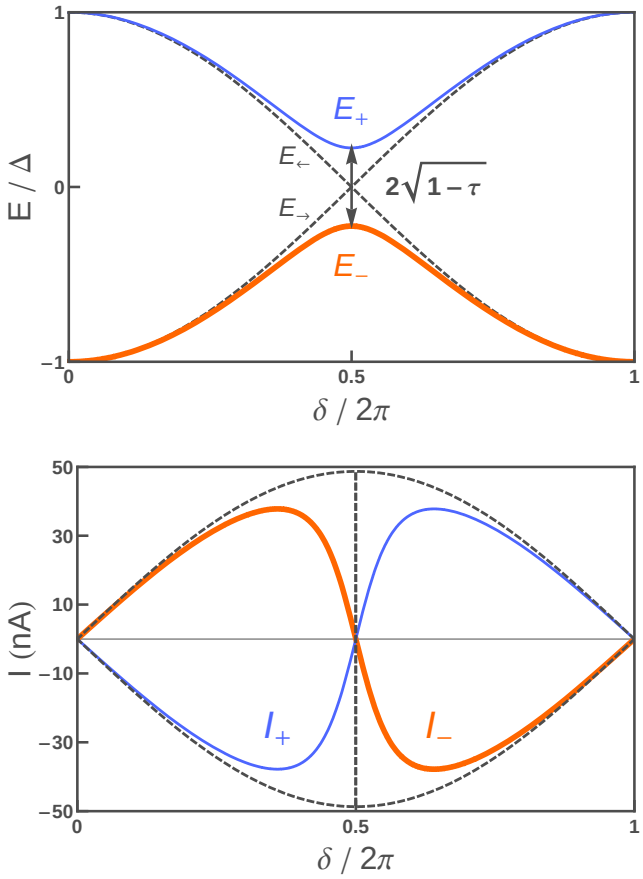

Fig. 5.5. Top: Adiabatic Andreev levels in a single channel of transmission $\tau = 0.97$ (solid curves) compared to the reflectionless ones (dashed curves). **Bottom:** Supercurrent carried by the upper (I_+) and lower (I_-) state calculated for $\Delta = 200\ \mu$eV compared to the reflectionless currents (dashed curves).

For a single channel of transmission τ, the frequency corresponding to the transition between the two states, called the "Andreev gap" and plotted in Fig. 5.6, is given by:

$$\nu_A(\delta) = \frac{\Omega_A(\delta)}{2\pi} = \frac{2\Delta}{h}\sqrt{1 - \tau \sin^2\left(\frac{\delta}{2}\right)}. \tag{5.8}$$

It presents a minimum at $\delta = \pi$:

$$\boxed{\nu_A(\pi) = \tfrac{2\Delta}{h}\sqrt{1-\tau}.} \tag{5.9}$$

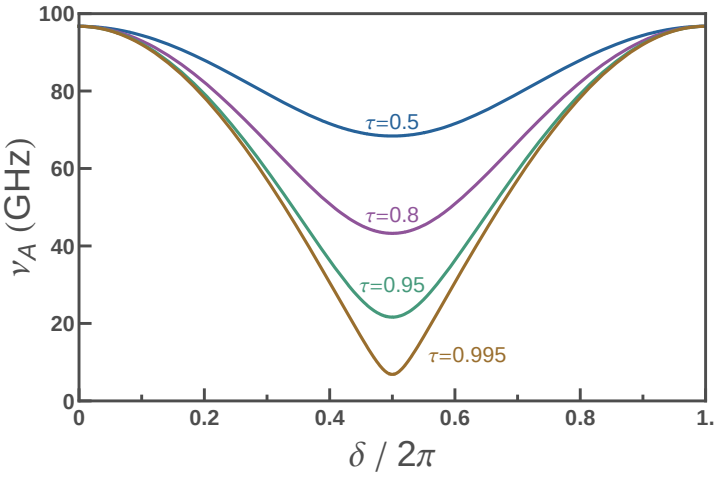

Fig. 5.6. Andreev gap as a function of the phase difference (from Eq. (5.8)), for aluminum single channel contacts of various transmissions, calculated for $\Delta = 200\ \mu$eV.

Because the number of transferred charges and the phase difference are conjugated variables [46], the corresponding supercurrents[5], shown in Fig. 5.5, are given by:

$$I_{\pm}(\delta) = \frac{1}{\varphi_0}\frac{\partial E_{\pm}(\delta)}{\partial \delta} = \mp\frac{e\Delta}{2\hbar}\frac{\tau \sin\delta}{\sqrt{1-\tau\sin^2\left(\frac{\delta}{2}\right)}}. \tag{5.10}$$

This corresponds to the dc Josephson effect in a phase-biased single channel of arbitrary transmission. In aluminum, where the superconducting gap Δ is typically of the order of 200 μeV, this current reaches at most $\simeq 50$ nA for the perfectly transmitted case.

When the structure is voltage-biased at small voltages $V \ll \Delta/e$, the phase varies linearly with time at a small speed $\dot{\delta} = V/\varphi_0$, and the Andreev levels move adiabatically within the superconducting gap Δ. As the motion is periodic, there is no energy transfer to the system on average and a purely ac current flows. This corresponds to the ac Josephson effect.

[5] The well-known sinusoidal Josephson relation for a tunnel junction is recovered by assuming a coupling structure consisting of a large collection of channels having all a vanishing transmission $\tau_i \ll 1$. In this case, the normal tunnel conductance is given by $G_N = \frac{1}{R_N} = \frac{2e^2}{h}\sum\tau_i$. Considering all channels, the current-phase relation can then be written

$$I(\delta) = \frac{e\Delta}{2\hbar}\sum_i \tau_i \sin\delta = I_0 \sin\delta,$$

where the critical current I_0 corresponds to the Ambegaokar-Baratoff expression [47] of Eq. (B.94).

To describe the general dynamics of the phase, one requires to consider the Hamiltonian of the system, and not only its energy levels. Restricting the system to just the two Andreev states, a two-level Hamiltonian $\mathcal{H}_{AS}$ has been introduced [17, 100, 101]. In the basis of the reflectionless states $\{|\leftarrow\rangle, |\rightarrow\rangle\}$, the Hamiltonian $\mathcal{H}^0_{|\rightleftarrows\rangle}$ is:

$$\begin{aligned}\mathcal{H}^0_{|\rightleftarrows\rangle}(\delta) &= \Delta \begin{pmatrix} \cos\frac{\delta}{2} & \sqrt{1-\tau}\sin\frac{\delta}{2} \\ \sqrt{1-\tau}\sin\frac{\delta}{2} & -\cos\frac{\delta}{2} \end{pmatrix} \\ &= \Delta \left[\cos\frac{\delta}{2}\hat{\sigma}_z + \sqrt{1-\tau}\sin\frac{\delta}{2}\hat{\sigma}_x\right] \end{aligned} \tag{5.11}$$

where we have introduced Pauli matrices $\hat{\sigma}_z$ and $\hat{\sigma}_x$ (see Appendix B.5 for details). This form of the Hamiltonian derives from the perturbation of the reflectionless states with a coupling term $\sqrt{1-\tau}\sin\frac{\delta}{2}$ between them. As the role of the continuum of states has been completely neglected, this Hamiltonian can only be valid close to $\delta = \pi$, where the states lie deep in the superconducting gap. By performing a rotation of the eigenbasis presented in Appendix B.5, one obtains the Hamiltonian $\mathcal{H}^0_{AS}$ in the basis of the Andreev states $\{|+\rangle, |-\rangle\}$:

$$\mathcal{H}^0_{AS}(\delta) = \begin{pmatrix} E_+ & 0 \\ 0 & E_- \end{pmatrix} = \frac{h\nu_A(\delta)}{2}\hat{\sigma}_z^{AS}, \tag{5.12}$$

where we introduced the new Pauli matrix $\hat{\sigma}_z^{AS}$. The physics of the system is therefore similar to the one of a spin 1/2 in a magnetic field, and the appropriate conceptual framework is thus the one of Nuclear Magnetic Resonance [102].

5.2 An experimental test-bed: superconducting atomic contacts

In order to probe these theoretical predictions, experiments have been performed on a very simple kind of system: atomic-size contacts between two superconducting electrodes (for a review, see [19]). Such a situation fulfills the criterion of a short, ballistic and coherent system. The number of conducting channels in a one atom contact is small, essentially determined by the number of valence orbitals of the species under consideration [103]. Moreover, the transmission of the channels are tunable over a broad range, and can be determined with great accuracy [18]. This set of transmission determines all the properties of the conductor [98], and is therefore usually coined the Personal Identity Number of the con-

tact [19, 44]. For these reasons, atomic contacts constitute a test-bed for mesoscopic physics [44].

In the Quantronics group we use the mechanically controllable break junction technique [104, 105], applied on micro-fabricated bridges [106], to create contacts of a few or even one atom. A suspended metallic thin-film microbridge (usually aluminum) is broken at cryogenic temperature by bending the macroscopic substrate on which it has been fabricated. The two resulting electrodes are then gently brought back into contact.

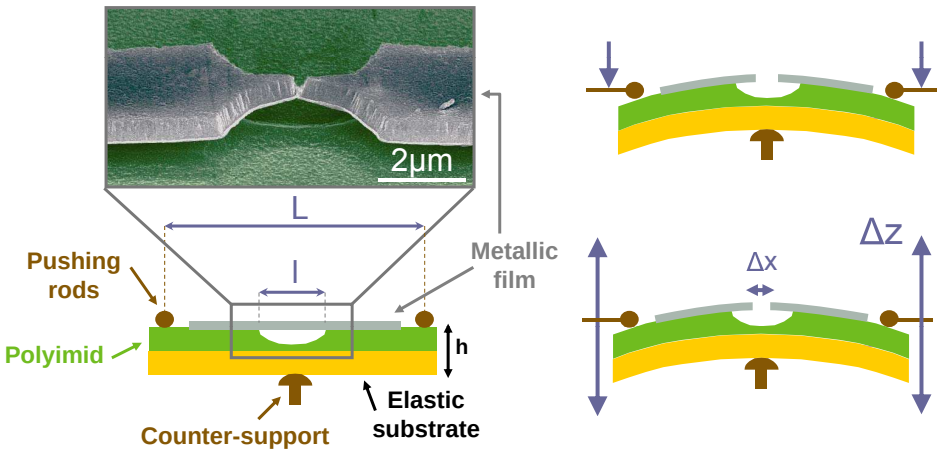

Fig. 5.7. Principle of the microfabricated break-junction technique. A thin microfabricated metallic bridge, suspended over a distance $l \simeq 2\mu$m, is broken by bending the elastic substrate (of thickness $h \simeq 500\ \mu$m) on which it was fabricated. The bending is achieved using a three-points mechanism, with a central counter-support and two pushing rods separated by $L \sim 16$ mm. A relative vertical displacement Δz of the pushing rods, corresponds to a change of the distance between the electrodes $\Delta x \simeq r\Delta z$ where $r = 6hl/L^2$ is of the order of 10^{-4} in typical experiments. Δz can be easily adjusted at the micron level, and the displacement between electrodes Δx is therefore controlled at the level of 100 pm or better [19, 44].

As compared to atomic contacts obtained for example with an STM tip [107], this technique has two major advantages:

- It provides very stable contacts (weeks at low temperatures)
- The contacts can be integrated in well defined on-chip circuits, an essential factor to address the physics of the Josephson effect.

If the electrodes are superconducting, the $I(V)$ characteristics provide a tool to extract the transmissions of all channels. The probability amplitude of the Multiple Andreev Reflections (MAR) processes, that are responsible for the current at finite voltage, are highly-non linear functions of the transmission, as was calculated in [108, 109, 110]. The predicted $I(V)$ curves are shown in Fig. 5.8 for a few values of the transmission.

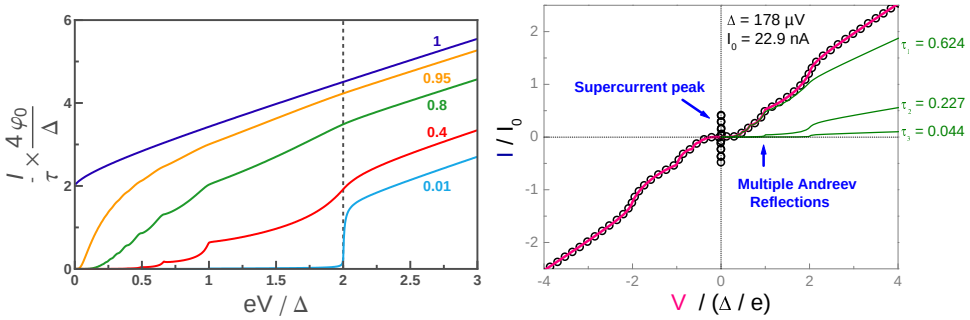

Fig. 5.8. Left: Theoretical $I(V)s$ for a single superconducting channel for various transmissions. **Right:** Example of an experimental $I(V)$ characteristics fitted by adding the contributions of three channels. This procedure yields the separate transmission of each channel.

Using the curves tabulated for each transmission, a fit of the experimental $I(V)$ characteristics of a superconducting atomic-sized contact allows to extract the number of channels and the unique set of transmissions $\{\tau_i\}$ describing the properties of the contact [18, 44], as is shown in Fig. 5.8. The fitting is performed using a Monte Carlo procedure that Gabino Rubio, from the Universidad Autónoma de Madrid, has kindly made available to us [111].

The uncertainty on the transmissions obtained by this fitting procedure depends of course on the uncertainty in the measurement of both voltage and current, and on the transmission of the channels participating in the contact. Typically, for channels with a large transmission the relative uncertainty achieved on τ_i is of the order of 0.1%. For channels having low transmissions ($\tau < .05$), this procedure fails to disentangle the contributions of the different channels, and yields a large error bar (see Chapter 1 of [44] for more details).

5.3 Supercurrent in atomic contacts

5.3.1 Supercurrent in current-biased contacts

The study of the Andreev states in superconducting atomic contacts started in the Quantronics group with the measurement of the dc supercurrent.

- In [112], the maximum supercurrent was accessed by measuring the switching current of current-biased contacts. In this case, the phase was not an externally tunable parameter, but a dynamical variable subject to random fluctuations. As in the experiments the dissipation, and thus the fluctuations, were under control, the results could be

compared with the predictions of the RCSJ model (see Chapter 2). The measured switching current could be well understood by considering just the contribution of the ground Andreev state of each channel, for all contacts containing channels with transmissions $\tau < 0.9$. However, for transmissions above this value, the measured switching currents were significantly above the expected ones. These deviations were attributed to non-adiabatic transitions (Landau-Zener type) to the upper state across the small Andreev gap. At that time only an ad-hoc model was proposed, which required an unrealistically high transition probability to explain the data. However, very recently Fritz and Ankerhold have developed a theory that takes into account the stochastic dynamics of the phase [113], which predicts, with reasonable values of the parameters, the appearance of switching currents higher than expected by the adiabatic theory. In any case, these experiments were the first to support convincingly the idea that the supercurrent is carried by the Andreev states.

- This idea was further supported by the excellent agreement found between theory and experiment concerning the crossover between the supercurrent branch and the dissipative MAR branch for voltage-biased contacts, presented in [114]. This crossover can be understood in terms of Landau-Zener transitions between the bottom and the upper Andreev states.

However, these experiments were actually only an indirect test of the prediction of Eq. (5.10), since the phase was not an external parameter that could be swept over its entire range. Although they constituted a significant step for the description of the mesoscopic Josephson effect in terms of Andreev states, the need for a direct measurement of the current-phase relation was clear.[6]

5.3.2 Supercurrent in phase-biased contacts

This was achieved by using a new setup which permits to either phase or voltage bias an atomic contact in a reversible manner [20, 36, 45]. In this way both the current-phase relation and the $I(V)$ characteristics could be measured for the very same atomic contact. Using the transmissions $\{\tau_i\}$ obtained from the $I(V)$, a quantitative agreement without any adjustable parameters was obtained between the measured and the expected current-phase relation.[7] This comparison was performed by just

[6] For a review on current-phase relations in Josephson systems, see [115].

[7] Koops *et al.* had already observed in 1996 a non-sinusoidal current-phase relation for Nb atomic contacts, but a quantitative comparison with theory could not be achieved at that time, since the transmissions of the channels $\{\tau_i\}$ were not measured simultaneously [116].

taking into account the contribution of the lower Andreev state of each channel.

5.4 Current-phase relation of well-characterized contacts

We now present measurements of the current-phase relation performed during this thesis using essentially the same technique as presented in the previous paragraph [20]. The results presented in this section were obtained on a sample, referred to further as Sample AC1, whose parameters are listed in Table 5.1. Several atomic contacts were tested on this sample with similar results.

5.4.1 Experimental setup

Measuring both the current-phase relation of an atomic contact and its $I(V)$ characteristics requires contradictory conditions:

- For the former, one needs to phase-bias the atomic contact. To do so, the atomic contact must be placed in a small superconducting loop and the flux threading the loop fixes the phase.
- For the latter, one needs to voltage-bias the same atomic contact, which cannot be achieved if it is shunted by the superconducting loop.

To fulfill both conditions, one must be able to open and close this loop *in situ* with a *reversible superconducting switch*. The setup presented in Fig. 5.9, which is related to the one of the Quantronium [117], uses a Josephson junction in this role. The atomic contact and the Josephson junction are embedded in a small superconducting loop, forming a device that was coined the "Atomic SQUID". The junction not only allows both biasing configurations; it is used to measure the loop current.[8] The critical current of the Josephson junction is chosen to be much larger than the one of a typical aluminum one-atom contact (~ 50 nA), so that the Atomic SQUID essentially behaves like a slightly perturbed Josephson junction.

5.4.2 Determining the transmissions of the channels in the contact

The $I(V)$ characteristics of the atomic contact denoted $I_{\mathrm{AC}}(V)$, especially the dissipative MAR current flowing when the bias voltage is smaller than $2\Delta/e$, has to be analyzed to deduce the number of channels and their

[8] Similar and related setups were used in [118, 119].

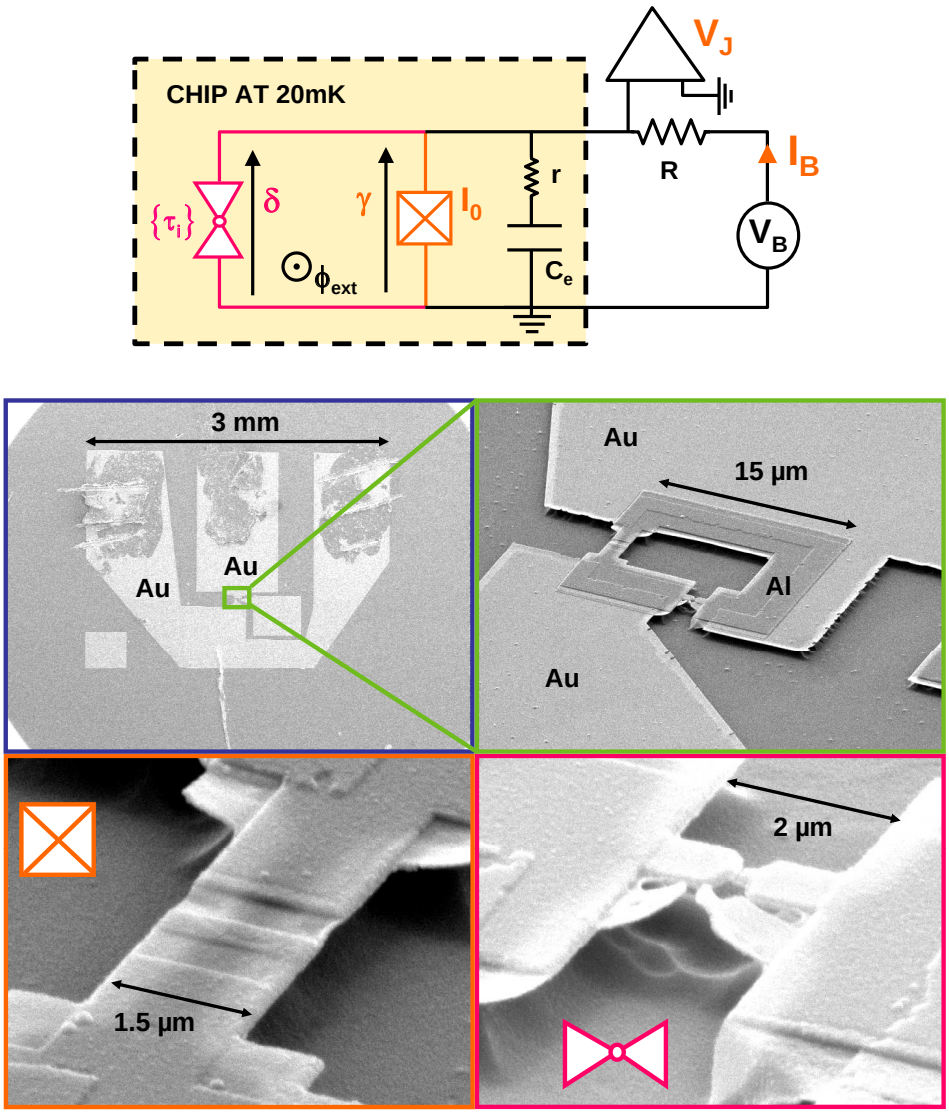

Fig. 5.9. Top: An aluminum atomic contact in parallel with a Josephson junction having a large critical current $I_0 = 310$nA forms an "Atomic SQUID". An on-chip capacitor $C_e \simeq 20$pF lowers the plasma frequency of the junction to 1.1 GHz and its associated spurious resistance $r \sim 0.5\,\Omega$ damps the dynamics of the phase to ensure a stable switching process. The Atomic SQUID is biased through a resistor $R = 200\,\Omega$ by a current I_B, and the voltage V_J across it is monitored to detect switching. **Bottom:** SEM micrographs of Sample AC1 at different scales. In the upper-right panel, the brighter pads are gold electrodes, while the darker part constituting the loop are made out of aluminum. The whole structure is deposited on top of a polyimide layer on a metallic substrate. The gold electrodes form the shunting capacitor C_e through the metallic substrate, and also act as quasiparticle traps (see Part III for details). The junction (lower-left panel) is fabricated with a double-angle evaporation through a suspended mask, which results in a parasitic metallic bridge of no importance, seen on the bottom-right panel.

Parameter	Sample AC1
Critical current I_0	310 nA
Capacitor C_e	$\simeq$ 20 pF
Plasma frequency ν_{p0}	$\simeq$ 1.1 GHz
Loop inductance L_L	$\simeq$ 10 pH

Table 5.1. Parameters of Sample AC1 presented in this section.

transmissions $\{\tau_i\}$. It is obtained from the $I(V)$ of the Atomic SQUID $I_{\mathrm{ASQUID}}(V)$. In principle, in the region at finite voltage below the superconducting gap $V \leq 2\Delta/e$, the current of the Atomic SQUID should correspond just to the one through the atomic contact, since the DC current flowing through the junction is expected to be zero. In practice however, a sizable current is observed experimentally in this region in the characteristics $I_{\mathrm{JJ}}(V)$ of the junction alone, which can be measured when the metallic bridge forming the atomic-size contact is fully open. This spurious current, which we think is related to resonances in the environment, leads to significant differences between $I_{\mathrm{AC}}(V)$ and $I_{\mathrm{ASQUID}}(V)$ in the region below the gap. Assuming that $I_{\mathrm{JJ}}(V)$ is not affected by the contact, $I_{\mathrm{AC}}(V)$ is then obtained by the subtraction:

$$I_{\mathrm{AC}}(V) = I_{\mathrm{ASQUID}}(V) - I_{\mathrm{JJ}}(V), \tag{5.13}$$

which is then fitted using the MAR theory to obtain the transmissions. The full procedure is illustrated for a particular atomic contact on Sample AC1 in Fig. 5.10.

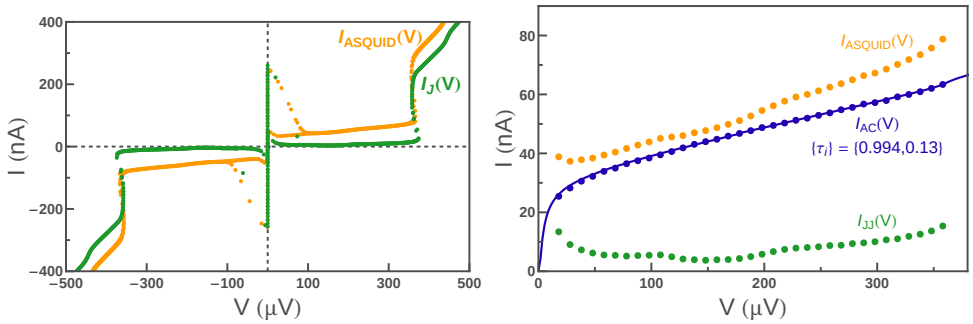

Fig. 5.10. Description of the procedure followed to extract the transmissions of the atomic contact in an Atomic SQUID. **Left:** Current-voltage characteristics of the Atomic SQUID $I_{\mathrm{ASQUID}}(V)$ and of the JJ alone $I_{\mathrm{JJ}}(V)$ (measured when the contact is completely open). **Right:** The same two curves and their difference $I_{\mathrm{AC}}(V)$, which corresponds to the atomic contact characteristics, in the range $0 \leq V \leq \frac{2\Delta}{e}$ (Eq. (5.13)). The best fit using MAR theory (solid line) yields the gap $\Delta = 183\,\mu$eV and the set of transmissions $\{0.994\,;\,0.13\}$.

5.4.3 Principle of the current-phase relation measurement

The superconducting loop allows to impose a phase difference across the atomic contact by applying an external magnetic flux ϕ_{ext}. If the loop is sufficiently small so that the screening flux can be neglected[9], the phase differences γ (across the tunnel junction) and δ (across the atomic-size contact) are linked through the external flux:

$$\delta = \gamma + \frac{\phi_{\text{ext}}}{\varphi_0} \equiv \gamma + \varphi, \tag{5.14}$$

where φ is the reduced flux threading the loop.

At zero temperature, the large Josephson junction switches out of its zero-voltage state for a phase difference $\gamma = \frac{\pi}{2}$ (a current I_0 flows through the junction). Assuming that the contributions of the junction and of the atomic contact can be separated, the critical current I^0_{ASQUID} of the Atomic SQUID is the sum of the critical current I_0 of the junction and of the flux-dependent critical current $I_{\text{AC}}(\delta)$ of the atomic contact:

$$I^0_{\text{ASQUID}}(\varphi) = I_0 + I_{\text{AC}}(\frac{\pi}{2} + \varphi). \tag{5.15}$$

Measuring the flux dependence of the critical current of the Atomic SQUID is thus a direct way to probe the current-phase relation of the atomic contact. In practice however, one measures the mean switching current of the Atomic SQUID, rather than its critical current.

5.4.4 Modulation of the switching current

Measurement technique

In the experiment, the mean switching current is determined accurately through the escape rate Γ, obtained itself from the escape probability P. The latter is measured using a train of bias-current pulses[10] for various values of the external flux and counting the number of pulses for which a voltage appears across the Atomic SQUID (as already described in Chapter 4 for a simple JJ). We plot in Fig. 5.11 the escape probability as a function of both the bias current and the flux. Clearly, the escape probability evolves very rapidly from 0 to 1 in a narrow range

[9] The geometric inductance L_L of the loop, typically 10 pH [120] is chosen so that it is negligible as compared to the inductance of both the Josephson junction $L_J \simeq 1$ nH and the atomic contact $L_{\text{AC}} \simeq 10$ nH. In this way, the phase drops essentially only across these two last elements.

[10] The pulses are as described in Chapter 4. Here, we used pulses with a duration $\tau_p = 1\,\mu$s of the measurement pulse (of height I_B), a sustain time $\tau_{\text{sus}} = 3\,\mu s$ and pulses were repeated every $t_{\text{signal}} = 50\,\mu s$.

of bias current which depends on the applied flux. In the following, we simply present the reduced bias current $s^*(\varphi) = I_B/I_0$ leading to an escape probability $P = 0.5$ (corresponding to a rate $\Gamma = 0.69$ MHz). This normalized switching current $s^*(\varphi)$ curve will be referred to as the (normalized) modulation curve.

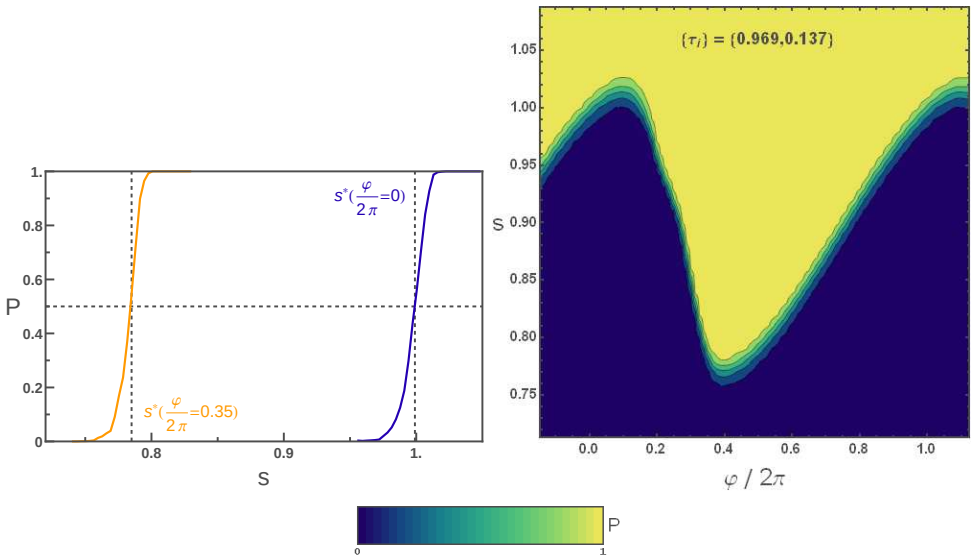

Fig. 5.11. Left: Escape probability for Sample AC1 as a function of the reduced bias current, for two values of the external flux. The two vertical dashed lines correspond to the reduced current $s^*(\varphi)$ leading to a escape probability $P = 0.5$. **Right:** Escape probability as a function of both the bias current and the flux.

Comparison with the current-phase relation

To explain the evolution of the escape probability in Fig. 5.11, a simple model is to consider, by analogy with Eq. (5.15), that the switching current of the Atomic SQUID is given by the sum of the switching current of the junction alone $I_{\rm sw}$ and of the current-phase relation of the atomic contact:

$$s^*_{\rm simple}(\varphi) \times I_0 = I^{\rm sw}_{\rm ASQUID}(\varphi) = I_{\rm sw} + I_{\rm AC}(\frac{\pi}{2} + \varphi). \tag{5.16}$$

In Fig. 5.12, the measured $s^*(\varphi)$ is compared with the predictions of this model, where $I_{\rm sw} = 0.89 \times I_0$ was measured when the contact was completely open. The agreement between the measured modulation curve and this simple model is good over most of the flux range, but clear deviations can be seen for flux values around $\varphi = \frac{\pi}{2}$. In order to completely

understand the measurements, one needs to consider the full dynamics of the phase in the potential of the Atomic SQUID.

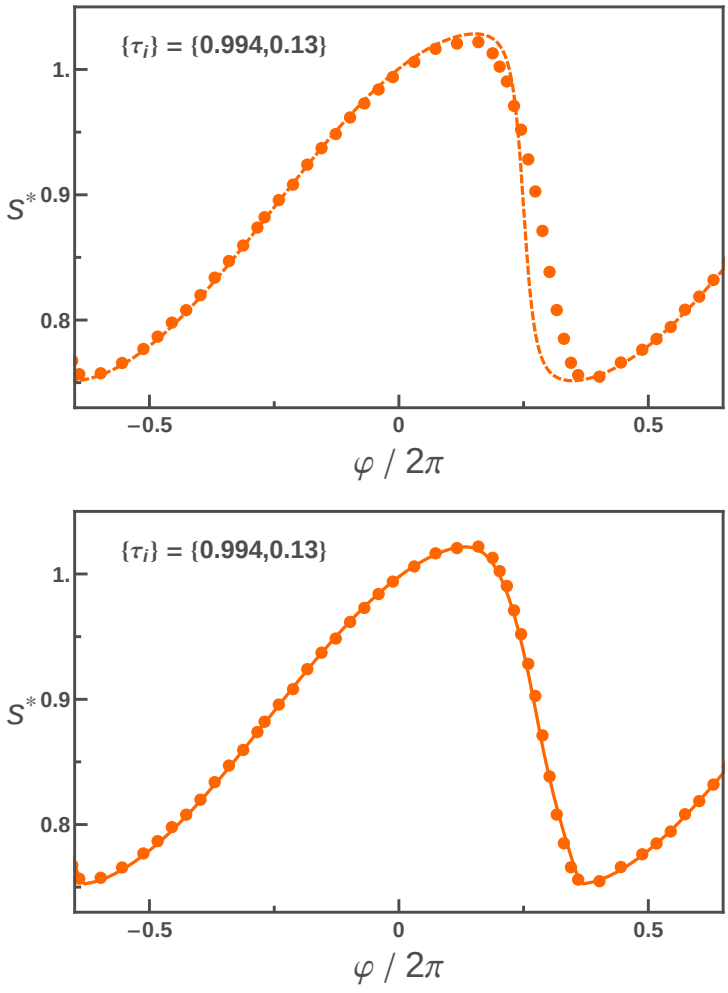

Fig. 5.12. Top: Measured (**symbols**) reduced bias current $s^*(\varphi)$ corresponding to an escape probability $P = 0.5$ as a function of the reduced flux threading the loop, for a contact having two channels of transmissions $\{0.994, 0.13\}$, in Sample AC1. The **dashed line** is the expected switching current $s^*_{\rm simple}$ of the Atomic SQUID (normalized to the critical current of the junction), predicted by the simple model of Eq. (5.16): it corresponds to the atomic contact contribution (the sum of the currents from the lower Andreev states of all channels), shifted horizontally by $\pi/2$ and vertically by the average switching current of the junction, measured independently. **Bottom:** Same experimental data. The **solid line** is the prediction $s^*_{\rm thy}(\varphi)$ of the full theory taking into account the complete potential $U_-(\varphi)$ of the Atomic SQUID and an effective temperature of 80 mK (measured independently on the junction alone).

Comparison with a model based on the complete phase dynamics

In the limit where the phase differences are linked by Eq. (5.14), the dynamics of the Atomic SQUID reduces to a one-variable problem similar to the Josephson junction presented in Chapter 1. This situation is described by a Langevin equation, with a force term that has three contributions: the bias current, the current through the Josephson junction and the current $I_A(\delta)$ through the atomic contact. This force derives from a potential given by:

$$\begin{aligned} U_-(\gamma) &= U_0(\gamma) + E_-(\gamma+\varphi) \\ &= -E_J[\cos(\gamma) + s\gamma] - \Delta\sum_i \sqrt{1-\tau_i \sin^2\frac{(\gamma+\varphi)}{2}}, \end{aligned} \quad (5.17)$$

where we used $I_A = \frac{1}{\varphi_0}\frac{\partial E_-}{\partial \delta}$, which assumes a low enough temperature to take only into account the contribution of the lower Andreev state (this hypothesis is discussed in Sec. 5.4.5). Hence, the potential is the sum of the contributions U_0 from the junction (E_J is the Josephson energy) and E_- from the lower Andreev state of the atomic contact. Using the mechanical analogy, one describes the phase dynamics as the motion of a particle in this modified tilted washboard potential. The particle is submitted to the random force corresponding to the Johnson-Nyquist noise of the resistor R. The noise associated to fluctuations of the population of Andreev states [121] is neglected at low temperature. The evaluation of the escape rate of the Atomic SQUID performed further is valid only if $E_J \gg \Delta$, in which case the modifications introduced by the atomic contact to the potential are small and the expressions for the escape out of the zero-voltage state given in Chapter 2 hold true for the Atomic SQUID.

In the experiment, the plasma frequency of the Atomic SQUID is reduced down to 1.1 GHz by a large capacitor C_e in parallel (see Fig. 5.9 and Table 5.1). With such a low plasma frequency, the escape out of the zero-voltage state occurs through thermal activation at all experimental temperatures, with a quality factor close to 5 (more details on a similar setup can be found in [36]).

The modulation curve is predicted assuming the escape rate is given by Eq. (2.30):

$$\Gamma \propto \exp\left[-\Delta U_-(s,\varphi)/k_B T_{\text{eff}}\right], \quad (5.18)$$

where ΔU_- is the barrier height for the Atomic SQUID. Neglecting the role of the prefactor (see Chapter 1), a constant escape rate at a given temperature corresponds to a constant barrier height ΔU_-. The effective escape temperature is assumed to be the one measured independently on

the junction alone: $T_{\text{eff}} = 80\,\text{mK}$.[11] This fixes the barrier height $\Delta U_{\text{exp}} \propto -k_B T_{\text{eff}} \ln \Gamma$, from which we extract the value $s^*_{\text{thy}}(\varphi)$ by solving the equation $\Delta U_-(s, \varphi) = \Delta U_{\text{exp}}$. The result of this calculation is compared to the measured modulation curve in Fig. 5.12. The agreement between the experiment and this theory, which contains no adjustable parameters and takes into account only the lower Andreev state of each channel, is excellent.

Why the modulation curve differs from the current-phase relation?

It is interesting to discuss the conditions for the Atomic SQUID switching current modulation curve to represent faithfully the current-phase relation of the atomic contact.

The potential for the sole junction presents a well where the phase is trapped, with a minimum $U_0^{\min}$ at position $\gamma_{\min}$ and a maximum $U_0^{\max}$ at position $\gamma_{\max}$ (see Fig. 5.13). The barrier height and the distance between the extrema are given by:

$$\Delta U_0 = U_0^{\max} - U_0^{\min}, \tag{5.19}$$

$$\Delta\gamma^0 = \gamma^0_{\max} - \gamma^0_{\min} = \pi - 2\arcsin s. \tag{5.20}$$

The latter is plotted as a function of the critical current and for different temperatures in Fig. 5.13 (for a typical value of the rate exponent $B = \Delta U / k_B T_{\text{eff}}$).

If the contact can be treated as a small perturbation, the effect of its lower Andreev state is to modify the potential of the junction, shifting in energy the minimum by $E_-(\gamma_{\min} + \varphi)$ and the maximum by $E_-(\gamma_{\max} + \varphi)$, as shown in Fig. 5.13. When computing the modulation curve, one considers the modification of the barrier height from ΔU_0 to $\Delta U_-(\varphi)$ which can be estimated as:

$$\Delta U_-(\varphi) = \Delta U_0 + d\,(\Delta U_0)\,(\varphi), \tag{5.21}$$

with a flux dependent term:

$$d(\Delta U_0)(\varphi) = E_-(\gamma_{\max} + \varphi) - E_-(\gamma_{\min} + \varphi). \tag{5.22}$$

If $E_-(\delta)$ varies smoothly with the phase on the scale of $\Delta\gamma^0$, this barrier height correction is, to a good approximation, proportional to the derivative of the Andreev energy, i.e. to the current phase relation of the channel:

[11] This measurement is performed when the contact is open. The effective temperature and the critical current of the Josephson junction are extracted from the dependence of the escape rate on the bias current, as was done in Chapter 4.

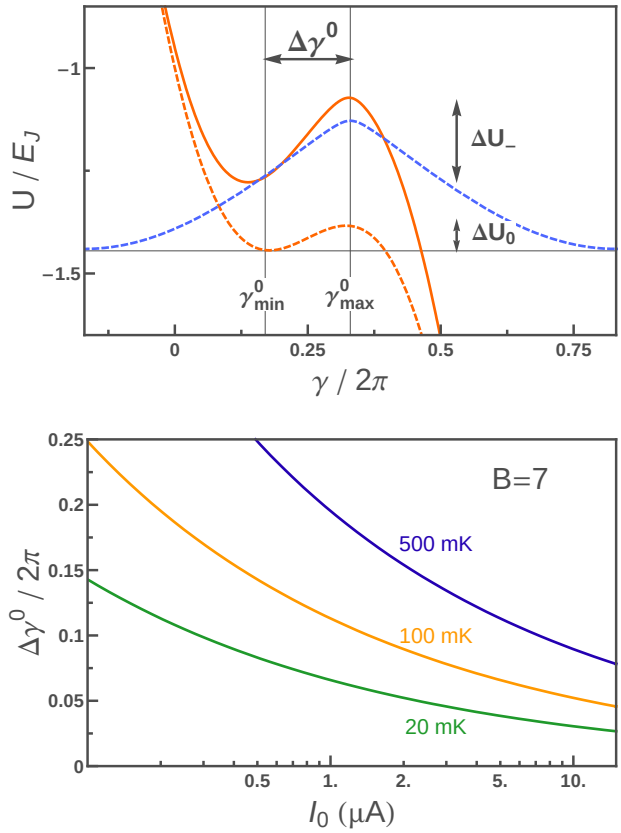

Fig. 5.13. Top: Complete potential of the Atomic SQUID $U_-(\delta)$ (solid line) given as a sum of U_0 (dashed line) and E_-(dashed line) shifted by a flux $\varphi = 0.17$, for $s = 0.9$ (biased current used in the experiment for a typical effective temperature of $T_{\rm eff} = 100\,{\rm mK}$), and the parameters of the experiment (curves are shifted vertically to be aligned). $\Delta\gamma^0$ corresponds to the width of the potential well in U_0. **Bottom:** Distance in phase $\Delta\gamma^0$ between the extrema of the potential well in U_0 as a function of the critical current of the junction, for a constant rate exponent $B = \Delta U/k_B T_{\rm eff} = 7$ and three different effective escape temperatures. The other experimental parameters are $\tau_p = 1\ \mu$s, and $C_e = 20\,{\rm pF}$.

$$d(\Delta U_0)(\varphi) \simeq \frac{\partial E_-}{\partial \delta} d\delta \propto I_-(\delta). \tag{5.23}$$

Therefore, to reproduce the current-phase relation of the atomic contact through the measurement of the switching current of the Atomic SQUID, it is necessary to choose parameters such that $\Delta\gamma^0$ is small enough for all values of the phase. As shown in Fig. 5.13, to reduce $\Delta\gamma^0$ it is convenient to work with I_0's as large as possible and at low temperature.

On the other hand, the higher the critical current of the junction, the smaller the relative modulation introduced by the atomic contact as shown in Fig. 5.14, thus requiring a higher resolution on the bias current in order to get a good signal to noise ratio. Moreover, although this is a

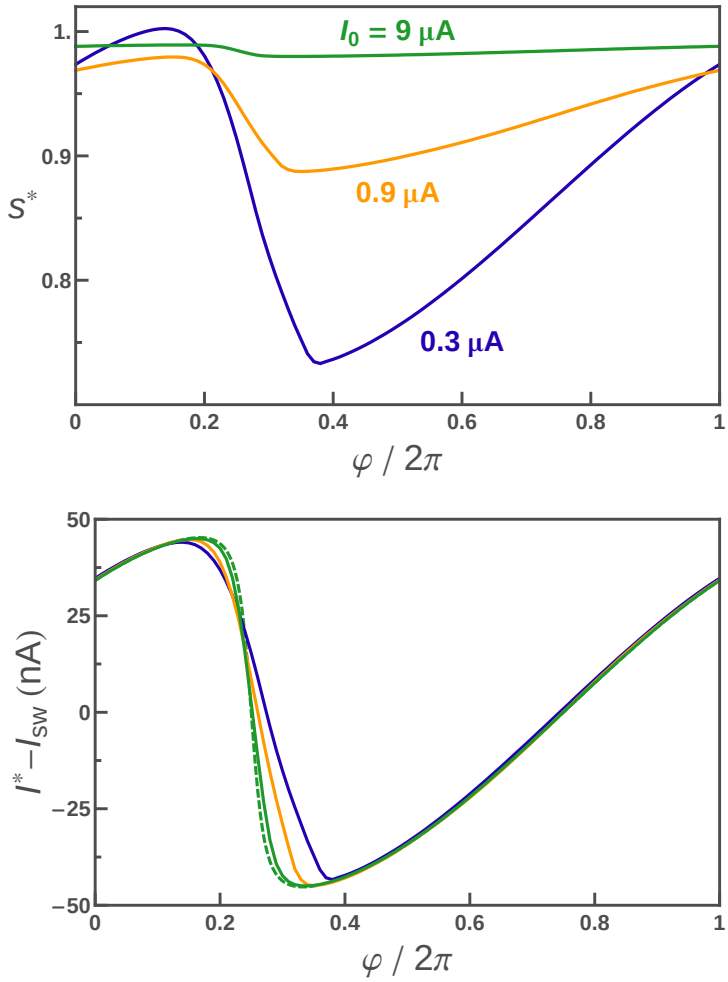

Fig. 5.14. Top: normalized modulation curves (normalized bias current $s^*(\varphi)$ corresponding to $P = 0.5$ as a function of the reduced flux), for an Atomic SQUID with a single channel of transmission $\tau = 0.995$, for three different junction critical currents ($I_0 = 0.3$, 0.9 , and 9 μA) (see also Fig. 5.13 for more details). **Bottom:** centered modulation curves ($I^* - I_{\rm sw}$, where $I_{\rm sw}$ is the switching current of the junction alone), compared to the current-phase relation calculated for a channel of transmission $\tau = 0.995$ (green dashed line) for the same parameters as in previous panel.

separate practical problem, the higher I_0 the higher the subgap current of the junction (see [36]), thus making it increasingly difficult to determine accurately the transmissions of the contact. In practice, reasonable values for the junction critical current are in the range $300\,\text{nA} \lesssim I_0 \lesssim 1\,\mu\text{A}$.

Under these conditions, as was shown in [20], the modulation curve corresponds faithfully to the current-phase relation for contacts containing channels of not too high transmissions (where E_- varies smoothly with δ). However, there can be significant deviations when the contact

contains at least one channel of high transmission, as shown in Fig. 5.12, because the Andreev energy can then vary rapidly with δ around $\delta = \pi$ on the scale of $\Delta\gamma^0$ ($\sim 0.15 \times 2\pi$ in this particular case).

In conclusion, at low temperature and for a junction critical current around ten times larger than the contact one, the switching current of the Atomic SQUID as a function of the flux represents quite well the current-phase relation of the contact, with small deviations which in practice become noticeable only for high transmissions ($\tau \geq 0.95$).

5.4.5 Thermal effects on the modulation curve

The modulation curve was also measured at temperatures higher than the base temperature of the dilution refrigerator, but where the parameters of the setup (I_0 and Δ) were not modified (see [47, 58] and Appendix B.6). It is observed that switching occurs at smaller currents, as expected, but also that the modulation curve gets rounded (see Fig. 5.15). This latter effect cannot be explained when only the lowest Andreev state is taken into account, as shown by the predictions in solid lines. The population of the upper Andreev state thus probably plays a role when temperature is increased. In this section, we describe the impact on the modulation curve of a thermal population of the Andreev states.

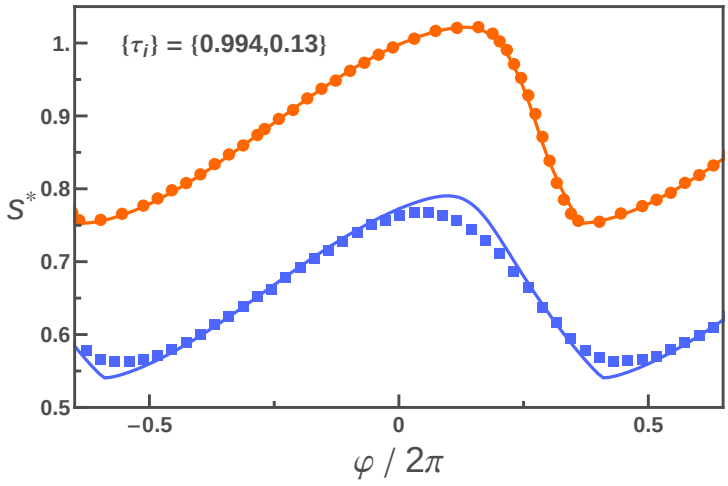

Fig. 5.15. Symbols: Measured modulation curve s^* for a contact with transmissions $\{0.994, 0.13\}$ at temperatures $T = 25\,\text{mK}$ and $T = 350\,\text{mK}$ (orange circles and blue squares). **Solid lines:** modulation curves calculated with $T_{\text{eff}} = 80\,\text{mK}$ (as measured on the junction alone, orange line) and $T_{\text{eff}} = 378\,\text{mK}$ (adjusted to fit the average current, blue line), when only the lower Andreev state is taken into account (no thermal population).

Equilibrium properties of an Andreev doublet at constant phase

Since the Andreev states are two fermionic states (detached from the continuum), there are four possible configurations for the population of the two-level system in each channel, as shown in Fig. 5.16. If we assume that they are populated according to a Boltzmann distribution at a temperature T_A, hereafter called the Andreev temperature, the partition function is:

$$Z = 2 + e^{-\beta_A E_-} + e^{-\beta_A E_+} = 2 + 2\cosh\left[\beta_A E_+\right], \tag{5.24}$$

where $\beta_A^{-1} = k_B T_A$. We have used the energy of each configuration given in Fig. 5.16.

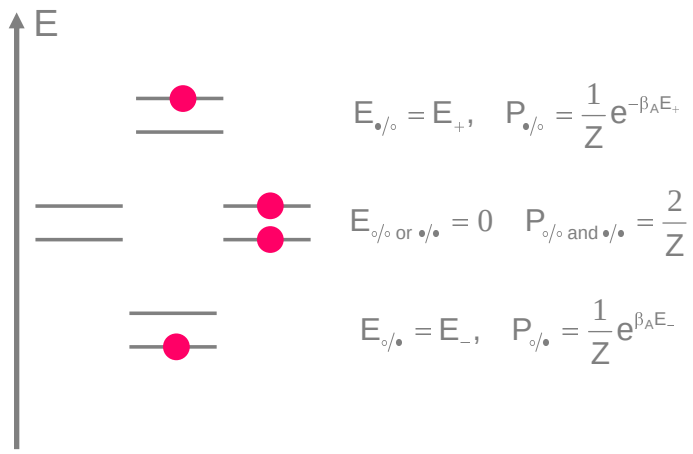

Fig. 5.16. The four possible configurations for an Andreev doublet. The ground state (energy E_-) corresponds to only the lowest Andreev state being occupied by a quasiparticle. There are two configurations with zero total energy, corresponding to the states being either both empty or both occupied. The fourth configuration (energy E_+) corresponds to a quasiparticle in the upper Andreev state only. These configurations are populated according to a Boltzmann distribution with temperature $k_B T_A = \beta_A^{-1}$.

The equilibrium current of each channel at a temperature T_A is then:

$$\langle I \rangle (\delta) = \frac{1}{Z}\left\{ I_+ e^{-\beta_A E_+} + I_- e^{-\beta_A E_-} \right\} = I_- \tanh\left[\frac{\beta_A E_+}{2}\right]. \tag{5.25}$$

where $\langle . \rangle$ denotes the thermal averaging in the following.[12] The function $\langle I \rangle (\delta)$ is shown in Fig. 5.17 for a channel with transmission $\tau = 0.995$, at temperatures from 0 to 600 mK.

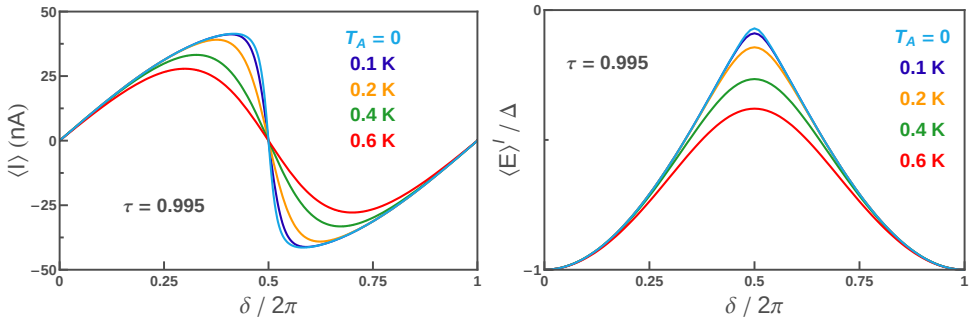

Fig. 5.17. Left: Equilibrium average current $\langle I \rangle$ for a single channel of transmission $\tau = 0.995$, and for Andreev temperatures T_A =0, 0.1, 0.2, 0.4, and 0.6 **Right:** Corresponding energy $\langle E \rangle^I$ obtained by integration of the average current, see Eq. (5.27).

Atomic SQUID modulation curve at large temperatures

To treat the case of the Atomic SQUID, one has to write the Langevin equation of the circuit.

Adiabatic approximation Assuming that the time needed to reach the thermal equilibrium population of the Andreev configurations is much shorter than all the times involved in the dynamics of the phase, the force associated to the atomic contact entering the Langevin equation for the circuit corresponds to the average current $\langle I \rangle$. This leads, as derived in [113], to the effective potential:[13]

$$\langle U \rangle^I (\gamma) = U_0(\gamma) + \sum_i \langle E \rangle_i^I (\gamma + \varphi), \tag{5.26}$$

where for each channel i:

$$\langle E \rangle_i^I = \varphi_0 \int_0^\delta \frac{\partial \langle I \rangle_i}{\partial \delta'} d\delta' - \Delta. \tag{5.27}$$

[12] One should note that this is just the same as considering that each channel is populated by a Fermi distribution; the upper state with a distribution $f(E_+)$ and the lower state with $f(E_-)$. Since $E_+ = -E_-$ and $I_+ = -I_-$, the thermal average contains a term $f(E_-) - f(E_+) = 1 - 2f(E_+) = \tanh\left[\frac{\beta_A E_+}{2}\right]$ [16, 115].

[13] this effective potential is very different from the one obtained using the average Andreev energy $\langle E \rangle$ used in [36, 45] because $\langle I \rangle \neq \frac{1}{\varphi_0} \frac{\partial \langle E \rangle}{\partial \delta}$.

This potential allows to calculate the modulation curve s^*. Let us recall that the calculation consists in solving, for each flux, the equation $\Delta U(s^*, \varphi) = \Delta U_{\rm exp}(T_{\rm eff})$, where $T_{\rm eff}$ is the effective escape temperature. In theory, one should consider the noise arising from both the Johnson-Nyquist noise of the environment and the telegraph noise due to the fluctuations of the Andreev populations [121]. In practice, we assume that the noise is white and can be described by an effective temperature. Figure 5.18 compares the experimental modulation curve measured at $T = 350$ mK (already shown in Fig.5.15) with this prediction. The effective temperature $T_{\rm eff} = 378$ mK is found from the fit of the average switching current, and we fixed $T_A = T_{\rm eff}$.

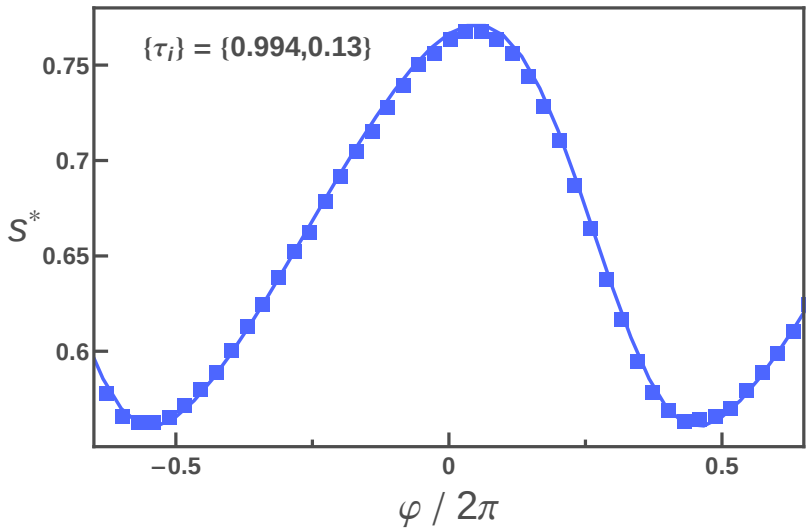

Fig. 5.18. Symbols: Measured modulation curve s^* at $T = 350$ mK, for the same contact as in Fig. 5.15. **Solid line:** Modulation curve calculated with the effective potential $\langle U \rangle^I$ using $T_{\rm eff} = 378$ mK (adjusted to fit the average switching current) and $T_A = T_{\rm eff}$.

Out of the adiabatic approximation Instead of using an average potential, a calculation can be made in the opposite limit, assuming slow transitions between the states [36, 45]. The predictions for the modulation curve is however very different from the experimental data when the transmission is close to 1, because its leads to the admixture of different switching processes, and deformations of the curve $P(s)$ compared to the case of Fig. 5.11. Such effects have not been observed at any temperatures, thus supporting the validity of the adiabatic approximation.

Conclusion From the experimental curves presented in Figs. 5.15 and 5.18, it appears that the modulation curve for this Atomic SQUID is very well understood within the adiabatic approximation at finite temperature. However, in a slightly modified type of sample, we have observed different and much stronger modifications of the modulation curve probably due to non equilibrium effects, as discussed in the next section.

5.5 Out-of-equilibrium effects

The experiments presented in the previous sections were performed with samples in which the on-chip lines connecting the Atomic SQUID to the outside world were made out of gold, a normal i.e. dissipative metal at low temperatures. On the contrary, in our first design to attempt Andreev spectroscopy and in order to minimize the dissipation which limits the life-time of the excited Andreev levels, we decided to fabricate all on-chip electrodes out of aluminum. Apart from this change of material, Sample AC2 was almost identical to the previous one (see Fig. 5.1), and in particular the critical current of the junction was $I_0 = 295$ nA, less than 5% smaller than before. However, as we will discuss now, this change of material had very strong consequences on the overall behavior of the system.

Figure 5.19 shows the escape probability as a function of both the flux and the reduced bias current, for an atomic contact with transmissions $\{0.999,\ 0.586,\ 0.171,\ 0.171\}$. As compared to Sample AC1 (see Fig. 5.11) the escape probability does not vary sharply from 0 to 1 for all values of the flux. In some flux ranges, the escape probability displays steps or oscillations as a function of the bias current. These features appear only in a region bounded by the expected modulation curve, and by another modulation curve calculated when neglecting the contribution of the very well transmitted channel. Similar effects were observed for other contacts on the same sample, as seen in Fig. 5.20. These effects are not limited to channels of high transmission, as some faint structure can be observed even for contacts with $\tau \sim 0.5$, but with a much smaller and hardly detectable amplitude.

A tentative explanation for this observation is that in this region, the very well transmitted channel contributes only partially, or even not at all, to the total current through the contact. This would arise if the two Andreev states in this channel were either both empty or both occupied. Although the underlying physics is neither understood nor under control, we think that a double occupation of the Andreev states of a channel could occur due to poisoning by external quasiparticles, pro-

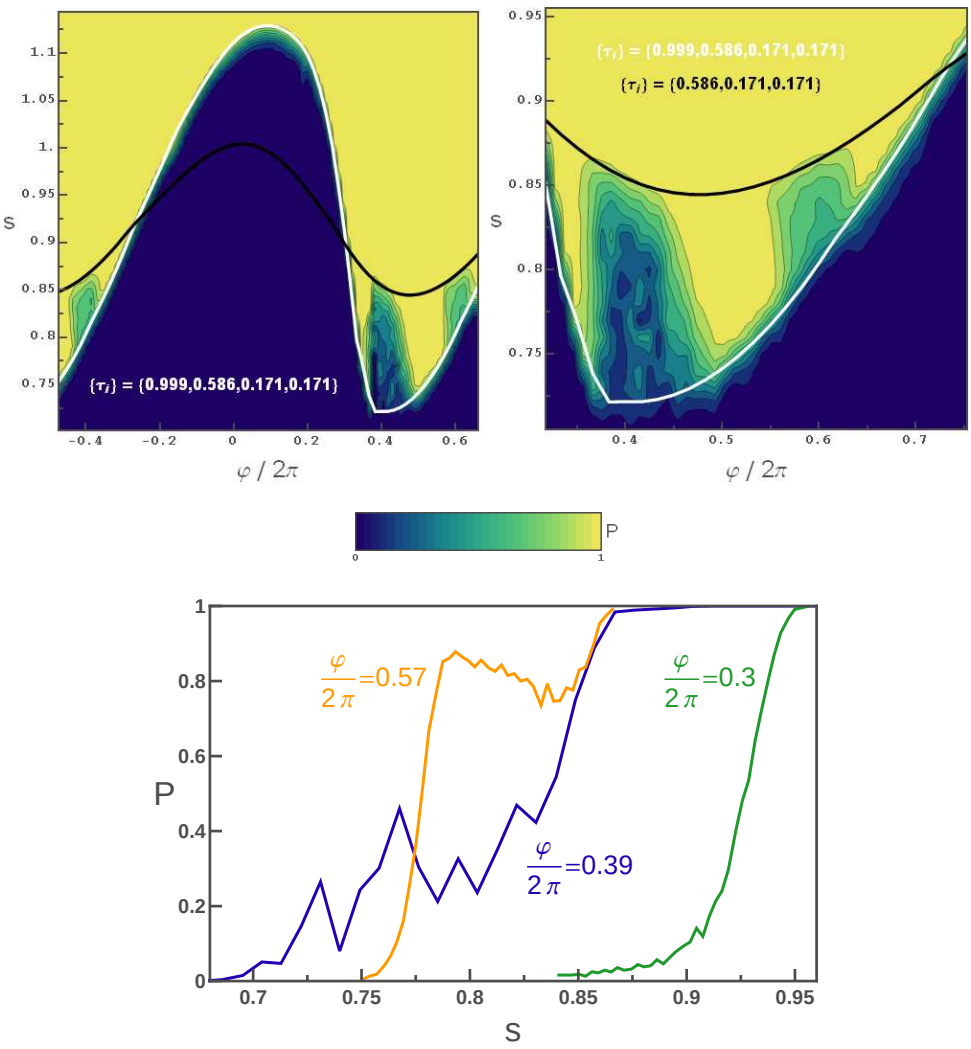

Fig. 5.19. Top: Escape probability as a function of the external flux and the bias current for Sample AC2, with an atomic contact of transmissions {0.999, 0.586, 0.171, 0.171} . The white line corresponds to the modulation curve calculated taking into account the contribution of the Andreev ground state of all the channels. The black line corresponds to the modulation curve calculated for {0.586, 0.171, 0.171}, i.e. excluding the contribution of the most transmitted channel. **Bottom:** Escape probability as a function of the reduced bias current for three different values of the applied flux.

duced for example when the SQUID switches into the dissipative state. Since the Andreev states have energies below the superconducting gap, the quasiparticles could easily get trapped into them. The fact that this effect only appeared on a sample having no large normal electrodes able to efficiently trap the quasiparticles strongly supports this hypothesis.

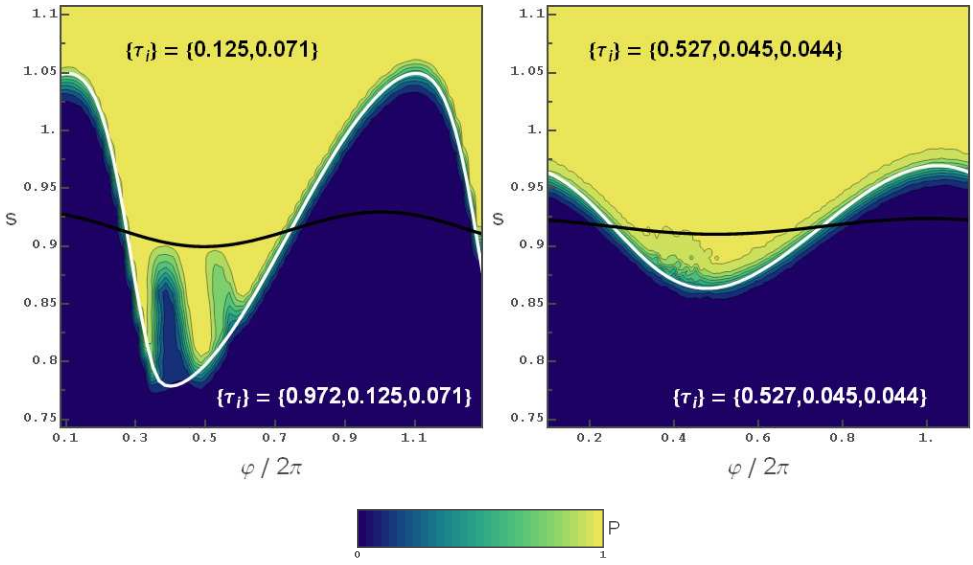

Fig. 5.20. Escape probability as a function of the external flux and the bias current for sample AC2, with two different atomic contacts.

There are several experimental facts which could help finding a thorough explanation of these effects. In the previous examples, the out-of-equilibrium effects were limited to the low switching current region (low compared to the mean switching current of the JJ alone). One can wonder why a symmetric effect is not seen in the upper region. One could understand this in the following way: the first pulses of a sequence create quasiparticles, that populate essentially the upper Andreev state of the very well transmitted channels. As long as this state is occupied, the critical current of the Atomic SQUID looses the contribution of this channel. If it happens in a flux region for which the critical current gets enhanced by the double occupancy, subsequent pulses of the same height would be unable to make the system switch. It is only after the quasiparticle gets untrapped, that switching occurs again. Quasiparticles are created once more, and after some time, populate the upper state. The previous blockade of switching repeats itself. This should result in intermittency of switching, a phenomenon that we indeed observed (see Fig. 5.21) and

that explains the large fluctuations observed on $P(s)$ for short measurement times (see bottom panel of Fig. 5.19).

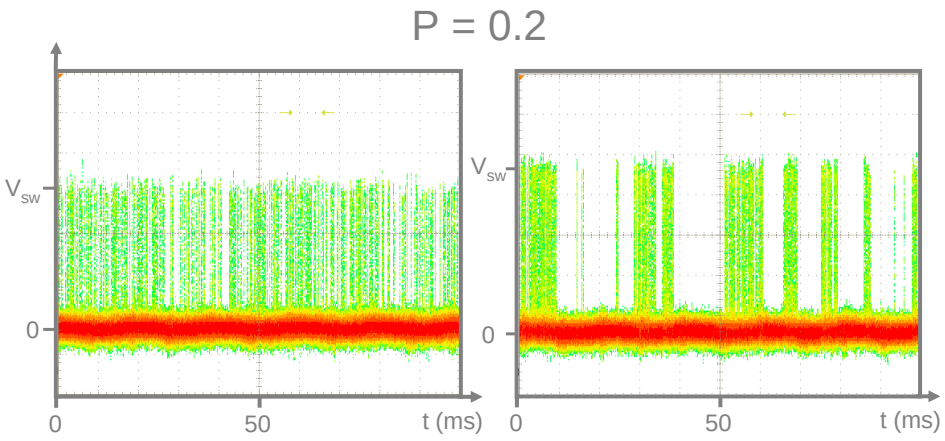

Fig. 5.21. Voltage across the Atomic SQUID as a function of time during a sequence of bias-current pulses (50 μs period). Each voltage pulse corresponds to a switching event. **Left**: at a flux value for which the $P(s)$ curve is normal. **Right**: Similar measurement, at a flux value for which it displays a step, showing intermittency attributed to the dynamics of quasiparticle trapping and untrapping in the upper Andreev state.

The escape probability in this regime depends on the ratio of the quasiparticle trapping and untrapping times. In the opposite situation where the critical current gets reduced by a trapped quasiparticle, nothing can be observed. As quasiparticles are created only when switching occurs, no effect can be seen for pulses smaller than the reduced bias current s^*_{thy} calculated when considering the contribution of all the channels. However, we found that even in this situation a non equilibrium effect is observed when a short but strong bias-current pulse is applied just before the measurement pulse, as shown in Fig. 5.22. This excitation induces the switching of the detector junction, thus creating quasiparticles (it is however not long enough to develop a detectable voltage pulse, and therefore is not counted in $P(s)$). Under this perturbation, a step appears in the curve $P(s)$, bounded as before by the theoretical predictions for the full contact and for the one in which the most transmitted channel is neglected.

Furthermore, we have measured the histogram of the switching-times along these peculiar steps, as shown in Fig. 5.23. The histograms, which should be a simple exponential in case the switching were a Poisson process, presented a clearly distinct behavior, with a peak at short times and a constant background. The peak can be interpreted as due to situations

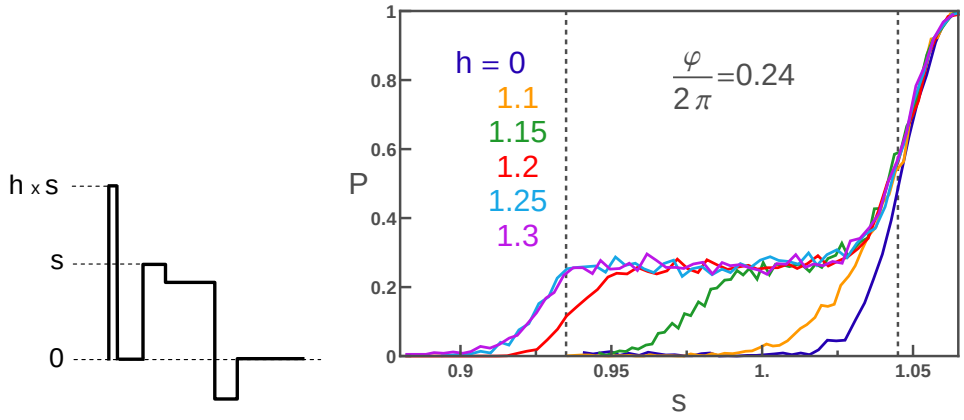

Fig. 5.22. Right: Escape probability $P(s)$ as a function of reduced bias current s, for different heights of a short bias pulse applied before the measurement pulse (see scheme on the **left**). The data was taken at $\varphi = 0.24 \times 2\pi$ for the contact shown in Fig. 5.19. A step develops on the $P(s)$ curve, which for this particular value of the flux is otherwise normally narrow (see the curve taken at $h = 0$). The vertical dashed lines at $s_1 = 0.935$ and $s_2 = 1.045$ correspond respectively to the black line in Fig. 5.19, therefore the modulation curve obtained when neglecting the contribution of the very well transmitted channel, and to the white line in Fig. 5.19, therefore to the normal modulation curve. It appears that the prepulse is efficient in producing quasiparticles that populate the upper Andreev state when $h \times s > 1.1$. If $s > 1.1/h$ (condition to populate the upper Andreev state) and $s > s_1$, the measurement pulse yields switching, and a step develops in $P(s)$. When h is larger than 1.2, the two conditions are always fulfilled at the same time, explaining why the curves at $h = 1.25$ and $h = 1.3$ superimpose.

where the upper Andreev level is already occupied at the beginning of the pulse: the switching current is therefore much smaller than the pulse height and switching occurs very early in the pulse. The background, which seems to remain unchanged along the step, could be attributed to situations where the upper Andreev level is unoccupied at the beginning of the measurement pulse, and gets occupied during the pulse.

We also noted that the non-equilibrium effects are sensitive to the dynamical properties of the measurement pulse, like the rise time. The effects tend to disappear when slowing the rise time of the bias pulse (see Fig. 5.24). However, when slowing down the whole measurement sequence, in particular by increasing the time between measurement pulses, the non-equilibrium features diminished but never disappeared completely.

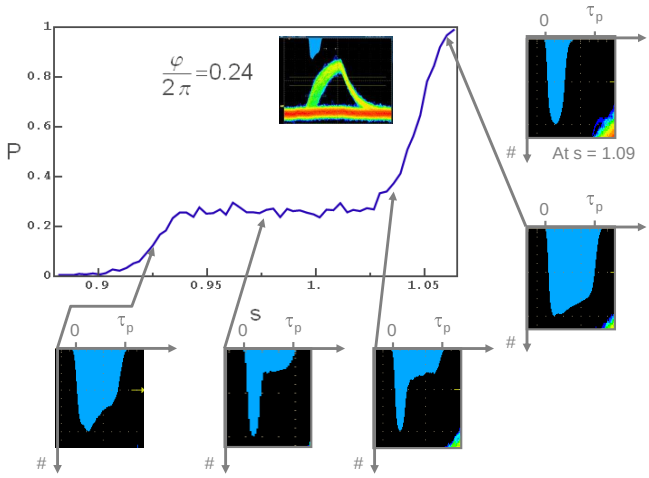

Fig. 5.23. Main panel: Escape probability P as a function of reduced bias current s, obtained at $\varphi = 0.24 \times 2\pi$ for the contact presented in Fig. 5.19 (when adding a prepulse with $h = 1.3$, see Fig. 5.22). **Small black panels:** histograms of the escape times during the bias-current pulse, measured for different positions along the $P(s)$ curve. Contrary to the normal case, in which there is no step in the $P(s)$ curve and for which the histogram is a simple exponential decay reflecting a Poisson process, the structure in the histograms along the step point out to the competition between two switching processes.

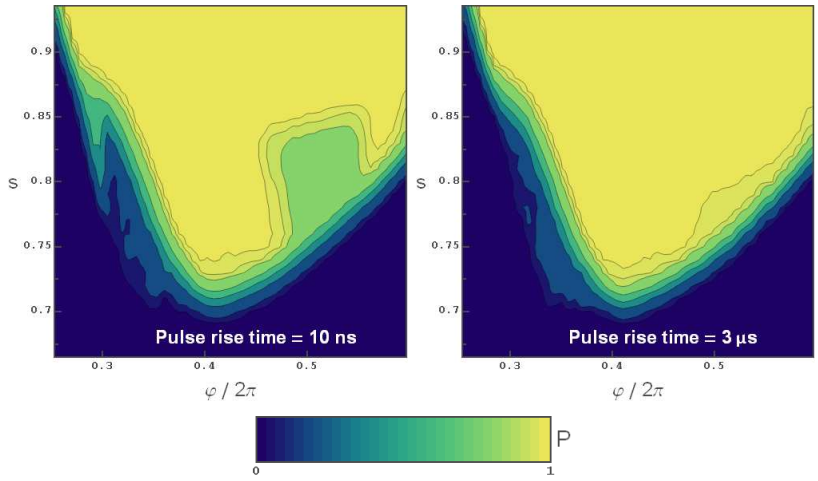

Fig. 5.24. Escape probability as a function of the external flux and the bias current measured on Sample AC2 for an atomic contact with transmissions {0.999, 0.696, 0.275, 0.26}. The escape probability is shown for two different rise times of the measurement pulse. The out-of-equilibrium effects tend to disappear for longer rise times.

5.6 Conclusions

In this chapter, we presented experiment probing the Andreev states in an atomic contact:

- By embedding an atomic contact in a superconducting loop together with a Josephson junction in a SQUID-like geometry, it is possible to measure both the current-phase relation of the atomic contact and its current-voltage characteristics. From the latter, one can extract the transmissions of the channels accommodated by the atomic contact, therefore allowing a direct comparison with the predictions for the current-phase relation based on the Andreev bound states theory. We recovered the results of [20] but also completed the description of measurement at temperatures large enough to populate the upper Andreev state.
- Our results on Sample AC1 at low temperature (as those obtained previously in the group) can be perfectly understood by considering that, in every channel of the contacts, only the lower Andreev state is occupied. However, with Sample AC2, very similar in parameters but where dissipation in the connecting electrodes was strongly reduced using a superconducting metal instead of normal one, we faced spurious effects that we tentatively attribute to the out-equilibrium population of the upper Andreev states by quasiparticles generated during the measurement pulses.

In the next chapter, we discuss the possibility to use the present setup to probe the upper Andreev state in a controlled manner by performing the spectroscopic measurement of the transition between Andreev states.

Chapter 6

Towards Andreev states spectroscopy

In this chapter we discuss the main requirements for achieving the spectroscopy of the Andreev states in a superconducting atomic contact using the Atomic SQUID setup. After having presented the ideal phase-bias case, we describe the adiabatic approximation well suited for treating the Hamiltonian of this system, and introduce a new description that goes beyond this approximation. We also evaluate the lifetime of the upper Andreev level, and show that its observation requires an electromagnetic environment with much lower dissipation, and a much more efficient excitation, than achieved in the setup presented in Chapter 5. We propose a new setup designed for Andreev state spectroscopy, and present a preliminary experiment that probes it.

How to probe the transition to the upper Andreev state ? The two Andreev states accommodated by a single channel of a superconducting atomic contact form an original kind of microscopic quantum two-level system (TLS) controlled by a macroscopic variable, the phase difference across the contact [100]. Experimentally, essentially the properties of the ground state have been probed up to now, through the supercurrent it carries, and a detailed measurement of the upper state is still lacking (although the experiments at finite temperature of the Chapter 5 constitute an indirect measurement). Achieving the spectroscopy of the transition between the two Andreev states is clearly an essential step to characterize the Andreev TLS. Furthermore, in the context of quantum information, Andreev TLSs have also been considered as possible solid state quantum bits [17, 122, 101, 43]. Although the use of atomic contacts in this direc-

tion has not really started, the coherence properties of Andreev TLSs are an important issue that could be addressed by spectroscopy experiments.

Achieving such a spectroscopy experiment requires:

1. A short Josephson weak-link with a number of channels small enough to disentangle their different Andreev TLSs;
2. A well-controlled method to fix the phase-difference across the contact and measure the states population;
3. That the Andreev transition can be induced by an external excitation matching the Andreev gap $\nu_A(\delta)$;
4. A long enough relaxation time of the upper state in order to detect its population within the time scale of the available measurement methods.

As shown in Chapter 5, the Atomic SQUID setup fulfils criteria 1 and 2, which raised hopes that it could allow the spectroscopy of Andreev states. We discuss now the last two requirements.

6.1 Predictions for the Andreev transition

6.1.1 Ideal phase-bias

In order to grasp the basic relevant parameters, we first assume here that the Atomic SQUID setup provides a perfect phase-biasing of the atomic contact. The only parameter controlling the Andreev states is the phase difference δ, and the energy difference between the Andreev levels varies from 2Δ at $\delta = 0$ down to the Andreev gap $2r\Delta$ at $\delta = \pi$, where $r = \sqrt{1-\tau}$ is the reflection probability. A modulation of the phase difference at a frequency $2r\Delta/h \leq \nu_{\rm exc} \leq 2\Delta/h$ is thus expected to populate the upper state when $\nu_{\rm exc} \simeq \nu_A(\delta)$. If the excitation is applied continuously, it can at best achieve a "saturation" of the transition, with equal populations of the two Andreev states. Since these states carry opposite currents, one expects a noticeable modification of the modulation curve of the switching current as depicted in Fig. 6.1.

Matrix element for the phase excitation of the Andreev transition

One has first to evaluate how a fluctuation of the phase difference across the contact couples to the Andreev TLS. Under a small phase perturbation $d\delta(t)$ around a phase difference δ_0, the Hamiltonian of the Andreev states defined in Eq. 5.12 is modified according to:

$$\mathcal{H}_{AS}(\delta) = \mathcal{H}^0_{AS}(\delta_0) + \varphi_0 \hat{I}_{AS}(\delta_0) d\delta(t), \tag{6.1}$$

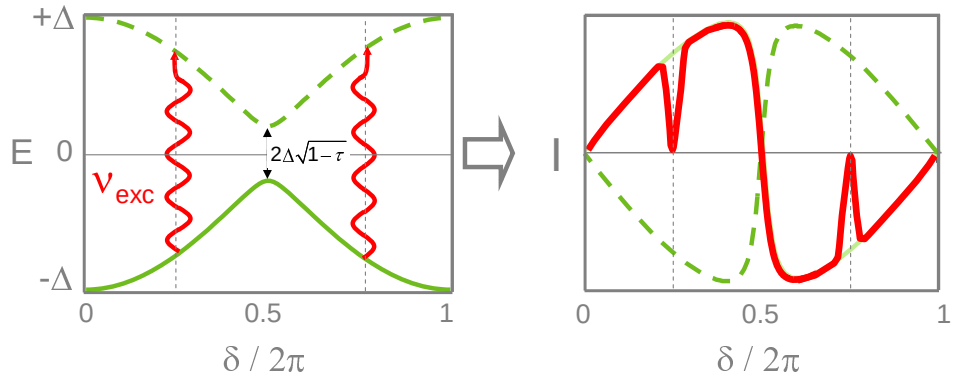

Fig. 6.1. Schematic response of a phase-biased atomic contact to a small phase modulation at frequency $\nu_{\rm exc}$, such that $2\Delta\sqrt{1-\tau} \leq \nu_{\rm exc} \leq 2\Delta$. **Left:** The upper Andreev level is populated for the phase difference at which the excitation frequency matches the Andreev gap: $\nu_{\rm exc} = \nu_A(\delta)$. **Right:** The population of the upper state should lead to a drastic change of the average current-phase relation (red thick line) at the corresponding phase difference.

where $\hat{I}_{AS}(\delta)$ is the current operator through the atomic contact (see Appendix B.5 and [101]):

$$\hat{I}_{AS}(\delta) = \frac{e\Delta^2}{\hbar E_+(\delta)}\left[-\frac{1}{2}\tau\sin(\delta)\,\hat{\sigma}_z^{AS} + r\hat{\sigma}_x^{AS}\right]. \tag{6.2}$$

The transverse part couples the two Andreev states with a matrix element $M_\perp(\delta)$ given by the expression:

$$M_\perp(\delta) = \varphi_0\left\langle +\left|\hat{I}_{AS}\right|-\right\rangle = \frac{\Delta\sqrt{1-\tau}}{2\sqrt{1-\tau\sin^2\frac{\delta}{2}}}. \tag{6.3}$$

The variations of this matrix element with the phase δ are shown in Fig. 6.2. A maximum occurs at $\delta = \pi$, with a sharpness that increases with the contact transmission.

Transition Frequency

The Andreev gap is shown in Fig. 6.3 for a single channel with transmission τ. Experimentally, for our microwave generators, and for the connectors installed in our dilution fridge, the range of accessible frequencies is restricted below $\simeq 20$ GHz. In the case of aluminium, with $\frac{\Delta}{h} \simeq 50$ GHz for thin layers, the condition $2r\Delta \leq 20$ GHz implies:

$$\tau \geq 0.95. \tag{6.4}$$

The phase difference interval where $\nu_{\rm exc}$ can coincide with the Andreev frequency in a very-narrow range around $\delta = \pi$, with a width that increases with the transmission, as can be seen in Fig. 6.3.

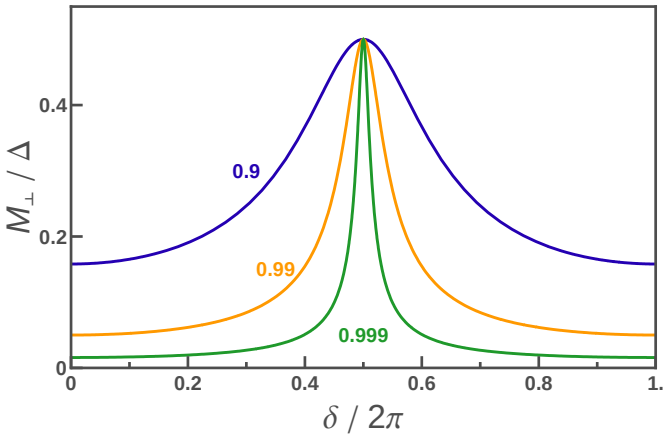

Fig. 6.2. Matrix element $M_\perp(\delta)$ from Eq. (6.3) between the lower and the upper state in the ideal phase-bias situation for $\tau = 0.9$, 0.99 and 0.999.

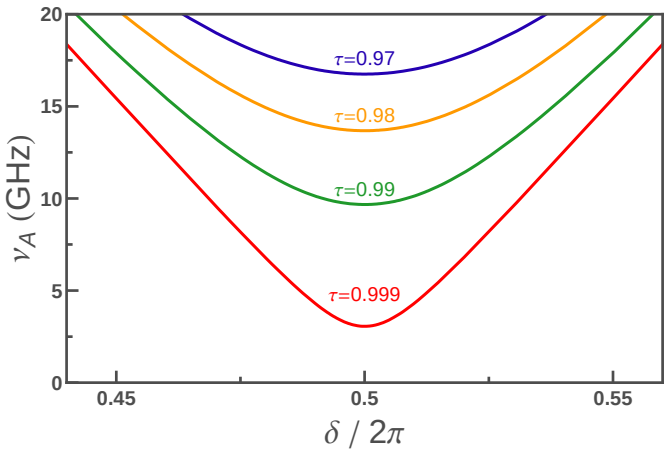

Fig. 6.3. Andreev frequency $\nu_A(\delta)$ for different transmissions of a single channel (calculated for $\Delta = 200\,\mu$eV) in the experimentally accessible frequency range ($0-20$ GHz). This limited frequency range requires channels with a large transmission $\tau \geq 0.95$.

Relaxation of the upper Andreev state

Relaxation of the upper Andreev state proceeds by transferring its energy to the environment of the contact, characterized by an impedance $Z(\omega)$. The Andreev levels are coupled to the different degrees of freedom of the environment, in particular the phonons [122] and the electromagnetic modes of the impedance connected across the contact. The electromagnetic channel is expected to dominate relaxation, characterized by its relaxation time $T_1(\delta) = \Gamma_1(\delta)^{-1}$. To calculate the relaxation rate, the impedance $Z(\omega)$ is described as an infinite set of harmonic oscillators at thermal equilibrium [46], and using the generic model of a two-level

system linearly coupled to this bosonic bath, as done for qubits (e.g. the Quantronium in [123]). The calculation of the relaxation rate can be found in [101] and is detailed in the Appendix B.5. At zero temperature, the relaxation rate is related to the matrix element $M_\perp$ that couples the two states and the impedance $Z(\omega)$ by the relation (see Eq. B.92):

$$\Gamma_1(\delta) = \frac{1}{\pi\nu_A}\left(\frac{M_\perp}{\hbar}\right)^2 \frac{\mathrm{Re}\left[Z(\Omega_A)\right]}{R_K} = \pi\frac{\Delta}{\hbar}\frac{\mathrm{Re}\left[Z(\Omega_A)\right]}{R_K}\frac{1-\tau}{\left(1-\tau\sin^2\frac{\delta}{2}\right)^{3/2}} \tag{6.5}$$

with $R_K = h/e^2$ is the resistance quantum. The variations of the relaxation rate with the phase are shown in Fig. 6.4. One notices that relaxation is the largest at $\delta = \pi$, precisely where the transition is best observable. The coherence time of a coherent superposition is determined by the decoherence rate $\Gamma_2 = \Gamma_\phi + \Gamma_1/2$, where Γ_ϕ is the dephasing rate due to fluctuations of the phase.

Due to this relaxation, it is questionable whether it is possible experimentally to probe this transition, what is now discussed.

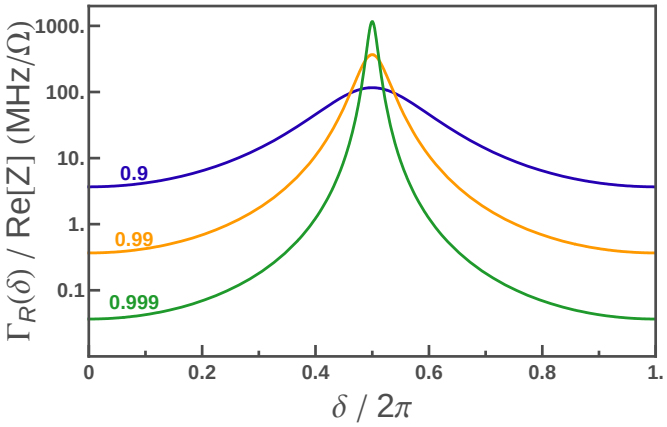

Fig. 6.4. Relaxation rate (Eq. (6.5)) of the upper state in an ideal phase-bias situation for $\tau = 0.9$, 0.99 and 0.999. Since the relaxation rate is proportional to the real part of the impedance across the Atomic SQUID at the Andreev frequency Ω_A, a small value of $\mathrm{Re}\left[Z(\Omega_A)\right]$ is requested to obtain a small enough relaxation rate.

Probing the transition

First of all, let us recall that the state of the system is probed using measurement current pulses of length τ_p. To probe the transition, a microwave excitation is applied, which induces coherent Rabi oscillations between

the two Andreev states. The corresponding Rabi frequency ν_R is proportional to the excitation amplitude. Relaxation of the upper Andreev state imposes constraints on this amplitude and on the measurement time τ_p in order to have an observable effect. The precise constraints depend on the exact protocol:

- The less demanding protocol consists in applying continuously microwaves during the measurement pulse. If the resonance condition is achieved, the population of the upper Andreev state is controlled by the parameter ν_R/Γ_1 . When this parameter is large enough $\nu_R/\Gamma_1 \gtrsim 1$, the upper state is significantly populated, and no further requirement is requested on the measurement time.
- If, on the contrary, one wishes to prepare the upper state with a short π pulse before the readout, the condition $\Gamma_1(\delta)\,\tau_p \lesssim 1$ is also requested.

In any case, achieving a long enough relaxation time is an important goal. In our setup, the achievable measurement pulses are in the range $\tau_p \sim [100\,\mathrm{ns} - 1\,\mu\mathrm{s}]$, and the inequality $\Gamma_1(\delta)\,\tau_p \lesssim 1$ with $\Gamma_1(\delta)$ given by Eq. (6.5) implies for the impedance across the setup to be very small. For example around $\delta = \pi$, for which the Andreev frequency is in the accessible range, but where the relaxation rate is the highest, the real part of the environment impedance must fulfill:

$$\mathrm{Re}\,[Z(\Omega_A)] \leq \frac{\hbar}{\pi\Delta}\sqrt{1-\tau} \times 1\,\mathrm{MHz} \times R_K \sim 10\,\mathrm{m}\Omega. \tag{6.6}$$

Although this inequality (6.6) is only requested for performing qubit-like manipulation of the Andreev TLS, which goes beyond the goal of this thesis, we tried to design an electromagnetic environment able to meet it.

6.1.2 The Atomic SQUID configuration

In the Atomic SQUID, however, the phase across the contact is not a parameter, but a dynamical variable with both thermal and quantum fluctuations. The real situation is thus different from the ideal phase-biasing situation considered previously and one has to consider now the dynamics of the full circuit.

Hamiltonian of the Atomic SQUID

We first derive the Hamiltonian of the simplified Atomic SQUID circuit sketched in Fig. 6.5, where the phase differences across the atomic contact (δ) and the junction (γ) are linked by the reduced flux through the loop

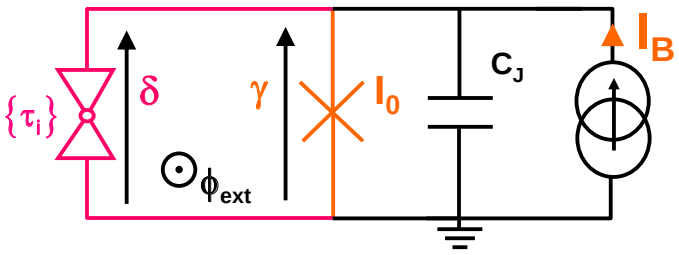

Fig. 6.5. Model circuit of an Atomic SQUID.

$\delta = \gamma + \varphi$. This circuit has a spin-like degree of freedom (due to the Andreev doublet), and a phase degree of freedom (due to the junction). As a basis of the Hilbert space for the whole system, we choose the tensorial products

$$\begin{cases} |\gamma, \leftarrow\rangle = |\gamma\rangle \otimes |\leftarrow\rangle \\ |\gamma, \rightarrow\rangle = |\gamma\rangle \otimes |\rightarrow\rangle \,. \end{cases} \tag{6.7}$$

of the phase states $|\gamma\rangle$ for the junction, and of the right $|\rightarrow\rangle$ and left-moving $|\leftarrow\rangle$ reflectionless states for the Andreev system. In this reflectionless basis $\{|\gamma, \leftarrow\rangle, |\gamma, \rightarrow\rangle\}$, the Hamiltonian of the Atomic SQUID takes the form:

$$\mathcal{H}_{\text{ASQUID}}(\gamma, \varphi) = \Delta \left[\cos \frac{\gamma + \varphi}{2} \hat{\sigma}_z + r \sin \frac{\gamma + \varphi}{2} \hat{\sigma}_x \right] - E_J \left[\cos \gamma + s\gamma \right] + \frac{p_\gamma^2}{2\varphi_0^2 C_J} \tag{6.8}$$

where p_γ is the reduced charge on the junction capacitance conjugated to the phase $[p_\gamma, \gamma] = i\hbar$. The kinetic energy term for the fictitious particle, of position γ and mass $m = C_J \varphi_0^2$ (see Table 2.1), represents the electrostatic Hamiltonian of the junction capacitance.

The Andreev part of the Hamiltonian is diagonal in the basis of the Andreev states $\{|+\rangle, |-\rangle\}$, which are related to the reflectionless states through the unitary transformation:

$$\begin{cases} |+\rangle = \cos \frac{\theta}{2} |\leftarrow\rangle + \sin \frac{\theta}{2} |\rightarrow\rangle \\ |-\rangle = -\sin \frac{\theta}{2} |\leftarrow\rangle + \cos \frac{\theta}{2} |\rightarrow\rangle \end{cases} \tag{6.9}$$

where $\theta = \arctan\left(r \tan \frac{\delta}{2}\right)$ (and $r = \sqrt{1 - \tau}$). We therefore introduce the adiabatic basis

$$\begin{cases} |\gamma, -\rangle = |\gamma\rangle \otimes |-\rangle \\ |\gamma, +\rangle = |\gamma\rangle \otimes |+\rangle \,. \end{cases} \tag{6.10}$$

This Atomic SQUID setup, in which an atomic contact with a spin-like degree of freedom is connected in parallel with a Josephson junction, bears strong similarity with the Quantronium [123], in which a superconducting single Cooper pair transistor, with an inner charge degree of freedom, is connected in parallel with a Josephson junction.

Adiabatic potential surfaces

Therefore, following Ankerhold and Grabert [124], we first consider the case where the phase is almost a classical variable, because of its large mass. Since the kinetic energy term $\frac{p_\gamma^2}{2\varphi_0^2 C_J}$ is negligible in this limit, the Hamiltonian is exactly diagonal with eigenvalues

$$\begin{cases} U_-(\gamma) = U_0(\gamma) + E_-(\delta) \\ U_+(\gamma) = U_0(\gamma) + E_+(\delta) \end{cases} \tag{6.11}$$

that determine two adiabatic potential surfaces, or manifolds ($U_0(\gamma) = -E_J\left[\cos(\gamma) + s\gamma\right]$ is the potential of the junction alone, as in Chapter 5).

To go one step further, one has to take into account the kinetic energy term. A simple first order approximation is to consider that the Andreev spin-like variable follows adiabatically the slow phase dynamics. We thus consider only the diagonal part of p_γ, i.e. the restriction $\widetilde{p}_\gamma$ of the momentum operator to the adiabatic manifolds. This adiabatic approximation is discussed in the next section. We will consider afterwards how to go beyond this approximation.

6.1.3 Dynamics in the adiabatic approximation

In the adiabatic approximation, one is left with two uncoupled manifolds. The question is thus to find the eigenstates in each manifold separately. Typical adiabatic potentials $U_-(\gamma)$ and $U_+(\gamma)$ are shown in Fig. 6.6.

Eigenstates and eigenenergies within the adiabatic approximation

In each manifold, the restriction of the momentum operator $\widetilde{p}_\gamma$ acts as:

$$\widetilde{p}_\gamma \psi_\pm(\gamma) = \frac{\hbar}{i}\frac{\partial \psi_\pm(\gamma)}{\partial \gamma}. \tag{6.12}$$

One is therefore left with two solvable one-dimensional Hamiltonians:

$$H_\pm = E_\pm(\gamma + \varphi) + U_0(\gamma) + \widetilde{p}_\gamma^2/(2C_J\varphi_0^2). \tag{6.13}$$

A good approximation to solve them is to treat the potential wells as harmonic potential wells. However, as can be seen in Fig. 6.6, the two

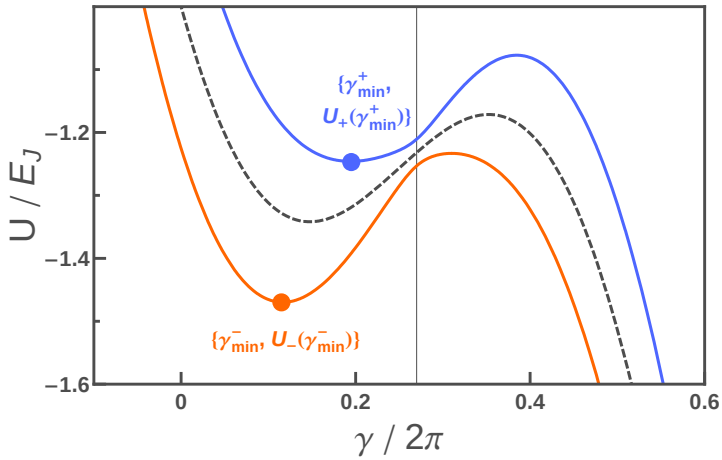

Fig. 6.6. Solid lines: Atomic SQUID potentials $U_-(\gamma)$ (bottom) and $U_+(\gamma)$ (top) at $\varphi = 0.23 \times 2\pi$ and $s = 0.8$. **Dashed line:** Potential $U_0(\gamma)$ of the junction calculated at $s = 0.8$ for $\tau = 0.995$. **Dots:** Potential minima at phases $\gamma^-_{\rm min}$ and $\gamma^+_{\rm min}$, with energies $U_-(\gamma^-_{\rm min})$ and $U_+(\gamma^+_{\rm min})$, respectively.

potentials are different, and, in particular, their curvatures at the respective minima, which determine the plasma frequencies, are not the same. The angular frequencies ω_- and ω_+ in the two Andreev manifolds are:

$$\omega_+ = \frac{1}{\sqrt{C_J \varphi_0^2}} \left. \frac{\partial^2 U_+}{\partial \gamma^2} \right)_{\gamma^-_{\rm min}} \tag{6.14}$$

$$\omega_- = \frac{1}{\sqrt{C_J \varphi_0^2}} \left. \frac{\partial^2 U_-}{\partial \gamma^2} \right)_{\gamma^+_{\rm min}} \tag{6.15}$$

In the adiabatic basis, the eigenstates of the system take the general form:

$$\begin{cases} |\psi_-\rangle = \int_{-\infty}^{+\infty} \psi_-(\gamma)\ |\gamma, -\rangle\, d\gamma, \\ |\psi_+\rangle = \int_{-\infty}^{+\infty} \psi_+(\gamma)\ |\gamma, +\rangle\, d\gamma, \end{cases} \tag{6.16}$$

where $\psi_\pm(\gamma)$ are the wave-functions in the upper and lower manifolds. With the harmonic assumption, the levels in the two manifolds, shown in Fig. 6.8, are just the solution of the harmonic oscillator (see p. 499 in [125]), labeled by integers m, $n = 0, 1, 2, ...$, with energies:

$$\begin{cases} \left|\psi_+^m\right\rangle \rightarrow U_+(\gamma^+_{\rm min}) + (m + \frac{1}{2})\hbar\omega_+ \\ \left|\psi_-^n\right\rangle \rightarrow U_-(\gamma^-_{\rm min}) + (n + \frac{1}{2})\hbar\omega_- \end{cases} \tag{6.17}$$

An accurate determination of the eigenstates and eigenenergies could be obtained, if needed, by resorting to the semi-classical approximation, or by diagonalizing the Hamiltonian using this harmonic oscillator basis.

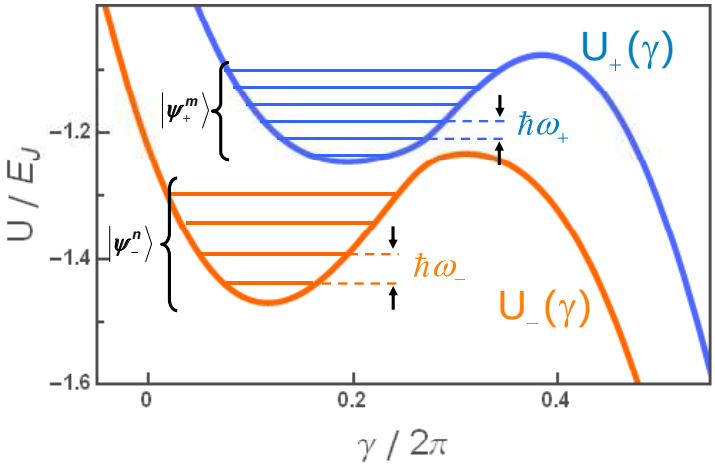

Fig. 6.7. Energy levels of a current-biased Atomic SQUID within the adiabatic approximation. The two Andreev manifolds live in the two different potentials $U_-(\gamma)$ and $U_+(\gamma)$. The curvature at the bottom of each well is different, this corresponses to two different plasma frequencies ω_- and ω_+.

Transition frequency

In the case of perfect phase-bias, the accessible transitions below 20 GHz appeared to be limited to a narrow phase range around $\delta = \pi$. We further develop this discussion for Atomic SQUIDs, where the transitions now take place from each populated state in the lower manifold to any other state in the upper manifold, which are empty at thermal equilibrium (the states in the lower manifold are populated according to Boltzmann distribution) (see Fig. 6.8).

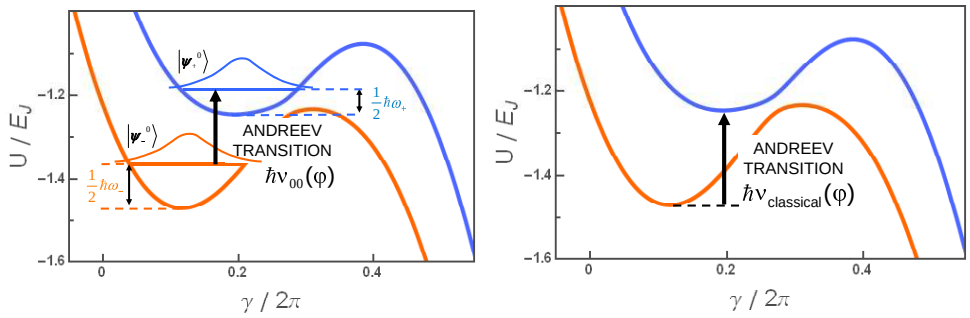

Fig. 6.8. Left: Scheme of the ground-state to ground-state transition $\hbar\nu_{00}(\varphi)$. The ground eigenstates levels in each potential $|\psi_-^0\rangle$ and $|\psi_+^0\rangle$ are shown as Gaussian curves in each well. **Right:** Scheme of the transition in the almost classical case $\nu_{\text{classical}}(\varphi)$.

With the levels determined in Eq. (6.17), the transition frequency $\nu_{nm}(\varphi)$ from the state $\left|\psi_-^n\right\rangle$ to the state $\left|\psi_+^m\right\rangle$ is given by:

$$\hbar\nu_{nm}(\varphi) = U_+(\gamma_{\min}^+) - U_-(\gamma_{\min}^-) + (m+\frac{1}{2})\hbar\omega_+ - (n+\frac{1}{2})\hbar\omega_-. \quad (6.18)$$

The ground-state to ground-state transition between the two manifolds, which is expected to be probed in the experiment, is thus at a frequency $\nu_{00}(\varphi)$ given by :

$$\hbar\nu_{00}(\varphi) = U_+(\gamma_{\min}^+) - U_-(\gamma_{\min}^-) + \frac{1}{2}\hbar(\omega_+ - \omega_-). \quad (6.19)$$

In the classical case, where the mass is large enough to neglect the zero-point motion, it reduces to:

$$\hbar\nu_{\text{classical}}(\varphi) = U_+(\gamma_{\min}^+) - U_-(\gamma_{\min}^-). \quad (6.20)$$

Knowing this, the question we need to answer for the experiment is the following: while measuring the modulation curve at low temperature, at what frequency should we irradiate the system to induce a transition to the ground state of the upper manifold? Clearly, we have to calculate the frequency along the modulation curve presented in Fig. 5.14 in Chapter 5. In other words we have to consider, for each value of the flux, the transition at a reduced bias current corresponding to a constant barrier height. In Fig. 6.9, we compare the two transition frequencies of Eqs. (6.19) and (6.20) calculated in this way, to the Andreev gap expected in the perfect phase-bias situation.

These transition frequencies can significantly depart from this ideal case. In the almost classical case, the lower the critical current of the junction the higher the minimal transition frequency, whose position is furthermore increasingly shifted in flux. This is due to the fact that, far from the perturbation case $E_J \gg \Delta$, there is a sizable shift between the potential minima $\gamma_{\min}^+$ and $\gamma_{\min}^-$. Therefore it is not possible to have them both simultaneously at the phase corresponding to the minimal transition frequency. Furthermore, when quantum fluctuations of the phase are significant (i.e. for larger plasma frequency), the transition frequency of Eq. (6.19) is appreciably increased compared to the Andreev gap and the almost classical case, due to the difference between the plasma frequencies ω_- and ω_+. In conclusion, with respect to the ideal phase-bias situation, the actual flux range for which the transition frequency is less than 20 GHz is shifted and narrower.

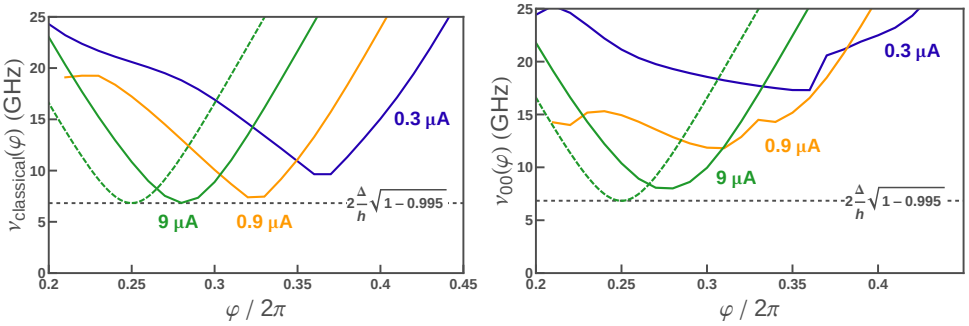

Fig. 6.9. Left: Transition frequency $\nu_{\rm classical}(\varphi)$ obtained from the difference between the minima of the adiabatic potentials, for $\tau = 0.995$ and three values of the critical current. This has been calculated along the modulation curve of Fig. 5.14, i.e. for a constant barrier height ΔU_-. The dashed curve corresponds to the ideal Andreev gap $\nu_A(\delta)$, expected in a perfect phase-bias situation. **Right:** Transition frequency $\nu_{00}(\varphi)$ of the ground-state to ground-state transition between the two Andreev manifolds, when considering a plasma frequency $\nu_{p0} = 30$ GHz for the junction alone, for $\tau = 0.995$ and three values of the critical current. This has been calculated along the same modulation curves as in the first panel. The dashed curve corresponds again to the Andreev gap $\nu_A(\delta)$.

Modification of the switching rate

When inducing a transition between the two Andreev manifolds, the escape rate gets modified because of the difference in the barrier height for both states. But is the rate increased or decreased ? And in particular, when operating at constant barrier height, as is done experimentally, what are the expected effects in comparison with the simple picture of Fig. 6.1 ?

To answer this question, we calculate, again along the same modulation curve as in Fig. 5.14, the quantity $\frac{\Delta U_+ - \Delta U_-}{E_J}$, when it is meaningful, i.e. when both potentials present a barrier.[1] This quantity, shown in Fig. 6.10, changes sign around $\varphi = \pi/2$, therefore in the region where the transition frequency is below 25 GHz (compare to Fig. 6.9). However, the transition frequency is not anymore centered at $\varphi = \pi/2$ for reasonable values of the critical current, therefore the simple picture of two opposite peaks looses its validity. The transition in this region is more complex than in the perfect bias case, and it is necessary to know for each flux whether the barrier height is increased or decreased to predict the expected change in switching current. **In particular, for some transition frequencies, the excitation could result in *two peaks in***

[1] For a small critical current, in some regions of the flux, the contribution of the lower Andreev state is sufficient to create a potential barrier in the full potential U_-, but because the upper Andreev state has an opposite contribution, the potential U_+ does not present a potential well.

***the same direction*, which is qualitatively different from what is expected in the case of ideal phase-bias.**

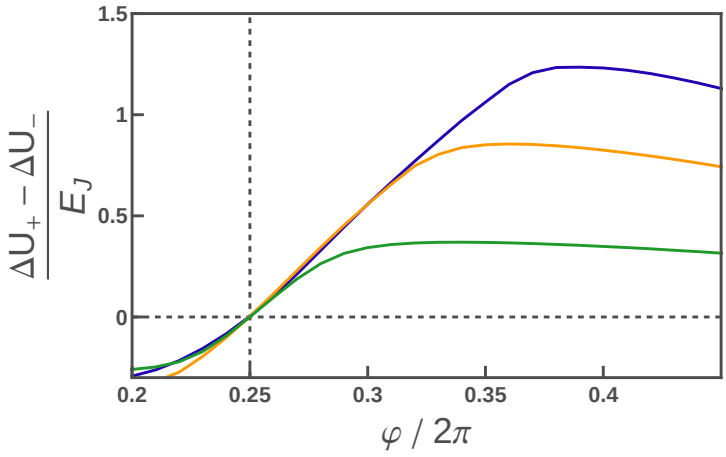

Fig. 6.10. Difference between the barrier height of the two potentials along the modulation curve for the same three values of the critical current as in Fig. 5.14.

Matrix Element for flux excitation

As compared to the perfect phase bias, the matrix element for a flux excitation now involves the wave-functions in each manifold. The matrix element between the state $\left|\psi_{-}^{n}\right\rangle$ and the state $\left|\psi_{+}^{m}\right\rangle$ incorporates the overlap between the wave-functions with the general expression:

$$M_{\perp}^{nm} = \int_{-\infty}^{+\infty} \psi^{n}(\gamma_{\min}^{-}, \sigma_{-})^{*}\, \psi^{m}(\gamma_{\min}^{+}, \sigma_{+}) \left\langle + \left| \frac{\partial \mathcal{H}_{AS}}{\partial \delta} \right| - \right\rangle d\gamma \tag{6.21}$$

In particular, one is interested in the ground-state to ground-state matrix element:

$$M_{\perp}^{00} = \int_{-\infty}^{+\infty} \psi^{0}(\gamma_{\min}^{-}, \sigma_{-})^{*}\, \psi^{0}(\gamma_{\min}^{+}, \sigma_{+}) \left\langle + \left| \frac{\partial \mathcal{H}_{AS}}{\partial \delta} \right| - \right\rangle d\gamma \tag{6.22}$$

The ground states in the two Andreev manifolds, denoted $\left|\psi_{-}^{0}\right\rangle$ and $\left|\psi_{+}^{0}\right\rangle$, have the ground state wave-functions of the harmonic oscillators depicted in Fig. 6.8:

$$\psi^{0}(\gamma_{min}^{i}, \omega_{i}) = \left(\frac{C_J \varphi_0^2 \omega^i}{\pi\hbar}\right)^{1/4} \exp\left(-\frac{C_J \varphi_0^2 \omega^i}{2\hbar}\left(\gamma - \gamma_{min}^{i}\right)^2\right) \tag{6.23}$$

The term $\left\langle + \left| \frac{\partial \mathcal{H}_{AS}}{\partial \delta} \right| - \right\rangle$ is the matrix element $M_\perp(\gamma + \varphi)$ calculated in the ideal phase-bias situation. A crude approximation for this matrix element $M_\perp^{00}$ is shown in Fig. 6.11, considering a junction with a plasma frequency of $\nu_{p0} = 30$ GHz. As can be seen from this figure, the matrix element is only slightly reduced when moving away from the perturbation limit.

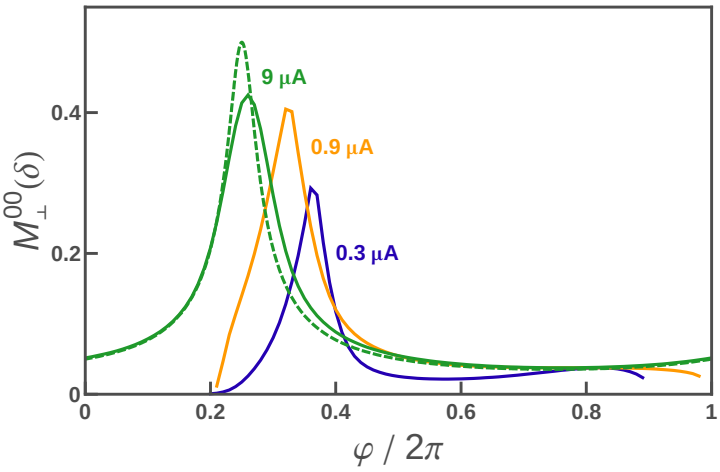

Fig. 6.11. Matrix element for flux excitation, calculated for the same three critical currents as in the previous figures, using the same width for the ground state wave-functions in both manifolds.

6.1.4 Beyond the adiabatic approximation

The decoupled manifold approximation has been always used up to now for analyzing experimental results on Atomic SQUIDs. We try here to go beyond this approximation in order to understand its validity range, evaluate the corrections, and treat experimental situations with large quantum fluctuations. This is done in a manner very similar to Fritz and Ankerhold [113], who treated the case of a simple current-biased atomic contact is treated.

Hamiltonian

In the reflectionless basis spanned by the states $|\gamma, \rightarrow\rangle$ and $|\gamma, \leftarrow\rangle$, the kinetic energy term takes a simple diagonal form. However, in the adiabatic state basis, the operator $p_\gamma = \frac{\hbar}{i}\frac{\partial}{\partial_\gamma}$ contains more terms than its restriction $\widetilde{p}_\gamma$ to the two manifolds because the adiabatic states vary with

γ. From the definition of the adiabatic states, one finds, in a conventional spin notation:

$$p_\gamma = \widetilde{p}_\gamma - \hbar(\theta'/2)' \hat{\sigma}_y^{AS}, \tag{6.24}$$

where:

$$\theta' = \frac{d\theta}{d\gamma} = \frac{r}{2} \frac{1}{1 - \tau \sin^2 \frac{\delta}{2}}. \tag{6.25}$$

The additional term in (6.24), which is non-diagonal, couples the two adiabatic manifolds. The full Hamiltonian written in the adiabatic basis $\{|\gamma, +\rangle, |\gamma, -\rangle\}$ is, in a matrix form:

$$H_{ASQUID} = \widetilde{H}_{ASQUID} + \frac{(2e)^2}{2C_J} \begin{pmatrix} \theta'^2/4 & \theta'' + \theta' \partial/\partial_\gamma \\ -(\theta'' + \theta' \partial/\partial_\gamma) & \theta'^2/4 \end{pmatrix} \tag{6.26}$$

where we called $\widetilde{H}_{ASQUID}$ the reduction to the two manifolds in the adiabatic approximation. This result is very similar to the one obtained in [113].

Eigenstates and eigenenergies beyond the adiabatic approximation

The Hamiltonian of Eq. (6.26) contains two types of corrections to the adiabatic Hamiltonian given in Eq. (6.13):

- The first one, associated to the diagonal part of the correcting term, modifies the potential term similarly for the two manifolds. However, the potential wells, whose minima occur at different values of the phase, are modified differently. Furthermore, θ' has a strong phase dependence in the vicinity of the phase $\delta = \pi$ for large transmissions. The small value of the charging energy $E_C = (2e)^2/2C_J \approx 30\,\mathrm{mK}$ makes however this correction small but for transmissions extremely close to one.
- The second correction, associated to the non-diagonal part of the correcting term, couples the two manifolds. It induces a small admixture of the adiabatic eigenstates, and yields a small change of their energies. This change, that can be readily evaluated using perturbation theory, is however small because the Andreev frequency is large compared to the coupling term.

6.1.5 Conclusion

We conclude that the adiabatic approximation provides a valid description of the Andreev states in an Atomic SQUID, but that their properties can significantly depart from the perfect biasing situation of a simple

atomic contact. We find in particular that fluctuations of the phase significantly increase the transition frequency compared to the perfect phase-biasing situation of a simple atomic contact, in particular the quantum fluctuations. This has important consequences for the observation of the Andreev transition, which is only possible in a very narrow range of parameters. We also conclude that the real part of the impedance across the contact must be very small in order to obtain a relaxation time comparable with the measurement time.

6.2 Design of an experimental setup

After this theoretical discussion on the requirements to excite and probe the upper Andreev state, realistic setups are now considered in this section. Using Sample AC1 presented in Chapter 5, we tried to excite the Andreev transition by adding a microwave current to the bias current of the SQUID. We did not observe any effect that could reliably be attributed to the excitation of an Andreev transition. We propose two tentative explanations for this failure:

- At microwave frequencies above a few GHz, the excitation current essentially flows in the shunting capacitor C_e, thus inducing only a small phase modulation across the contact, and hence a small population of the upper Andreev level.
- Following the discussion on relaxation given in the preceding section, the dissipation might have been too large in this sample to induce a sufficient population of the upper Andreev state, in particular due to the electrodes in gold.

Elaborating upon these considerations, we propose the following requirements for a new experiment on the spectroscopy of Andreev states:

- The excitation signal has to be coupled efficiently in the GHz range to the atomic contact.
- The dissipation in the environment of the atomic contact should be sufficiently small to achieve a long enough lifetime of the upper Andreev state, hence sharp spectroscopic lines.

Before discussing possible solutions, it is useful to point out the basic elements that any setup must contain (see Fig. 6.12):

- To measure the current in the atomic contact, a Josephson junction has to be connected in parallel. This junction, with a typical critical current between 300 nA and 1 μA and a typical size of 1 μm^2, has an intrinsic capacitance $C_J \simeq 100$ fF [87], and a characteristic plasma frequency $\nu_p \simeq 25$ GHz (for aluminum).

- Slow dc bias and measurements lines are needed to measure the $I(V)$ characteristics of the contact, to determine its transmissions, and to detect the voltage appearing at switching. The bias line includes a resistor $R \simeq 200\,\Omega$ as shown in Fig. 5.9, while large resistors are added on the measurement lines. In a crude approximation, the ensemble of these lines can be simply modeled as a single resistor $R_0 = 250\,\Omega$ in parallel with the junction (corresponding to R in series with the heavily attenuated $50\,\Omega$ bias line).

As seen from the atomic contact, the impedance $Z_{\rm bare}(\omega)$ of this minimal environment is:

$$Z_{\rm bare}(\omega) = \left(\frac{1}{R_0} + jC_J\omega + \frac{1}{jL_J\omega}\right)^{-1} \tag{6.27}$$

Using typical values for the Josephson junction, it appears that the dissipative part $\mathrm{Re}\,[Z_{\rm bare}(\omega)]$ is higher than $1\ \Omega$ in all the frequency range $[5 - 20\,\mathrm{GHz}]$ corresponding to accessible Andreev transition frequencies (see also Fig. 6.13 described further in text). This setup thus clearly does not meet the criterion on dissipation of Eq. (6.6) because the contact is not isolated from the resistor in the relevant frequency range.

6.2.1 Environment

Analysis of the previous setup

In the setup presented in Chapter 5 and sketched in Fig. 6.12(1), a large on-chip parallel capacitor $C_e = 20\,\mathrm{pF} \gg C_J$ is connected in parallel with the junction. In this case, the impedance seen from the atomic-sized contact is:

$$Z_C(\omega) = \left(\frac{1}{R_0} + jC_e\omega + \frac{1}{jL_J\omega}\right)^{-1} \tag{6.28}$$

Note that, in order to avoid the losses due to the spurious resistor r represented in Fig. 5.9, we have fabricated on-chip capacitors with superconducting aluminum electrodes. We therefore neglect r hereafter. This large capacitor has several functions:

- From the point of view of the atomic contact, it shunts the resistance of the measurement lines at large frequency.
- It filters spurious noise from the measurement lines.
- It reduces the plasma frequency of the junction at about 1 GHz, which ensures that switching occurs in the thermal regime.
- As a consequence, it also shunts the resistor R_0 in the range of accessible Andreev frequencies $[5 - 20\,\mathrm{GHz}]$, diminishing the dissipation.

However, as shown in Fig. 6.13, this setup fulfills only marginally the criterion on the dissipation of Eq. (6.6), and a better design is needed.

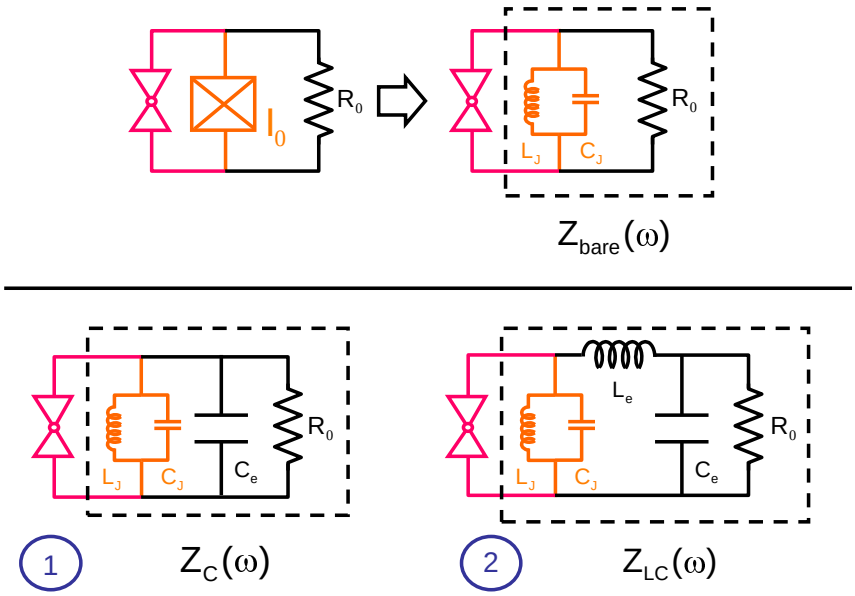

Fig. 6.12. Top: The atomic-sized contact is loaded by an impedance $Z(\omega)$. In order to measure the current-phase relation of the contact, this impedance consists at least of a Josephson junction and of a measurement and bias line, which is represented in a simple model by a resistor $R_0 = 250\,\Omega$. Considering the Josephson junction as the parallel combination of an inductor L_J and the intrinsic capacitance C_J, the simplest case is the impedance $Z_{\rm bare}(\omega)$. **Bottom - Left:** Previous setup presented in Chapter 5 corresponding to an impedance $Z_C(\omega)$, where the capacitor loading the junction is increased with a large extra capacitor C_e (left). **Bottom - Right:** New proposed setup corresponding to an impedance $Z_{LC}(\omega)$, where an inductance L_e is added between the Josephson junction and the capacitor C_e to decouple the superconducting loop from the outside world at high frequency.

New setup

Inspired by the work of the group of Olivier Buisson in Grenoble [126, 127, 128, 129], we consider now a new setup presented in Fig. 6.12(2), in which an inductance inserted between the large shunting capacitor and the junction reduces the dissipation seen from the atomic contact over a wide frequency range. In this case, the impedance of the environment is:

$$Z_{LC}(\omega) = \left(\frac{1}{jL_J\omega} + jC_J\omega + \frac{1}{jL_e\omega + \left(\frac{1}{R_0} + jC_e\omega\right)^{-1}} \right)^{-1} \tag{6.29}$$

This inductance enhances the high-frequency filtering provided by the large capacitor C_e, and the environment now presents two clearly separated modes:

- A high-frequency mode which is essentially the bare plasma frequency of the junction, thus close to $(L_J C_J)^{-1/2}$, slightly modified by the inductance of the environment. The corresponding frequency is

$$\nu_{\text{high}} \simeq \frac{1}{2\pi}\sqrt{\frac{1}{(\frac{1}{L_e}+\frac{1}{L_J})^{-1}C_J}}. \tag{6.30}$$

- A low-frequency mode corresponding to the LC-oscillator formed by L_e and C_e, slightly modified by the inductance of the Josephson junction:

$$\nu_{\text{low}} \simeq \frac{1}{2\pi}\sqrt{\frac{1}{(L_e+L_J)C_e}} \tag{6.31}$$

As can be seen in Fig. 6.13, in the frequency range of interest, this circuit allows to considerably reduce the real part of the impedance of the environment, down to below a mΩ, thus fulfilling the criterion on dissipation of Eq. (6.6). We have thus chosen to implement this new setup, in which dissipation due to the environment is expected to be reduced by at least one order of magnitude compared to the previous one.

6.2.2 Excitation

The population of the excited Andreev states has to be achieved through a modulation of the phase difference across the contact at the Andreev frequency in the range $[5-20\,\text{GHz}]$. Two methods are possible:

- As discussed in Chapter 5, a bias-current excitation $\Delta s \cos\omega_{\text{exc}} t$ can be applied to the Atomic SQUID, which should result in a phase excitation. However, the large capacitor C_e connected in parallel with the sample (see Fig. 6.12) shunts the Atomic SQUID at the relevant Andreev frequencies.
- A phase excitation can be obtained by adding an ac modulated flux $\Delta\varphi \cos\omega_{\text{exc}} t$ to the dc flux through the loop, as in [129]. The induced high-frequency current flows essentially in the superconducting loop provided that the environment presents a large enough impedance at that frequency. This is the case for the new setup with inductive lines.

In conclusion, to solve both the relaxation and the excitation problems we implemented a setup with an on-chip LC filter and a flux microwave antenna.

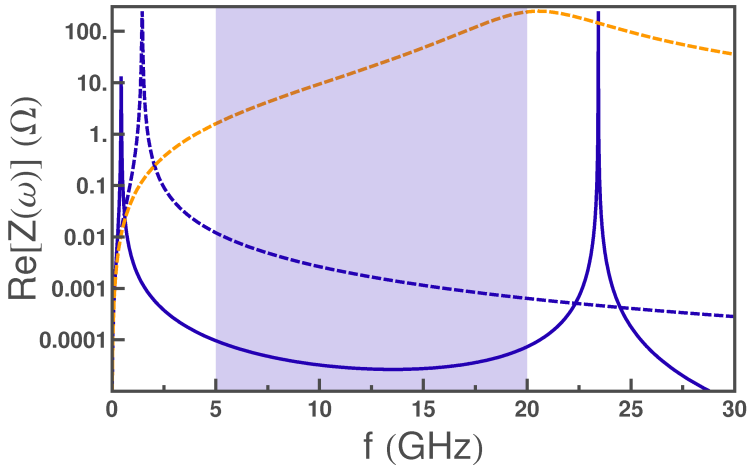

Fig. 6.13. Dissipation seen from the atomic contact for different setups. Shaded region corresponds to range of accessible Andreev frequencies. **Dashed orange line - Bare setup:** $\mathrm{Re}\,[Z_{\mathrm{bare}}(\omega)]$ corresponding to the simplest case where the Atomic SQUID consists only of a bare Josephson junction of inductance $L_J \simeq 0.6\,\mathrm{nH}$ and capacitor $C_J \simeq 100\,\mathrm{fF}$ in parallel with the lines of resistance $R_0 = 250\,\Omega$. **Dashed blue line - Previous setup:** $\mathrm{Re}\,[Z_C(\omega)]$, corresponding to the setup presented in Chapter 5, where a large capacitor $C_e = 20\,\mathrm{pF}$ is added in parallel of the Atomic SQUID, to lower the resonant modes around 1 GHz. **Solid line - New setup:** $\mathrm{Re}\,[Z_{LC}(\omega)]$ corresponding to the case where a low frequency LC-oscillator, with an inductance $L_e = 2\,\mathrm{nH}$ and lossless capacitor $C_e = 50\,\mathrm{pF}$, is placed in parallel with the Atomic SQUID. The environment now present two well separated modes.

6.2.3 Sample design

The proposed new setup is summarized in Fig. 6.14, with the following characteristics:

- The flux excitation is produced by a microwave current flowing in a superconducting wire close to the Atomic SQUID. To ensure a proper transmission of microwaves over a wide frequency range, the wire is placed at the end of a $50\,\Omega$ on-chip coplanar wave-guide.
- The Atomic SQUID has to be fabricated on a flexible substrate in order to break the metallic bridge, and control the opening of the atomic contact. In previous setups, this substrate was metallic. However, it is difficult to design a $50\,\Omega$ coplanar waveguide on a metallic substrate. For this reason, we decided to use Kapton wafers, an elastic insulating material.
- Efficient coupling of the microwaves at all frequencies can only be achieved with proper connections to the sample. However this is difficult to achieve in our case because the sample must be bent, and cannot therefore be rigidly attached. In the previous setup, the sample was connected using spring-loaded pins that could follow the bending

of the sample, but have very poor microwaves properties. In our new setup we clamp the sample on one side with two SMA launchers, and bend it from the other side, as shown in Fig. 6.14. These changes required to completely redesign the bending mechanism and the sample fabrication, as discussed in Chapter 7.

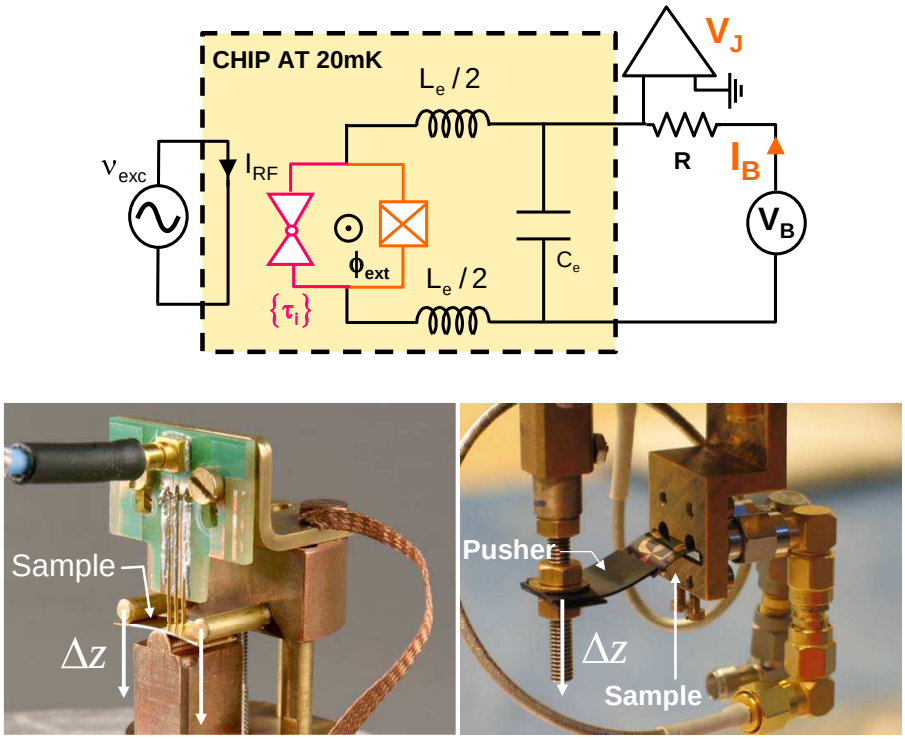

Fig. 6.14. Top: New setup for an Atomic SQUID experiment as compared to Fig. 5.9 (see text for details). **Bottom:** The new sample holder and bending mechanism (right) allows to properly contact the sample at all frequencies using SMA connectors, compared to the previous system (left). More details are found in Chapter 7.

6.3 Probing the new on-chip environment with a standard SQUID circuit

In order to test this two-mode electromagnetic environment, we performed an experiment on a sample (Sample SQUID) containing, in place of the Atomic SQUID, a dc-SQUID with two identical Josephson junctions (see Fig. 6.14). Because the loop is very small, this SQUID behaves

essentially as a single tunable Josephson junction [120], but the SQUID geometry has two important practical advantages:

- It allows to test the effect of the on-chip antenna, which is designed to couple through an induced flux.
- Applying a dc flux through the SQUID loop allows to tune its critical current, and thus to reduce its plasma frequency. Since it was not obvious before performing the experiment that the plasma frequency of the Josephson junction could be accessed with our microwave circuitry, limited below 25 GHz, this possibility ensured that the plasma frequency could be tuned within the accessible range.

6.3.1 Sample SQUID parameters

The parameters of Sample SQUID are presented in Fig. 6.15 and summarized in Table 6.1. The junctions, with an area $S \simeq 1.4 \times 0.65 = 0.9\,\mu\text{m}^2$ and a nominal capacitance of about 0.09 pF[2] each, have a normal state resistance of 400Ω at low temperature, corresponding to an expected critical current of 780 nA (see Eq. B.94). The inductance L_e was obtained using thin 1 μm-wide and 400 μm-long aluminum wires with normal state resistance $R_{\text{wire}} = 125\Omega$ at low temperature, similar to those in [127, 129]. The origin of the inductance of this wire is twofold:

- The geometric inductance, which for a wire of length l is $L_{\text{geo}} \simeq \mu_0 l$. The two lines had a length of 380 μm, resulting in a total nominal geometric inductance $L_{\text{geo}} \simeq 1.0$ nH. More refined formulas yield almost the same value.
- The kinetic inductance, which is due to the inertia of the Cooper pairs, can be calculated using Eq. (3. 125) in [58] which gives the complex conductivity of a superconducting wire. The expression for the kinetic inductance is
$$L_{\text{kin}} = \frac{\hbar}{\pi}\frac{R_{\text{wire}}}{\Delta} \tag{6.32}$$
which results in a total nominal kinetic inductance of the two lines $L_{\text{kin}} \simeq 0.1$ nH.

One thus expects a total nominal inductance $L_e \simeq 1.1$ nH. The large capacitor C_e has been designed on-chip with a nominal value of 55 ± 5 pF (measured at room temperature at 100 kHz).

From its geometry, the nominal inductance L_L of the loop is of the order of 25 pH, much smaller than the typical inductance $L_J = 0.3$ nH of one Josephson junction, as estimated from its normal resistance. In this

[2] we supposed here that the junction capacitance per unit area is 100 fF/μm^2 [87].

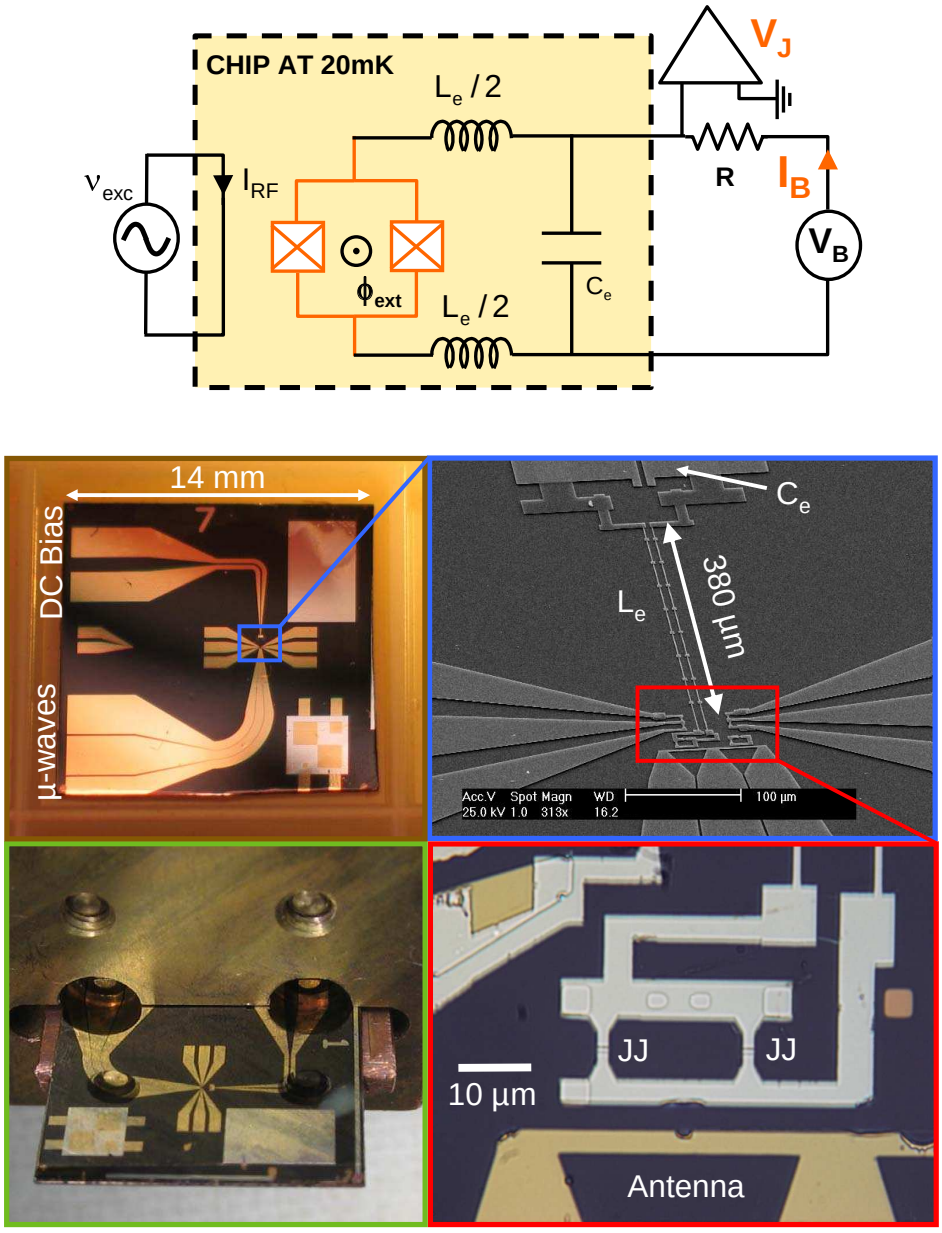

Fig. 6.15. Top: Schematic of the setup. A SQUID of two Josephson junctions of critical current $I_0 \simeq 0.75\,\mu$A each is connected to an inductive environment made of L_e and C_e. An on-chip antenna is realized with a wire placed close to the loop, which is able to induce a flux at high frequencies. **Bottom:** Pictures of Sample SQUID, taken at large scale with a binocular (top left) and at smaller scale with an optical microscope (bottom right) or a SEM (top right). The bottom left panel shows the sample holder.

Parameters	Nominal	Measured / Estimated
Junction R_J		400 Ω
Junction I_0	785 nA (AB)	750 nA
Junction C_J	0.09 pF	0.07 pF
SQUID bare plasma frequency	26 GHz	28.5 GHz
Environment C_e	55 pF	55 ± 5 pF
Wire R_{wire}	125 Ω	
Environment L_e	1.1 nH	0.7 nH
Environment bare frequency	0.65 GHz	0.8 GHz
Loop inductance L_L	25 pH	20 pH
Loop inductance asymmetry η		0.25
I_0 asymmetry α	0	0.01

Table 6.1. Parameters of the Sample SQUID presented in this section.

limit[3] the SQUID behaves as a single flux-tunable Josephson junction, as presented in Fig. 6.16. If the two junctions are identical, the critical current of the equivalent junction is simply:

$$I_0^S = 2I_0 \left|\cos\left(\frac{\varphi}{2}\right)\right| \tag{6.33}$$

where I_0 is the critical current of one junction.

6.3.2 I(V) characteristics

An $I(V)$ characteristics of Sample SQUID is shown in Fig. 6.17. This curve was taken at a flux value which maximizes the supercurrent branch at zero-voltage. The sizable sub-gap current and the gap back-bending behavior, typical of aluminum junctions, are discussed in the Appendix A.1.

6.3.3 Escape rate

Switching current & SQUID parameters

We measured the modulation of the switching current of the SQUID using the technique presented in [20] and in Chapter 5. One measures the escape probability as a function of the flux, and monitors the value I_{sw} corresponding to a constant escape probability $P = 0.6$. The resulting modulation curve is shown in Fig. 6.17. The switching current range from

[3] More precisely, using the notations of [120], one defines the parameter $b = L_J/L_L$. For large b, the two-dimensional potential of the SQUID reduces to a one-dimensional situation [120]. This is the case here, since $b \simeq 10$.

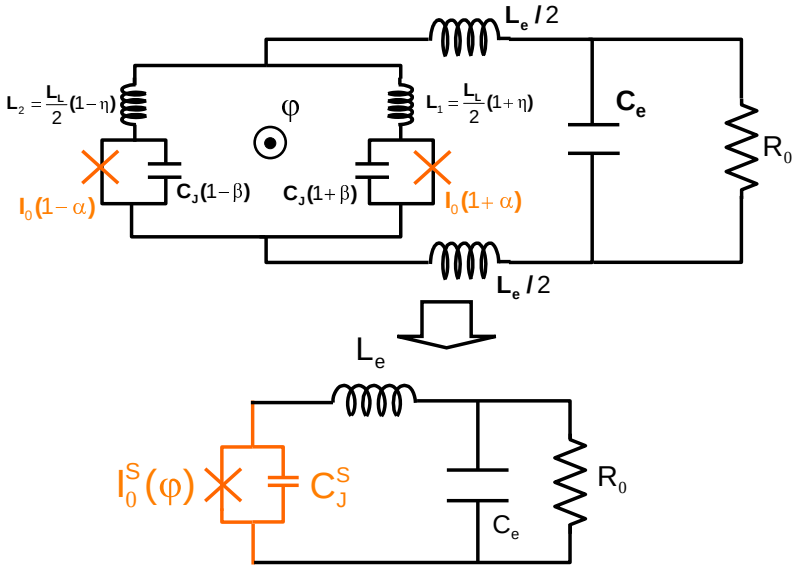

Fig. 6.16. Top: Complete nominal description of the setup in terms of lumped-element model. This includes asymmetries between critical current and capacitors of the junction, and asymmetries between the inductance of the two arms of the SQUID. **Bottom:** Simplified circuit that was considered here, under the assumption that the asymmetries in critical current and junction capacitors are small, and that the inductance of the loop is negligible compared to the Josephson inductance. The system reduces to a simple Josephson junction of flux-tunable critical current with a resonant circuit in parallel.

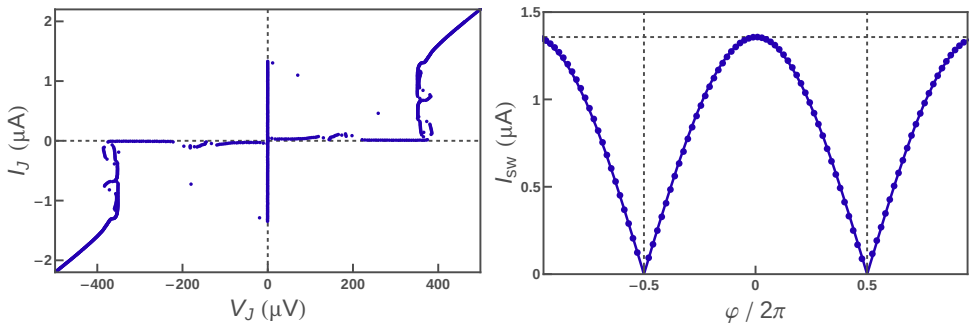

Fig. 6.17. Left: $I(V)$ characteristics of the SQUID for a flux $\varphi = 0$ that maximizes the size of the supercurrent branch. **Right:** Measured switching current $I_{\rm sw}$ (corresponding to an escape probability $P = 0.6$) as a function of the reduced flux (dots) and fit of the experimental result with Eq. (6.35), using $I_{\rm sw}^{\rm max} = 1.355\,\mu$A (solid line).

$I_{\rm sw}^{\rm max} = 1.355\,\mu$A to almost zero for some values of the flux.[4] Although the switching current differs from the critical current, it is well accounted

[4] Below 50 nA, the switching process is overwhelmed by spurious noise, and the switching current was no longer measurable with our setup.

for[5] by the expression:

$$I_{\mathrm{sw}} = I_{\mathrm{sw}}^{\max} \left| \cos\left(\frac{\varphi}{2}\right) \right|. \tag{6.34}$$

as seen in Fig. 6.17.

This good agreement between the simple modulation formula (6.34) and the measured values of the switching current is a first hint that the SQUID behaves as a single junction with fully tunable critical current.

We also measured the switching current for both positive and negative bias pulses. The difference $\Delta I_{\mathrm{sw}} = I_{\mathrm{sw}}^{+} - I_{\mathrm{sw}}^{-}$ between these two switching currents is shown in Fig. 6.18. The theoretical description of switching in a dc SQUID can be found in [120]. This work shows that, in most circumstances, the difference in switching current is equal to the difference in critical current. Moreover, this difference in critical current can be calculated numerically as a function of three parameters α, L_L, and η which correspond respectively to the asymmetry in critical current, the total inductance of the loop, and the asymmetry in inductance between the two arms of the SQUID (see Fig. 6.16). We neglected here the asymmetry in capacitance β between the junctions, since it is expected to be extremely small [120, 129]. The experimental curve of Fig. 6.18 is well fitted using $L_L = 20\,\mathrm{pH}$, $\eta = 0.25$ and $\alpha = 0.01$, and no other good combination of parameters can be found. This fitting procedure thus yields a determination of the parameters of the superconducting loop, and confirms both that the asymmetry in critical current is small and that the loop inductance is negligible as compared to the Josephson inductance, which validates the one-dimensional hypothesis.

The SQUID is hereafter treated as a single Josephson junction, for which the predictions for the switching out of the zero-voltage state presented in Chapter 2 apply.

Escape rate

Using the nominal parameters of the SQUID, the plasma frequency at $\varphi = 0$ is expected to be $\nu_{p0} = 28.5\,\mathrm{GHz}$ at zero bias, corresponding to a crossover temperature $T_{CO} = 220\,\mathrm{mK}$. At a fridge temperature of $T = 20\,\mathrm{mK}$, switching of the SQUID is thus expected to be due to Macroscopic Quantum Tunneling [51]. We have investigated both regimes:

- A first measurement of the escape probability as a function of the bias current was performed at 300 mK, a temperature higher than T_{CO}, but

[5] The absolute value of the flux threading the loop is not known, but the zero has been adjusted manually to compensate offsets.

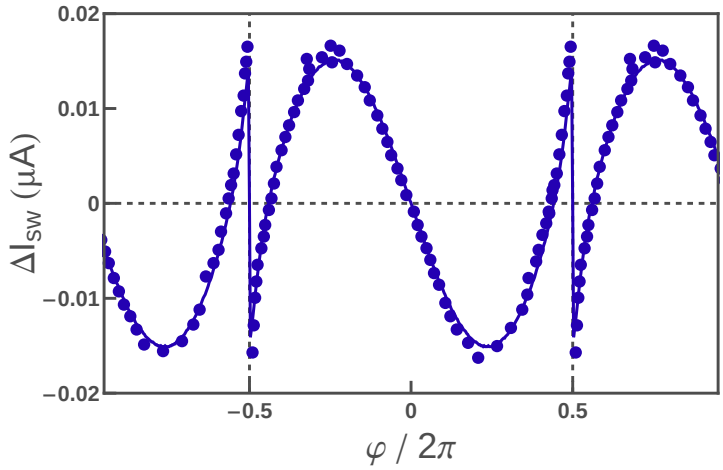

Fig. 6.18. Dots: Difference in switching currents $\Delta I_{\rm sw} = I_{\rm sw}^{+} - I_{\rm sw}^{-}$ measured for opposite signs of the bias current. **Solid line:** Best fit of the experimental result using numerical prediction for the difference in switching current (calculation presented in Appendix) that appears to be extremely similar to the difference of the critical current. This yields the values $L_S = 20$ pH, $\eta = 0.25$ and $\alpha = 0.01$.

still low enough for the critical current to have its zero temperature value, as shown in Appendix B.6. In the thermal regime, the environment weakly affects the escape rate, since it only enters its prefactor. Fitting this curve with the procedure presented in Section 4.4.1 and the expression (2.30) for the escape rate, one obtains $I_0 = 1.505\,\mu$A. We also checked that the critical current follows the prediction:

$$I_0(\varphi) = I_0 \left|\cos\left(\frac{\varphi}{2}\right)\right|. \tag{6.35}$$

- At lower temperature, the escape proceeds through MQT. The escape rate is expected to be strongly affected by the low-frequency mode of the environment, as described in Section 2.2.2 and in the Appendix of [64]:

$$\Gamma_q(T) = \Gamma_q(0) \exp\left\{-B_q \frac{L_J}{L_e}\left[\frac{5}{2} - 15\frac{k_B T}{\hbar\omega_p}\right]\right\} \tag{6.36}$$

in a perturbation approach assuming $\frac{L_J}{L_e} \ll 1$, $\hbar\omega_p \gg k_B T \gg \hbar\omega_e$ and for a sufficiently large quality factor for the low frequency mode of the environment. There are thus two combined effects : on the one hand, the environment modifies the quantum dynamics of the phase, which yields a first correction to the bare exponent B_q. On the other hand, the environment is also responsible for thermal noise at finite temperature, which induces fluctuations of the potential, and brings a second correcting term proportional to temperature. In this

experiment, the nominal value of the inductance L_e is 1.1 nH, while the Josephson inductance of the SQUID $L_J = \frac{\varphi_0}{I_0\sqrt{1-s^2}}$ is about 0.5 nH at $s = 0.9$ and $\varphi = 0$, and reaches much larger values when the critical current is reduced by applying the flux. Equation (6.36) is valid only well below the crossover temperature and for $\frac{L_J}{L_e} \ll 1$. **At this temperature and for such a low inductance L_e, the effect of the environment is probably not a perturbation of the MQT regime, and the expression (6.36) might not be valid for our whole range of parameters.** In Fig. 6.19, we present the escape probability as a function of the reduced bias current for four different temperatures, at $\varphi = 0$ (largest critical current and minimal inductance L_J). The fit of these curves with Eq. (6.36), considering $I_0 = 1.505\ \mu$A and $C_J^S = 0.14$ pF, yields an inductance $L_e = 1.5$ nH, reasonably close to our rough estimate 1.1 nH. However, experiments described below and probing the high frequency mode indicate that the actual inductance is smaller, and not larger, than our estimate. We attribute this discrepancy to the fact that the corrections to the escape rate arising from thermal fluctuations of the low-frequency mode of the environment are not accurately described by Eq. (6.36).

Although it was not possible to completely characterize the escape rate, it appeared that the reduced switching current $s_{\rm sw} = I_{\rm sw}/I_0$ was practically constant (~ 0.9) for all values of flux. Therefore, the switching current is proportional to the critical current, consistent with the good fit appearing in Fig. 6.18.

6.3.4 Frequency response under a flux excitation

In this section, we present results concerning the frequency response of our dc-SQUID, under a flux excitation.

Predictions

The resonance modes of the circuit, calculated assuming the SQUID is a tunable inductor, are the zeros of the total admittance $Y_{\rm tot}(\omega)$ as seen from the bias line. Using Eq. (6.29) and modeling the SQUID as the parallel combination of L_J^S and C_J^S, this admittance $Y_{\rm tot}(\omega)$ is:

$$Y_{\rm tot}(\omega) = (Z_{LC}(\omega))^{-1} = \frac{1}{jL_J^S\omega} + jC_J^S\omega + \frac{1}{jL_e\omega + \left(\frac{1}{R_0} + jC_e\omega\right)^{-1}} \quad (6.37)$$

and the two modes are given from Eq.(6.30) and Eq.(6.31) by:

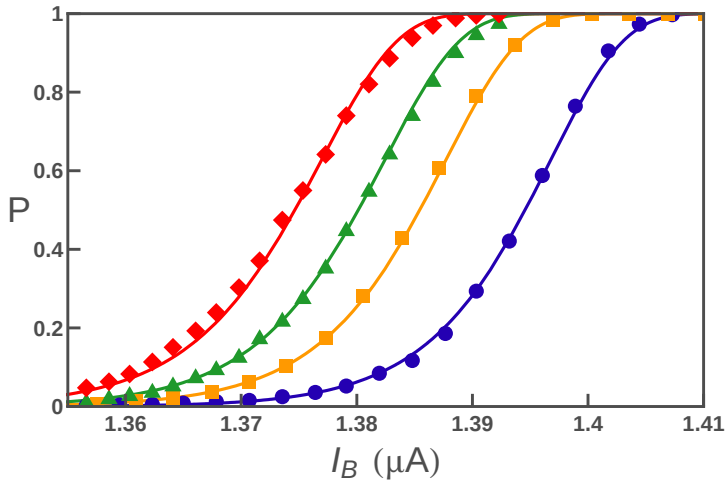

Fig. 6.19. Dots: Measured switching probability using a pulse length $\tau = 1\ \mu$s for four different temperatures (T = 35 mK (circles), 55 mK (squares), 65 mK (triangles) and 75 mK (diamonds)), at $\varphi = 0$ where the critical current is maximum. **Solid lines:** Fits using Eq. (6.36), considering $I_0 = 1.505\ \mu$A, $C_J = 0.14$ pF, $L_e = 1.5$ nH, and the temperatures T = 93 mK, 111 mK, 121 mK and 131 mK.

$$\begin{cases} \nu_{\text{high}} \simeq \frac{1}{2\pi}\left[(\frac{1}{L_e} + \frac{1}{L_J^S})^{-1} C_J^S\right]^{-1/2} \\ \nu_{\text{low}} \simeq \frac{1}{2\pi}\left[(L_e + L_J^S) C_e\right]^{-1/2} \end{cases}. \tag{6.38}$$

that differ from the bare plasma frequency ν_{p0} of the SQUID and the bare frequency of the environment ν_e:

$$\begin{cases} \nu_{\text{high}} \simeq \frac{1}{2\pi}\left[L_J^S C_J^S\right]^{-1/2} \\ \nu_{\text{e}} \simeq \frac{1}{2\pi}\left[L_e C_e\right]^{-1/2} \end{cases}. \tag{6.39}$$

The flux-modulation of the Josephson inductance:

$$L_J^S(\varphi) = \frac{\varphi_0}{2I_0\left|\cos\left(\frac{\varphi}{2}\right)\right|}, \tag{6.40}$$

leads to the flux-modulation of the two mode frequencies ν_{low} and ν_{high} shown in Fig. 6.20. The high frequency mode, which corresponds to the actual plasma frequency of the SQUID, is strongly affected by the inductance of the environment. When the critical current drops at $\varphi = \pi$, the inductance of the Josephson junction strongly increases and the bare plasma frequency of the SQUID goes to zero. But the actual high frequency mode of the full circuit does not follow this behavior because of the inductance of the environment. The actual plasma frequency of the

system is always larger than $\frac{1}{2\pi}\sqrt{\frac{1}{L_e C_J^S}} \simeq 16$ GHz. This frequency corresponds to a crossover temperature $T_{CO} = 120$ mK. As a consequence, at the lowest fridge temperature the escape rate of the SQUID should be dominated by MQT, whatever the flux.

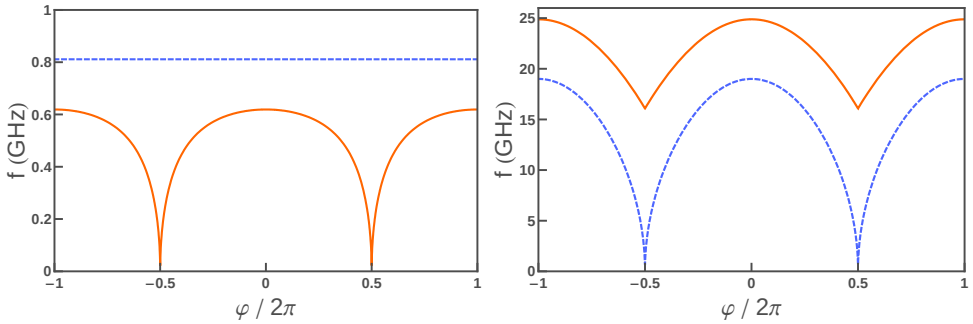

Fig. 6.20. Left: Low frequency mode $\nu_{\rm low}$ of the SQUID at $s = 0.9$ (orange solid line), compared to the bare resonant frequency of the environment ν_e (blue dashed). **Right:** High frequency mode $\nu_{\rm high}$ of the SQUID at $s = 0.9$ (orange solid line) compared to the bare plasma frequency ν_{p0} of the SQUID (blue dashed).

Experimental protocols

In order to probe the frequency response of the system to a flux excitation, we have measured the escape probability following two protocols:

- A constant flux-excitation at fixed frequency is applied, and the bias current of the dc-SQUID is modified to tune its modes.
- A constant bias current is applied, and the frequency of the flux-excitation is swept. This protocol could however be used only at low excitation frequency, because the transmission of the microwave line varies too much with frequency above a few GHz.

According to the phenomenon of resonant activation [59], one expects an increase of the escape probability when the excitation frequency approaches an eigenfrequency of the system. A similar experiment was performed in [127], and results of numerical simulations comparing flux excitation and bias-current excitation are shown in Appendix B.2, confirming this simple idea. Let us stress here that most of our experiments were performed at modulation amplitudes yielding an escape rate order of magnitudes above the thermal equilibrium value (in absence of excitation). Therefore, they cannot be described quantitatively by the well-known res-

onant activation theory [61], and in particular by the frequency response function of Eq. 2.39.

Flux line calibration

The mutual inductance between the antenna and the SQUID was measured, with 200 μA square pulses 4 μs long, to be:

$$M_\phi = 0.8\,\text{pH}. \tag{6.41}$$

In practice, this is enough to explore a flux range of about $\Delta\varphi = \pi/5$ without exceeding the critical current of the antenna.

High-Frequency mode

Following the first protocol presented above, the escape probability was measured as a function of the bias current in presence of a microwave excitation, at four different frequencies, and for a flux φ such that $I_0^S(\varphi) = 0.67\ \mu$A. The variations of the escape probability are shown in Fig. 6.21. Compared to a reference curve obtained without microwave excitation, the switching probability curve displays a broad peak around a current $I_{\text{RA}}(\nu_{\text{exc}})$ smaller than the switching current. Above this current, the escape probability recovers the behavior in absence of excitation. One observes that the value of $I_{\text{RA}}(\nu_{\text{exc}})$ decreases when the excitation frequency ν_{exc} is increased.

We attribute this broad peak to the excitation of the high frequency mode of the circuit, which agrees with the observed decrease of $I_{\text{RA}}(\nu_{\text{exc}})$ with ν_{exc}. This measurement, performed at large power, cannot be quantitatively compared with the resonant activation theory presented in [61], and we suppose that $I_{\text{RA}}(\nu_{\text{exc}})$ corresponds to the situation where the excitation frequency matches the local value of the high frequency mode. The poor transmission of the bias-current line prevented us from performing standard resonant activation experiments as detailed in [61].

The frequencies measured in this way are plotted in Fig. 6.22 as a function of the reduced bias current, and compared with the predicted frequency ν_{high}. From the best fit, we obtained the values $L_e = 0.7$ nH and $C_0 = 0.14$ pF . The figure also shows that the bare plasma frequency that would be expected in absence of the environment for the same capacitor, or even by adjusting the capacitor, would not fit the data. This comparison supports the fact that the high frequency mode is strongly pushed upward in frequency by the inductance of the environment.

In order to complete this description, we performed a measurement of the switching probability as a function of both the bias current and the

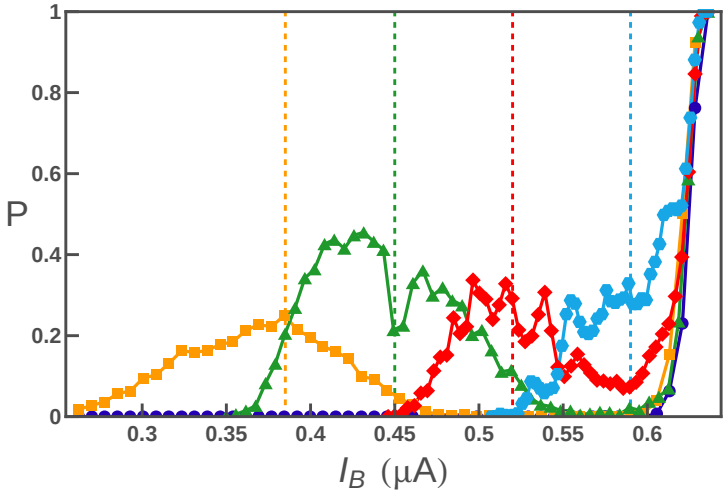

Fig. 6.21. Evolution of the switching probability when a microwave flux excitation is added through the antenna, taken a $\varphi = 0.35$ corresponding to $I_0^S = 0.67\,\mu$A. Different curves correspond to different frequencies (circles: no excitation, squares : 23.7 GHz, triangles: 22.7 GHz, diamonds: 21.7 GHz, hexagons : 20.7 GHz). Vertical grid lines correspond to the supposed frequency matching condition, whose positions are reported in Fig. 6.22.

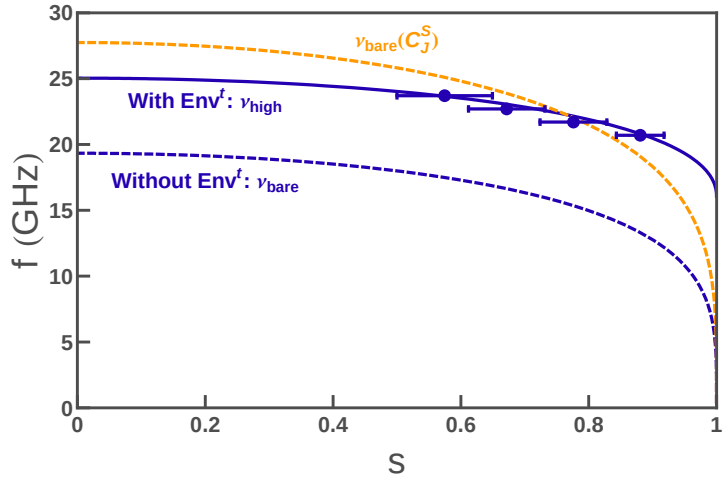

Fig. 6.22. Dots: Values of the local reduced bias current s and the frequencies corresponding to the bumps presented in Fig. 6.21 for $\varphi = 0.35$ resulting in $I_0^S = 0.67\,\mu$A. **Solid line:** Best fit for the high-frequency mode of the system, yielding $C_J^S = 0.14\,$pF, and $L_e = 0.7\,$nH. **Dashed blue line:** Prediction for the bare plasma frequency with same parameters. **Dashed orange line:** Best fit for the bare plasma frequency using the junction capacitance as a fitting parameter, and yielding $C_J^S = 0.07\,$pF.

flux under a microwave excitation at 24.3 GHz. The results are shown in Fig. 6.23.

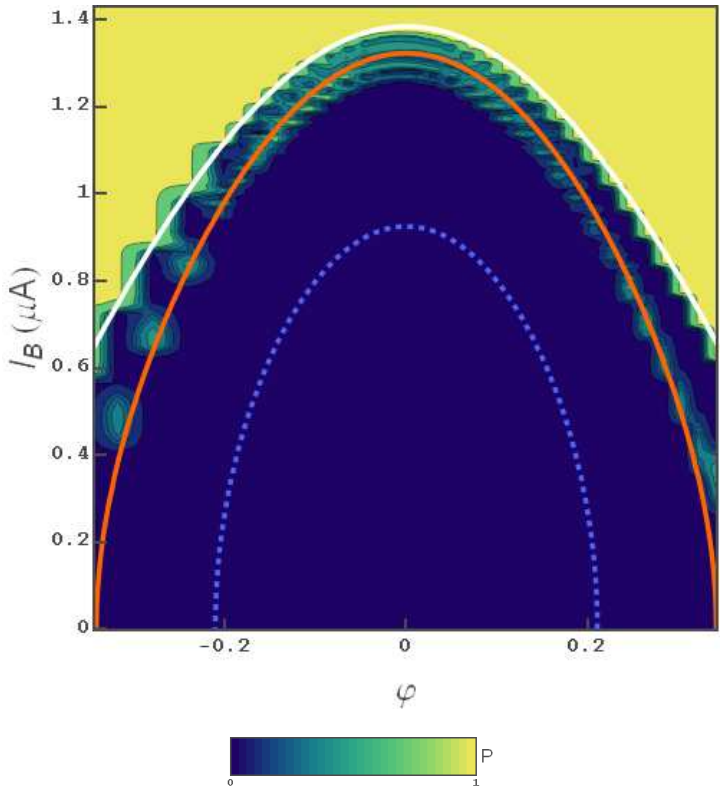

Fig. 6.23. Escape probability as a function of the flux and the bias current, when a constant microwave flux excitation at frequency 24.3 GHz is added on the antenna. The transition between $P = 0$ (dark) and $P = 1$ (bright) appears at the switching current $I_{\rm sw}$ already presented in Fig. 6.21. The bright spots below this transition correspond to the typical bumps shown in Fig. 6.21. **White solid line:** Predicted current-flux locus where the switching probability is $P = 0.5$ in absence of microwaves. **Orange solid line:** Predicted current-flux locus where the high-frequency mode matches 24.3 GHz. **Blue dashed line:** Locus where the bare plasma frequency matches 24.3 GHz.

The transition between $P = 0$ and $P = 1$ corresponds, as before, to the unperturbed switching current $I_{\rm sw}$. In addition, one observes, below the switching transition line, spots corresponding to the bumps appearing in Fig. 6.21, where the excitation frequency matches the high-frequency mode of the system. This figure also shows the locus where the high-frequency mode is expected to match the excitation frequency 24.3 GHz, considering again $L_e = 0.7$ nH and $C_0 = 0.14$ pF. The good agreement between this line and the position of the bumps further supports that the bumps are associated to the high-frequency mode of the circuit. For the sake of comparison, the line corresponding to the resonance condition for the bare plasma frequency is also shown.

In the range of flux close to $\varphi = 0$, the effect of the microwave excitation is not limited to the single bump visible in Fig. 6.21. As can be seen in Fig. 6.24, multiple bumps can be observed around the expected value for ν_{high}. This feature is not understood presently, but might be due to the simultaneous excitation of the high-frequency mode and the low-frequency modes, yielding different peaks at frequencies ν_{high}, $\nu_{\text{high}} + \nu_{\text{low}}, \ldots$

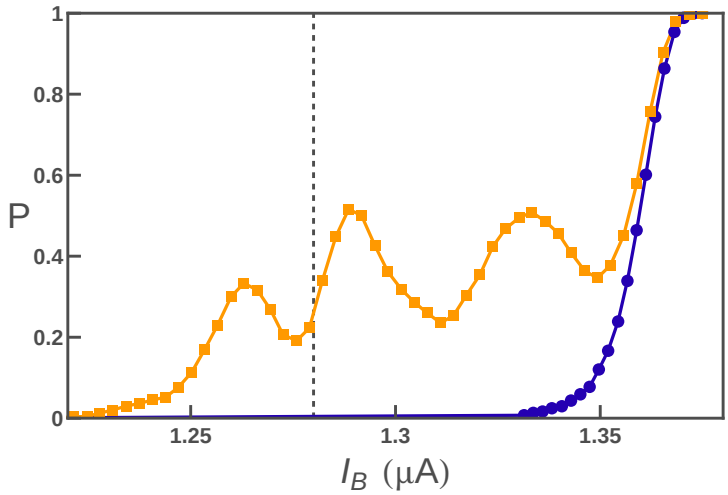

Fig. 6.24. Symbols: Escape probability without (circle) and with (squares) microwave excitation at 24.3 GHz. Close to $\varphi = 0$, the curve does not present just a single bump as in Fig. 6.21, but several distinct bumps. **Dashed line:** Predicted position in bias current where the excitation frequency matches the high-frequency mode, using the parameters extracted from Fig. 6.21.

Low frequency mode

The activation of the low frequency mode could be directly performed using the second protocol, in which the frequency is swept, because the microwave transmission of the flux line was roughly constant in the relevant frequency range. In absence of any excitation, the current was tuned to yield an escape probability $P = 0.1$. Then, the escape probability is monitored while a microwave excitation with varying frequency is applied to the flux modulation line, as shown in Fig. 6.25. A strong increase of the escape probability appears in the vicinity of 600 MHz.

This position of the peak, which can even be a double peak, is modified by the flux, as shown in Fig. 6.26 which reproduces the same measurement for all values of the flux. We attributed the peaks to the low frequency mode of the system, and compared it to the predicted values for the parameters $I_0 = 1.505\ \mu$A, $L_e = 0.7$ nH, $C_e = 55$ pF. Although

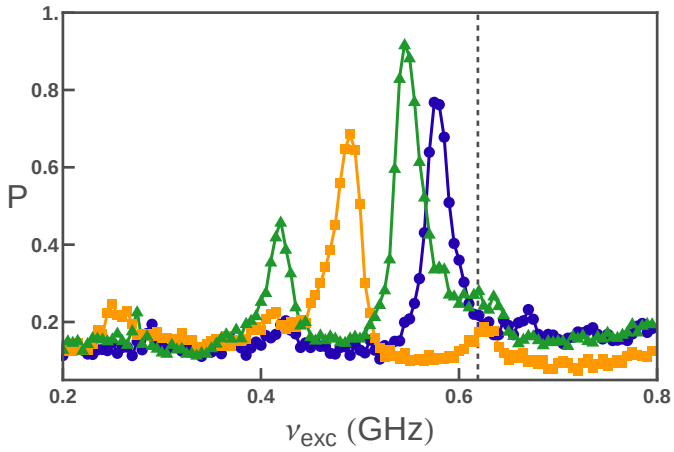

Fig. 6.25. Symbols: Measured escape probability under microwave excitation as a function of frequency. For three values of the flux ($\varphi = 0.2$ (circles), $\varphi = 0.35$ (triangles) and $\varphi = -0.45$ (squares)), the bias current is fixed in absence of microwave excitation to obtain $P = 0.1$. The excitation is then switched on, and the escape probability is monitored at the same bias current while sweeping the excitation frequency at constant power. **Dashed line:** Predicted maximum position of the low frequency mode with $I_0 = 1.505\,\mu$A, $L_e = 0.7$ nH, $C_e = 55$ pF.

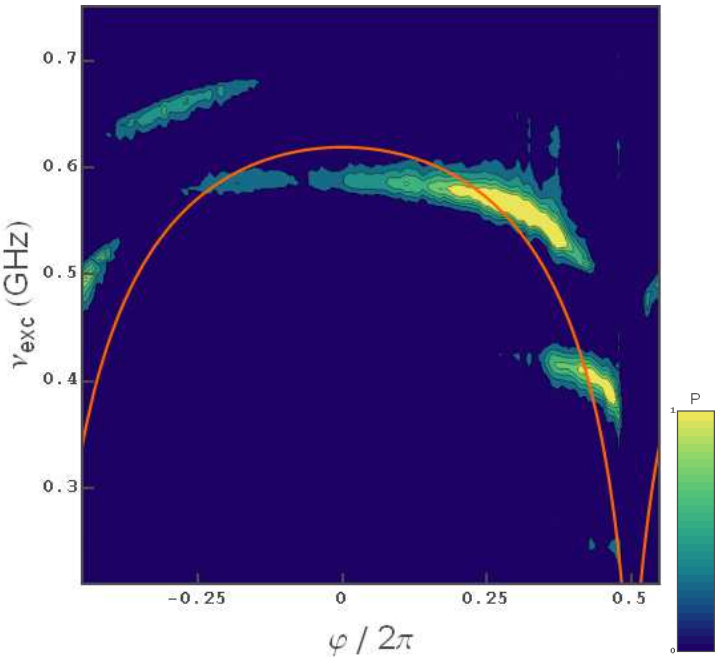

Fig. 6.26. Escape probability as a function of the flux and the excitation frequency. **Solid line:** Current-flux locus where the low-frequency mode matches the excitation frequency, for the same parameters as used in Fig. 6.25.

no quantitative comparison could be achieved, the peaks fall close to the predicted frequency for the low frequency mode. A tentative explanation for the splitting of the peaks at some values the flux, and for the overall behavior of the peaks, is to consider a coupling to modes of the large scale electromagnetic environment (typically the metallic box in which the sample is enclosed, which has a typical size of a few centimeters due to the large mechanical elements needed for the bending of the sample in experiments on atomic contact, see Chapter 7 for details).

6.3.5 Conclusion

Using a conventional SQUID geometry, we have characterized the parameters of the electromagnetic environment proposed for an Atomic SQUID experiment with a new design. We accessed the superconducting loop parameters using the difference in switching current for positive and negative bias current. From measurements of the switching rate of the system in the MQT regime in which the escape rate is strongly affected by the environment inductance, we obtained an estimated value for this added inductance L_e. Finally, we probed the two modes of this SQUID with a flux excitation fed trough the on-chip antenna. This SQUID experiment sets the stage for a new Atomic SQUID experiment aiming towards the spectroscopy of Andreev states, and operated in the quantum regime for the phase across the contact.

Part III

Sample Fabrication and Measurement Techniques

Chapter 7

Sample Fabrication

Most of the techniques used to fabricate the samples measured during this thesis are standard, based on optical/e-beam lithography and metal evaporation. However, the design of capacitors deserves some description, as well as the fabrication on bronze or plastic substrates, used in the experiments on atomic contacts. For completeness, we give in this chapter the detailed recipes that we employed in the fabrication of the samples for two types of experiments, noise detection (samples JJD) and atomic contacts (samples AC and SQUID).

7.1 Samples JJD for noise detection experiments

7.1.1 Large scale patterns

Samples JJD1 and JJD2 were fabricated on 2-inches, thermally oxidized high resistivity silicon wafers (10^3 to $10^4\,\Omega\,$cm), with nominal oxide thickness of 500 nm.[1] Using a high resistivity wafer avoids unwanted capacitive coupling between large electrode through the wafer. On this wafer, photo-lithography is used to define on-chip large contact pads, capacitors and resistors, using the masks shown in Fig. 7.1. For capacitors, we used a technique developed in the group by François Nguyen [130], in which each capacitor is obtained by two electrodes overlapping the same third electrode buried below a thin dielectric layer (silicon nitride). As a result, one obtains two capacitors in series. Mask B1 is used to define the bottom electrodes, fabricated out of Al. Silicon nitride is then sputtered on the whole wafer, and top electrodes are defined with mask C1. In a

[1] We measured 545 nm by interferometry, using a Filmetrics F20.

last step, resistors are fabricated using mask D6 and evaporation of thin chromium films.

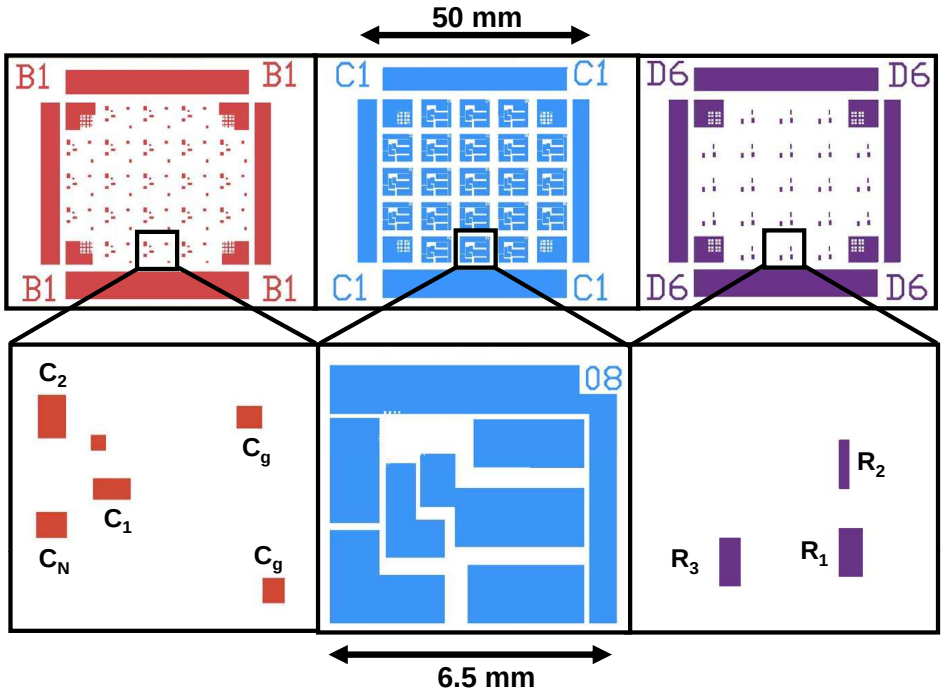

Fig. 7.1. Masks used for the photo-lithography for the Samples JJD1 and JJD2. Colored regions are transparent in the mask, while white areas are opaque. B1 defines the bottom electrodes of capacitors, C1 the large size electrodes and alignment marks for e-beam lithography, and D6 the resistors (Sample JJD2 only). Bottom panels represent the design at the scale of individual chips.

Masks fabrication

The masks for large scale patterns did not need to have a very high resolution, we therefore used a cheap method to obtain them: all masks are printed at once[2] using a high resolution laser printer (12000 dpi) on an A4 transparency foil, with an effective resolution of the order of 10μm. The pattern is then transferred on a chromium coated glass:

- the part of the transparency corresponding to one mask is sandwiched between a transparent glass and a glass coated with chromium and a positive optical resist (Clariant AZ5206);
- the sandwich is UV-exposed during 25 s using the MJB3 mask aligner (see Sec. 7.4.1);

[2] by MKM Electronique.

- after 50 s development in MF319, the chromium layer is etched chemically (50 s in chromium-etch) to remove it in the exposed regions;
- the remaining resist is removed in acetone, and the mask is cleaned with isopropanol.

First step: capacitors and large contact pads

- Using Mask B1, 30 nm-thick bottom aluminum electrodes are deposited with an electron-gun evaporator.
- The complete wafer is covered with a $\simeq 30$ nm-thick dielectric layer, silicon nitride ($\varepsilon_r = 7.5$), using magnetron sputtering [130].
- Using Mask C1, 30 nm-thick aluminum electrodes are deposited, defining an overlap with the bottom electrodes at places where capacitors are required. A 3 nm-thick gold layer is added on top to protect aluminum from oxidation, therefore facilitating further contacts to this layer. Alignment marks for e-beam lithography are defined at the same time.

The capacitance per unit area obtained using this method is

$$C_S = 2.35 \pm 0.2\,\mathrm{nF/mm^2}. \tag{7.1}$$

It is measured at 100 kHz using a RLC-meter (see [130] for more details). The sum A of the areas of the two overlaps forming each capacitance shown in Fig. 7.2 is given in Table 7.1 (the capacitance is $C_S A/4$). This technique produces very reliable and reproducible capacitors ($\pm 10\%$ spreading of the capacitance value and for 95% of them a leakage resistance larger than 5 MΩ).

Capacitor	Area ($\mathrm{mm^2}$)
C_J	0.00216
C_1	0.388
C_2	0.588
C_g	0.234
C_N	0.318

Resistor	Area ($\mathrm{mm^2}$)	Squares
R_1	0.55×0.45	0.8
R_2	0.24×0.48	2
R_3	0.55×0.45	0.8

Table 7.1. Left: Total overlap area of the capacitors produced in Samples JJD1 and JJD2 **Right:** Dimensions of the on-chip chromium resistors on Sample JJD2.

Second step: resistors

In Sample JJD1, the wafer was then prepared for electronic lithography and diced into chips. It is only after junctions were fabricated that SMC

resistors were glued on the sample using silver epoxy, in order to implement R_1, R_2 and R_3. As shown in Appendix A.2, the experimental measurements indicated that the thermalization of the resistors was not sufficient, and we decided to use a different technique for sample JJD2. We added a lithography step to fabricate the resistors with chromium thin films. Using Mask D6, a 10 nm-thick chromium layer was deposited by Joule evaporation at 0.4 nm/s, yielding a sheet resistance of the order of $215 \pm 20\,\Omega/\square$ at room temperature, $250 \pm 20\,\Omega/\square$ at 4.2 K

7.1.2 e-beam lithography

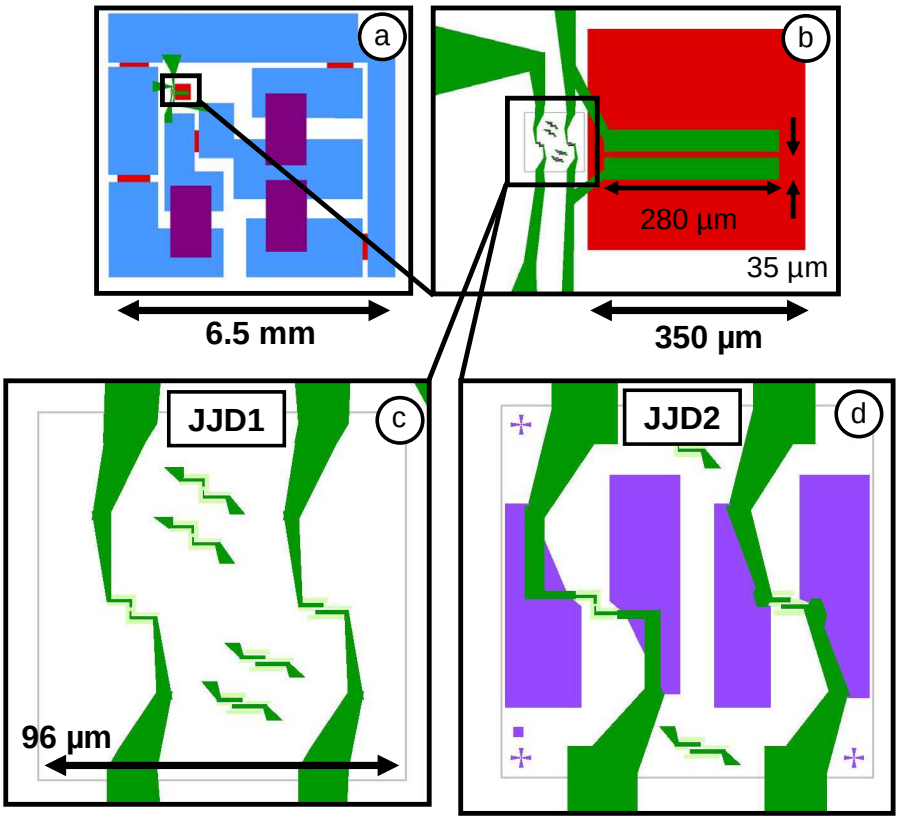

Fig. 7.2. e-beam lithography design (green) of the samples JJD1 and JJD2. (a) Overview at the scale of the whole chip; (b) zoom on the capacitor C_J, defined by the overlap with the red bottom aluminum electrode covered with silicon nitride; (c) junctions design of Sample JJD1, at the scale of the ×1000 writing field of the electron microscope; (d) junctions design of Sample JJD2, with gold quasiparticle traps (violet).

To prepare for e-beam lithography, the wafer is covered with a bilayer of electro-sensitive resist (MMA-MAA and PMMA) (see recipes in 7.4). A 7 nm-thick additional layer of aluminum is added on top of the resist to avoid charging effects during alignment on the aluminum marks, which requires a large current[3] (200 pA at 25 kV). The wafer is then diced.

Sample JJD1

Design The pattern shown in Fig. 7.2 is drawn in the resist by e-beam lithography. The exposure dose is 250 μC/cm^{-2}, except in two zones:

- the boxes defining the junctions, where the dose is 350 μC/cm^{-2};
- the so-called "undercut boxes", where the dose is reduced, typically down to 90 μC/cm^{-2}. In these regions, the dose is sufficient to expose the MMA, which is more electrosensitive that the PMMA. During development, the MMA is dissolved below the PMMA, which remains overhanging. This allows subsequent evaporation of metals under large angles.

The aluminum layer is removed during 1 min 30 s in KOH. The sample is then cleaned with isopropanol, developed for 35 s to 40 s in MIBK, and finally rinsed for 50 s in isopropanol.

Junction fabrication The PMMA bridge formed with e-beam lithography is used to form Josephson junctions using the shadow mask evaporation technique:

- a layer of 20 nm of aluminum is deposited at 1 nm/s at an angle +25°;
- the layer is oxidized at 30 mbar during 10 min in a mixture Ar/O_2 (80/20);
- a second layer of 80 nm of aluminum is deposited at the opposite angle, −25°.

The resulting overlaps are shown in Fig. 7.3. Using this procedure, it is possible to obtain junctions with areas S of the order of 1 μm^2 that have a resistance $R_J \simeq 500 \pm 50\,\Omega \times S/\mu\text{m}^2$. This value increases by 5% after two weeks at room temperature, and by 10% if the sample is placed during 90 min at 80°C. The resistance is more sample-dependent on smaller junctions, where edge effects probably play a significant role.

[3] Such a large current is needed to distinguish the aluminum pads below the resist.

On-chip resistors Resistors R_1, R_2 and R_3 are Surface Mount Components (Vishay P0603, series P, reference P0603Y2000 DB, with dimensions $1.52 \times 0.75 \times 0.5\,\mathrm{mm}^3$). They are glued on the sample with a conductive epoxy glue (Epotek EE-129-4) that reticulates at room temperature in 24 h. However, this glue appeared to be not sufficiently conductive and we added silver paint on top of it to improve the electronic conductivity.[4]

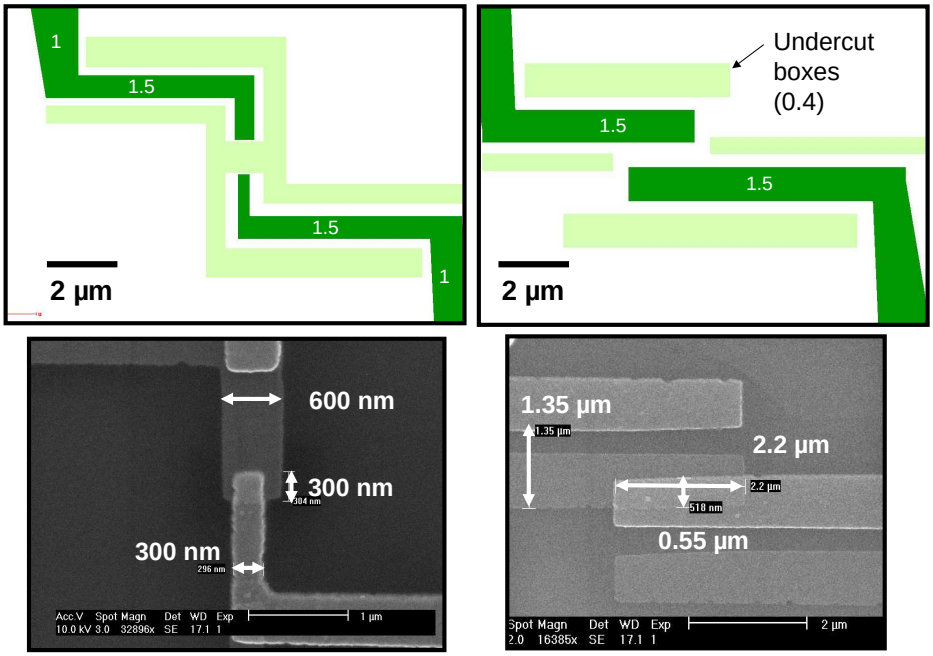

Fig. 7.3. Sample JJD1. **Left:** Noise source junction design (top) and micrograph (bottom). Numbers in the design indicate the relative exposure doses. **Right:** detector junction.

Sample JJD2

On Sample JJD2, we added quasiparticles traps to the previous design. Two e-beam lithography steps were thus needed:

- in a first step, the violet pattern of Fig. 7.2(d) is exposed, together with new alignments marks. This pattern is used to define the 30 nm-thick gold quasiparticles traps (a layer of 2 nm of Ti is deposited prior to gold to improve sticking). The sample is then covered again with a bilayer of MMA and PMMA, but thanks to the good contrast of the

[4] A better solution is to use the silver epoxy from CircuitWorks, that performs much better.

gold alignment marks, no additional aluminum had to be deposited on top;
- in a second step, the green area of Fig. 7.2(d) are exposed after alignment with the previous pattern, and the junctions are fabricated as for sample JJD1. One thus obtains large overlaps of the aluminum electrodes near the junctions and the gold quasiparticle traps.

7.2 Samples AC1 and AC2 for atomic contacts experiments

7.2.1 Wafer preparation

Atomic contacts are obtained by bending the substrate on which a suspended bridge was designed (see Chapter 5). The samples therefore need to be fabricated on a flexible substrate: silicon wafers cannot be used. For samples AC1 and AC2, we used commercial 0.3 mm-thick bronze plates (chrysocal, $CuSn_3Zn_9$), cut into 3-inches wafers. In order to allow microfabrication on it, the wafer must first be polished then planarized with a 2 μm-thick polyimide layer (for details, see [45]). It is then covered with a bilayer of MMA and PMMA. Since the wafer is conducting, no additional layer is needed here to perform the e-beam lithography.

7.2.2 Lithography

The whole design of the samples was defined by e-beam lithography.

e-beam lithography The design of samples AC1 and AC2 is presented in Fig. 7.4. On Sample AC1, the large scale patterns were designed in a first step, and realized with gold thin films: we deposited 30 nm of gold over 2 nm of Ti in the pattern shown in blue in Figs. 7.4(a,d,e). The sample was then covered again with the bilayer MMA/PMMA and an additional layer of 7 nm of aluminum to allow alignment with the second e-beam step (green in Fig. 7.4). On the contrary, sample AC2, for which all the electrodes were made out of aluminum, could be made in a single step. The metallic films were deposited with a two-angle evaporation:

- a 40 nm-thick layer of aluminum is deposited at a rate of 1 nm/s under a $+20°$ angle;
- it is oxidized at 15 mbar during 10 min in a mixture Ar/O_2 (80/20);
- a 60 nm-thick layer of aluminum is deposited at a rate of 1 nm/s under a $-20°$ angle.

The Josephson junction had an area of 1.2 μm^2. Using this procedure, we obtain for junctions with areas S of the order of 1 μm^2 a resistance $R_J \simeq 700 \pm 70\,\Omega \times S/\mu\text{m}^2$.

After the two angle evaporations of Al, one obtains two parallel images of the bridge. However, the window in the PMMA mask gets partially plugged during the first evaporation, and most of the time the second metallic bridge does not come out completely. Even if it does, only the last of the two bridges to break would be relevant anyway.

Etching To suspend the bridge, the polyimide underneath is etched in a reactive ion etcher (RIE). The sample is maintained at 200°C during the etching, by placing it on a hot, large metallic block before pumping the chamber of the RIE machine. This increases the etching rate and makes it more isotropic. The etching conditions are:

- flow of 50 sccm of O_2 and 2 sccm of SF_6 at a total pressure of 0.25 mbar;
- auto-polarization voltage close to 40 V.

The vertical etching depth is monitored by laser interferometry. Etching 1 μm in the vertical direction is sufficient to free the metallic bridge from the surface, and suspend it over $l = 2$ μm. Note that the junction was designed wide enough not to get suspended during this step.

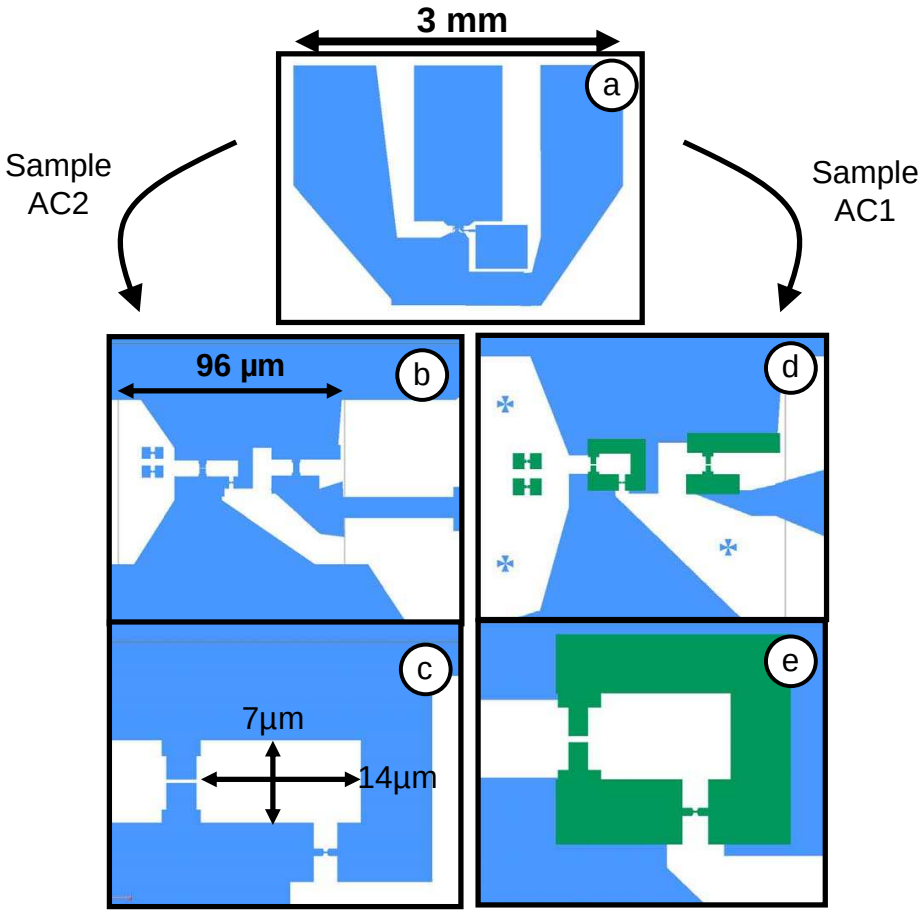

Fig. 7.4. e-beam lithography design for Samples AC2 (a,b,c) & AC1 (a,d,e), at large scales. For AC1, the design is performed in two steps (first step in blue, second step in green). The junction is obtained on the left arm of the loop, the suspended bridge on the bottom arm. When bent, the sample elongates in the horizontal direction.

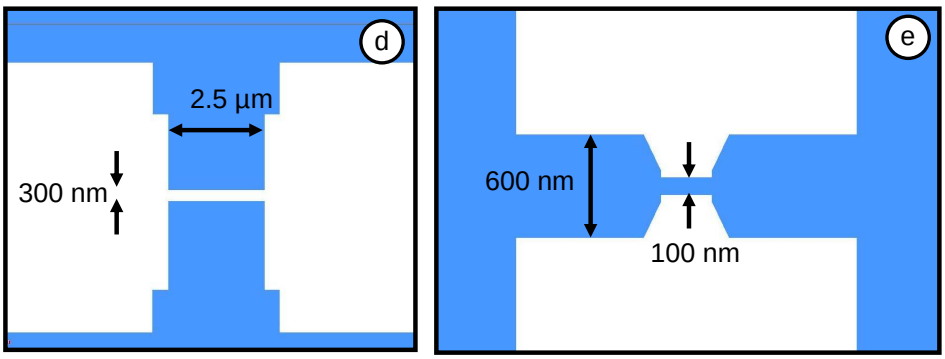

Fig. 7.5. Design of sample AC2**: left:** junction; **right:** metallic bridge

7.3 SQUID sample

7.3.1 Wafer preparation

Sample SQUID was fabricated on a chip prepared with the same large scale design of samples for Andreev-states spectroscopy. The goal is to achieve a good coupling of the microwaves to the flux line. We therefore designed a 50 Ω coplanar waveguide (seen on the bottom of Fig. 7.7(b)) with a central conductor that at the edge of the sample is large enough to match the central pin of a SMA launcher (see Fig. 8.3). This was only possible on an insulating substrate: it is not possible to obtain a 50 Ω coplanar waveguide with such a wide central conductor on the metallic substrate used for samples AC1 and AC2, which had only a 2 μm-thick dielectric. As a consequence, we moved to 500 μm-thick Kapton wafers (Kapton HN from DuPont), an insulating plastic material with $\varepsilon_r = 3.2$.

Kapton plates are first cut into 2 inches wafers. The wafer is polished using a polisher P320 MECAPOL from PRESI. To do so, the wafer is first glued with wax on a large metallic block:

- A rough polishing is then performed using Nylon disks and diamond paste with a 9μm-large grains, during 30 min at 150 rpm. This removes the largest scratches, and diminished the thickness of the wafer by typically 50 μm.
- Three fine polishing steps (6 μm, 3 μm, and 1 μm) follow, with soft disks at 150 rpm. The local residual rugosity is eventually of the order of 50 nm, with some deeper scratches.

Planarization is improved using a polyimide layer. We used a solution of pure PI2610 (HD MicroSystems). This solution is spun at 3000 rpm after a slow ramp of 30 s, terminated by 3 s at 6000 rpm to avoid edge effects. The wafer is baked 1 h in an oven at 180°C (baking on hot plate creates bubbles in the layer), and cured for one hour at 350°C in a vacuum chamber under a residual pressure of 10^{-6} mbar. The final thickness of the layer is typically 2.5 μm. This process reduces the local rugosity to less than 5 nm, and fills most of the scratches.

7.3.2 Photo-lithography

Four masks[5], shown in the top half of Fig. 7.7, are then used to fabricate (on seven chips 14 mm×14 mm per wafer), the capacitors (masks 1, 2 and 3), the quasiparticle traps (mask 4), the on-chip antenna and the large contact pads (mask 3). The chips are here significantly larger than

[5] Chromium masks fabricated on quartz by Toppan Photomasks.

samples AC1 and AC2 because their size is determined by the two SMA connectors making the contacts (see Fig. 8.3).

In this SQUID experiment, an LC environment is fabricated on-chip. The inductance is obtained with thin and long wires connected to capacitively coupled pads. In order to make the capacitors, we did not use the same method as described in section 7.1.1 because we were concerned with the mechanical response of silicon nitride when bending the substrate. The geometry of the capacitors remains the same: two electrodes overlap a common bottom electrode buried under the dielectric. We chose to use 5 to 10 nm-thick aluminum oxide (AlOx) as a dielectric. This is in principle thick enough to prevent any significant Josephson coupling. In practice the dielectric was obtained by depositing a stack of several 1.5 nm-thick layers, oxidized one-by-one. A difficulty with this method is that the edges of the bottom electrode are not completely covered with the thin AlOx layer, creating possibly short circuits with the top electrode. To circumvent this difficulty, we chose to coat the wafer with a new polyimide layer after the deposition of AlOx, and define openings on the bottom capacitor electrodes using mask 2, so that the edges remain covered with polyimide. In a last step we then deposit the top electrodes. Theses steps are illustrated in Fig. 7.6.

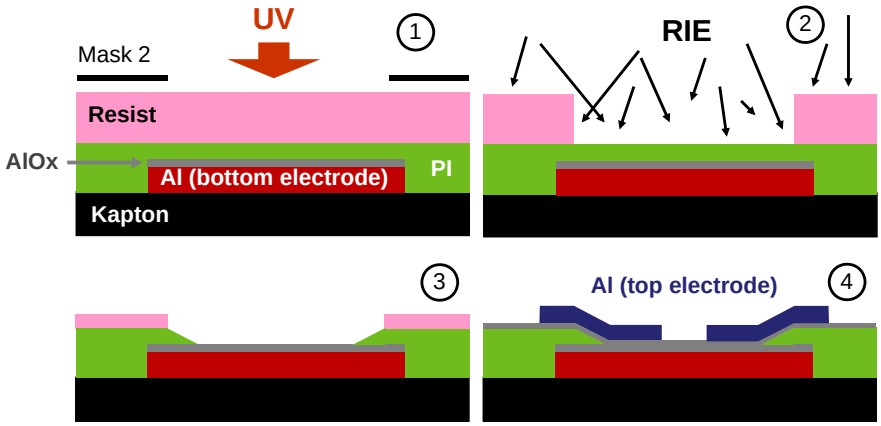

Fig. 7.6. Scheme for the fabrication of capacitor C_e for the SQUID sample. **Red:** bottom electrode (Al); **grey:** dielectric (AlOx); **green:** polyimide layer to protect the edges; **blue:** top electrodes (see text for details).

Mask 1: bottom capacitor electrodes

- The pattern of mask 1 is exposed on the resist bilayer LOL-S1805 (see recipe in section 7.4.1) to define the geometry for the 40 nm-

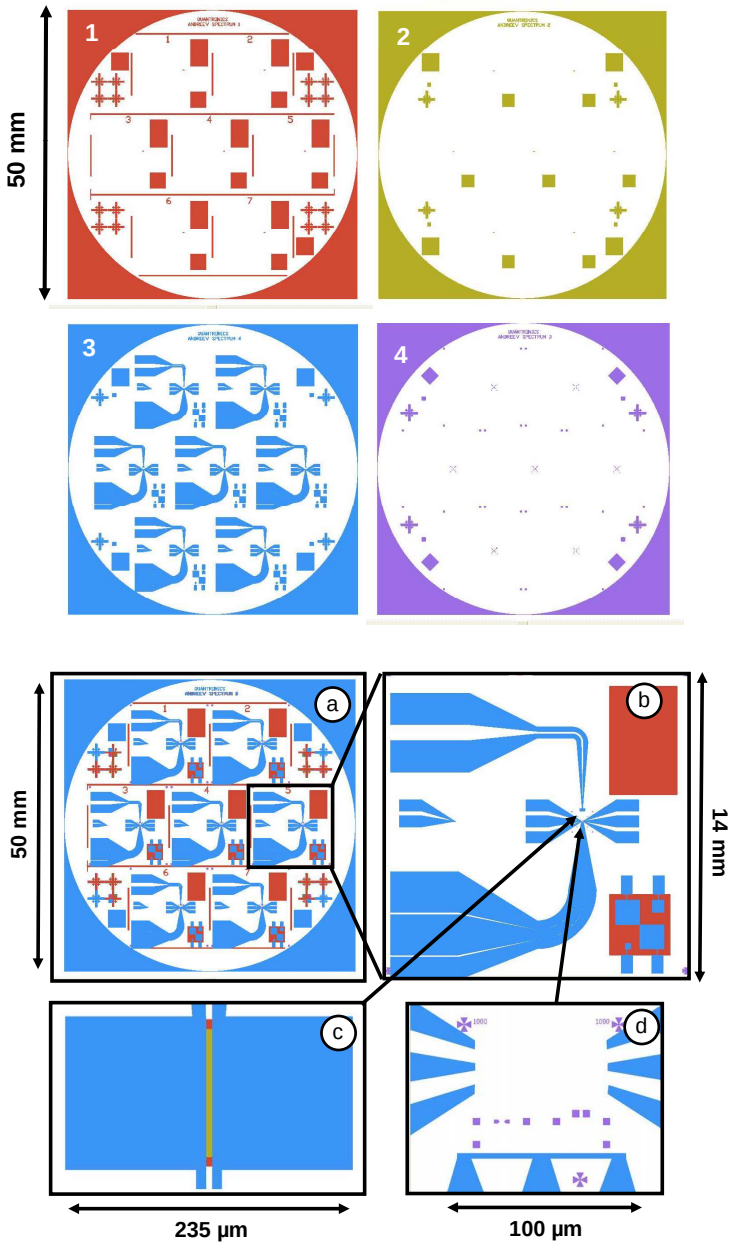

Fig. 7.7. Masks (1, 2, 3 and 4) used for Sample SQUID. Colored regions are transparent in the mask, while white areas are opaque. **(a)** Result of the overlap of the 4 patterns; **(b)** single chip; **(c)** capacitor C_e, with bottom electrode (red) and opening in polyimide (green) visible only between the two top electrodes (blue); **(d)** central region where the SQUID and the on-chip inductors are fabricated using e-beam lithography. The magenta squares are gold quasiparticle traps.

thick aluminum electrodes (deposition at 1 nm/s). To diminish the grain size, the films is deposited on the wafer held at low temperature ($\simeq -150°C$) using a liquid nitrogen flow cooling. After warming up to room temperature, it is oxidized during 15 min at 800 mbar in Ar/O_2 (80/20).

- Four 1.5 nm aluminum layers are deposited at room temperature, at a rate of 0.1 nm/s, each oxidized at 200 mbar during 5 min in Ar/O_2 (80/20).

Mask 2: openings in polyimide layer The next step is the deposition of the polyimide protecting layer: the polyimide layer is prepared with a solution of PI2610 and N-methyl-2-pyrrolidone mixed 1:1. This solution is spun for 60 s at 6000 rpm a using a slow starting ramp, then baked and cured as described in section 7.3.1. The final thickness, as measured by interferometry, is 150 ± 20 nm. It turns out that, after this procedure, the wafer slighlty shrinks by ~ 0.1 to 0.2% (which represents 5 to 10 μm on the diameter), which makes further alignment steps very delicate.

Using Mask 2 and the S1813 recipe, which gives a thicker resist (1.4 μm), windows are opened in the resist, then transferred in the polyimide layer by reactive ion etching in oxygen, until almost 900 nm of the resist is etched. Since the resist layer is much thicker than the polyimide layer, but is etched only twice as fast, this completely removes the polyimide layer. The remaining resist is eventually removed in acetone.

Mask 3: top electrodes and connections pads Using the third mask and the LOL+S1805 recipe, we deposited a new aluminum layer which defines the top electrodes of the capacitors and the large scale contact pads.

- Prior to the deposition of aluminum, the dielectric layer is made thicker: four 1.5 nm thick layers of aluminum are deposited at room temperature, at 0.1nm/s, and oxidized at 500 mbar during 5 min each;
- the 30 nm-thick aluminum layer is deposited at 1 nm/s at room temperature;
- to avoid the oxidation of this layer and facilitate the connection to it, we deposit on top of it a 3 nm-thick gold buffer layer at 0.5nm/s. This technique however was not satisfactory: spurious contact resistances between this layer and the next one were frequently found. We suspect the formation of a gold-aluminum intermetallic with poor conductivity.

With this technique, the capacitor $C_e = 55 \pm 5$ pF (corresponding to 5.5 ± 0.5 nF/mm^2) was obtained with a good reproducibility. However,

several capacitors presented a significant leakage (between 100 kΩ and a few MΩ). This leakage is nevertheless low enough to play no role in the experiment.

Mask 4: quasiparticle traps The last mask is used by applying the recipe LOL2000+S1805 to deposit quasiparticle traps (30 nm-thick gold layer on 2 nm of titanium).

7.3.3 e-beam lithography

The wafer is then prepared for e-beam lithography by deposition of a standard MMA/PMMA bilayer, plus a 10 nm-thick aluminum layer. This metallic layer is necessary to prevent charging effects on this insulating substrate. The substrate is then cut into samples using a guillotine. The design presented in Fig. 7.8 is exposed to obtain the SQUID loop and the inductive lines connecting to the capacitor:

- The two 380 μm-long, 1 μm-wide lines form the inductor L_e. At regular spacings, the lines are made wider. The reason is that, in the planned experiment with atomic contacts, the last fabrication step is the etching of the substrate to free the bridge. Since the lines forming the inductances are very narrow, they also get suspended: wider areas allow to anchor them on the substrate. A similar design was used in Ref. [44] for long resistive lines. This pattern is exposed with a dose of 400 μC/cm^{-2}.
- The loop containing the two junctions is aligned on the quasiparticles traps visible in Fig. 7.7(d).

Here, the exposed chip is developed for 50 s in MIBK:isopropanol 1:3. A two-angle evaporation is then performed:

- 20 nm of aluminum are deposited at 1 nm/s under an angle of +25°;
- oxidation follows at 6 mbar during 7 min in Ar/O_2 (80/20);
- finally, 80 nm of aluminum is deposited at 1 nm/s under an angle of −25°.

In the SQUID sample that was measured, the Josephson junctions had an area of 1.2 μm^2 and a resistance $R_J \simeq 400\,\Omega$.

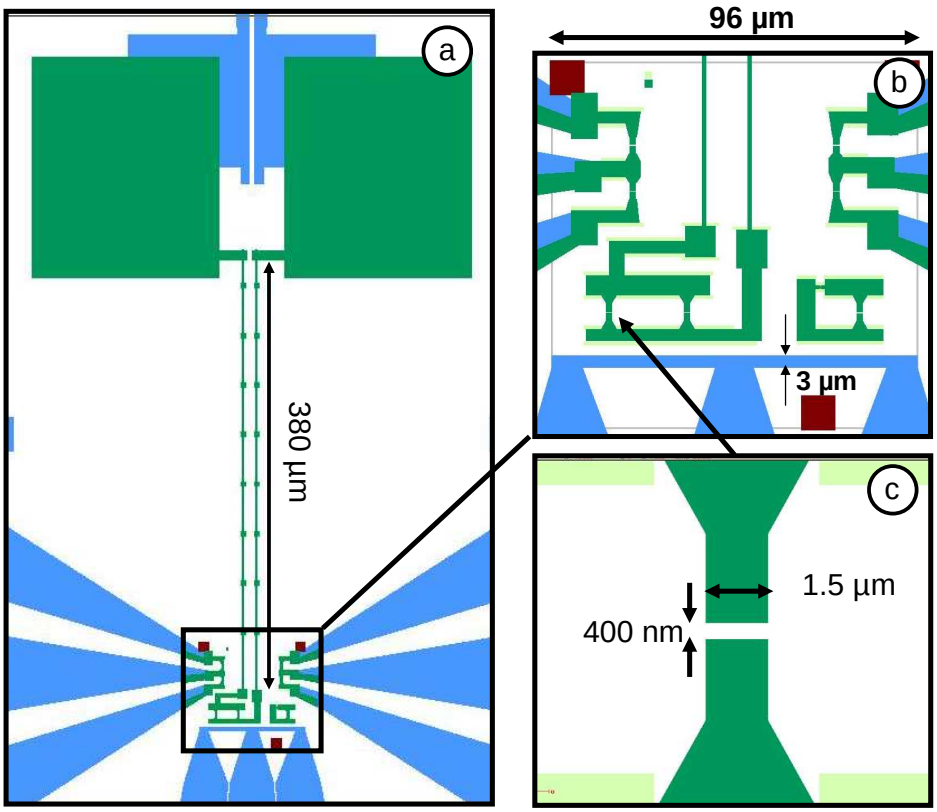

Fig. 7.8. E-lithography pattern of Sample SQUID.

7.4 Lithography recipes

The fabrication of the samples required both photo-lithography and e-beam lithography. The principle of the lithography relies on the use of resists coatings, sensitive either to UV light or to the electron beam. In both cases, multi-layers were used, first to improve the quality of the lithography, but also to allow angle evaporations. The exposed regions are dissolved in a development step, leaving cavities where metal can be deposited by evaporation. The remaining resist is then removed (lift-off process), and the metallic design is revealed. We give in this chapter the parameters of the various recipes that we used.

7.4.1 Photo-lithography

Resist-spinning

Prior to resist deposition, a primer (Shipley Microposit) is deposited on the wafer, and after 30 s waiting time, spun 60 s at 3000 rpm.

LOL2000 + S1805 recipe Filtered Shipley resist LOL2000 is poured and spun at 3000 rpm during 60 s , then baked at 155°C on a hot plate for 5 min, resulting in a thickness of typically 200 nm. Shipley resist S1805 is then poured and spun at 2000 rpm during 60 s, then baked at 120°C on a hot plate during 60 s. The layer thickness is 500 nm.

S1813 recipe Shipley resist S1805 is poured and spun at 4000 rpm during 60 s, then baked at 120°C during 60 s. The layer thickness is 1.4 μm.

Exposure

The wafer is then exposed through a chromium mask using a mask aligner. Two different mask aligners were used :

- A MJB3-SUSS Aligner (lamp with power density 5 mW.cm^{-2}). The exposure time is 15 s.
- A MJB4-SUSS Aligner (lamp with power density 25 mW.cm^{-2}). The exposure time is 3 s.

The wafer is developed using MF-319 (Shipley): 40 s for LOL2000+S1805, 90 s for S1813.

Lift-Off

After metal deposition, the resist is removed in acetone and ultrasonic bath during 2 min. In the case of LOL2000, the wafer is then dipped between 5 and 10 min in R1165 remover (Shipley).

7.4.2 e-beam lithography : MMA/PMMA bilayer

A scanning electron microscope is used to expose the pattern of a future mask on an electro-sensitive resist.

Resist spinning

- A bottom layer of meta-acrylate/meta-acrylate acid (MMA/MAA (8.5) EL 11 from MicroChem) is spun at 2000 rpm during 60 s, then

baked at 170°C on a hot plate for 60 s. This step is performed twice to obtain a thickness of 900 nm.
- A top layer of polymethyl-meta-acrylate (PMMA A6 950 from MicroChem) is deposited and spun at 5500 rpm during 60 s, then baked at 170°C during 15 min, yielding a typical thickness of 250 nm.

Additional conducting layer

In case of an insulating wafer (SQUID sample) or when one needs a large current to see aluminum alignment crosses below the resist (samples JJD), the wafer is covered with a few nm of Al, typically 10 nm deposited at 0.1nm/s, to avoid charging effects. After exposure, this layer is removed in a bath of KOH during 90 s, then cleaned with isopropanol. This additional layer does not change significantly the electronic lithography procedure, except in two cases:

- When the exposure current is large (above few tens of nA), the aluminum sometime gets damaged during the lithography and cannot be removed easily after exposure, which creates defects in the geometry.
- When the sample is left for too long in KOH (above two-three minutes), the PMMA gets slightly developed.

Exposure & Development

The sample is exposed in a Philips XL30 SFEG microscope using Elphy Quantum from Raith. The electron beam is steered on the areas of the resist that are to be removed. The time spent on each zone depends on the current, and is fixed to yield a typical charge density of $250\,\mu\mathrm{C/cm^{-2}}$ (fine details are exposed with a density increased by a factor up to 1.6). The exposure is performed with a beam current in the range of 15 pA for the smaller details, and up to 70 nA for coarse patterns (such a current results in a loss of resolution which is then unimportant).

The sample is then developed in methyl-iso-butyl keton (MIBK) diluted 1:3 in volume with isopropanol for 35 s to 55 s depending on the design (a longer development time allows larger undercut). This development removes both the exposed PMMA and the MMA/MAA. After this development step, the sample is dipped for 50 s in isopropanol.

7.4.3 Metal deposition and lift-off

Metals used in these experiments were deposited using two very similar electron gun evaporators (fabricated by PLASSYS). Pressures in the chamber are between 10^{-7} and 10^{-6} mbar depending of the evaporator.

The deposition rate is monitored through the resonant frequency of a crystal, typically 0.1 nm/s to 1 nm/s. The sample holder is carried by a rotating arm which allows to perform the evaporation at an angle. For details, see Ref. [36]. When needed, oxidation is performed by closing the loadlock containing the sample. A mixture of 80% argon, 20% oxygen is then let in the loadlock for $\sim$ 10 min. After deposition, the resist is removed in a hot acetone bath (65°C) during 20 min.

Chapter 8

Low-Noise Measurement Techniques

8.1 Sample Holder & Bending Mechanism

8.1.1 Samples JJD1 & JJD2

Samples JJD1 and JJD2 were glued with silver paint on a printed circuit board mounted on the sample holder shown in Fig. 8.1. Connections are done using aluminum wire-bonding. Copper brade is used to thermally connect the sample holder to a plate thermally anchored to the mixing chamber of a dilution refrigerator with a base temperature $T = 20\,\mathrm{mK}$.

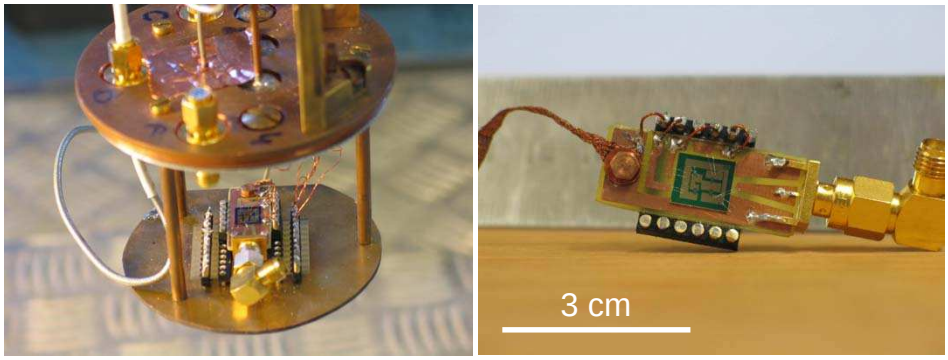

Fig. 8.1. Sample holder for the Samples JJD1 and JJD2.

8.1.2 Samples AC1 & AC2

For Samples AC1 and AC2, we used the mechanically controllable break junction technique (MCBJ) presented in details in [44, 45], based on the three point mechanism briefly presented in Chapter 5.

8.1.3 Bending mechanism

Sample SQUID was mounted in a new bending mechanism that we designed for further experiments on atomic contacts. Photographs and schematics views of the setup are shown in Figs. 8.2 and 8.3. The sample is held on one side by two screws pressing the sample against two SMA launchers. A pusher, seen on the left side of Fig. 8.3(b), pushes the opposite end of the sample downwards.

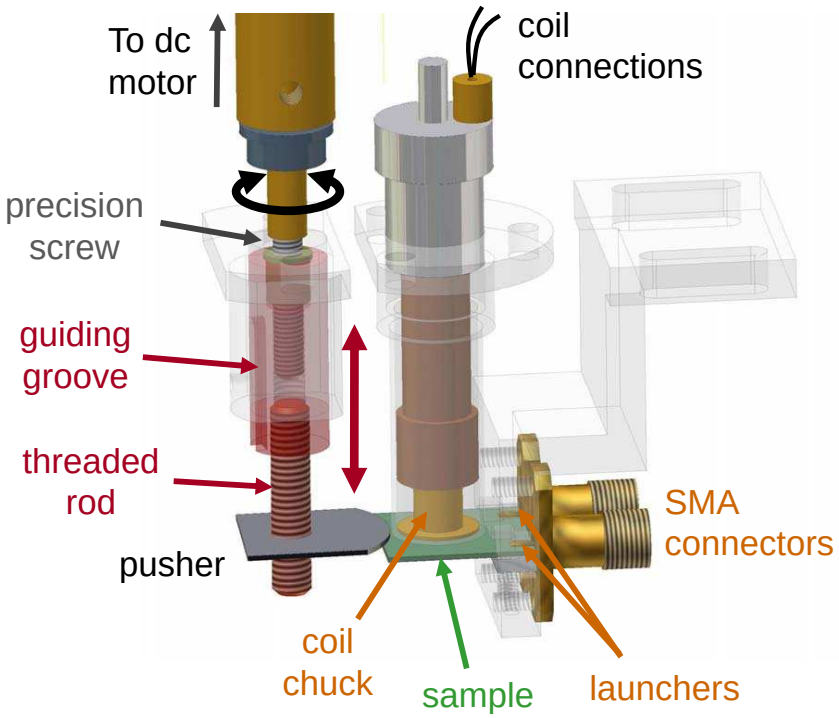

Fig. 8.2. Setup for sample holder, coil holder and bending mechanism. Transparent parts are all screwed on the same copper plate, attached to the mixing chamber of the fridge. On the left, the bending mechanism: a precision screw, driven by a room temperature dc motor, makes a threaded rod move up or down along a guiding groove, which prevents the rod from rotating. A second screw attached to the rod holds a Kapton pusher (grey), which presses at the free end of the sample (green) held on the other side by the two SMA launchers. A superconducting coil with 5 mm inner diameter (only the coil holder is shown) is placed less than 1 mm above the sample. It is screened by a thin metallic cup (transparent).

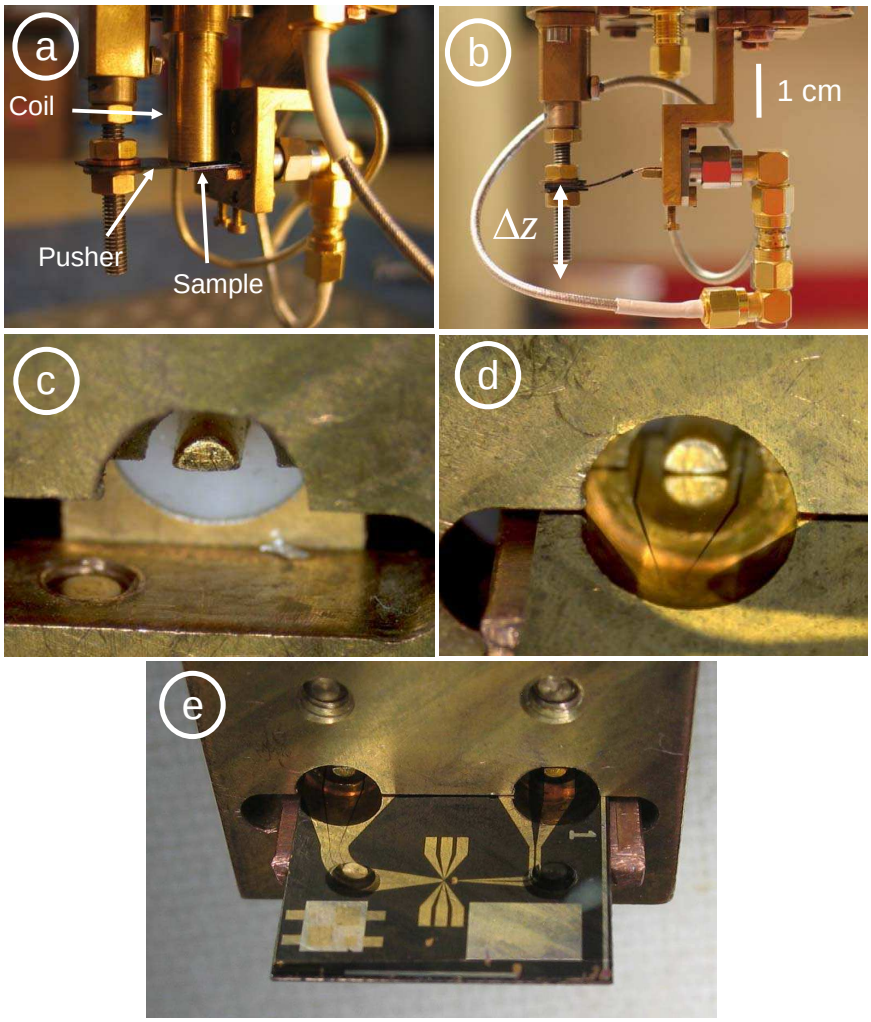

Fig. 8.3. Sample holder designed for Andreev states spectroscopy and used for the measurements on sample SQUID. **(a,b)** The sample (14 mm×14mm, 500 μm-thick Kapton substrate) is held tightly against two SMA launchers, by pushing with two screws a small piece of copper, also visible in **(d)** and **(e)**, on the back of the substrate. A small superconducting coil is placed in a copper electrostatic shield placed immediately above the sample (the coil is absent in **(b)**). In **(a)**, the sample is not yet bent, in **(b)** it is noticeably strained. **(c)** SMA Launcher, without sample; one of the pushing screws shows out on the bottom left; **(d)** SMA launcher with sample: the pin contacts the central line of the coplanar waveguide on the sample; **(e)** sample in position (coil and pusher removed) The right launcher connects to the current bias line. The left to the microwave antenna.

8.2 Cryostat wiring

All the experiments were performed in an Oxford Instruments Kelvinox 300 dilution refrigerator. Electrical connections are performed using:

- for low-frequency measurements, four lossy twisted pairs connections acting as RC distributed filters above a few MHz. Each of theses lines was equipped, at the lowest temperature stages, with a micro-engineered RC distributed low pass (below a few MHz) filter [131, 132] and inductive filters (see in [36]).
- for pulses and microwave excitations, three large bandwidth coaxial lines (-20 dB at 20 GHz in absence of additional attenuators). Various MiniCircuits LC filters reduce the bandwidth to the desired range.

A large attenuation (typically 50 to 60 dB) is necessary to reduce the amplitude of the Johnson-noise associated to the room temperature impedances [131] and make it comparable or smaller than the noise of the impedances placed at 20 mK. Large amplitude signals are therefore used at room temperature, and thermally anchored attenuators are placed at each stage. The wiring used for each experiment is presented schematically in Figs. 8.4, 8.5, and 8.6.

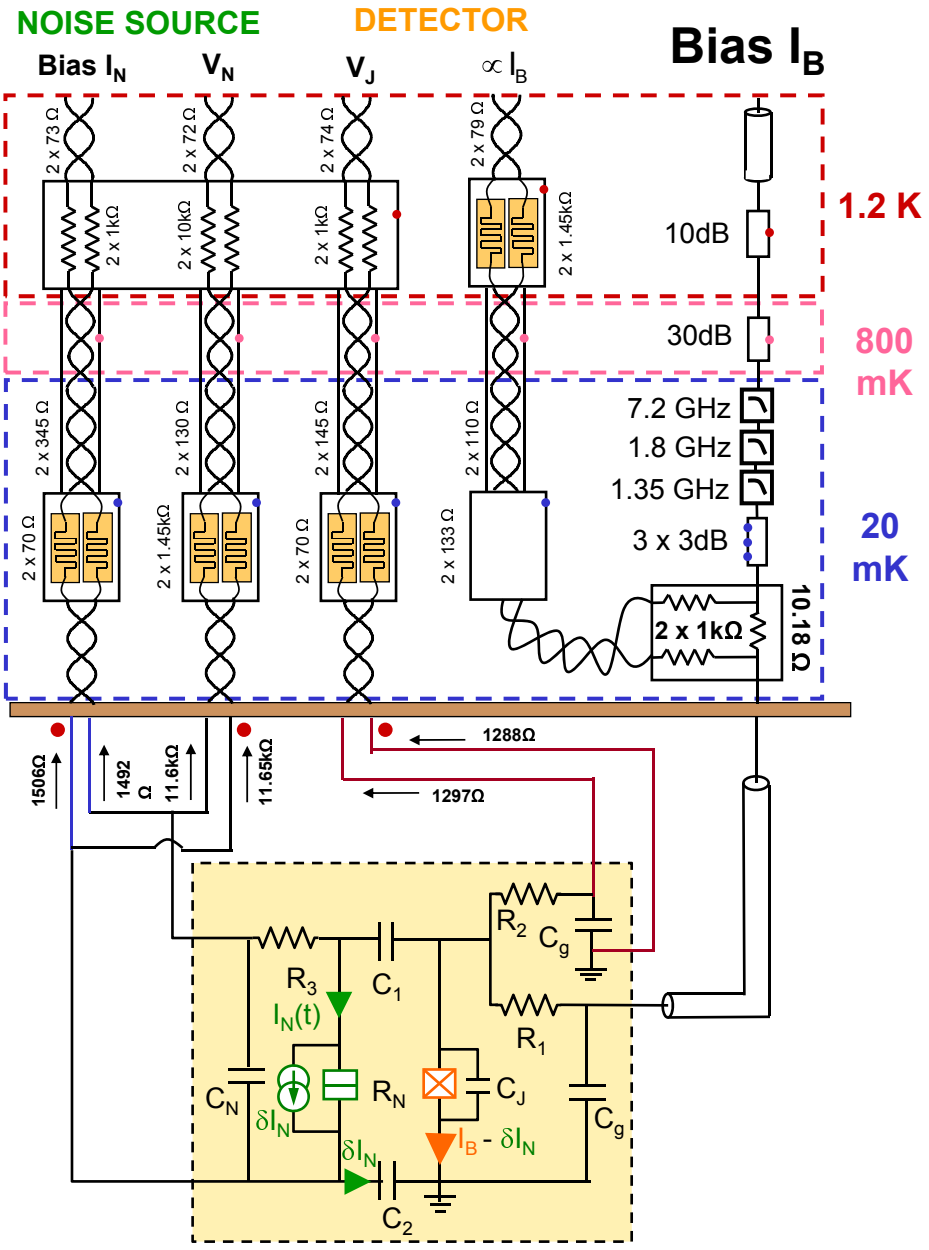

Fig. 8.4. Cryostat wiring used for samples JJD1 and JJD2. The boxes with meander lines symbolize home-made micro-fabricated filters. The figures just below the brown plate indicate the total resistance of each line (at room temperature). The bias line is equipped with commercially available attenuators and low-pass filters. The bias current is determined accurately from the voltage across a 10.18 Ω placed at 20 mK.

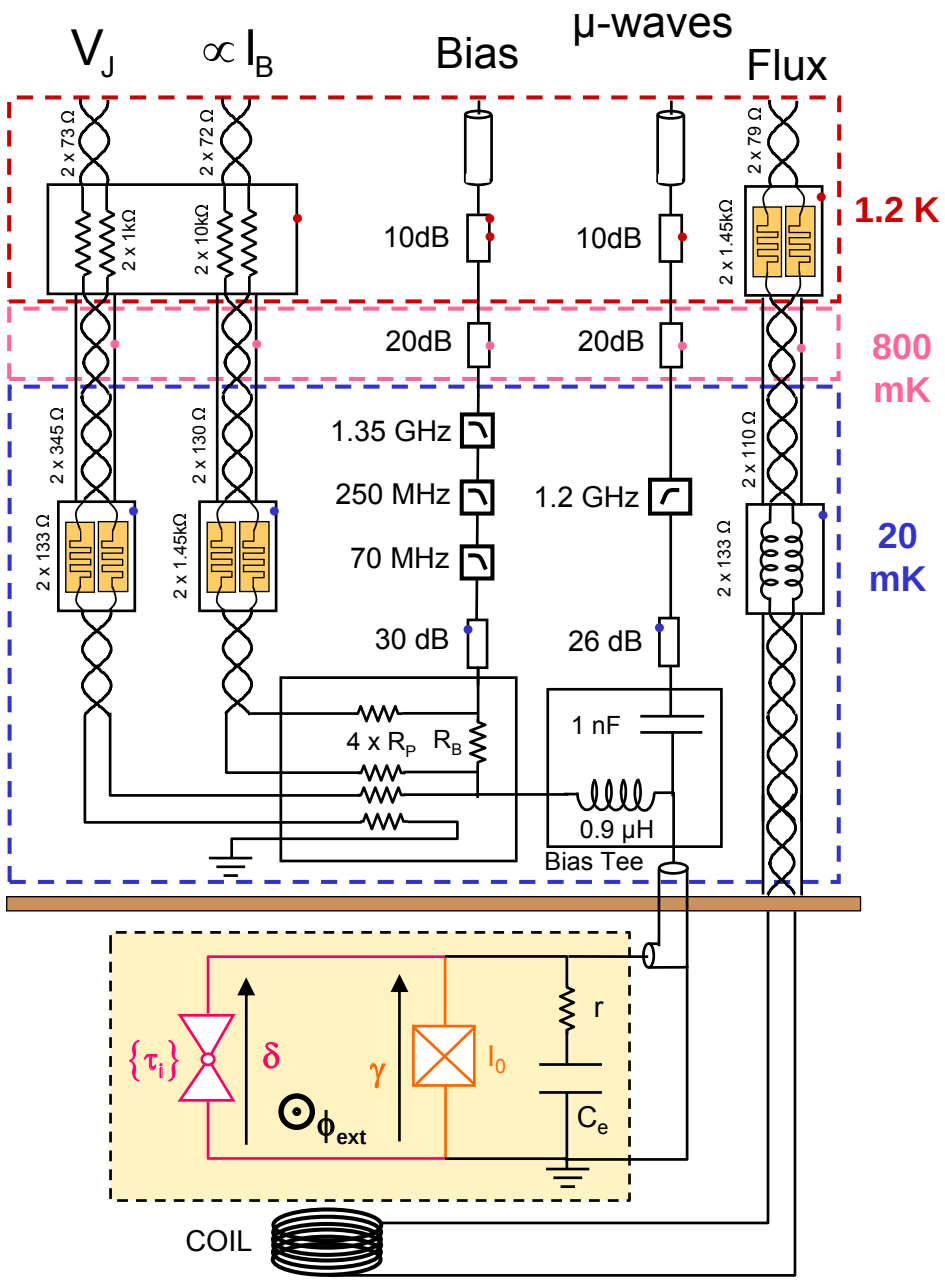

Fig. 8.5. Cryostat wiring used for samples AC1 and AC2. Resistors R_P are 980 Ω and the bias resistor is $R_B = 216\,\Omega$. A bias tee (Anritsu K250) placed at 20 mK allows to inject both the dc bias and the microwaves on the same line of the chip. The dc flux biasing line is also heavily filtered.

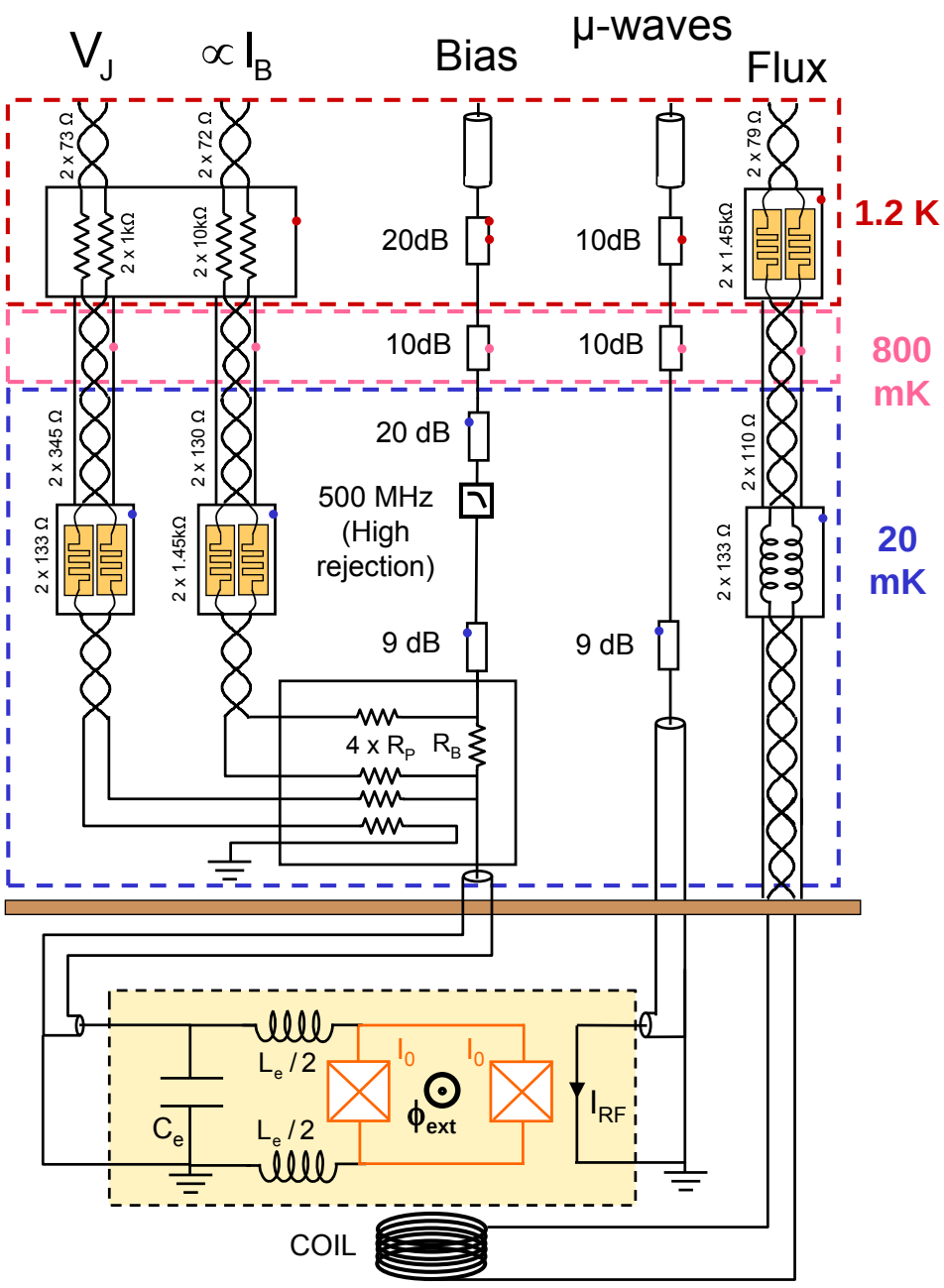

Fig. 8.6. Cryostat wiring used for sample SQUID. Resistors R_P are 1200 Ω and the bias resistor is $R_B = 237\ \Omega$. The measurement pulses are fed through the bias line, which is heavily attenuated and filtered with commercially available components placed at different temperatures, as indicated. The microwave line feeding the on-chip flux antenna is only equipped with attenuators.

8.3 Room temperature connections and instruments

8.3.1 Biasing

Current pulses are synthesized with an arbitrary waveform generator Agilent 33250A. The signal is attenuated at room temperature by 30 dB.

In the experiments on samples JJD1 and JJD2, the tunnel junction acting as the noise source was kept floating from the ground and connected to a stabilized dc voltage source Yokogawa 7651 through two very large resistors R_L, either 1.5 MΩ or 4.9 MΩ depending on the desired current range.

8.3.2 Microwave excitation

In the SQUID experiments, microwave signals were generated using a Rohde & Schwarz SMR20 microwave source for frequencies below 20 GHz and an Anritsu MG3694B for frequencies above 20 GHz.

8.3.3 Amplification and measurements

The small voltages measured with the lossy twisted pairs are amplified by low noise voltage preamplifiers NF LI75A ($1.2\,\mathrm{nV}/\sqrt{\mathrm{Hz}}$, 1 MHz bandwidth, ×100 gain), followed by Stanford amplifiers SR560 with selectable gain and bandwidth. The $I(V)$ characteristics are registered with a Nicolet Pro 44 high-resolution digital oscilloscope. The switching voltage pulses are counted using two PM6680 counters (Fluke or Philips).

Part IV
Appendix

Appendix A

Additional measurements

A.1 Back-Bending in the $I(V)$ characteristics of Josephson junctions

The theoretical $I(V)$ characteristics of a Josephson junction within the RCSJ model is sketched in Fig. A.1, and compared with a typical $I(V)$ characteristics of one of our Al-AlOx-Al Josephson junctions (Sample JJD1 presented in Chapter 4).

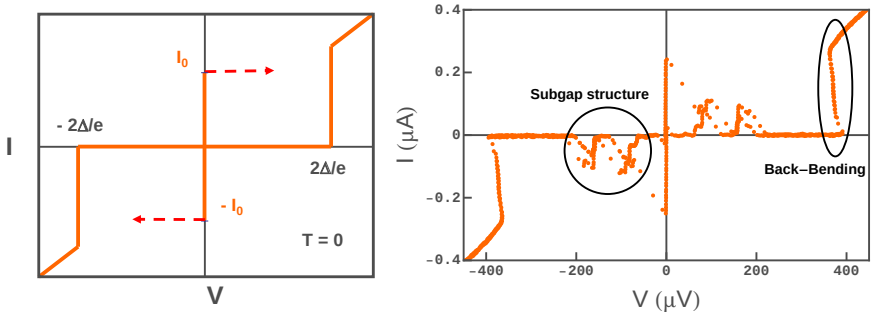

Fig. A.1. Comparison between a theoretical $I(V)$ characteristics of a Josephson junction (**left**) and an experimental $I(V)$ characteristics of Sample JJD1 (presented in Chapter 4) (**right**).

As can be seen on this figure, our Al-AlOx-Al Josephson junctions present two unexpected features:

- When the voltage approaches $|V| \simeq 2\Delta/e$, the transition to the dissipative regime does not appear as a vertical branch. The voltage across the junction decreases when the current increases. There is

a reduction of the apparent superconducting gap: we call this feature "back-bending". In some samples, the behavior can be even more complicated, as presented below.

- When the voltage across the junction is smaller than twice the superconducting gap $|V| < 2\Delta/e$, the current is not zero everywhere. In this junction, current peaks can be seen; in other samples, a background current is found. This sub-gap current is commonly attributed to pinholes in the tunnel barrier, which correspond to well transmitted channels, or to inelastic tunneling of Cooper pairs through the barrier, the energy $2eV$ being transferred to modes in the electromagnetic environment [133] or in the junction itself if it is long enough to stand resonant modes [3].

In the following, we present a brief overview of the back-bending.

A.1.1 Experimental facts

The shape presented in Fig. A.1 is not universal, but based on the numerous experiments performed on Josephson junctions, it is possible to draw some general trends:

- The back-bending is not visible in the $I(V)$'s shown in [3]. In this reference, the junctions have large critical currents (of the order of 1 mA and more), and are made with various metals (Sn, Pb, Nb,...) but not in aluminum which has a low critical temperature (therefore increasing the cryogenic constraints). In contrast, for small aluminum junctions with areas ranging from 0.1 μm^2 up to few μm^2, and with critical currents from a few nA up to a few μA, the $I(V)$ characteristics presents a back-bending, as observed in the Quantronics group as well as in several other groups worldwide. Remarkably, the back-bending is NOT observed on junctions obtained with Al atomic contacts, in which the $I(V)$ accurately agrees with theory [44, 112]. **The back-bending behavior is found systematically in small critical current Josephson junctions with overlapping aluminum electrodes.**

- The temperature dependence of the back-bending is shown for the noise source of Sample JJD1 in Fig. A.3. At $T \simeq 570$ mK, the back-bending has almost disappeared, with a total apparent gap which is reduced according to the BCS theory. One should note here that due to the low critical temperature of aluminum, junctions with aluminum electrodes are commonly measured in dilution fridges at a few tens of

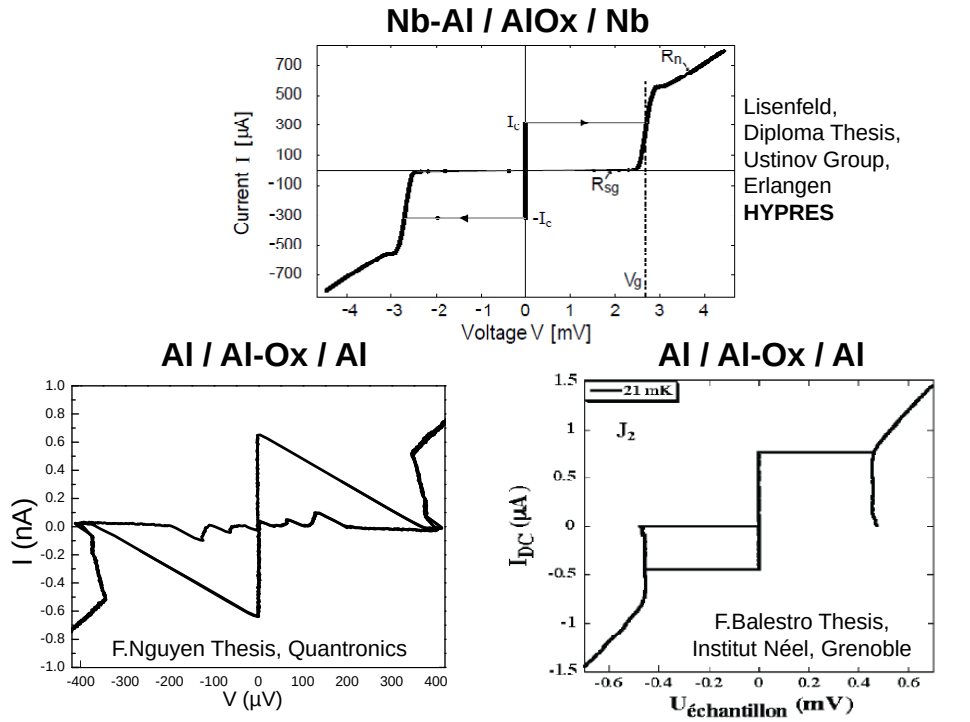

Fig. A.2. Comparison of $I(V)$ characteristics of Josephson junctions made with different fabrication processes. **Top:** large area Niobium Josephson junction made at HYPRES showing no back-bending. **Bottom:** Aluminum Josephson junctions with sub-μA critical current made in Quantronics group **(left)** and in Institut Néel **(right)**.

mK, therefore much lower than the critical temperature, while junctions in niobium are often measured at 4.2K, which is only half of the critical temperature. **The back-bending disappears when increasing temperatures.**

- For two junctions fabricated with exactly the same procedure, the shape of the back-bending is similar. Figure A.4 compares the junctions of Samples JJD1 and JJD2 presented in Chapter 4. The left panel shows the large junctions ($\sim 1\,\mu\mathrm{m}^2$) that are used as detectors, the right panel shows the small junctions ($\sim 0.1\,\mu\mathrm{m}^2$) used as noise sources. All junctions have very similar large scale electrodes, but differ in the overlap size. In the case of JJD2, quasiparticle traps are placed in contact with the electrodes (see Fig. 4.23), and this does not seem to tremendously affect the back-bending. In all cases, the slope presents strong variations, with nose-like features both at the bottom and at the top of the curve. In some cases, a bistable behavior is found (see junctions of Sample JJD2). One observes that the two types of

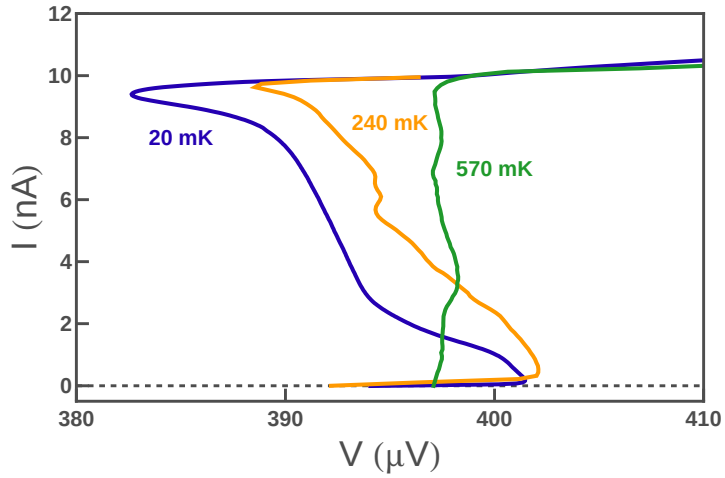

Fig. A.3. Temperature dependence of the back-bending in the noise source of Sample JJD1.

junctions (large and small) have very comparable characteristics, but that the difference in voltage between the bottom and the top of the branch is much larger in the larger junctions, where the current is also larger.

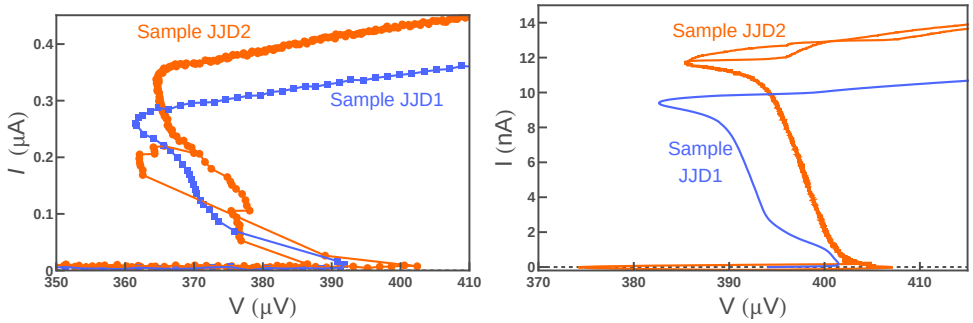

Fig. A.4. Shape of the $I(V)$ characteristics at $V = 2\Delta/e$ for samples JJD1 and JJD2 presented in Chapter 4. **Left:** Large critical current detector junctions. **Right:** Small critical current junctions used as noise sources.

- **A curious feature is found in SQUIDs, where the back-bending is systematically not monotonic**, as shown in Fig. A.5: voltage oscillations are observed as the current increases. Such a feature has been observed in SQUIDs fabricated in the Quantronics group, at Institut Néel [129], and at T.U. Delft [134]. Note that this structure is not very sensitive to the flux through the SQUID loop.

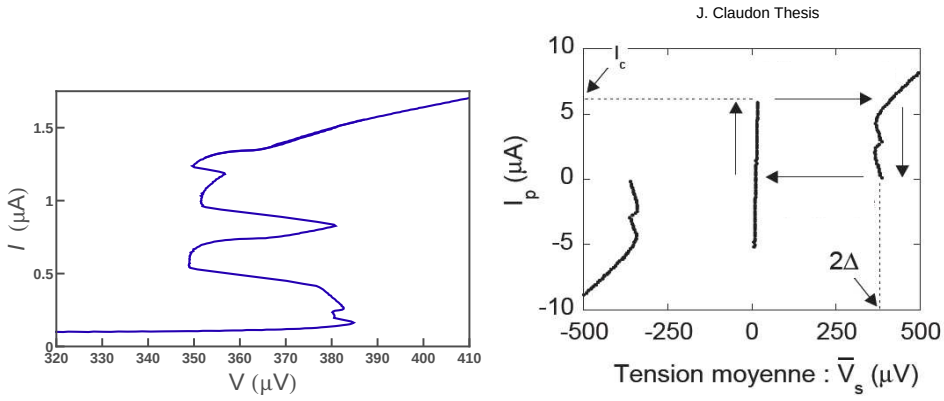

Fig. A.5. $I(V)$ characteristics of SQUIDs. **Left:** $I(V)$ characteristics of the SQUID presented in Chapter 6. **Right:** $I(V)$ characteristics of a SQUID in the PhD thesis of J. Claudon [129].

A.1.2 Theoretical description

A tentative explanation of back-bending is that the current flowing through the junction at $V = 2\Delta/e$ creates quasiparticles at a rate I/e, and that these quasiparticles yield a reduction of the gap similar to that observed when temperature is increased[1], and thus a reduction of the voltage. This scenario agrees with the effect being larger in junctions with larger critical currents, but no quantitative explanation is available, and it does not fit with all experimental facts:

- why should the effect appear for junctions with aluminum electrodes only? Is it due to the metal, in which case the quasiparticle recombination rate should be computed to explain the difference, or to the temperature at which the measurement is performed?
- how can the slope of the $I(V)$ have a non-monotonous dependence in the current?
- why should the effect be particularly strong and non-monotonous in SQUIDs?

Some efforts done presently by Alfredo Levy Yeyati and Sebastian Bergeret give a first possible description: a self-consistent calculation of the local superconducting gap for a junction voltage-biased close to twice the bulk superconducting gap can yield more than one solution [136]. The back-bending behavior might thus be due to averaged transitions between metastable values of the gap. However, no definitive theoretical

[1] In intrinsic Josephson junctions present in high-Tc materials, back-bending is systematically observed, but the explanation seems to be related with the change of resistivity with temperature of highly resistive layers [135], not with a change of the gap.

microscopic model has been proposed to account quantitatively for the back-bending. We think that such a model should consider quasiparticle recombination and quasiparticle diffusion in the junction electrodes. If the explanation outlined above is correct, one expects back-bending to be more pronounced in junctions with narrow connecting wires made of a superconductor with a larger gap than the junction electrodes, and less pronounced in devices when large normal electrodes are contacted close to the junction.

A.2 Heating effects in switching measurements

In the experiments described in Chapter 4 aiming at measuring noise with a Josephson junction as a detector, sequences of bias-current pulses were applied to the junction through a resistor $R_1 = 200\,\Omega$ placed on-chip. It appeared that electron heating in this resistor was large enough to increase the effective escape temperature, an effect probed experimentally and evaluated here.

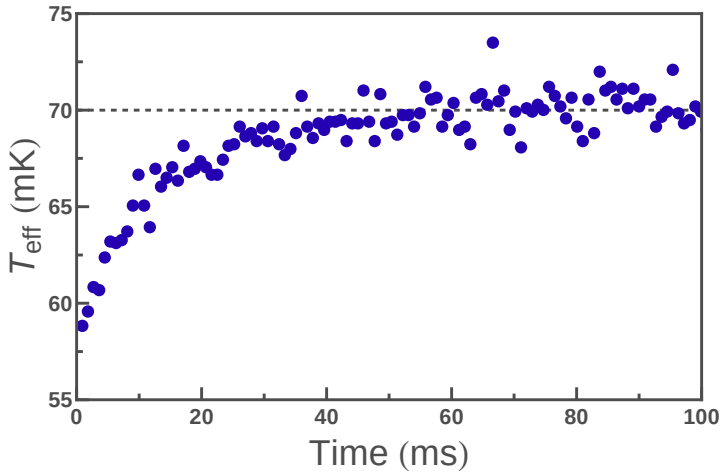

Fig. A.6. Rise of the effective escape temperature with the measurement time. Temperature is calculated from a local escape probability (obtained from the density of escape events in a period of time corresponding to 100 measurement pulses).

In order to probe this heating effect, we sent a long train of pulses (16000), and monitored the times of all escape events using a timer. This allows to determine which pulses give rise to switching. The switching probability $P(t)$ as a function of time is estimated using the number of switching events in small subsets of 50 pulses. The probability $P(t)$ converted into an effective escape temperature is shown in Fig. A.6, in an

experiment performed at the base temperature, with current pulses of amplitude $I_J \simeq 0.4\,\mu$A during a time $\tau_p \simeq 1\,\mu$s, followed by a sustain at $I_{\rm sus} = 0.8\,I_J$ during $\tau_{\rm sus} = 3\,\mu$s, repeated every $t_{\rm signal} = 9\,\mu$s. The observed increase of the escape temperature demonstrates that the current pulses heat the environment of the Josephson junction, producing a sizable increase of the effective escape temperature $\Delta T_{\rm eff} \simeq 15\,$mK from 55 mK to 70 mK. Considering that the resistor R_1 is the only one in the environment of the junction that gets heated by the current, and using Eq. 4.23, the increase $\Delta T_{\rm eff}$ implies an increase of the electronic temperature in R_1:

$$\Delta T_1 = \frac{R_1}{R_{||}} \Delta T_{\rm eff} \simeq 35\,{\rm mK}. \tag{A.1}$$

This increase can be compared to the prediction given in [137], where the case of a bias resistor heated by such a train of pulses is explicitly treated. For the signal used in this experiment, the average power dissipated in the resistor R_1 is

$$\mathcal{P} = \frac{\tau}{t_{\rm signal}} R_1 I_J^2 + \frac{t_{\rm sustain}}{t_{\rm signal}} R_1 I_{\rm sus}^2. \tag{A.2}$$

For the experimental values, one obtains $\mathcal{P} = \frac{1}{9} R_1 I_J^2 + \frac{3}{9} R_1 \left(0.8\,I_J\right)^2 \simeq 5$ pW. The prediction for the electronic temperature requires to compare the voltage $R_1 I_J = 80\,\mu V$ to the characteristic temperature $T_\Sigma = \left(\frac{P}{\Sigma\Omega}\right)^{1/5} \simeq 66$ mK, where Σ is the electron-phonon coupling constant (typically $\Sigma = 2\,{\rm nW}/\mu{\rm m}^3/{\rm K}^5$) and Ω is the volume of the resistor (typically $\Omega = 0.01 \times 200 \times 1000 = 2000\,\mu{\rm m}^3$). This temperature corresponds to the limit when cooling occurs only through the coupling to a bath of zero-temperature phonons. Here, $eR_1 I_J \gg k_B T_\Sigma$, and one predicts that the average electronic temperature reaches at equilibrium

$$T_e = \left(T_{ph}^5 + T_\Sigma^5\right)^{1/5} \simeq 70\,{\rm mK}, \tag{A.3}$$

with T_{ph} the phonons temperature. Taking for the initial temperature of the resistor the escape temperature at the first pulse, 55 mK, the predicted temperature change of R_1 is $\Delta T_1 \simeq 15\,$mK, half the value given by Eq. (A.1). Hence, if this theory captures the correct order of magnitude of the heating, it is not quantitative. One possible interpretation is that the SMC resistor R_1 used in this experiment, which was glued on the sample with silver epoxy, was not well thermalized, and that the current pulses heated the resistor as a whole: T_{ph} should not be taken as a constant in the calculation. In the following experiments, the SMC resistor was replaced with a Cr film evaporated directly on the sample.

The temperature rise time can also be simply calculated using [137]. The average temperature should be reached after a typical electron-phonon time τ_{e-ph}:

$$\tau_{e-ph} = \frac{\gamma}{(\Sigma T_{\Sigma}^3)} \simeq 0.2\,\text{ms}. \tag{A.4}$$

where $\gamma = (\pi^2/3)\, k_B^2 \nu_F$ is the heat capacity coefficient [137], with ν_F the density of states at Fermi energy. The rise time observed in the experiment, 10 ms, is much larger than this estimation, indicating that the observed heating is probably more than just electron heating, as discussed previously.

We performed another test using pulses of different duration τ_p: Eq. (A.2) predicts that, whatever the mechanism, the temperature increase due to the current pulses depends on the two ratios $\frac{\tau_p}{t_{\text{signal}}}$ and $\frac{t_{\text{sustain}}}{t_{\text{signal}}}$. When changing the pulse duration τ_p, we adjusted the sustain time and repetition rate (through t_{sustain}) so that the average power is constant. Resulting $B^{2/3}$ plots are shown in Fig. A.7 for three different values of τ_p, corresponding to different ranges of switching current. The alignment between the three sets of point indicates that the escape temperature is indeed the same in the three experiments.

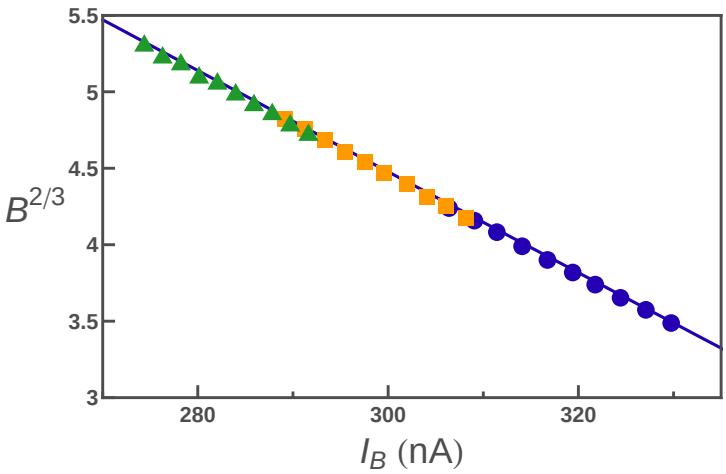

Fig. A.7. $B^{2/3}$ function for three pulse durations τ_p: 0.53 μs (blue circles), 3.93 μs (orange squares) and 20.98 μs (green triangles). All points are aligned, the effective temperature is thus similar for all the three sets of data (data taken on Sample JJD2).

Appendix B

Miscellaneous

B.1 Approximations for the tilted washboard potential

We present here the cubic approximations for the potential

$$U(x,s) = -E_J\left(\cos x + sx\right) \tag{B.1}$$

that appears in the description of the dynamics of a JJ [11, 31, 32, 73] to calculate the escape rate, and in particular the corrective term B_3 due to the third moment of noise.

B.1.1 Cubic approximation

Using $\tilde{x} = x - x_{\text{well}}$, with x_{well} the position of a minimum of the potential, Eq. (B.1) becomes:

$$U(x,s) = -E_J\left[\sqrt{1-s^2}\cos\tilde{x} - s\sin\tilde{x} + s\left(\tilde{x} + x_{\text{well}}\right)\right] \tag{B.2}$$

which can be approximated, neglecting the constant term, by a generic cubic potential

$$U_{\text{cubic}}(\tilde{x},s) = E_J\alpha(s)\left[\frac{\tilde{x}^2}{2} - \frac{\tilde{x}^3}{3\tilde{x}_b(s)}\right] \tag{B.3}$$

with appropriate parameters $\alpha(s)$ and $\tilde{x}_b(s)$. The minimum and maximum of the cubic potential are found at $\tilde{x}(s) = 0$ and $\tilde{x}(s) = \tilde{x}_b(s)$. The height of the barrier is then

$$\Delta U_{\text{cubic}} = U_{\text{cubic}}(\tilde{x}_b,s) = E_J\alpha(s)\frac{\tilde{x}_b^2(s)}{6} \tag{B.4}$$

and the plasma angular frequency is:

$$\omega_p^{\text{cubic}}(s) = \omega_{p0}\sqrt{\alpha(s)}. \tag{B.5}$$

B.1.2 Taylor expansion

For $1-s \ll 1$, the width of the well, given by $x_b - x_{\text{well}} = \pi - 2\arcsin(s)$, is close to 0, so that $\tilde{x} \ll 1$ in the region of the well. A Taylor expansion of Eq. (B.2) yields:

$$\begin{cases} \alpha^{TE}(s) = \sqrt{1-s^2} \\ \tilde{x}_b^{TE}(s) = \frac{2\sqrt{1-s^2}}{s} \end{cases} \tag{B.6}$$

The height of the barrier is then $\Delta U^{TE} = E_J \frac{4\left(1-s^2\right)^{3/2}}{6s}$. This approximation for the barrier height deviates from the exact one by more than 1 % as soon as $s < 0.95$. This partly explains why the first calculation performed by J. Ankerhold in [31, 32], denoted j_{FP1} in Chapter 2, is only valid close to $s \simeq 1$. However, it yields the correct plasma frequency: $\omega_p^{TE}(s) = \omega_{p0}\left(1-s^2\right)^{1/4}$.

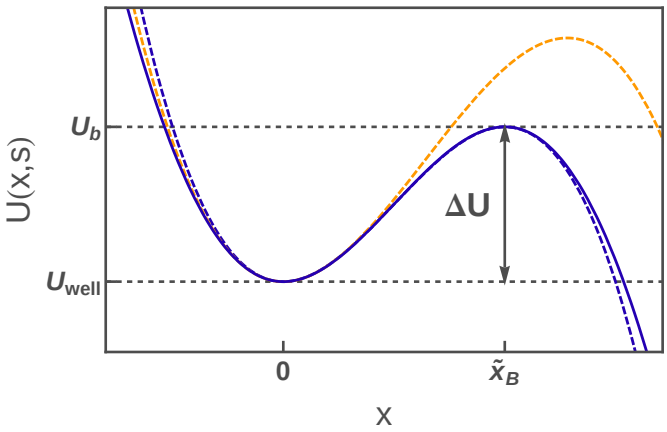

Fig. B.1. Solid line: Exact potential $U(x,s)$ for $s = 0.7$. **Dashed orange line:** cubic potential denoted U^{TE} in text. **Dashed blue line** cubic potential denoted U^{BI}, that yields the correct barrier height at all values of s.

B.1.3 Bilocal interpolation

An effective cubic potential with the correct barrier height at all values of s is obtained by imposing $\partial_{\tilde{x}}\, U_{\text{cubic}}(0,s) = 0$ and $\partial_{\tilde{x}}\, U_{\text{cubic}}(\tilde{x}_b,s) = 0$. This yields:

$$\begin{cases} \alpha^{BI}(s) = \frac{3\left[\sqrt{1-s^2}-s\tilde{x}_b(s)\right]}{\left(\frac{1}{2}\tilde{x}_b(s)\right)^2} \\ \tilde{x}_b^{BI}(s) = 2\arctan\frac{\sqrt{1-s^2}}{s} \end{cases} . \tag{B.7}$$

This approximation has been used by K. Glaum [73] to calculate the function j_{FP2} presented in Chapter 2, which is therefore valid for all values of s. The plasma frequency is however slightly ill-estimated in this approximation.

B.2 Resonant activation through the modulation of the critical current

Resonant activation in a Josephson junction [59], introduced in Chapter 2, consists in the increase of the switching rate when a small AC modulation of the bias current is applied at a frequency slightly below the plasma frequency. A related phenomenon occurs when the flux through a SQUID is ac-modulated, as used experimentally in Chapter 6 and thoroughly exploited in [127, 129]. In Chapter 6, the SQUID is operated in a regime where it behaves as a single Josephson junction with a critical current modulated by the flux $I_0^S(\varphi) = 2I_0\left|\cos\left(\frac{\varphi}{2}\right)\right|$, where φ is the reduced dc applied flux (see Chapter 6 for notations). The current-phase relation of the SQUID is given by:

$$I^S(\gamma) = I_0^S(\varphi)\sin(\gamma) \tag{B.8}$$

where γ is the phase difference across the SQUID. We consider here a RCSJ model for the SQUID. The equations describing the two cases are:

- In presence of an ac modulation of the bias-current $I_{RF}\cos(\omega_{\mathrm{exc}}t)$, the equations for the phase dynamics are:

$$\begin{cases} \frac{1}{\varphi_0}V = \dot{\gamma} \\ C_J\varphi_0^2\ddot{\gamma} + \frac{\varphi_0^2}{R}\dot{\gamma} + E_J^S\left[\sin\gamma - s\right] = \varphi_0\delta I(t) + \varphi_0 I_{RF}\cos(\omega_{\mathrm{exc}}t) \end{cases} \tag{B.9}$$

  where $\delta I(t)$ is the thermal noise current in the shunt resistor and $E_J^S = \varphi_0 I_0^S$.
- In presence of a harmonic modulation of the applied flux through the SQUID loop $\frac{\phi_{RF}}{2\pi}\cos\omega_{\mathrm{exc}}t$, the equations of the phase dynamics take a slightly different form:

$$\begin{cases} \frac{1}{\varphi_0}V = \dot{\gamma} \\ C_J\varphi_0^2\ddot{\gamma} + \frac{\varphi_0^2}{R}\dot{\gamma} + \varphi_0 \times I_0^S\left(\varphi + \frac{\phi_{RF}}{2\pi}\cos\omega_{\mathrm{exc}}t\right) \times \left[\sin\gamma - s\right] = \varphi_0\delta I(t). \end{cases} \tag{B.10}$$

In this last set of equations (B.10), the flux excitation yields an excitation term analogous to the current excitation found in (B.9) together with other terms. Practically, one can see the flux modulation as a modulation of the critical current of a simple junction. One can wonder whether the response function of a Josephson junction under a critical current excitation is similar to that observed for a current-bias excitation.

We have evaluated this response function in the two cases by monitoring the increase of the escape rate in presence of a harmonic excitation on the bias-current or on the critical current of a Josephson junction, using the simulation algorithm presented in Chapter 3. We integrated step by step the equation:

$$\ddot{\gamma} + \frac{1}{Q_0}\dot{\gamma} = F + \xi \tag{B.11}$$

with the forces:

$$\begin{cases} F = -\sin\gamma + s + \mathrm{exc}(t) & \text{for the bias current modulation} \\ F = -(1 + \mathrm{exc}(t))\sin\gamma + s & \text{for the critical current modulation.} \end{cases} \tag{B.12}$$

where $\mathrm{exc}(t) = A \times \cos(ft)$ is the excitation and ξ the random fluctuations. We show in Fig. B.2 that the response function of the switching rate is very similar in both situations, with a resonant activation curve that peaks below the plasma frequency and gets sharper at larger quality factor.

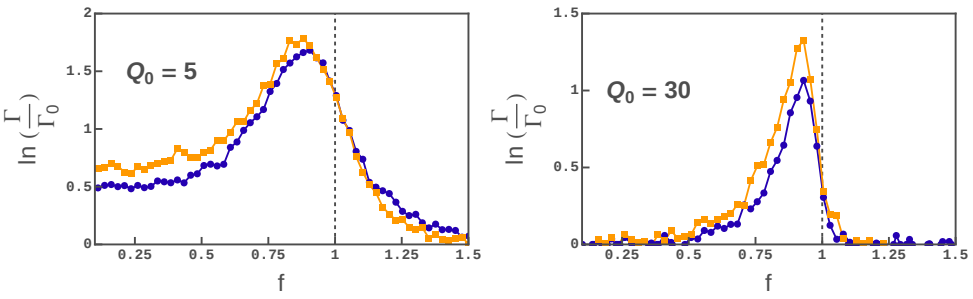

Fig. B.2. Response function of the resonant activation by a **current excitation (blue circles)** or to a **flux excitation (orange squares)** on a SQUID behaving like a single tunable junction (large b [120]) for two quality factors as a function of the reduced excitation frequency f. The amplitudes of each excitation has been set to yield a similar increase of the escape rate. Vertical grid lines corresponds to the plasma frequency.

B.3 Moments and Cumulants, and Poisson Process.

In this appendix, we present the distinction between central moments and cumulants. Since central moments and cumulants don't differ for the first three orders, the distinction is not performed along this dissertation. Details of the derivations presented here are found in [72].

B.3.1 Definitions

Let X be a random variable. The realizations of X are governed by a probability law.

- If X takes discrete values, the law is defined by the probability mass function $P(X = k)$ for the variable to take value k;
- If X is a continuous variable, the law is defined by the probability density function $f(x)$. The cumulative distribution function is defined by

$$F(x) = P(X < x) = \int_{-\infty}^{x} f(t)dt \tag{B.13}$$

B.3.2 Average value & moments

- For a discrete variable, the average value of a function $\lambda(x)$ is defined as:

$$E\left[\lambda\left(X\right)\right] = \sum_{i} \lambda\left(x_i\right) P\left(X = x_i\right). \tag{B.14}$$

- For a continuous variable, the average value of a function $\lambda(x)$ is defined as:

$$E\left[\lambda\left(X\right)\right] = \int_{\mathbb{R}} \lambda\left(x\right) f(x)dx. \tag{B.15}$$

- The arithmetic mean m is the average value of $\lambda\left(x\right) = x$, the variance is the average value of $\lambda\left(x\right) = \left(x - m\right)^2$. The moment of order n is

$$\mu_n = E\left[X^n\right] \tag{B.16}$$

  and the central moment of order n is

$$S_n = E\left[\left(X - m\right)^n\right]. \tag{B.17}$$

B.3.3 Generating function & cumulants

Moment generating function

One defines the moment generating function as:

$$M(z) = E\left[e^{zX}\right] \tag{B.18}$$

For a continuous variable, one has

$$M(z) = \int_{-\infty}^{+\infty} e^{zx} f(x)dx \tag{B.19}$$

hence

$$f(x) \propto \int_{-\infty}^{+\infty} e^{-zx} M(z)dx. \tag{B.20}$$

The probability law is completely characterized by the moment generating function. Moreover, the exponential term can be expanded into:

$$M(z) = \int_{-\infty}^{+\infty} \sum_{k=0}^{\infty} \frac{(zx)^k}{k!} f(x)dx = \sum_{k=0}^{\infty} \frac{(z)^k}{k!} \int_{-\infty}^{+\infty} x^k f(x)dx = \sum_{k=0}^{\infty} \mu_k \frac{z^k}{k!} \tag{B.21}$$

Hence, by a derivation at the order n:

$$M^{(n)}(z) = \sum_{k=n}^{\infty} \mu_k k(k-1)\dots(k-n+1)\frac{z^{k-n}}{k!} \tag{B.22}$$

and by taking $t = 0$, only the term in $n = k$ is kept and one recovers the moments of the distribution:

$$M^{(n)}(0) = \mu_n \frac{n(n-1)\dots(n-n+1)}{n!} = \mu_n \tag{B.23}$$

The moment of order n is given by the derivative at order n of the moment generating function evaluated at zero, and using all moments, it is possible to reconstruct the moment generating function. Therefore **the probability density function is perfectly characterized by the moments**. However, the moment generating function is not optimal, especially when two variables X and Y are used:

$$M_{X+Y}(z) = E\left[e^{z(X+Y)}\right] = E\left[e^{zX}\right] E\left[e^{zX}\right] = M_X(z)M_Y(z) \tag{B.24}$$

The resulting moment generating function is a product of two polynomial. Hence, the moments of the sum of the two variables is NOT simply linked to the moments of each variable. Indeed, if $M_X(z) = 1+\mu_{1X}z+\mu_{2X}\frac{z^2}{2}+\dots$ and $M_Y(z) = 1 + z + \mu_{2Y}\frac{z^2}{2} + \dots$ then

$$M_{X+Y}(z) = 1 + (\mu_{1X} + \mu_{1Y})\, z + \left(\mu_{1X}\mu_{1Y} + \frac{\mu_{2X}}{2} + \frac{\mu_{2Y}}{2}\right)\frac{z^2}{2}. \tag{B.25}$$

The moments of the random variable $X + Y$ are then:

$$\begin{cases} \mu_{1(X+Y)} = \mu_{1X} + \mu_{1Y} \\ \mu_{2(X+Y)} = 2\mu_{1X}\mu_{1Y} + \mu_{2X} + \mu_{2Y} \end{cases} \tag{B.26}$$

The second moment is thus obviously NOT a simple combination of the second moments of the two random variables X and Y. To solve this difficulty, it is common to use instead the cumulants generating function.

Cumulants generating function

One defines the cumulants generating function as:

$$C(z) = \ln\left(E\left[e^{zX}\right]\right) = \ln\left(M(z)\right). \tag{B.27}$$

From this definition, the cumulants are given by

$$C(z) = \sum_{k=1}^{\infty} \kappa_k \frac{z^k}{k!} \tag{B.28}$$

therefore

$$C^{(n)}(0) = \kappa_n. \tag{B.29}$$

Again, the probability density function can be obtained from the cumulants using the Edgeworth series, so that **the cumulants perfectly characterize a probability law**. Now, $C_{X+Y}(z) = C_X(z) + C_Y(z)$, so that the cumulants of X and Y simply add to obtain the cumulants of the random variable $X + Y$. The cumulants are obtained by derivation of a compound function at the order n. The coefficients of such derivation are calculated by the Faa di Bruno's formula. This yields for the equivalence between moments and cumulants:

$$\mu_n = \kappa_n + \sum_{k=1}^{n-1} \binom{n-1}{k-1} \kappa_k \mu_{n-k} \tag{B.30}$$

therefore:

$$\begin{cases} \mu_1 = \kappa_1 = m \\ \mu_2 = \kappa_2 + \kappa_1^2 \\ \mu_3 = \kappa_3 + 3\kappa_2\kappa_1 + \kappa_1^3 \\ \mu_4 = \kappa_4 + 4\kappa_3\kappa_1 + 3\kappa_2^2 + 6\kappa_2\kappa_1^2 + \kappa_1^4 \end{cases} \tag{B.31}$$

The link can also be performed with the central moment generating function $M_c(z) = E\left[e^{z(X-m)}\right]$. In this case, all terms in κ_1 disappear, so that:

$$\begin{cases} S_1 = 0 \\ S_2 = \kappa_2 \\ S_3 = \kappa_3 \\ S_4 = \kappa_4 + 3\kappa_2^2 \end{cases} \tag{B.32}$$

which shows that the distinction between central moments and cumulants has no meaning for the second and third moment.

B.3.4 Examples

Gaussian law

The Gaussian law is governed two parameters m and σ and has a probability density function given by:

$$f(x) = \frac{1}{\sigma\sqrt{2\pi}} \exp\left(-\frac{(x-m)^2}{2\sigma^2}\right). \tag{B.33}$$

When calculating the moment generating function

$$E\left[e^{zX}\right] = \int_{-\infty}^{+\infty} e^{zx} f(x)dx, \tag{B.34}$$

the terms in the exponential are of the form:

$$-\frac{(x-m)^2}{\sigma^2} + zx = -\frac{1}{2\sigma^2}\left[\Big(x-(m+\sigma^2 z)\Big)^2 - 2m\sigma^2 z - \sigma^4 z^2\right] \tag{B.35}$$

Hence,

$$\begin{aligned} E\left[e^{zX}\right] &= \frac{1}{\sigma\sqrt{2\pi}}\left[\int_{-\infty}^{+\infty} \exp\left(-\frac{\big(x-(m+\sigma^2 z)\big)^2}{2\sigma^2}\right) f(x)dx\right] \exp\left(mz+\frac{\sigma^2 z^2}{2}\right) \\ &= \exp\left(mz+\frac{\sigma^2 z^2}{2}\right) \end{aligned} \tag{B.36}$$

and the cumulant generating function is

$$C(z) = mz + \frac{\sigma^2 z^2}{2}. \tag{B.37}$$

The cumulants are thus $\kappa_1 = m$, $\kappa_2 = \sigma^2$ and all higher order cumulants are zero. Moreover, central moments of order n are zero if $n = 2p+1$ is odd ($p \in \mathbb{N}$). Indeed, using $u = \frac{X-m}{\sigma}$, they are given by:

$$S_{2p+1} = \frac{1}{\sqrt{2\pi}} \int_{-\infty}^{+\infty} u^{2p+1} \exp\left(-\frac{u^2}{2}\right) du = 0 \tag{B.38}$$

because the integrand is odd.

Poisson law

The Poisson law is a discrete law, where the probability mass function is governed by a parameter γ:

$$P\left(X=k\right)=\frac{\gamma^k}{k!}e^{-\gamma}. \tag{B.39}$$

If the variable X corresponds to the number of occurrences during a time τ,

$$P\left(X=k\right)=\frac{\left(\Gamma\tau\right)^k}{k!}e^{-\Gamma\tau} \tag{B.40}$$

where Γ is called the rate. The moment generating function is obtained as:

$$M(z)=\sum_{k=0}^{\infty}e^{zk}\frac{e^{-\gamma}\gamma^k}{k!}=e^{-\gamma}\left[\exp\left(\gamma e^z\right)\right]=e^{\gamma\left(e^z-1\right)} \tag{B.41}$$

therefore

$$C(z)=\ln\left(e^{\gamma\left(e^z-1\right)}\right)=\gamma\left(e^z-1\right) \tag{B.42}$$

and $C^{(n)}(0)=\gamma$, so that all cumulants are equal to γ. In particular, the second and third central moments are equals.

Exponential law The exponential law is governed by a parameter γ, and $f(x)=\gamma\exp\left(-\gamma x\right)$. Moments are $\mu_1=\frac{1}{\gamma}$ and $\mu_2=\frac{2}{\gamma^2}$, so that $S_1=0$ and $S_2=\frac{1}{\gamma}$.

B.3.5 Poisson Process

A stochastic process is a series of random variables following a given probability law, indexed by time. More specifically, a Poisson process defines a series of successive events by the following:

- The time intervals between the different events are independents variables (memory-less process)
- The probability that an event happens during an infinitesimal interval $[t,t+dt]$ is independent of t and is given by Γdt, where Γ is called the rate.
- Two events can not happen in the same infinitesimal interval dt.

Number of events in a given time t

Let $N(0,t)$ be the number of events between 0 and T. $N(0,t)$ is often called the counter process. The moment generating function of N is $M_t(z) = E\left[z^{N(0,t)}\right]$. For a time $t+dt$:

$$\begin{aligned} M_{t+dt}(z) &= E\left[z^{N(0,t+dt)}\right] \\ &= E\left[z^{N(0,t)+N(t,t+dt)}\right] \\ &= E\left[z^{N(0,t)}\right] E\left[z^{N(t,t+dt)}\right] \\ &= M_t(z)\left[(1-\Gamma dt)z^0 + (\Gamma dt)\, z^1\right] \end{aligned} \tag{B.43}$$

Hence:

$$M_{t+dt}(z) = M_t(z)\left[1+\Gamma dt\,(z-1)\right] \tag{B.44}$$

so that

$$\frac{dM_t(z)}{M_t(z)} = \Gamma\,(z-1)\,dt \tag{B.45}$$

and finally $M_t(z) = \exp\left(\Gamma t\,(z-1)\right)$. This function is the moment generating function of a Poisson law, so that the number of events during a time t is given by a Poisson law of parameter Γt.

Times between two successive events

Let $d\tau$ denote the time between two successive events. If the number of events during a time t is given by a Poisson law of parameter Γt, then the probability that $d\tau$ is higher than t is equal to the probability that no event happens during a time t, given by $P(d\tau > t) = P(N=0) = e^{-\Gamma t}$ from Eq. (B.40). Such a cumulative distribution function corresponds to probability density function

$$f(x) = \Gamma e^{-\Gamma x} \tag{B.46}$$

Hence, the time between to successive events in a Poisson process is given by an exponential law of parameter Γ. Conversely, the probability than an event happens before time t is $P(d\tau \leq t) = 1 - e^{-\Gamma t}$, which appears in switching experiments.

Example of the tunnel junction

Let us consider a single channel tunnel junction of transmission $\tau_t \ll 1$. When it is voltage-biased, the transfer of charges are rare and independent, so that tunneling events follow a Poisson process. Moreover,

tunneling happens in both direction, so that the tunnel junction is the place of two independent Poisson processes. One defines $N_{\rightarrow}$ the number of charges being transferred during a time τ from left to right by the first process at a rate $\Gamma_{\rightarrow}$, and $N_{\leftarrow}$the number of charge transferred by the other process in the opposite direction at a rate $\Gamma_{\leftarrow}$. The difference $N = N_{\rightarrow} - N_{\leftarrow}$, which corresponds to the effective transferred charge, follows a Skellam distribution (the difference of two Poisson distributions). Calling $\Delta_\Gamma = \Gamma_{\rightarrow} - \Gamma_{\leftarrow}$ and $\mu_\Gamma = \frac{\Gamma_{\rightarrow}+\Gamma_{\leftarrow}}{2}$, the cumulants generating function of N, $C_N(z)$, is found as:

$$C_N(z) = C_{N_{\rightarrow}}(z) - C_{N_{\leftarrow}}(z) = \Delta_\Gamma \tau \left(e^z - 1\right). \tag{B.47}$$

Therefore all cumulants are equal to $\Delta_\Gamma \tau$. The rates are given from the detailed balance $\Gamma_{\rightarrow}/\Gamma_{\leftarrow} = \exp\left[eV/k_BT\right]$ where V is the voltage on the junction, one hence recovers the Poisson distribution if $|eV| \gg k_BT$.

B.3.6 Numerical estimation of the rate

In Chapter 3, the escape rate of a Josephson junction is evaluated through numerical simulation of the dynamics. The escape rate can be estimated using the escape time and the escape probability using different methods already presented in Sec.3.2.1. We present here more details on these methods, and derive the variance of the two estimators as a function of the escape probability P.

First method

One defines for each run i the Bernoulli random variable S_i of parameter P as:

$$S_i = \begin{cases} 1 \text{ if the particle escapes, with probability } P \\ 0 \text{ otherwise, with probability } 1-P \end{cases} \tag{B.48}$$

The expected mean value of the variable S_i is just the escape probability P:

$$\langle S_i \rangle = P = \Psi_1(\Gamma) \tag{B.49}$$

where:

$$\Psi_1(\Gamma) = 1 - e^{-\Gamma \tau_p}. \tag{B.50}$$

A straightforward estimator of the escape probability is:

$$\hat{P} = \frac{1}{N} \sum_{i=1}^{N} S_i \tag{B.51}$$

and therefore an estimator $\hat{\Gamma}_1$ of the escape rate is:

$$\hat{\Gamma}_1 = \Psi_1^{-1}(\hat{P}) \tag{B.52}$$

where Ψ_1^{-1} is the inverse function. Using the central limit theorem when $N \to \infty$ for the mean of Bernoulli variables of parameters P, one obtains:

$$\hat{P} \simeq P + \frac{U}{\sqrt{N}}\sqrt{P(1-P)} \tag{B.53}$$

where U is a normally distributed variable with zero mean and variance 1. Therefore, the estimator of the rate is:[1]

$$\hat{\Gamma}_1 \simeq \Gamma + \frac{U}{\sqrt{N}}\sqrt{P(1-P)}\frac{1}{\Psi_1'(\Gamma)}. \tag{B.54}$$

Since

$$\Psi_1'(\Gamma) = -\frac{1}{\Gamma}(1-P)\log(1-P), \tag{B.55}$$

where "log" corresponds here to the natural logarithm, the error on the rate through this estimation is obtained from the variance of the estimator as:

$$\frac{\Delta\hat{\Gamma}_1}{\Gamma} \times \sqrt{N} = \frac{1}{\log(1-P)}\frac{P}{1-P} \tag{B.56}$$

Second method

In this case, one uses the escape times as a variable. But since the particle does not always escape, the variable is:

$$\tau_i = \begin{cases} \tau_{\text{esc}} \text{ if the particle escapes} \\ \tau_p \text{ otherwise} \end{cases} \tag{B.57}$$

The expected mean value (see Eq. (3.27)) of the variable τ_i is:

$$\langle \tau_i \rangle = \frac{1}{\Gamma}(1 - e^{-\Gamma\tau_p}) = \Psi_2(\Gamma) \tag{B.58}$$

and the expected variance, calculated the same way, is:

$$\begin{aligned} \text{Var}[\tau_i] &= \langle \tau_i^2 \rangle - \langle \tau_i \rangle^2 \\ &= \frac{1}{\Gamma^2}\left[1 - (1-P)^2 + 2(1-P)\ln(1-P)\right]. \end{aligned} \tag{B.59}$$

A straightforward estimator of the mean escape time is:

$$\hat{\tau} = \frac{1}{N}\sum_{i=1}^{N}\tau_i. \tag{B.60}$$

[1] Using $\left(f^{-1}\right)' = 1/\left(f' \circ f^{-1}\right)$.

A possible estimator $\hat{\Gamma}_2$ of the escape rate is:

$$\hat{\Gamma}_2 = \Psi_2^{-1}(\hat{\tau}) \tag{B.61}$$

where Ψ_2^{-1} is the inverse function of Ψ_2. However, Ψ_2^{-1} does not have an analytical expression, therefore this estimator can not be easily used. Moreover, this error with estimator is not the lowest one, as detailed now. Indeed, using the central limit theorem when $N \to \infty$ for the estimator $\hat{\tau}$, one obtains:

$$\hat{\tau} \simeq \frac{P}{\Gamma} + \frac{U}{\sqrt{N}}\sqrt{\mathrm{Var}[\tau_i]} \tag{B.62}$$

where U is again a normally distributed variable with zero mean and variance 1. Therefore, one obtains for the estimator of the rate:

$$\hat{\Gamma}_2 \simeq \Gamma + \frac{U}{\sqrt{N}}\sqrt{\mathrm{Var}[\tau_i]}\frac{1}{\Psi_2'(\Gamma)}. \tag{B.63}$$

Since

$$\Psi_2'(\Gamma) = -\frac{1}{\Gamma^2}\left(P + (1-P)\log(1-P)\right), \tag{B.64}$$

the error on the rate through this estimation is obtained with the same technique as for the first method as:

$$\frac{\Delta\hat{\Gamma}_2}{\Gamma} \times \sqrt{N} = \frac{\sqrt{1-(1-P)^2 + 2(1-P)\ln(1-P)}}{P + (1-P)\ln(1-P)}. \tag{B.65}$$

This error with this estimator is presented in Fig. B.3 and compared to the first one. This estimator has the advantage that it gives a reliable result (a small error) when P approaches 1, which is not the case of $\hat{\Gamma}_1$. However, as explained above, it is very uneasy to use and the error with this estimator is larger than with the first method as soon as $P \leq 0.73$.

To obtain both a reliable and easily implemented estimator, one combines the two variables, escape probability and escape times. Starting from Eq. (B.58), one uses $\hat{P}$ as an estimated value of $(1 - e^{-\Gamma\tau_p})$. This defines the estimator:

$$\hat{\Gamma}_3 = \frac{\hat{P}}{\hat{\tau}} \tag{B.66}$$

which is indeed a function of two variables. Following L. Tournier [77], one applies the multidimensional central limit theorem:

$$\begin{aligned}\hat{\Gamma}_3 &\simeq \frac{P + \frac{U}{\sqrt{N}}\sqrt{P(1-P)}}{\frac{P}{\Gamma} + \frac{U'}{\sqrt{N}}\sqrt{\mathrm{Var}[\tau_i]}} \simeq \Gamma\frac{1 + \frac{U}{\sqrt{N}}\sqrt{\frac{1-P}{P}}}{1 + \frac{U'}{\sqrt{N}}\frac{\sqrt{\mathrm{Var}[\tau_i]}}{P/\Gamma}} \\ &\simeq \Gamma\left(1 + \frac{U}{\sqrt{N}}\sqrt{\frac{1-P}{P}} - \frac{U'}{\sqrt{N}}\frac{\sqrt{\mathrm{Var}[\tau_i]}}{P/\Gamma}\right)\end{aligned} \tag{B.67}$$

where U and U' are two *correlated* normally distributed variables. Now, the error of the estimation is obtained by calculating the variance of the last two terms of Eq. (B.67). In this calculation, the covariance of the two variables enters [77], which *reduces* the total error. Finally, the error simply writes for all values of P:

$$\frac{\Delta\hat{\Gamma}_3}{\Gamma} \times \sqrt{N} = \frac{1}{\sqrt{P}}. \tag{B.68}$$

The prediction for the error on the rate obtained for the different estimators is shown in Fig. B.3. It is clear that $\hat{\Gamma}_3$ takes the best of both worlds, and represents a very easy-to-use and accurate estimator for all values of P. We used this estimator for the simulations presented in Chapter 3.

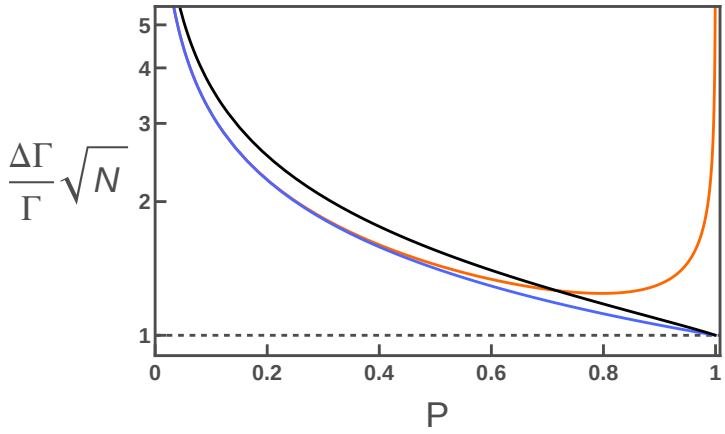

Fig. B.3. Orange line: Error for the estimator $\hat{\Gamma}_1$ that uses only the escape probability **Black line:** Error for the estimator $\hat{\Gamma}_2$ that uses only the escape times. **Blue line:** Error for the estimator $\hat{\Gamma}_3$ that uses both variables.

B.4 Details on the simulations

B.4.1 Technical specifications

The program in C++ presented in the following section, which calculates the escape rate of a particle out of a metastable well, has been run under Ubuntu using a Pentium Xeon E5440 (2.83 GHz), which contains two quad-core processors. It thus allows to launch eight different jobs simultaneously, on the same machine.

The simulation time depends crucially on the escape rate: for a rate exponent B in the range $[5-12]$, the predicted mean escape time in units of the inverse of the plasma frequency, approximately given by

$$\langle \tau_i \rangle \simeq 4\pi e^B \tag{B.69}$$

is in the range $[150-160000]$ (see Chapter 3 for details). To have a sufficient escape probability (and therefore a low error), the probing time τ_p has to be typically twice as large as this mean escape time. With a time step of $d\tau = 0.02$ and for $N = 10^4$ samples, this corresponds to a number of iterations $n_{\rm it}$ in the range $[150.10^6 - 160.10^9]$. For a single processor, neglecting transfer times, 10^6 iterations take $\simeq 0.8$ s, so that achieving a sufficient precision on the escape rate can be crudely summarized in the form:

$$B \in [5-12] \Rightarrow [2\,\text{min} - 20\,\text{h}] \tag{B.70}$$

Note that for the simulations probing the effect of Poisson noise, we sometimes used $N = 10^5$ instead of 10^4.

B.4.2 Example of a program

```
#include <iostream>
#include <sstream>
#include <fstream>
#include <string>
#include "random.h" // random number generator of J. Houdayer
#include "math.h"
#include "poisson_generator.C" // from Numerical Recipes in C++

using namespace std;
goodrandom Random;

//**** PHYSICAL PARAMETERS ****//
int seed=1; // to initialize the random numbers generator
double Q0=5,s,T=0;
double In=160,e=0.005;
const double gammaEsc=4; // Limit in phase to detect escape
double pi=3.1415927;

//**** SIMULATION PARAMETERS ****//
double dtau=0.02, tauP=250000, N=10000;
double biaslow=0.845, biasstep=0.02, biashigh=0.881;
double bias;
double signe=1;

//**** FUNCTIONS ****//

// B_gaussien() - Gaussian Noise - Returns a normally distributed
// random variable.

inline double B_gaussien(double factor){
return factor*(Random.Gaussian());}  // corresponds to Eq. 3.19
```

```
// B_asym() - Asymetric Noise - Returns a random variable
// distributed according to a Poisson law

inline double B_asym(){
long int toto=1110101001;  // for initialization of the generator
return e*(poidev(In*dtau,&toto)-In*dtau);} // corresponds to Eq. 3.21

// Escape() - Used to compute the dynamics
// for a given set of parameters and returns the escape time.
// Corresponds to the algorithm presented in Eq. 3.17

double Escape(double* tau, double* gamma){

*gamma=asin(s);
*tau=0;  double v=0;
double bruitT=sqrt(2*T/Q0*dtau);
double F1=0,F2=0;
double bruit, dgamma,dv;

  while(*gamma>-gammaEsc && *gamma<gammaEsc && *tau<tauP-dtau){
    bruit=B_gaussien(bruitT)+B_asym();
     F1=-sin(*gamma)+s;
     dgamma=v*dtau*(1-0.5/Q0*dtau)+0.5*F1*dtau*dtau+0.5*bruit*dtau;
     *gamma+=dgamma;
     F2=-sin(*gamma)+s;
      dv=-dgamma/Q0+0.5*(F1+F2)*dtau+bruit;
     v+=dv;
     *tau=*tau+dtau;
  };

  return 0;
};

// Pswitch - Used to repeat the dynamics N times
// for the same set of parameters

double Pswitch(double *proba, double *rate){

double tau=0.0,gamma=0.0,time=0.0;
*proba=0.0;*rate=0.0;

for(int run=1;run<=N;++run){
Escape(&tau,&gamma);
time+=tau/N;
if(gamma>gammaEsc||gamma<-gammaEsc) *proba+=1/N;
};

*rate=*proba/time;
return 0;
};

// Esse - Used to calculate the escape rate for various bias values.

double Esse(){

ostringstream fichier; fichier<<"..."<<".dat"; // To store into a file
ofstream res(fichier.str().c_str(),ios_base::app);
```

```
for (bias=biashigh;bias>=biaslow;bias=bias-biasstep){
s=signe*bias;
double proba=0.0,rate=0.0;
Pswitch(&proba,&rate);
res<<s<<"\t"<<proba<<"\t"<<rate<<endl;
};

return 0;
};

/* ################################## */
// MAIN: RATE FOR VARIOUS BIAS VALUES.

int main(){
Random.Seed(seed);
Esse();
};

/* ################################## */
```

B.5 The Andreev Levels Qubit

In this section, we detail the calculation of the matrix element of Eq. (6.3) between Andreev state presented in Chapter 6, and derive the relaxation rate to recover the results of Desposito and Levy Yeyati [101].

B.5.1 Hamiltonian and eigenstates

In absence of any perturbation, the "free" Hamiltonian in the basis $\{|\leftarrow\rangle, |\rightarrow\rangle\}$ is:

$$\mathcal{H}^0_{|\rightleftarrows\rangle} = \Delta \begin{pmatrix} \cos\frac{\delta}{2} & r\sin\frac{\delta}{2} \\ r\sin\frac{\delta}{2} & -\cos\frac{\delta}{2} \end{pmatrix} \tag{B.71}$$

$$= \Delta \left[\cos\frac{\delta}{2}\hat{\sigma}_z + r\sin\frac{\delta}{2}\hat{\sigma}_x \right] \tag{B.72}$$

with $r = \sqrt{1-\tau}$, where we used the Pauli matrices in the basis $\{|\leftarrow\rangle, |\rightarrow\rangle\}$:

$$\hat{\sigma}_z = \begin{pmatrix} 1 & 0 \\ 0 & -1 \end{pmatrix} \text{ and } \hat{\sigma}_x = \begin{pmatrix} 0 & 1 \\ 1 & 0 \end{pmatrix}. \tag{B.73}$$

To diagonalize, one introduces the angle θ as

$$\tan\theta = \frac{r\sin\frac{\delta}{2}}{\cos\frac{\delta}{2}} = r\tan\frac{\delta}{2}. \tag{B.74}$$

The rotation matrix $\mathcal{R}_\theta = \begin{pmatrix} \cos\frac{\theta}{2} & \sin\frac{\theta}{2} \\ -\sin\frac{\theta}{2} & \cos\frac{\theta}{2} \end{pmatrix}$ performs a rotation (see Eq. (22) p. 421 in [125]) to the basis $\{|+\rangle, |-\rangle\}$ with

$$\begin{cases} |+\rangle = \cos\frac{\theta}{2}|\leftarrow\rangle + \sin\frac{\theta}{2}|\rightarrow\rangle \\ |-\rangle = -\sin\frac{\theta}{2}|\leftarrow\rangle + \cos\frac{\theta}{2}|\rightarrow\rangle \end{cases} \tag{B.75}$$

and the Hamiltonian in this basis becomes

$$\mathcal{H}^0_{AS} = \begin{pmatrix} E_+ & 0 \\ 0 & E_- \end{pmatrix} \tag{B.76}$$

where $\{|+\rangle, |-\rangle\}$ are obviously the eigenstates of the Hamiltonian with eigenvalues $E_\pm = \pm\Delta\sqrt{1-\tau\sin^2\frac{\delta}{2}}$. One should note the relation:

$$\begin{aligned} \frac{\partial|+\rangle}{\partial\delta} &= \frac{\theta'}{2}|-\rangle \\ \frac{\partial|-\rangle}{\partial\delta} &= -\frac{\theta'}{2}|+\rangle \end{aligned} \tag{B.77}$$

where we defined

$$\theta' = \frac{\partial\theta}{\partial\delta} = \frac{r}{2}\frac{1}{1-\tau\sin^2\frac{\delta}{2}}. \tag{B.78}$$

Using the Pauli matrices $\hat{\sigma}_z^{AS}$ and $\hat{\sigma}_x^{AS}$ in the eigenbasis $\{|+\rangle, |-\rangle\}$, the free Hamiltonian is

$$\mathcal{H}^0_{AS} = E_+\hat{\sigma}_z^{AS}. \tag{B.79}$$

B.5.2 Matrix element for the transition

In presence of a perturbation $d\delta(t)$ around a value δ_0, the Hamiltonian can be written in the linear perturbation approach:

$$\mathcal{H}_{AS}(\delta) = \mathcal{H}^0_{AS}(\delta_0) + \frac{\partial\mathcal{H}^0_{AS}}{\partial\delta}d\delta(t) \tag{B.80}$$

where $\frac{\partial\mathcal{H}^0_{AS}}{\partial\delta}$ is proportional to the current operator:

$$\hat{I}_{AS} = \frac{1}{\varphi_0}\frac{\partial\mathcal{H}^0_{AS}}{\partial\delta}. \tag{B.81}$$

Using Eq. (B.79), the current operator in the basis of the Andreev states is:

$$\hat{I}_{AS} = \frac{1}{\varphi_0}\left[\frac{\partial E_+}{\partial\delta}\hat{\sigma}_z^{AS} + E_+\frac{\partial\hat{\sigma}_z^{AS}}{\partial\delta}\right]. \tag{B.82}$$

Using the relations (B.77), one has

$$\frac{\partial \hat{\sigma}_z^{AS}}{\partial \delta} = \frac{r}{2}\frac{\Delta^2}{E_+^2}\hat{\sigma}_x^{AS}. \tag{B.83}$$

The current is thus, in the basis of the Andreev states:

$$\hat{I}_{AS} = \frac{e\Delta^2}{\hbar E_+}\left[-\frac{1}{2}\tau \sin(\delta)\,\hat{\sigma}_z^{AS} + r\hat{\sigma}_x^{AS}\right] \tag{B.84}$$

which is the expression in [101]. One defines the non-diagonal matrix element $M_\perp$:

$$M_\perp = \varphi_0 \left\langle + \left| \hat{I}_{AS} \right| - \right\rangle = \frac{\Delta r}{2\sqrt{1-\tau \sin^2 \frac{\delta}{2}}} \tag{B.85}$$

and the diagonal term M_z:

$$M_z = \varphi_0 \left\langle + \left| \hat{I}_{AS} \right| + \right\rangle = \varphi_0 I_+(\delta). \tag{B.86}$$

Due to the finite matrix-element $M_\perp$ at finite reflection, the Andreev states are not the eigenstates of the current operator. A phase excitation will thus induce transitions between the levels.

Relaxation

One considers in the following that the population in the excited Andreev state α_e decays due to relaxation as:

$$\alpha_e \propto e^{-t/T_1} \tag{B.87}$$

where T_1 is the relaxation time ($\Gamma_1 = T_1^{-1}$ is the relaxation rate). Denoting Andreev gap the energy difference between the Andreev states $\hbar\Omega_A$, the relaxation rate is obtained from the Fermi Golden Rule ($k_B T \ll \hbar\Omega_A$) ([123], Eq. 3.29):

$$\Gamma_1 = \frac{1}{T_1} = \frac{\pi}{2}\left(\frac{D_\perp}{\hbar}\right)^2 S_\delta(\Omega_A). \tag{B.88}$$

The phase fluctuations $S_\delta(\omega)$ induced by the environment are related to the voltage fluctuations $S_V(\omega)$ across the set of harmonic oscillators representing the impedance $Z(\omega)$ in parallel by ([123], Eq. 3.59):

$$S_\delta(\omega) = \frac{1}{\varphi_0^2\omega^2} S_V(\omega) = \frac{4\pi}{\hbar R_K \omega^2} S_V(\omega). \tag{B.89}$$

From the quantum fluctuation-dissipation theorem, the noise spectral density is

$$S_V(\omega) = \frac{\hbar\omega}{2\pi}\left[\coth\left(\frac{\hbar\omega}{2k_BT}\right)+1\right]\mathrm{Re}\left[Z(\omega)\right] \simeq \frac{\hbar\omega}{\pi}\mathrm{Re}\left[Z(\omega)\right]H\left(\omega\right) \tag{B.90}$$

at zero temperature, with $H\left(\omega\right)$ the Heaviside function ([123], Eq. 3.102). The relaxation rate is thus ([123], Eq. 3.66):

$$\Gamma_1 = \frac{8\pi}{\hbar}\frac{M_\perp^2}{2\Delta\sqrt{1-\tau\sin^2\frac{\delta}{2}}}\frac{\mathrm{Re}\left[Z(\Omega_A)\right]}{R_K}. \tag{B.91}$$

Using Eq. (B.85), one obtains

$$\Gamma_1 = \pi\frac{\Delta}{\hbar}\frac{\mathrm{Re}\left[Z(\Omega_A)\right]}{R_K}\frac{1-\tau}{\left(1-\tau\sin^2\frac{\delta}{2}\right)^{3/2}} \tag{B.92}$$

which is the term W_R obtained in [101].

B.6 Critical current of a Josephson junction with electrodes having different gaps

We present in this section the expression for the temperature dependence of the critical current of a Josephson junction formed with electrodes having different gaps. We had to deal with this issue when treating the data on sample JJD1, in which the JJ detector had 20 nm and 80 nm thick Al electrodes. In this range, the gap significantly depends on thickness. Typically, for a layer ticker than 50 nm, the gap recovers the bulk value of $\Delta = 180\,\mu$eV for aluminum, while the gap can be increased up to $\Delta = 250\,\mu$eV when lowering the thickness below 10 nm [130]. For our junctions, the gaps of the two electrodes were thus significantly different. Since the expressions found in the litterature [3, 138, 139] are not expressed in a transparent way (or even erroneous [138]), we rederive the results here.

B.6.1 The superconducting gap

The gap as a function of the temperature is obtained numerically from Eq. (3.52) and (3.53) in [58], yielding at zero temperature the well-known

$$\Delta(0) = 1.76\,k_BT_C. \tag{B.93}$$

B.6.2 Symmetric electrodes

One first starts with the description of the simple case where the two electrodes have the same superconducting gap $\Delta(T)$.

Zero temperature

From Refs. [2, 47, 139], one obtains the Ambegaokar-Baratoff formula for the critical current at zero temperature:

$$I_0(0) = \frac{\pi}{2}\frac{\Delta(0)}{eR_J} \tag{B.94}$$

where R_J is the normal resistance of the junction.

Finite temperature

From [47, 139], the dependence in temperature of the critical current is:

$$I_0(T) = \frac{\pi}{2}\frac{\Delta(T)}{eR_J}\tanh\left(\frac{1}{2}\frac{\Delta(T)}{k_BT}\right), \tag{B.95}$$

therefore

$$\frac{I_0(T)}{I_0(0)} = \frac{\Delta(T)}{\Delta(0)}\tanh\left(\frac{1}{2}\frac{\Delta(T)}{k_BT}\right). \tag{B.96}$$

B.6.3 Asymmetric electrodes

We now consider the case where the two electrodes have different superconducting gaps Δ_1 and Δ_2. It is assumed without loss of generality that $\Delta_2 > \Delta_1$. One defines $\overline{\Delta} = \frac{\Delta_1+\Delta_2}{2}$ and $\delta = \frac{\Delta_2-\Delta_1}{2\overline{\Delta}}$. The calculation of the critical current starts from the prediction of [47, 139]:

$$I_0(T) = \frac{\pi k_BT}{R_J}\Delta_1(T)\Delta_2(T)\sum_{l=0,\pm1,\ldots}\left[\left(\omega_l^2+\Delta_1^2(T)\right)\left(\omega_l^2+\Delta_2^2(T)\right)\right]^{-1/2}, \tag{B.97}$$

where $\omega_l = (2l+1)\pi k_BT$.

Zero temperature

Close to $T = 0$, the values of $\omega_l = (2l+1)\pi k_BT$ are close one to another. The summation over l is thus replaced by an integral using $x = \omega_l$ as a variable. This yields a critical current at zero temperature[2]:

$$I_0(0) = \frac{\overline{\Delta}(1+\delta)}{eR_J}K\left[1-\left(\frac{1+\delta}{1-\delta}\right)^2\right] \underset{\delta\to0}{\simeq} \frac{\pi}{2}\frac{\overline{\Delta}}{eR_J}\left(1-\frac{3}{4}\delta^2\right) \tag{B.98}$$

where $K(y)$ is the complete elliptic integral of the first kind, with $K(0) = \frac{\pi}{2}$.

[2] The corresponding expression in [138] has an incorrect square-root in the argument of the function K.

Finite temperature

Assuming $\delta \ll 1$,

$$\left[\left(\omega_l^2+\Delta_1^2\right)\left(\omega_l^2+\Delta_2^2\right)\right]^{-1/2} \simeq \left(\omega_l^2+\overline{\Delta}^2\right)^{-1}\left(1-\frac{\overline{\Delta}^2\delta^2}{\omega_l^2+\overline{\Delta}^2}+\frac{2\overline{\Delta}^4\delta^2}{\left(\omega_l^2+\overline{\Delta}^2\right)^2}\right). \tag{B.99}$$

The sum in Eq. (B.97) simplifies to:

$$\frac{I_0(T)}{I_0(0)} = \frac{\pi}{2K\left(1-\left(\frac{\Delta_1(0)}{\Delta_2(0)}\right)^2\right)}\frac{\tanh\left(\frac{\overline{\Delta(T)}}{2T}\right)}{\frac{\Delta_1(0)}{2}\left(\frac{1}{\Delta_1(T)}+\frac{1}{\Delta_2(T)}\right)}\left(1+\frac{\delta^2}{4}u(T)\right) \tag{B.100}$$

where

$$u(T) = -1+\frac{\overline{\Delta}}{\sinh\frac{\overline{\Delta}}{T}}+\frac{\left(\overline{\Delta}/T\right)^2}{2\cosh^2\frac{\overline{\Delta}}{T}}. \tag{B.101}$$

In order to quantify the effect of the difference between the gaps, we compare the predictions for two sets of parameters which give the same critical current at low temperature. We take the parameters of Sample JJD1 (see Chapter 4), with $I_0 = 0.358\,\mu$A at low T and $R_J = 900\,\Omega$. These values are obtained with identical gaps from Eq. (B.94) for $\Delta_1 = \Delta_2 = 205\,\mu$eV. The opposite limit is obtained by taking $\Delta_1 = 180\,\mu$eV, the lowest (bulk) value for aluminum thin films. Equation (B.98) gives then $\Delta_2 = 236\,\mu$eV. The corresponding temperature dependencies[3] for the critical current are shown in Fig. B.4. For the range of temperatures probed in the experiment (see Fig. 4.20), which correspond to a critical current reduction of 10 % at most, the two predictions (for symmetric or asymmetric electrodes) don't differ significantly, which justifies a fit with a single gap value even if the thicknesses of the two electrodes forming the junctions were very different (20 and 80 nm).

[3] The precise convergence to 1 at $T = 0$ is obtained by going one order further in δ^2 in Eq. (B.100).

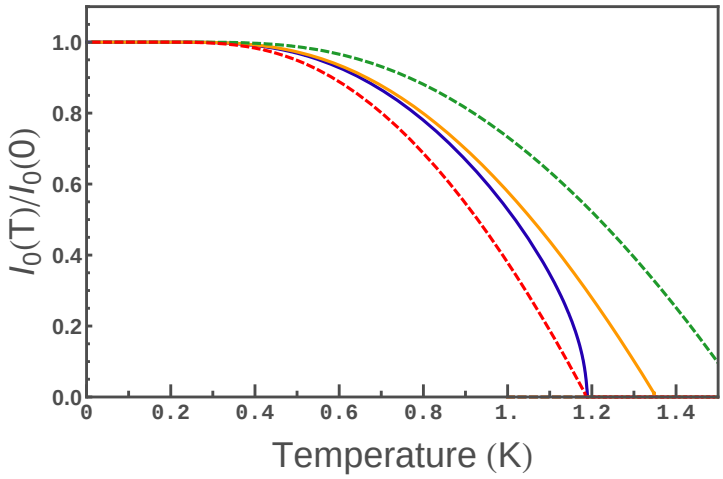

Fig. B.4. Solid lines: Josephson junction critical current as a function of temperature for $\Delta_1(0) = \Delta_2(0) = 205\,\mu$eV (orange - right) or $\Delta_1(0) = 180\,\mu$eV, $\Delta_2(0) = 236\,\mu$eV (blue - left). **Dashed lines:** Critical current from Eq. (B.96) for $\Delta(0) = 180\,\mu$eV (red - left) and $\Delta(0) = 236\,\mu$eV (green - right).

B.7 Attenuators

We present here a simple model for 50 Ω attenuators, which allows to calculate the attenuation when the output impedance differs from 50 Ω, but also to quickly identify an attenuator that has lost its label.[4]

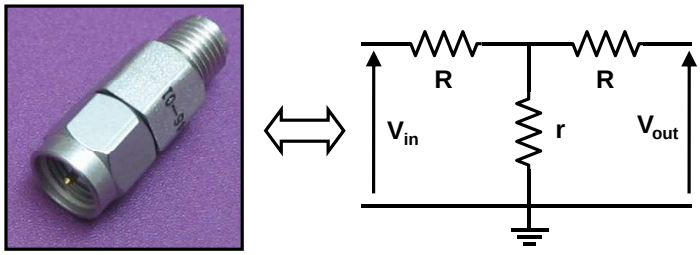

Fig. B.5. Model for an attenuator, with three resistances placed on a T.

An attenuator or a series of attenuators can be modeled by three resistances R, r and R on a symmetric T-shaped circuit, as shown in Fig. B.5. For an attenuator with an attenuation a in dB, the constraints on R and r are that when a 50 Ω impedance is connected at the output

[4] When mounting attenuators in the dilution refrigerator, we usually remove the label to obtain a good thermal contact between the attenuator and a copper clamp placed around it.

- the ratio of the output voltage to the input voltage is $\alpha = \frac{V_{\text{out}}}{V_{\text{in}}} = 10^{-a/20}$;
- the equivalent resistance seen from the input is $50\,\Omega$;

which imposes

$$\begin{cases} R = 50\,\frac{1-\alpha}{1+\alpha} \\ r = 100\,\frac{\alpha}{1-\alpha^2}. \end{cases} \tag{B.102}$$

The corresponding plot is shown in Fig. B.6. Table B.1 gives the values of r, R, $r+R$ and $2R$ for standard attenuation values. The two last combinations correspond to the resistance measured between one port and ground, and between the two ports, when the attenuator is disconnected. They allow to identify an attenuator with a simple ohm-meter.

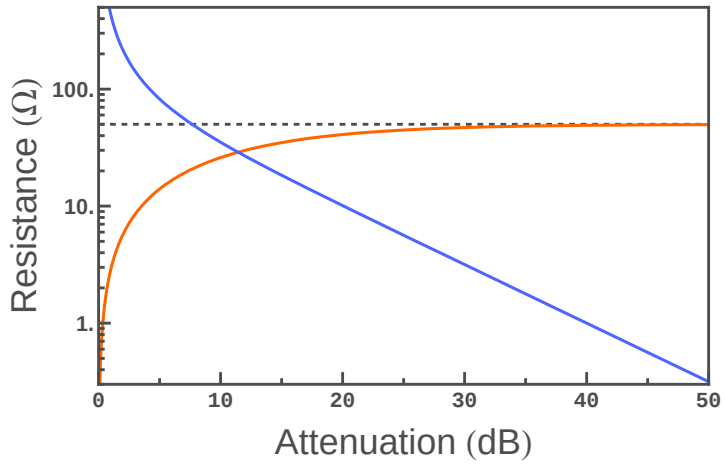

Fig. B.6. Resistance R (blue) and r (orange) as a function of the attenuation a in dB, for the model given in Fig. B.5.

Attenuation (dB)	1	2	3	6	10	20	30
r (Ω)	433	215	142	67	35	10	3.2
R (Ω)	2.9	5.7	8.5	17	26	41	47
$r+R$ (Ω)	436	221	150	84	61	51	50
$2R$ (Ω)	5.8	11.5	17	33	52	82	94

Table B.1. Parameters for the model given in Fig. B.5 for standard attenuations. The two last lines give the two combinations that can be measured with an ohm-meter on disconnected attenuators.

B.8 Correspondence between names

In this thesis	In the lab logbook
Sample JJD1	FCS 7
Sample JJD2	FCS 10
Sample AC1	PASTIS 1
Sample AC2	MAS 39
Sample SQUID	PAL 3

Table B.2. Correspondence between the samples names in this thesis and those appearing in the lab logbook.

Bibliography

1. P. W. Anderson and J. M. Rowell, *Probable Observation of the Josephson Superconducting Tunneling Effect*, Phys. Rev. Lett. **10**, 230 (1963). 1
2. B. Josephson, *Possible new effects in superconductive tunnelling*, Phys. Lett. **1**, 251 (1962). 1, 15, 263
3. A. Barone and G. Paterno, *Physics and Applications of the Josephson effect* (Wiley, New York, 1982). 1, 2, 15, 236, 262
4. H. Kramers, *Brownian motion in a field of force and the diffusion model of chemical reactions*, Physica **7**, 284 (1940). 2, 25, 61
5. H. Grabert, P. Olschowski, and U. Weiss, *Quantum decay rates for dissipative systems at finite temperatures*, Phys. Rev. B **36**, 1931 (1987). 2, 24, 30
6. J. Clarke and A. I. Braginski, editors, *The SQUID Handbook: Applications of SQUIDs and SQUID Systems II* (Wiley, New York, 2006). 2
7. M. Mück, C. Welzel, and J. Clarke, *Superconducting quantum interference device amplifiers at gigahertz frequencies*, App. Phys. Lett. **82**, 3266 (2003). 2
8. L. Spietz, K. Irwin, and J. Aumentado, *Input impedance and gain of a gigahertz amplifier using a dc superconducting quantum interference device in a quarter wave resonator*, App. Phys. Lett. **93**, 082506 (2008). 2
9. L. Levitov and G. Lesovik, *Charge-transport statistics in quantum conductors*, JETP Lett. **55**, 555 (1992). 2, 4
10. S. Pilgram, K. E. Nagaev, and M. Büttiker, *Frequency-dependent third cumulant of current in diffusive conductors*, Phys. Rev. B **70**, 045304 (2004). 2
11. H. Grabert, *Theory of a Josephson junction detector of non-Gaussian noise*, Phys. Rev. B **77**, 205315 (2008). 2, 5, 8, 33, 37, 43, 44, 45, 46, 48, 60, 64, 80, 110, 119, 130, 243
12. D. Urban and H. Grabert, in preparation. 2, 7, 73, 100, 110, 111, 119, 120, 121
13. A. Andreev, Sov. Phys. JETP **19**, 1228 (1964). 3, 138
14. A. Furusaki and M. Tsukada, *A unified theory of clean Josephon junctions*, Physica B (Amsterdam) **165-166**, 967 (1990). 3
15. C. Beenakker, *Universal limit of critical-current fluctuations in mesoscopic Josephson junctions*, Phys. Rev. Lett. **67**, 3836 (1991). 3
16. P. F. Bagwell, *Suppression of the Josephson current through a narrow, mesoscopic, semiconductor channel by a single impurity*, Phys. Rev. B **46**, 12573 (1992). 3, 138, 160
17. A. Zazunov, V. S. Shumeiko, E. N. Bratus', J. Lantz, and G. Wendin, *Andreev Level Qubit*, Phys. Rev. Lett. **90**, 087003 (2003). 3, 9, 144, 169
18. E. Scheer, P. Joyez, D. Esteve, C. Urbina, and M. Devoret, *Conduction channel transmissions of atomic-size aluminum contacts*, Phys. Rev. Lett. **78**, 3535 (1997). 3, 144, 146

19. N. Agraït, A. Levy Yeyati, and J. van Ruitenbeek, *Quantum properties of atomic-sized conductors*, Phys. Rep. **377**, 81 (2003). 3, 128, 144, 145
20. M. L. Della Rocca *et al.*, *Measurement of the Current-Phase Relation of Superconducting Atomic Contacts*, Phys. Rev. Lett. **99**, 127005 (2007). 3, 10, 137, 147, 148, 157, 168, 192
21. Y. M. Blanter and M. Buttiker, *Shot Noise in Mesoscopic Conductors*, Phys. Rep. **336**, 1 (2000). 4, 33, 35, 91, 97
22. L. Saminadayar, D. C. Glattli, Y. Jin, and B. Etienne, *Observation of the e/3 Fractionally Charged Laughlin Quasiparticle*, Phys. Rev. Lett. **79**, 2526 (1997). 4
23. R. de Picciotto *et al.*, *Direct observation of a fractional charge*, Nature **389**, 162 (1997). 4
24. X. Jehl, M. Sanquer, R. Calemczuk, and D. Mailly, *Detection of doubled shot noise in short normal-metal/ superconductor junctions*, Nature **405**, 50 (2000). 4
25. R. Cron, M. F. Goffman, D. Esteve, and C. Urbina, *Multiple-Charge-Quanta Shot Noise in Superconducting Atomic Contacts*, Phys. Rev. Lett. **86**, 4104 (2001). 4, 128
26. Y. V. Nazarov, editor, *Quantum Noise in Mesoscopic Physics* (Kluwer Academic Publishers, Dordrecht, 2003). 4
27. B. Reulet, J. Senzier, and D. Prober, *Environmental effects in the third moment of voltage fluctuations in a tunnel junction*, Phys. Rev. Lett. **91**, 196601 (2003). 4, 73, 75
28. J. Tobiska and Y. V. Nazarov, *Josephson Junctions as Threshold Detectors for Full Counting Statistics*, Phys. Rev. Lett. **93**, 106801 (2004). 5, 78
29. J. P. Pekola *et al.*, *Shot-Noise-Driven Escape in Hysteretic Josephson Junctions*, Phys. Rev. Lett. **95**, 197004 (2005). 5, 78
30. J. P. Pekola, *Josephson Junction as a Detector of Poissonian Charge Injection*, Phys. Rev. Lett. **93**, 206601 (2004). 5
31. J. Ankerhold, *Detecting Charge Noise with a Josephson Junction: A Problem of Thermal Escape in Presence of Non-Gaussian Fluctuations*, Phys. Rev. Lett. **98**, 036601 (2007). 5, 33, 37, 40, 41, 42, 48, 64, 80, 126, 243, 244
32. J. Ankerhold, *Erratum: Detecting Charge Noise with a Josephson Junction: A Problem of Thermal Escape in Presence of Non-Gaussian Fluctuations*, Phys. Rev. Lett. **99**, 139901 (2007). 5, 33, 37, 40, 41, 42, 48, 64, 243, 244
33. E. V. Sukhorukov and A. N. Jordan, *Stochastic Dynamics of a Josephson Junction Threshold Detector*, Phys. Rev. Lett. **98**, 136803 (2007). 5, 33, 37, 40, 42, 43, 44, 45, 65, 80
34. L. Billings, M. I. Dykman, and I. B. Schwartz, *Thermally activated switching in the presence of non-Gaussian noise*, Phys. Rev. E **78**, 051122 (2008). 5, 33, 40
35. B. Huard *et al.*, *Josephson junctions as detectors for non-Gaussian noise*, Annalen der Physik **16**, 736 (2007). 5, 37, 40, 49, 53, 67, 73, 78, 80, 81
36. B. Huard, *Interactions between electrons, mesoscopic Josephson effect and asymmetric current fluctuations (available on the website tel.ccsd.cnrs.fr)*, PhD thesis, Université Paris 6, 2006. 5, 10, 73, 78, 80, 88, 147, 154, 157, 160, 161, 224, 228
37. A. V. Timofeev, M. Meschke, J. T. Peltonen, T. T. Heikkilä, and J. P. Pekola, *Wideband Detection of the Third Moment of Shot Noise by a Hysteretic Josephson Junction*, Phys. Rev. Lett. **98**, 207001 (2007). 6, 39, 46, 47, 73, 78, 79, 80, 99, 115
38. Q. Le Masne, H. Pothier, N. O. Birge, C. Urbina, and D. Esteve, *Asymmetric Noise Probed with a Josephson Junction*, Phys. Rev. Lett. **102**, 067002 (2009). 7, 35, 44, 46, 48, 62, 67, 73, 81, 82, 110, 115, 119, 120
39. L. Levitov and G. Lesovik, *Charge distribution in quantum shot noise*, JETP Lett. **58**, 230 (1993). 7
40. J. Cuevas and W. Belzig, *Full counting statistics of multiple Andreev reflections*, Phys. Rev. Lett. **91**, 187001 (2003). 8, 85, 128
41. E. V. Sukhorukov and A. N. Jordan, *Achieving the Threshold Regime with an Overscreened Josephson Junction*, Phys. Rev. Lett. **102**, 086806 (2009). 8, 130

42. P. de Gennes, *Superconductivity of Metals and Alloys* (Addison-Wesley, New York, 1989). 8
43. G. Wendin and V. Shumeiko, arxiv:cond-mat/0508729, 2007. 9, 169
44. R. Cron, *Atomic Contacts: a Test-Bed for Mesoscopic Physics (available on the website tel.ccsd.cnrs.fr)*, PhD thesis, Université Paris 6, 2001. 10, 145, 146, 220, 226, 236
45. M. Chauvin, *The Josephson effect in superconducting atomic contacts (available on the website tel.ccsd.cnrs.fr)*, PhD thesis, Université Paris 6, 2005. 10, 140, 147, 160, 161, 213, 226
46. M. Devoret, *Quantum Fluctuations* (Elsevier, Amsterdam, Netherlands, 1997), chap. Quantum Fluctuations in Electrical Circuits, p. 351. 16, 143, 172
47. V. Ambegaokar and A. Baratoff, *Tunneling Between Superconductors*, Phys. Rev. Lett. **10**, 486 (1963). 17, 87, 88, 96, 143, 158, 263
48. W. C. Stewart, *Current-Voltage Characteristics of Josephson Junctions*, App. Phys. Lett. **12**, 277 (1968). 17
49. D. E. McCumber, *Effect of ac Impedance on dc Voltage-Current Characteristics of Superconductor Weak-Link Junctions*, J. App. Phys. **39**, 3113 (1968). 17
50. P. Hänggi, P. Talkner, and M. Borkovec, *Reaction-rate theory: fifty years after Kramers*, Rev. Mod. Phys. **62**, 251 (1990). 24, 25, 41, 54, 60, 64, 95
51. M. H. Devoret *et al.*, *Quantum Tunneling in Condensed Media* (Elsevier Science Publishers, 1992), chap. Macroscopic quantum effects in the current-biased Josephson junction, p. 313. 24, 30, 124, 194
52. W. Coffey, Y. P. Kalmykov, and J. Waldron, *The Langevin Equation* (World Scientific Publishing Co., London, 2003). 25
53. H. Risken, *The Fokker-Planck Equation* (Springer, Berlin, 1989). 25
54. E. Pollak, H. Grabert, and P. Hänggi, *Theory of activated rate processes for arbitrary frequency dependent friction: Solution of the turnover problem*, The Journal of Chemical Physics **91**, 4073 (1989). 26
55. H. Grabert, *Escape from a Metastable Well: The Kramers Turnover Problem*, Phys. Rev. Lett. **61**, 1683 (1988). 26, 61, 67
56. V. I. Mel'nikov, *The Kramers problem: Fifty years of development*, Phys. Rep. **209**, 1 (1991). 26, 27, 28, 67, 84
57. S. Linkwitz, H. Grabert, E. Turlot, D. Esteve, and M. H. Devoret, *Escape rates in the region between the Kramers limits*, Phys. Rev. A **45**, R3369 (1992). 26, 51, 59
58. M. Tinkham, *Introduction to superconductivity (Second Edition)* (Dover Publications, Inc. Mineola, NY, 1996). 27, 84, 158, 190, 262
59. M. H. Devoret, J. M. Martinis, D. Esteve, and J. Clarke, *Resonant Activation from the Zero-Voltage State of a Current-Biased Josephson Junction*, Phys. Rev. Lett. **53**, 1260 (1984). 28, 198, 245
60. S. Linkwitz and H. Grabert, *Enhancement of the decay rate of a metastable state by an external driving force*, Phys. Rev. B **44**, 11901 (1991). 28
61. M. H. Devoret, D. Esteve, J. M. Martinis, A. Cleland, and J. Clarke, *Resonant activation of a Brownian particle out of a potential well: Microwave-enhanced escape from the zero-voltage state of a Josephson junction*, Phys. Rev. B **36**, 58 (1987). 28, 39, 42, 124, 199
62. J. Ankerhold, *Quantum Tunneling in Complex Systems* (Springer, Berlin, 2007). 29
63. D. Esteve, M. Devoret, and J. Martinis, *Effect of an arbitrary dissipative circuit on the quantum energy levels and tunneling of a Josephson junction*, Phys. Rev. B **34**, 158 (1986). 30
64. J. M. Martinis and H. Grabert, *Thermal enhancement of macroscopic quantum tunneling: Derivation from noise theory*, Phys. Rev. B **38**, 2371 (1988). 30, 31, 32, 33, 37, 38, 195
65. J. T. Peltonen, A. V. Timofeev, M. Meschke, and J. P. Pekola, *Detecting Current Noise with a Josephson Junction in the Macroscopic Quantum Tunneling Regime*, JLTP **142**, 135 (2007). 30, 33, 37, 39, 47, 73, 79, 80

66. A. J. Leggett, *Quantum tunneling in the presence of an arbitrary linear dissipation mechanism*, Phys. Rev. B **30**, 1208 (1984). 30
67. A. N. Cleland, J. M. Martinis, and J. Clarke, *Measurement of the effect of moderate dissipation on macroscopic quantum tunneling*, Phys. Rev. B **37**, 5950 (1988). 31
68. T. Novotny, *Josephson junctions as threshold detectors of full counting statistics: open issues*, J. Stat. Mech. **2009**, 1050 (2009). 33
69. J. Ankerhold and H. Grabert, *How to Detect the Fourth-Order Cumulant of Electrical Noise*, Phys. Rev. Lett. **95**, 186601 (2005). 33, 130
70. T. T. Heikkilä, P. Virtanen, G. Johansson, and F. K. Wilhelm, *Measuring Non-Gaussian Fluctuations through Incoherent Cooper-Pair Current*, Phys. Rev. Lett. **93**, 247005 (2004). 33
71. G. Lesovik, *Non-Gaussian fluctuations of the current and voltage in quantum conductors*, JETP Lett. **60**, 806 (1994). 33, 78
72. N. van Kampen, *Stochastic processes in physics and chemistry* (North-Holland, 2001). 35, 247
73. K. Glaum and J. Ankerhold, private communication. 42, 243, 245
74. L. Schulman, *Technics and Applications of Path Integration* (Wiley, New York, 1981). 43
75. H. Grabert, private communication. 46, 48
76. E. Turlot, *Dynamique de l'effet tunnel quantique macroscopique d'une jonction Josephson (in French) (available on the website tel.ccsd.cnrs.fr)*, PhD thesis, Université Paris 11, 1990. 51, 57, 59
77. L. Tournier, private communication. 55, 255, 256
78. B. Mishra and T. Schlicka, *The notion of error in Langevin dynamics.*, J. Chem. Phys. **105**, 299 (1996). 57
79. B. Reulet, L. Spietz, C. Wilson, J. Senzier, and D. Prober, *Measurement of non-Gaussian shot noise: influence of the environment*, Proceedings of the SPIE International Symposium on Fluctuations and Noise (2004). 73, 75
80. Y. Bomze, G. Gershon, D. Shovkun, L. S. Levitov, and M. Reznikov, *Measurement of Counting Statistics of Electron Transport in a Tunnel Junction*, Phys. Rev. Lett. **95**, 176601 (2005). 73, 75, 76, 118
81. G. Gershon, Y. Bomze, E. V. Sukhorukov, and M. Reznikov, *Detection of Non-Gaussian Fluctuations in a Quantum Point Contact*, Phys. Rev. Lett. **101**, 016803 (2008). 73, 75, 76, 77, 129
82. M. Kindermann, Y. V. Nazarov, and C. W. J. Beenakker, *Feedback of the electromagnetic environment on current and voltage fluctuations out of equilibrium*, Phys. Rev. B **69**, 035336 (2004). 74
83. K. E. Nagaev, *Cascade Boltzmann-Langevin approach to higher-order current correlations in diffusive metal contacts*, Phys. Rev. B **66**, 075334 (2002). 74
84. S. Gustavsson *et al.*, *Counting Statistics of Single Electron Transport in a Quantum Dot*, Phys. Rev. Lett. **96**, 076605 (2006). 78
85. J. Peltonen, A. Timofeev, M. Meschke, T. Heikkilä, and J. Pekola, *Detecting non-Gaussian current fluctuations using a Josephson threshold detector*, Physica E **40**, 111 (2007). 78, 79
86. D. Vion, M. Götz, P. Joyez, D. Esteve, and M. H. Devoret, *Thermal Activation above a Dissipation Barrier: Switching of a Small Josephson Junction*, Phys. Rev. Lett. **77**, 3435 (1996). 83
87. H. Pothier, *Blocage de Coulomb et transfert d'électrons un par un (in English) (available on the website tel.ccsd.cnrs.fr)*, PhD thesis, Université Paris 6, 1991. 83, 184, 190
88. G. Ingold and Y. V. Nazarov, *Single Charge Tunneling* (Plenum, New York, 1992), chap. 2, p. 21. 91
89. J. M. Kivioja *et al.*, *Observation of Transition from Escape Dynamics to Underdamped Phase Diffusion in a Josephson Junction*, Phys. Rev. Lett. **94**, 247002 (2005). 99

90. J. M. Kivioja *et al.*, *Weak coupling Josephson junction as a current probe: effect of dissipation on escape dynamics*, New Journal of Physics **7**, 179 (2005). 99
91. V. M. Krasnov *et al.*, *Collapse of Thermal Activation in Moderately Damped Josephson Junctions*, Phys. Rev. Lett. **95**, 157002 (2005). 99
92. J. Männik *et al.*, *Crossover from Kramers to phase-diffusion switching in moderately damped Josephson junctions*, Phys. Rev. B **71**, 220509 (2005). 99
93. P. Joyez, P. Lafarge, A. Filipe, D. Esteve, and M. H. Devoret, *Observation of parity-induced suppression of Josephson tunneling in the superconducting single electron transistor*, Phys. Rev. Lett. **72**, 2458 (1994). 99
94. P. Lafarge, *Macroscopic Charge Quantization in Metallic Nanostructures (available on the website tel.ccsd.cnrs.fr)*, PhD thesis, Université de Paris 6, 1993. 103
95. D. F. Urban and H. Grabert, *Feedback and rate asymmetry of the Josephson junction noise detector*, Phys. Rev. B **79**, 113102 (2009). 121
96. R. Deblock, E. Onac, L. Gurevich, and L. P. Kouwenhoven, *Detection of Quantum Noise from an Electrically Driven Two-Level System*, Science **301**, 203 (2003). 124
97. A. Martin-Rodero *et al.*, *Quantum Noise in Mesoscopic Physics* (Kluwer Academic Publishers, Dordrecht, 2003), chap. 3. 128
98. S. Datta, *Electronic Transport in Mesoscopic Systems* (Cambridge University Press, Cambridge, 1997). 137, 144
99. P. F. Bagwell, R. Riedel, and L. Changa, *Mesoscopic Giaever and Josephson junctions*, Physica B **203**, 475 (1994). 139
100. D. A. Ivanov and M. V. Feigel'man, *Two-level Hamiltonian of a superconducting quantum point contact*, Phys. Rev. B **59**, 8444 (1999). 144, 169
101. M. A. Despósito and A. Levy Yeyati, *Controlled dephasing of Andreev states in superconducting quantum point contacts*, Phys. Rev. B **64**, 140511 (2001). 144, 169, 171, 173, 259, 261, 262
102. A. Abragam, *The Principles of Nuclear Magnetism* (Clarenton Press, Oxford, 1961). 144
103. E. Scheer *et al.*, *The signature of chemical valence in the electrical conduction through a single-atom contact*, Nature **394**, 154 (1998). 144
104. J. Moreland and J. W. Ekin, *Electron tunneling experiments using Nb-Sn "break" junctions*, J. App. Phys. **58**, 3888 (1985). 145
105. C. J. Muller, J. M. van Ruitenbeek, and L. J. de Jongh, *Experimental observation of the transition from weak-link to tunnel junction*, Physica (Amsterdam) **191C**, 485 (1992). 145
106. J. van Ruitenbeek *et al.*, *Adjustable nanofabricated atomic size contacts*, Rev. Sci. Instrum. **67**, 108 (1996). 145
107. D. M. Eigler, C. P. Lutz, and W. E. Rudge, *An atomic switch realized with the scanning tunnelling microscope*, Nature **352**, 600 (1991). 145
108. G. B. Arnold, *Superconducting tunneling without the tunneling Hamiltonian. II. Subgap harmonic structure*, JLTP **68**, 1 (1987). 145
109. D. Averin and A. Bardas, *ac Josephson Effect in a Single Quantum Channel*, Phys. Rev. Lett. **75**, 1831 (1995). 145
110. J. Cuevas, A. Martin-Rodero, and A. Levy Yeyati, *Resonant tunneling through a small quantum dot coupled to superconducting leads*, Phys. Rev. B **54**, 7366 (1996). 145
111. J. J. Riquelme *et al.*, *Distribution of conduction channels in nanoscale contacts: Evolution towards the diffusive limit*, Europhysics Letters **70**, 663 (2005). 146
112. M. F. Goffman *et al.*, *Supercurrent in Atomic Point Contacts and Andreev States*, Phys. Rev. Lett. **85**, 170 (2000). 146, 236
113. H. Fritz and J. Ankerhold, *Nonadiabatic transitions between adiabatic surfaces: Phase diffusion in superconducting atomic point contacts*, Phys. Rev. B **80**, 064502 (2009). 147, 160, 182, 183
114. M. Chauvin *et al.*, *Crossover from Josephson to Multiple Andreev Reflection Currents in Atomic Contacts*, Phys. Rev. Lett. **99**, 067008 (2007). 147

115. A. A. Golubov, M. Y. Kupriyanov, and E. Il'ichev, *The current-phase relation in Josephson junctions*, Rev. Mod. Phys. **76**, 411 (2004). 147, 160
116. M. C. Koops, G. V. van Duyneveldt, and R. de Bruyn Ouboter, *Direct Observation of the Current-Phase Relation of an Adjustable Superconducting Point Contact*, Phys. Rev. Lett. **77**, 2542 (1996). 147
117. D. Vion *et al.*, *Manipulating the Quantum State of an Electrical Circuit*, Science **296**, 886 (2002). 148
118. H. Miyazaki, A. Kanda, and Y. Ootuka, *Current-phase relation of a superconducting quantum point contact*, Physica C **437-438**, 217 (2006). 148
119. Z. Dai and A. Marchenkov, *Subgap structure in resistively shunted superconducting atomic point contacts*, App. Phys. Lett. **88**, 203120 (2006). 148
120. V. Lefevre-Seguin, E. Turlot, C. Urbina, D. Esteve, and M. H. Devoret, *Thermal activation of a hysteretic dc superconducting quantum interference device from its different zero-voltage states*, Phys. Rev. B **46**, 5507 (1992). 151, 190, 192, 194, 246
121. D. Averin and H. T. Imam, *Supercurrent Noise in Quantum Point Contacts*, Phys. Rev. Lett. **76**, 3814 (1996). 154, 161
122. A. Zazunov, V. S. Shumeiko, G. Wendin, and E. N. Bratus', *Dynamics and phonon-induced decoherence of Andreev level qubit*, Phys. Rev. B **71**, 214505 (2005). 169, 172
123. A. Cottet, *Implementation of a quantum bit in a superconducting circuit (available on the website tel.ccsd.cnrs.fr)*, PhD thesis, Université Paris 6, 2002. 173, 176, 261, 262
124. J. Ankerhold and H. Grabert, *Enhancement of Macroscopic Quantum Tunneling by Landau-Zener Transitions*, Phys. Rev. Lett. **91**, 016803 (2003). 176
125. C. Cohen-Tannoudji, B. Diu, and F. Laloë, *Mécanique Quantique* (Hermann, Paris, 1973). 177, 260
126. F. Balestro, J. Claudon, J. P. Pekola, and O. Buisson, *Evidence of Two-Dimensional Macroscopic Quantum Tunneling of a Current-Biased dc SQUID*, Phys. Rev. Lett. **91**, 158301 (2003). 186
127. F. Balestro, *Dynamique quantique d'un SQUID-DC (in French) (available on the website tel.ccsd.cnrs.fr)*, PhD thesis, Université Joseph Fourier, Grenoble, France, 2003. 186, 190, 198, 245
128. J. Claudon, F. Balestro, F. W. J. Hekking, and O. Buisson, *Coherent Oscillations in a Superconducting Multilevel Quantum System*, Phys. Rev. Lett. **93**, 187003 (2004). 186
129. J. Claudon, *Oscillations cohérentes dans un circuit quantique supraconducteur: le SQUID dc (in French) (available on the website tel.ccsd.cnrs.fr)*, PhD thesis, Université Joseph Fourier, Grenoble, France, 2005. 186, 187, 190, 194, 238, 239, 245
130. F. Nguyen, *Cooper Box Circuits: two-qbit gates, single-shot readout, and current to frequency conversion*, PhD thesis, Université Paris 6, 2008. 207, 209, 262
131. D. Vion, P. F. Orfila, P. Joyez, D. Esteve, and M. H. Devoret, *Miniature electrical filters for single electron devices*, J. App. Phys. **77**, 2519 (1995). 228
132. H. le Sueur and P. Joyez, *Microfabricated electromagnetic filters for millikelvin experiments*, Rev. Sci. Instrum. **77**, 115102 (2006). 228
133. T. Holst, D. Esteve, C. Urbina, and M. H. Devoret, *Effect of a Transmission Line Resonator on a Small Capacitance Tunnel Junction*, Phys. Rev. Lett. **73**, 3455 (1994). 236
134. P. Bertet, private communication. 238
135. J. C. Fenton, P. J. Thomas, G. Yang, and C. E. Gough, *System for fast time-resolved measurements of c-axis quasiparticle conductivity in intrinsic Josephson junctions of Bi2Sr2CaCu2O8*, App. Phys. Lett. **80**, 2535 (2002). 239
136. A. Levy Yeyati, private communication. 239
137. B. Huard, H. Pothier, D. Esteve, and K. E. Nagaev, *Electron heating in metallic resistors at sub-Kelvin temperature*, Phys. Rev. B **76**, 165426 (2007). 241, 242

138. E. P. Balsamo, G. Paternò, A. Barone, P. Rissman, and M. Russo, *Temperature dependence of the maximum (dc) Josephson current*, Phys. Rev. B **10**, 1881 (1974). 262, 263
139. V. Ambegaokar and A. Baratoff, *Tunneling Between Superconductors*, Phys. Rev. Lett. **11**, 104 (1963). 262, 263